



**HAL**  
open science

# Clinical application of laser Doppler holography in ophthalmology

Léo Puyo

► **To cite this version:**

Léo Puyo. Clinical application of laser Doppler holography in ophthalmology. Physics [physics]. Université Paris sciences et lettres, 2019. English. NNT : 2019PSLET022 . tel-02881930

**HAL Id: tel-02881930**

**<https://pastel.hal.science/tel-02881930>**

Submitted on 26 Jun 2020

**HAL** is a multi-disciplinary open access archive for the deposit and dissemination of scientific research documents, whether they are published or not. The documents may come from teaching and research institutions in France or abroad, or from public or private research centers.

L'archive ouverte pluridisciplinaire **HAL**, est destinée au dépôt et à la diffusion de documents scientifiques de niveau recherche, publiés ou non, émanant des établissements d'enseignement et de recherche français ou étrangers, des laboratoires publics ou privés.



**THÈSE DE DOCTORAT**

**DE L'UNIVERSITÉ PSL**

Préparée à l'ESPCI Paris  
Institut Langevin

**Application clinique de l'holographie laser Doppler en  
ophtalmologie**

Soutenue par

**Léo PUYO**

Le 30 septembre 2019

École doctorale n°564

**Physique en Ile de France**

Spécialité

**Physique**

**Composition du jury :**

Gereon HÜTTMANN Professeur, University of Lübeck	<i>Président</i>
Maciej WOJTKOWSKI Professeur, Polish Academy of Sciences	<i>Rapporteur</i>
Martial GEISER Professeur, HES-SO Valais-Wallis	<i>Rapporteur</i>
Corinne FOURNIER MCF, Université Jean Monnet	<i>Examinatrice</i>
Alain GAUDRIC Professeur émérite, Hôpital Lariboisière	<i>Examineur</i>
Mathias FINK Professeur, ESPCI - Institut Langevin	<i>Directeur de thèse</i>
Michel PAQUES PU-PH, Hôpital des Quinze-Vingts	<i>Co-directeur de thèse</i>
Michael ATLAN CR, ESPCI - Institut Langevin	<i>Examineur</i>





# Remerciements

Je me sens très chanceux d'avoir eu l'opportunité de travailler sur ce sujet de thèse : un immense merci à toi Michael. Pour m'avoir guidé dans le milieu de la recherche, pour m'avoir beaucoup appris, pour ton enthousiasme inépuisable, et pour avoir partagé ta passion. Merci Michel, pour ta confiance en ce projet, ta curiosité, et de m'avoir consacré de ton temps. Merci Mathias, d'avoir accepté d'être directeur de ma thèse et partagé tes connaissances scientifiques, mais aussi pour ta bienveillance et tes chaleureux encouragements à persévérer. Je remercie les membres du jury d'avoir bien voulu s'intéresser à mes travaux, et d'avoir fait le déplacement pour assister à la soutenance. En particulier merci à MM. Hüttmann, Wojtkowski, et Geiser qui venaient de loin.

Merci Jean-Pierre Huignard, d'avoir toujours répondu présent pour répondre à des questions d'holographie. Merci à tous ceux du groupe Paris : Céline, Marie, Romain, Kristina, Serge, Claude, Elena. En particulier, un grand merci à Kate pour une myriade de coups de main filés à droite à gauche. Merci à tous les stagiaires avec qui j'ai pu travailler. En particulier Armand Touminet, Thomas Andal, Louis Pallegoix, et la ribambelle à peu près infinie de ceux qui ont travaillé sur Holovibes.

J'adresse de chaleureux remerciements à Philippe Bonnin et Alain Gaudric, qui ont eu la patience de m'expliquer les rudiments de leurs disciplines, et d'avoir partagé leur enthousiasme. Il y a bien des personnes que je dois remercier pour des échanges scientifiques fort utiles, et pour lesquels j'ai aussi dé l'amitié : merci mes chers collègues de l'institut Langevin. Merci Slava, mon sputnik de thèse, et aussi Pedro, Jules, Peng, Julie.

Je n'oublie bien sûr pas mes autres camarades de l'institut Langevin. A commencer par mes co-bureaux : Romain (d'ailleurs, bonjour Romain), Mathieu, Claire, Samuel, Vincent, Clément, Kassandra. Merci surtout à Margaux, pas d'avoir essayé de me faire découvrir d'autres horizons cinématographiques, bien tenté. Merci Simon pour ces dépannages Adobe Illustrator et ces conversations que seules peuvent avoir les personnes munis du pass UGC Illimité. Merci aussi à ceux des bureaux R33 : merci Guillaume B., Jeanne, Elise, François L., William, Guillaume DMDH. et Gauthier, pour votre chaleureux accueil et votre confortable divan. Je garde aussi quelques pensées pour ceux du bureau R31 : Maxime, Paul, Kammel. Merci Bart pour ces séances de babyfoot musclées ! Merci aux plus vieux aussi d'avoir été accueillants avec les p'tits nouveaux : Nicolas, François B., Nathan, Olivier.

Merci mes amis d'en dehors de la recherche : mes cousin.e.s. pour votre indéfectible amitié. Merci Jo' pour tes encouragements, et Quentin de m'avoir permis de garder les pieds dans l'étrier pendant ces trois années. Et enfin merci à toute ma famille pour votre soutien, et de n'avoir pas trop pris ombrage du temps que j'ai consacré à ma thèse.



Figure 1: "Look again at that dot. That's here. That's home. That's us. On it everyone you love, everyone you know, everyone you ever heard of, every human being who ever was, lived out their lives. The aggregate of our joy and suffering, thousands of confident religions, ideologies, and economic doctrines, every hunter and forager, every hero and coward, every creator and destroyer of civilization, every king and peasant, every young couple in love, every mother and father, hopeful child, inventor and explorer, every teacher of morals, every corrupt politician, every "superstar," every "supreme leader," every saint and sinner in the history of our species lived there—on a mote of dust suspended in a sunbeam." C. Sagan, Pale blue dot [1].

# Contents

<b>Introduction</b>	<b>7</b>
<b>1 Blood flow in the eye and its imaging</b>	<b>9</b>
1.1 About the eye . . . . .	9
1.1.1 Retinal vasculature . . . . .	9
1.1.2 Choroidal vasculature . . . . .	10
1.1.3 The physiology of blood flow . . . . .	12
1.1.4 Eye movements . . . . .	14
1.1.5 Vascularization in pathologies . . . . .	15
1.2 Imaging blood flow in the eye . . . . .	18
1.2.1 Invasive optical methods: FA and ICG-A . . . . .	19
1.2.2 OCT and OCT-A . . . . .	19
1.2.3 Laser speckle contrast . . . . .	22
1.2.4 Doppler ultrasound . . . . .	23
1.2.5 Laser Doppler flowmetry . . . . .	24
<b>2 Holography and laser Doppler</b>	<b>27</b>
2.1 Basic principles of holography . . . . .	27
2.1.1 Fresnel Domain . . . . .	27
2.1.2 Angular Spectrum domain . . . . .	29
2.1.3 Boundary between reconstruction domains . . . . .	30
2.2 Laser Doppler measurements . . . . .	32
2.2.1 Doppler broadening . . . . .	32
2.2.2 Wideband approach . . . . .	33
2.2.3 Narrowband approach . . . . .	35
2.2.4 Dual imaging channel laser Doppler holography . . . . .	35
<b>3 Imaging retinal blood flow</b>	<b>41</b>
3.1 Article: In-vivo laser Doppler holography of the human retina . . . . .	41
3.2 Ocular safety: ISO 15004-2 (2007) . . . . .	59
3.3 Adaptability of the field of view . . . . .	60
3.4 Aberrations correction . . . . .	62
<b>4 Imaging the choroid</b>	<b>65</b>
4.1 Article: Choroidal vasculature imaging with laser Doppler holography . . . . .	65
4.2 Placement of the subject eye . . . . .	85
4.3 Large LDH color montage . . . . .	86
4.4 Depth of field . . . . .	87
4.5 Difference of spectrum panorama . . . . .	87

<b>5</b>	<b>Blood flow waveform analysis</b>	<b>89</b>
5.1	Article: Waveform analysis of retinal and choroidal blood flow with laser Doppler holography . . . . .	89
5.2	Retinal, cilio-retinal, and choroidal arterial waveforms . . . . .	113
5.3	Polarization: PBS - BS comparison . . . . .	113
5.4	Influence of $g_w$ parameter on the results . . . . .	115
5.5	Subtraction of baseline signal . . . . .	115
5.6	Measurements with Doppler ultrasound . . . . .	117
<b>6</b>	<b>Conclusions and perspectives</b>	<b>121</b>
6.1	Conclusion . . . . .	121
6.2	Perspectives . . . . .	122
6.3	Supplementary materials . . . . .	126
6.4	Scientific contribution . . . . .	130
<b>7</b>	<b>Résumé en français</b>	<b>131</b>
7.1	Introduction . . . . .	131
7.2	L'holographie laser Doppler . . . . .	134
7.2.1	Mesures laser Doppler . . . . .	134
7.2.2	Présentation de l'instrument . . . . .	135
7.2.3	Traitement des images . . . . .	136
7.3	Premiers résultats dans la rétine <i>in vivo</i> . . . . .	138
7.3.1	Mesures de flux dans les artères et veines de la rétine . . . . .	141
7.3.2	Différenciation artério-veineuse . . . . .	142
7.4	Application à l'imagerie de la choroïde . . . . .	143
7.4.1	Le LDH révèle non-invasivement la choroïde . . . . .	144
7.4.2	Différenciation artério-veineuse par analyse des débits . . . . .	145
7.4.3	Différenciation artério-veineuse rétinienne et choroïdienne . . . . .	147
7.5	Conclusion et perspectives . . . . .	147
	<b>Bibliography</b>	<b>150</b>

# Acronyms

AD: Alzheimer's disease AMD: age-related macular degeneration  
AOMs: acousto-optic modulators  
B-scan: brightness scan (two-dimensional cross-sectional view)  
CLRA: cilio-retinal artery  
COV: coefficient of variation  
CRA: central retinal artery  
CRV: central retinal vein  
DPSD: Doppler power spectrum density  
ICG-A: indocyanine green angiography  
IOP: intra-ocular pressure  
LDH: laser Doppler holography  
LSFG: laser speckle flowgraphy  
MPE: maximum permissible exposure  
OCT(A): optical coherence tomography (angiography)  
ONH: optic nerve head  
(P)BS: (polarized) beamsplitter  
RPE: retinal pigment epithelium  
SD-OCT: spectral domain optical coherence tomography  
SNR: signal to noise ratio  
(S)PCA: (short) posterior ciliary artery  
SS-OCT: swept-source optical coherence tomography  
STFT: short-time Fourier transform  
VEGF: vascular endothelial growth factor



# Introduction

Sight is a dominant sense [2], and the dearest of all for many people. Loss of vision dramatically affects the quality of life by compromising one's ability to engage in day-to-day activities. Consequently, vision loss is a condition well associated with depression in old age, making people affected by vision impairment 2 to 3 times more likely to be depressed than average [3]. The general population in developed countries is aging, which comes along with an increasing prevalence of age-related macular degeneration (AMD) and glaucoma. Likewise, the contemporary lifestyle and modern dietary choices are favorable to the development of diabetic retinopathy. The proliferation of these sight threatening diseases represents a major public health issue for the coming years. Early diagnostic of conditions such as AMD, glaucoma, diabetic retinopathy is all the more important that the development of these diseases can be stopped or at least very effectively slowed down. In all too many cases, the outcome of these diseases could be and should be avoided. The development of optical coherence tomography (OCT) in the last decades has illustrated the fantastic return on investment of ophthalmic technologies [4]. Research in ophthalmology is therefore at the crossroads between these humanistic and economic reasons.

Blood flow operates the supply in oxygen and glucose to the body and the evacuation of metabolic waste, which makes it an essential constituent of the body's health. Blood flow is one way or another associated to many diseases and especially ocular pathologies, and as such, it is a fundamental piece of the puzzle to tackle these diseases. First, because disposing of a way of measuring blood flow could prove useful as a research tool to understand the pathophysiology of diseases: it is often not known whether a blood flow decrease is the cause or consequence of tissue damage. According the role it plays in a disease pathogenesis, blood flow could then be of importance for an early screening or even prevention. Last but not least, blood flow could be used to monitor the efficiency of an administrated treatment given for the purpose of improving vascular perfusion. An abnormal blood perfusion is also deeply rooted in the pathophysiology of some other critical diseases. For example, Alzheimer's disease (AD), which is the most common neurodegenerative disorder and is characterized by amyloidosis of brain tissues, seems to be closely linked with reduced cerebral blood flow. Cerebral blood flow is diminished in AD [5], is associated with the disease progression, and recent studies suggests that blood flow decrease precedes the neurodegeneration [6], and may even be a primary cause of the disease [7]. The retina is a peripheral sensory organ which shares embryonic origins with the brain, and whose vasculature originates from the cerebral vasculature. Thus, retinal blood flow and cerebral blood flow exhibit similarities in vascular responses, so retinal blood flow could be an interesting surrogate mean to assess cerebral blood flow. Particularly, monitoring retinal blood flow could potentially allow for the study of functional hyperaemia of the brain (increased blood flow supply in response to an increase of cerebral activity).

This PhD thesis aimed at introducing a blood flow imaging technique called laser Doppler holography (LDH) into the field of ophthalmology in order to study the vasculature of the posterior pole. LDH had previously demonstrated its ability to perform non-invasive and full-field blood flow measurements with a high temporal resolution, but only in rodents [8, 9, 10, 11]. The possibilities offered by LDH in the field of clinical

ophthalmology are explored in this thesis. The manuscript is organized as follows:

The first Chapter gives an overall presentation of the ocular circulation. A particular attention is devoted to the retinal and choroidal vasculatures, and how ocular blood flow is affected in common pathological conditions. Then an overview is given of the technologies that have been developed for ocular blood flow assessment in the last decades.

In Chapter 2, we introduce the basic concepts on which LDH relies: namely digital holography and laser Doppler techniques. We detail for both of these techniques the role played by the spatial and temporal sampling of images and how to implement a dual imaging channel configuration in LDH.

In Chapter 3, it is demonstrated that with a fast camera, LDH is able to image blood flow changes in the human retina during cardiac cycles with a resolution of a few milliseconds. The laser Doppler broadening is analyzed with a short-time Fourier transform, and a blood flow contrast is drawn from the high-pass filtered Doppler power spectrum density. The contributions of ocular movements and pulsatile blood flow can be isolated in the Fourier analysis. We also explore the requirements in terms of camera sampling frequency and the limitation in temporal resolution achievable by the short-time Fourier transform analysis.

The fourth Chapter focuses on how LDH allows to reveal the choroidal vasculature. This feature is particularly advantageous as the choroid is challenging to image because of the optical barrier formed by the layers of photoreceptor and epithelial cells. LDH images of the choroid show a contrast quality similar to that of state of art instruments based on indocyanin-green angiography and optical coherence tomography, but unlike these methods LDH additionally provides quantitative measurements related to the flow. This ability is used to bring to light large differences of blood flow between choroidal arteries and veins, which can be exploited to perform an arteriovenous differentiation of choroidal vessels based on a color composite fusion of low and high frequency power Doppler images. The higher Doppler frequency shifts of light scattered in choroidal arteries allows LDH to be especially efficient to reveal them, in some cases from their formation at short posterior ciliary arteries until the arterioles branching.

Finally, in Chapter 5 we explore the possibility of separating the different contributions to the power Doppler. A spatio-temporal filtering is applied to data obtained with the same experimental setup as before, allowing to extract the blood flow waveform in retinal vessels. The flow waveform in retinal arteries and veins measured provides results more consistent with what is expected than before. Additionally, we demonstrate the use of a resistivity index mapping to characterize the flow waveform in arteries and veins which allows to perform unambiguous identification of retinal arteries and veins on the basis of their distinct systolodiastolic variations. Finally, we explore the possibility to monitor blood flow variations over cardiac cycle simultaneously in the choroid and retina.

# Chapter 1

## Blood flow in the eye and its imaging

### 1.1 About the eye

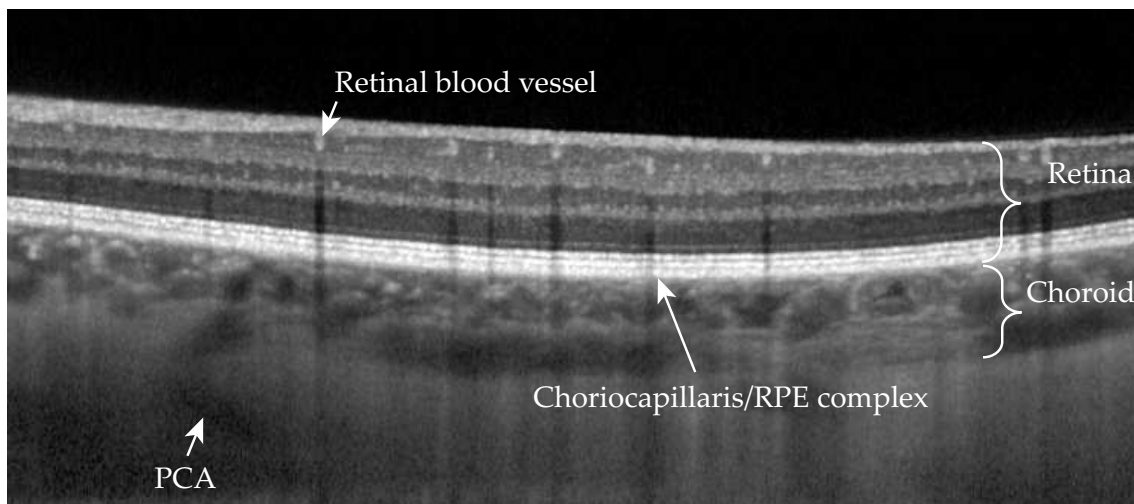


Figure 1.1: Cross-sectional view of the fundus with optical coherence tomography. The retinal and choroidal layers are separated at the level of the choriocapillaris/RPE complex. The retina supplies the neural retina whereas the choroid feeds the photoreceptor and RPE. The bright discs in the retina leaving shadows below them (projection artifacts) are retinal blood vessels. Some large and intermediate size choroidal vessels can be seen in the choroidal compartment, as well as a posterior ciliary artery in the sclera.

#### 1.1.1 Retinal vasculature

The retinal vasculature originates from the central retinal artery (CRA) and supplies the neural retina. The CRA is supplied by the ophthalmic artery and gives rise to arteries that supply the four quadrants of the retina (called inferior and superior, nasal and temporal quadrants). The large arteries (typical diameter  $100 - 150 \mu\text{m}$ ) run centrifugally from the optic disc and divide into smaller and smaller arteries, until they divide into retinal capillaries with a lumen diameter of  $3.5 - 6 \mu\text{m}$  [12]. In 18% of cases, in the vicinity of the optic nerve head, there may be a cilio-retinal artery derived from a choroidal artery which also contributes to the supply of the retinal vasculature. Depending on the region, there are between one and four capillary plexuses in the retina, stacked one on top of the other to feed the different neural cell layers of the retina [13]. Interestingly, there are no retinal

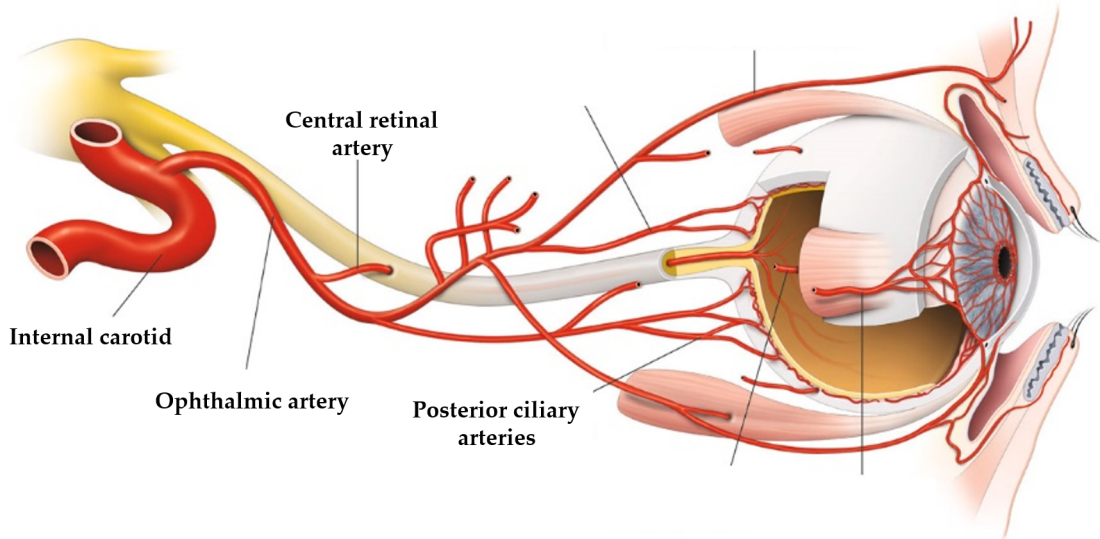


Figure 1.2: Schematic of the ocular vasculature: the internal carotid gives rise to the ophthalmic artery which itself branches into the central retinal artery and several posterior ciliary arteries. The central retinal artery enters the eye via the optic nerve and supplies the retinal vasculature, the blood is then drained by the central retinal vein. The choroid circulation is supplied by the posterior ciliary arteries and drained by the vortex veins.

capillaries in the fovea in a  $400\ \mu\text{m}$  wide area (fovea avascular zone). As blood circulates within the capillaries, it delivers oxygen to the cells through the intermediary of red blood cells (RBCs), and other substances such as nutrients, while evacuating metabolic waste. The retinal vasculature is located in the neural layers of the retina. As these layers are transparent, retinal vessels can be easily imaged optically.

### 1.1.2 Choroidal vasculature

The choroid supplies the outer retina with a blood flow delivered by the posterior ciliary arteries, which are branches of the ophthalmic artery just like the CRA. Between 10 and 20 short PCAs (SCPAs) emerge through the sclera into the eye around the optic nerve head in varying distributions to supply different areas of the choroid [12, 15]. There are also two long PCAs (nasal and temporal) per eye which supply the anterior portion of the choroid as well as the iris and ciliary body. Like any other vasculature, the arteries branch into smaller and smaller arterioles to finally supply the choroidal capillary plexus, which is called choriocapillaris. This choriocapillaris is a single layered and particularly dense capillary network which feeds the outer retina through the thin Bruch's membrane. The choriocapillaris constitutes the only blood supply to the photoreceptor and retinal pigment epithelium (RPE) cells. The venous drainage is done centrifugally with respect to the fovea; the smallest vein start draining flow close to the macular region and converge towards the very large vortex veins (up to  $300\ \mu\text{m}$ ) at high eccentricity. There is at least one vortex vein per quadrant, and a total number up to eight per eye [12]. Interestingly, the choroidal vasculature largely differs from the retinal vasculature in many important respects. First, the choroidal blood flow is estimated to be more than an order of magnitude greater than the retinal blood flow [16]. Another specificity that has long intrigued researchers is the small oxygenation difference between choroidal arteries and veins: the oxygen extraction rate has been found to be only 5% compared to 40% in the retinal vasculature [17]. Moreover, the choroidal arteriovenous network is asymmetrically organized: unlike almost all other vasculature in the human body, the blood flow in arteries and veins goes in the same direction. It has been suggested that it helps regulating the

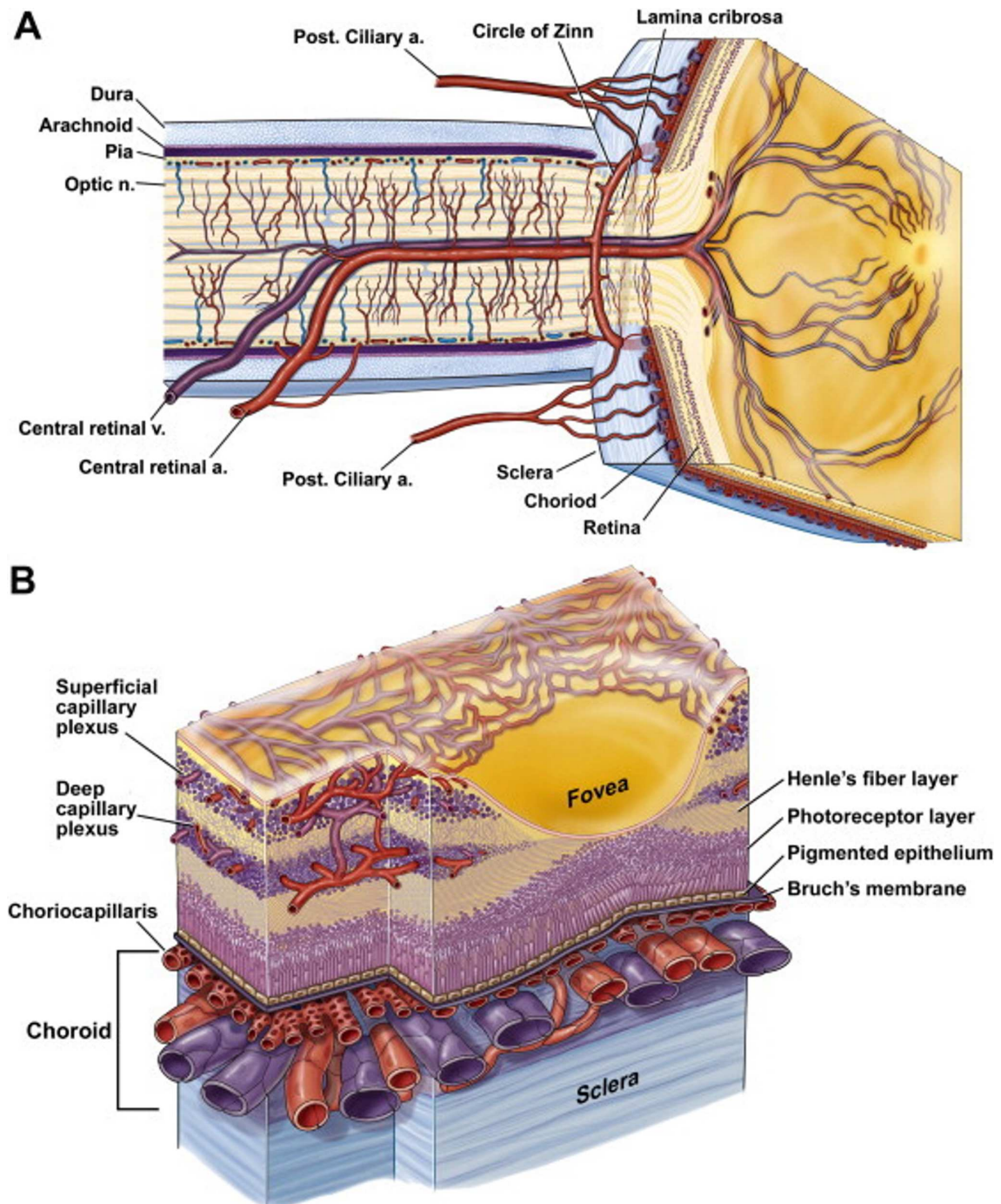


Figure 1.3: Drawings by Dave Schumick (adapted from [12]). A) Cross-sectional schematic in the optic disc region. The central retinal artery and vein are entangled in the optic nerve sheath with the nerve fibers. At the exit of the disc, the central retinal artery branches into four arteries that supply the four retinal quadrants. Short posterior ciliary arteries are seen as they enter the eye through the sclera to supply the choroid. B) 3D schematic of the eye fundus in the macular region. In the retina, different capillary plexuses supplying the neural retina are seen, except in the fovea where there are no retinal vessels. Below the retina are the photoreceptor and pigmented epithelium (RPE) layers. These two layers are supplied through the thin Bruch's membrane by the choriocapillaris. In the choroid, smaller vessels (arterioles and venules) are closer to the surface while large vessels are beneath, in the usually denominated Sattler and Haller layers.

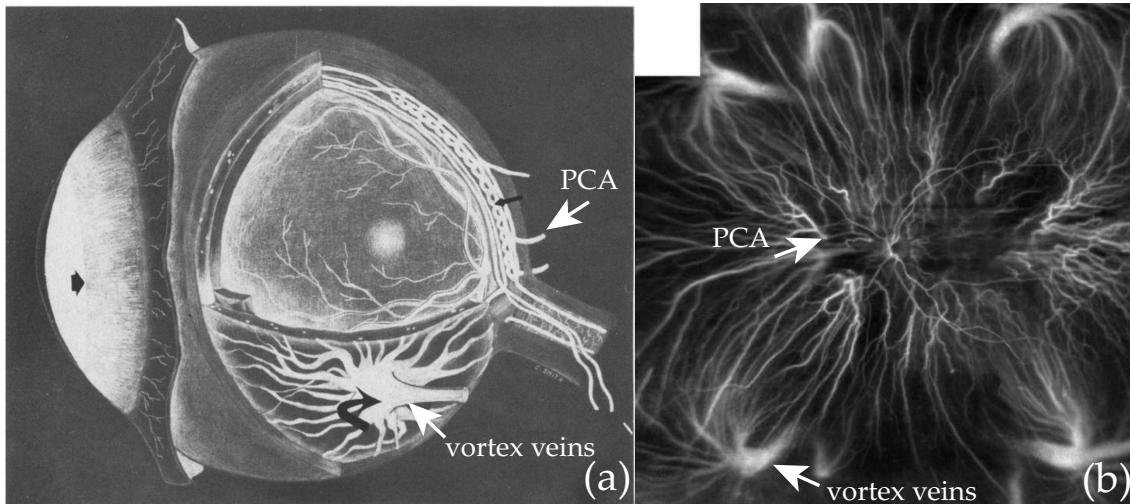


Figure 1.4: Choroidal vasculature. (a) Schematic representation of the eye showing the flow circulation in the choroid. The choroidal blood flow enters the eye through the posterior ciliary arteries (PCA) and is drained by the large vortex veins. These vortex (or vorticoses) veins drain the choroid and ciliary body circulation. There are at least one vortex vein per quadrant, and up to 8 vortex veins per eye in total. (b) Image obtained by line-scanning laser Doppler flowmetry (adapted from [14]). Choroidal arteries emerge from the sclera close to the optic disc, and vortex veins are in the periphery.

retinal temperature, either by cooling it to compensate for the photothermal heat, or by heating it to compensate for the eye direct exposure to the air temperature [18, 19, 20]. Finally, it could be mentioned that the choroidal capillaries have a greater size than retinal capillaries:  $3 - 18 \mu\text{m}$  (depending on the eccentricity), which makes for an especially low vascular resistance.

Compared to the retinal vasculature, the choroid is considerably more difficult to image which is why its physiology and role in ocular diseases are not fully understood. Firstly, because the RPE layer above the choroid optically acts a diffuser. Secondly, the greater velocities in choroidal vessels calls for faster acquisition rate in order to sample the speckle pattern fluctuation at an adequate rate.

### 1.1.3 The physiology of blood flow

The purpose of the vascular circulation is to supply every organ of the body with blood at a flow rate adapted to the level of metabolic activity of the organ. For adipose tissue, metabolic requirements are low whereas they are high for cerebral tissue. The flow rate is determined locally by the pressure gradient and vascular resistance according to an equation analogous to Ohm's law in electricity:

$$\Delta P = QR_h \quad (1.1)$$

Where  $\Delta P$  is the pressure gradient (quantified in mmHg),  $Q$  is the flow rate, i.e. the volume of blood circulating per unit time (usually expressed in mL/min), and  $R_h$  the hemodynamic resistance, i.e. the opposition to the passage of flow due to friction or shear force on the vascular wall. For a laminar fluid, the resistance value depends of the blood viscosity  $\mu$ , the vessel length  $l$ , and the vessel diameter  $r$ , and is given by the Hagen–Poiseuille law:

$$R_h = \frac{8\mu l}{\pi r^4} \quad (1.2)$$

As resistance is inversely proportional to the fourth power of vessel radius, changes in arteriole diameter result in large changes in vascular resistance. Thus in practice vascular

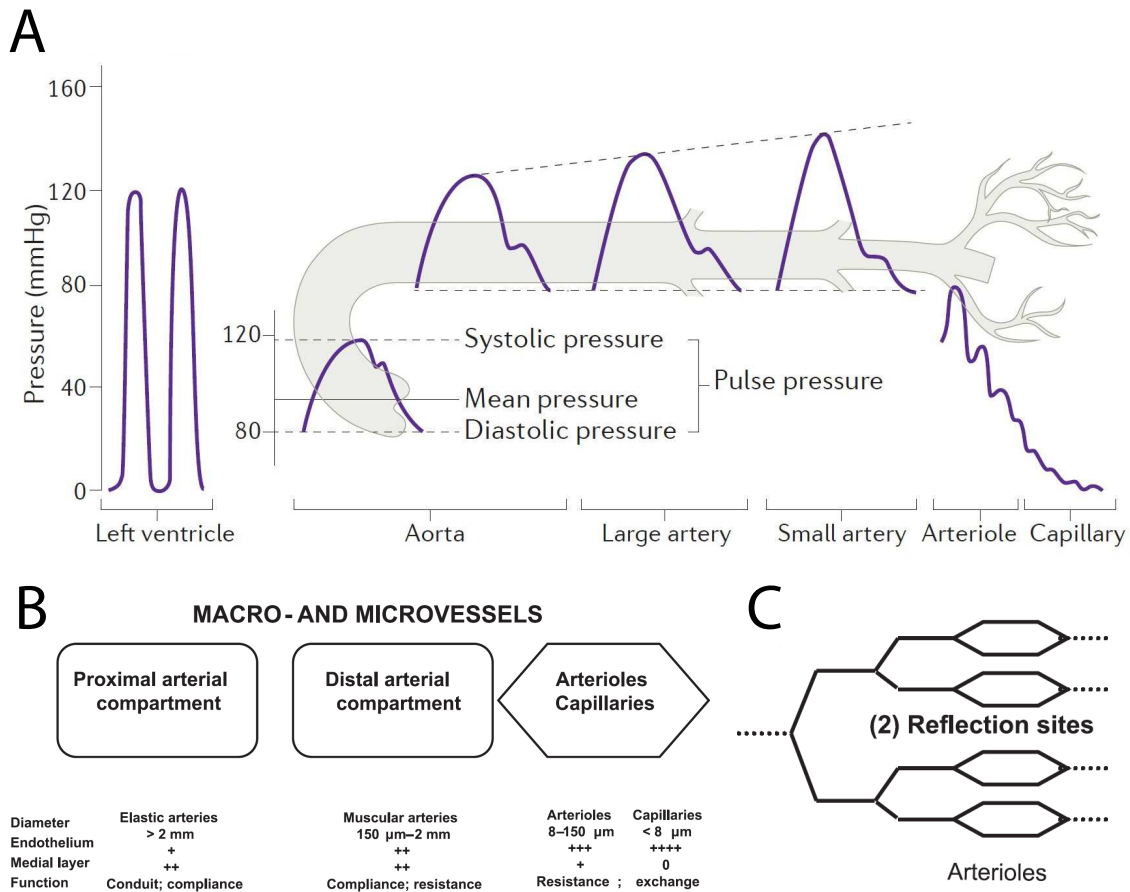


Figure 1.5: Physiology of blood flow. (A) Flow and pressure waveforms variations along the circulatory system (schematic adapted from [21]): the flow output from the left ventricle is intermittent, but the waveform is dampened in the aorta because of the high arterial compliance. In the arterioles, the modulation depth and mean arterial pressure is reduced because of the high vascular resistance so as to avoid increased pressure in the capillary bed. (B) (adapted from [22]): physiological characteristics of arteries and associated function: the vessel walls of large arteries (conduction arteries) and arterioles (distribution arteries) are differently constituted reflecting their different roles. (C) (adapted from [22]): Arteriolar bifurcations are the main sites of wave reflexions due to the impedance mismatch they induce.

resistance is regulated by changing the vessel radius.

The blood flow waveform gives the flow rate as a function of time; this function is very dependent upon the site of measurement with respect to the circulatory system. As shown in Fig. 1.5(A), the waveform profile varies along the vasculature, because as shown in Fig. 1.5(B), the physiological characteristics of arteries also vary along the vasculature. The cardiac cycle works the following way: the contractile activity of the heart generates a dynamic pressure, and a stroke volume is intermittently ejected from the left ventricle. The waveform initially looks like a rectangular function where systole marks the maximum pressure and diastole marks the minimum pressure. The propagation speed of the pressure wave is called pulse waveform velocity. The flow travels into the aorta and other large elastic arteries where it is dampened because of the high arterial compliance (capacity of a vessel to distend itself when the pressure increases). Elastic arteries distend during the systolic pressure increase, then recoil with the diastolic blood pressure fall. The aorta dilates in such way that it increases its volume by about 60% so the flow wave transfers as much energy to the aorta. This blood volume is then progressively given back to the flow

waveform with the result of decreasing systolic flow and increasing diastolic flow. This distend and recoil phenomena in elastic arteries is known as the Windkessel effect. In the analogy with an electrical circuit, arterial compliance plays the role of a capacity.

Further in the vascular tree, the blood flows into smaller arterioles and the precapillary sphincter. The vessels walls in these arterioles is made of smooth muscles that allow to change the caliber so as to contract or dilate and effectively change the local vascular resistance. This way the blood flow to a given organ can be regulated according to its needs (in response to the autonomic nervous system or local processes). When blood vessels dilate, the blood flow is increased due to a decrease in vascular resistance. The network of small arteries and arterioles creates a vascular resistance in which a nearly steady flow is achieved in the capillary, which facilitates oxygen extraction and protects them from microvascular damage.

Finally, the impedance mismatch between large vessels and arteriolar bifurcations is responsible for the generation of wave reflections, which is another phenomena that plays a role in shaping the blood flow waveform. The retrograde reflected waves superimpose with the forward (anterograde) wave. As explained further in section 1.1.5, the arterial stiffness is a key factor in the effect induced by waves reflection and possible pressure amplification. In the absence of wave reflections, the pressure and flow waves would have similar shapes. However, as reflections are present, the pressure and flow waves differ in shape.

In order to finely regulate the blood perfusion, other parameters can come into play such as variations of stroke volume, and heart rate frequency. The vascular circulation is here crudely described as other much more complex mechanisms and models could be evoked. However a conclusion that can already be drawn from this description of the factors shaping the blood flow physiology, is that in order to make measurements as relevant as possible to the tissue perfusion, they should be done as close as possible from the microvascular bed. It has been proposed to measure the vascular resistance of a given organ with the following index, termed resistivity index or Pourcelot index [23]:

$$RI = \frac{V_{systole} - V_{diastole}}{V_{systole}} \quad (1.3)$$

During the systolic peak pressure, the flow wave has no problem being pushed in all branches of the vasculature. However during diastole the pressure falls, and organs with a high vascular resistance resist the circulation of the low pressure flow. As a result, the diastolic end flow is lower in organs with a higher vascular resistance, resulting in a higher resistivity index. The retinal vasculature supplies a fragile neural tissue, so it has a low vascular resistance (roughly around 0.6-0.7 as measured with Doppler ultrasound in the central retinal artery), and the choroid has an even lower vascular resistance (around 0.5 as measured with the same instrument in the posterior ciliary arteries).

#### 1.1.4 Eye movements

Even when doing one's best to fixate exactly still, the human eye is in constant motion. These fixational eye movements are thought to be necessary to counteract the visual fading occurring during fixation due to adaptive neural mechanisms [24]. Thus it is thought that the purpose of these movements is not to stabilize the retina but to overcome the adaptation of neural cells response. Fixational eye movements can have a disastrous effect for ophthalmic instruments: for scanning instruments they call for non-linear registration procedures whereas for full-field instruments they introduce motion blur or phase instability. They are especially troublesome for blood flow measurements because the order of magnitude of the retinal displacement speed can be compared to the blood flow velocity. Fixational eye movements can be sorted into three main types, characterized by their frequency of occurrence, amplitude, and displacement speed (based on [25, 26]):

- Tremors are aperiodic motions with a bandwidth up to 150 Hz. It is the eye motion that has the smallest amplitude (typically 20 arc-seconds, i.e.  $1.5 \mu\text{m}$  with a conversion factor of  $273 \mu\text{m}$  for a degree of visual angle). The amplitude of tremors is very small, about the same as the theoretical resolution limit for diffraction limited ophthalmic instruments (which is not our case). However despite their small amplitude, tremors may contribute for example to the overall Doppler broadening and hinder our measurements.
- Drifts occur simultaneously with tremors; the motion they induce is slower but has a larger amplitude. During drifts, the image of the retina can be displaced by approximately a few dozen microns. The global motion of the eye is dominated by drifts and is quite monotonic until a microsaccade happens.
- Microsaccade is the fastest eye fixational eye movement, and also the one with the largest amplitude: 5 – 20 arcmin ( $25 - 100 \mu\text{m}$ ) with a speed up to 10 degrees per second (3 mm/s). Micro-saccades are different from saccades which occur when changing the locus of fixation. They happen at a rate of 3-4 per second and last for about 25 ms. Their purpose is to compensate for the drift retinal displacement so as to have the image of the fixated object form on the fovea again. Microsaccades make it very complicated to image the retina for any ophthalmic instruments, but because they last for a very short period of time, they can simply be ignored. As a side note, it is possible to reduce their frequency of occurrence for subjects familiar with ophthalmic examinations.

These motions can be even more dramatically problematic for patients with fixational issues: blinking may be more frequent and the amplitudes, velocities, and frequencies of occurrence of all type of movements can be amplified [26]. The effect on the laser Doppler broadening of such movements can hardly be immediately compared to the contribution of blood flow, because in the first case, all the cells of the fundus contribute to the Doppler broadening whereas in the second case only the RBCs play a role.

Movement	Amplitude	Displacement speed (arcmin/s)
Tremors	20 arcsec	50
Drifts	3 arcmin	20
Micro-saccades	10 arcmin	600

Table 1.1: Typical values for fixational eye movements in normal subjects.

### 1.1.5 Vascularization in pathologies

All the necessary substances such as nutrients and oxygen are delivered to cells by blood. Blood is also involved in the crucial tasks of metabolic wastes disposal, and body thermoregulation. In a word, blood perfusion plays a central role in maintaining the body running. Thus it is not surprise that an abnormal blood perfusion is often associated with diseases, and the eye is no exception.

#### Glaucoma

Glaucoma is a group of eye diseases which result in damage to the optic nerve (neuropathies) and vision loss. Worldwide, glaucoma is the second-leading cause of blindness after cataract. The most common type is open-angle glaucoma clinically characterized by pathological optic disc cupping. Less common types include closed-angle glaucoma and normal-tension glaucoma. Open-angle glaucoma develops slowly over time, starting with a decrease in peripheral vision followed by central vision which can ultimately lead to irreversible blindness. Intraocular pressure is considered as the major known causative risk

factor for the development and progression of glaucoma [27, 28]. However optic nerve damage may also occur with normal intra-ocular pressure (normal-tension glaucoma). As the eye cavity is at intra-ocular pressure, and retinal blood vessels are non-rigid, intra-ocular pressure influences blood flow; this has been particularly noticed in cases of spontaneous venous pulsations associated with glaucoma [29]. Perfusion to the retina and especially to the optic nerve head depends on the difference between ophthalmic artery pressure and intra-ocular pressure. Consequently, an increase in intra-ocular pressure goes with a decrease in perfusion pressure. Reduced blood flow in glaucoma has been shown with different measurement techniques but generally it is not known whether reduced blood flow is a cause or consequence of glaucoma [30, 31, 32]. The progression of the disease can be stopped but the early detection of glaucoma is very difficult: it is still usually diagnosed with a visual field examination. Recently, blood flow monitoring methods based on laser speckle flowgraphy (technique discussed further) have showed that it is possible to detect flow abnormalities in normal tension glaucoma [33].

### **Diabetic retinopathy**

Diabetic retinopathy is a retinal disease caused by diabetes mellitus. It is another leading cause of blindness, especially in countries where sedentary lifestyle and obesity is common as they are risk factors for the development of diabetes mellitus. The first stage is non-proliferative and has no symptoms. If unaware of their diabetes, patients usually do not notice any signs of early diabetic retinopathy because their vision remains unchanged. Unlike for glaucoma, the screening of diabetic retinopathy can be done in the early stages of the disease relatively easily. However the retina can be significantly damaged before any changes in the vision are noticeable. Diabetic retinopathy is characterized by an hyperpermeability of retinal blood vessels and the formation of microaneurysms. There follows a cycle of decrease in vessel perfusion, hypoxia, production of retinal VEGF, and resulting pathological neo-vascularization in proliferative diabetic retinopathy [34]. Laser photocoagulation and anti-VEGF treatments can be used to stop the development of the disease. Retinal blood flow is hypothesized to play a role during the development of diabetic retinopathy [35, 36]. Evidence suggests that hyperglycemia decreases retinal blood flow in early diabetes, then blood flow increases as the diseases progresses [37, 38].

### **Age-related macular degeneration**

Age-related macular degeneration (AMD) is an ocular disease that results in a loss of vision, starting with the center of the visual field. It is the most common cause of vision loss in people over the age of fifty in the US. AMD exists under the dry (non-exudative) and wet (exudative) forms, with the dry form making up to 90% of cases. In the wet form, anti-VEGF medication regularly injected into the eye slows the disease progression. However to this date, the therapeutic solutions found to stop the progression of AMD are unsatisfying. The disease show, among other manifestations, a dysfunction in the choriocapillaris - RPE complex. It is not always clear if it is the decrease in choriocapillaris perfusion that provokes the death of RPE cells or the loss of RPE cells that ends up with a choriocapillaris atrophy. It seems that in eyes with geographic atrophy, the RPE degenerates first while choriocapillaris loss is secondary, and conversely, in eyes with exudative AMD, degeneration of the choriocapillaris occurs while the RPE is still functional [39]. The ischemia that follows induces a production of vasoproliferative factors such as VEGF which results in choroidal neovascularization.

As far as ocular blood flow goes, AMD has more to do with choroidal blood flow than retinal blood flow. The choriocapillaris is of special interest for the study of AMD pathogenesis. However the investigation of the role played by the choroid has been so far studied through the lens of the choroidal thickness, which is insufficient to appreciate the

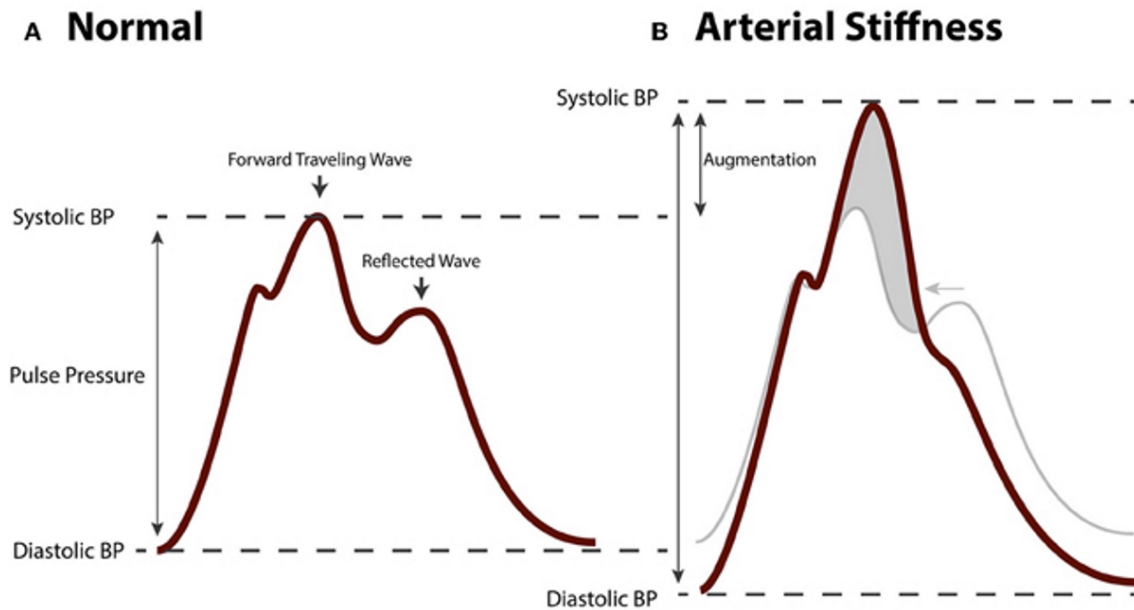


Figure 1.6: Modification of the blood flow with arterial stiffening. In normally elastic arteries, the Windkessel effect is at play and reflected pressure travel at a slower velocity. In the presence of arterial stiffness, the Windkessel effect is compromised and the pulse wave velocity is increased, resulting in a higher pulse pressure. Moreover, the amplification of the pressure wave is no longer distal but close to the heart which is another source of cardiovascular issues.

choriocapillaris perfusion. Therefore quantitative flow measurements in the choroid could prove more relevant to understand the disease progression. From laser Doppler flowmetry researches, it is known that choroidal blood flow decreases with ageing [40], and it is especially reduced in patients with AMD accordingly with the disease progression [41]. Moreover, it has been shown that there is an increase in vascular resistance in SPCAs (increased pulsatility and decreased end-diastolic blood flow velocity) in cases of AMD [42]. The decreases in flow occurs before the formation of the choroidal neovascularization, which suggests that these changes may have a role in the development of this choroidal neovascularization. Finally, considering that AMD and cardiovascular diseases have similar risk factors such as hypertension, it is plausible that the overall vascular circulation plays a role in AMD development.

### Arterial stiffness

In the elderly and people subject to arteriosclerosis, the viscoelastic properties of arterial walls are altered and arteries become more rigid. This loss of compliance is called arterial stiffness. It is associated with an increased risk of cardiovascular events. Arterial stiffness compromises the buffering function of large elastic arteries produced by the Windkessel effect. Thus it results in higher pulse pressure (i.e. the difference between systolic and diastolic blood pressure). It has another effect on the flow waveform by increasing the pulse wave velocity. The reflected pulse wave propagates faster in stiffer arteries (10-12 m/s or more instead of 5-7 m/s in compliant arteries) and superimposes during the systolic peak instead of the early diastole, which results in even higher pulse pressure [22]. This effect is illustrated in Fig. 1.6. Arterial stiffness is also a risk factor for arterial hypertension [21] which is a medical condition characterized by an abnormally high blood pressure. It is one of the main causes of cardiovascular, cerebrovascular and neurodegenerative complications. Arterial hypertension is especially deleterious when coupled to diabetic retinopathy [43].

Other ocular diseases closely to the vascular circulation include branch retinal vein

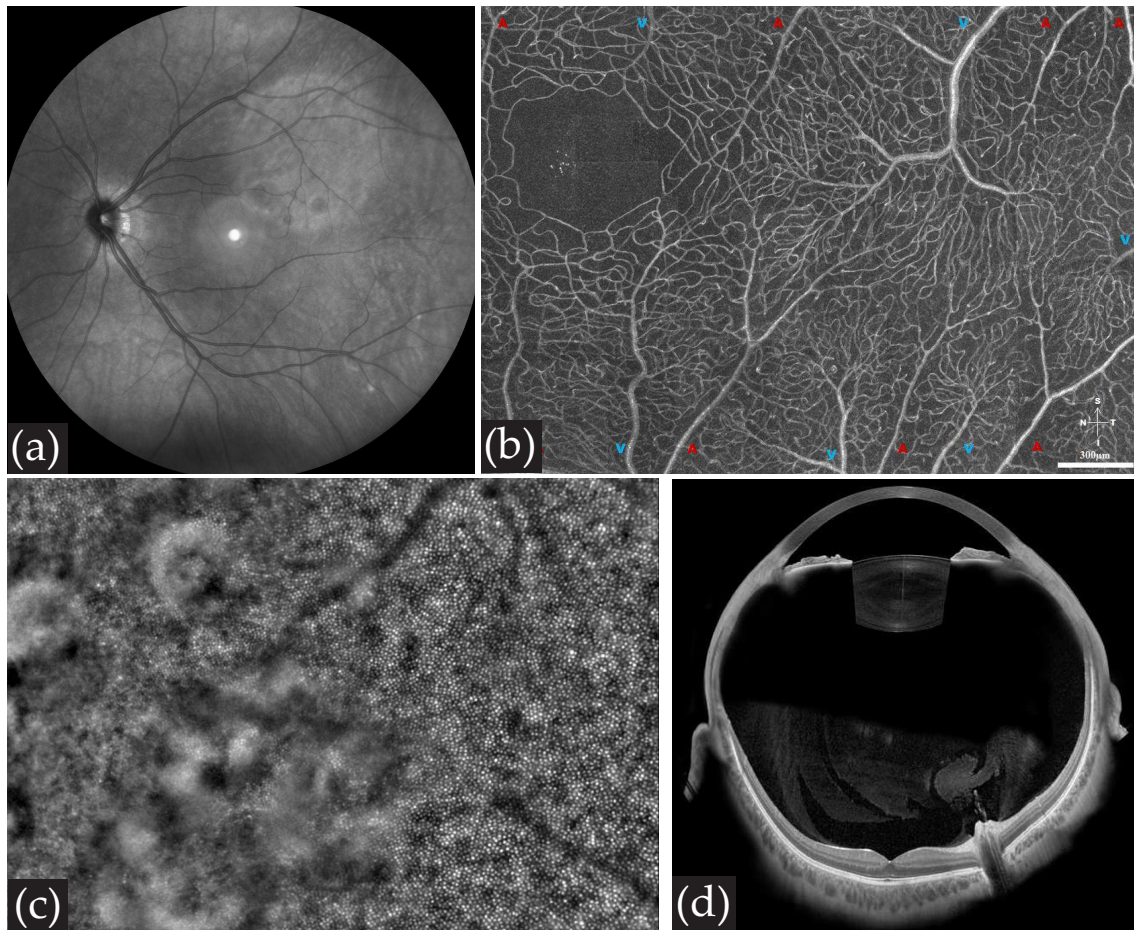


Figure 1.7: Imaging the eye with various modalities. (a) Scanning laser ophthalmoscopy (SLO), one of the most common ophthalmic instruments, provides en-face reflectance images of the retina (the choroid is not revealed). (b) Adaptive optics SLO (AO-SLO) revealing the retinal microvasculature close to the fovea with a diffraction limited resolution (adapted from the Burns Lab website, similar images can be found in [44]). (c) Adaptive optics flood illumination image (rtx1, Imagine Eyes) showing the photoreceptor mosaic. (d) OCT montage of the whole eye-ball (adapted from Heidelberg engineering website).

occlusion, central retinal artery occlusion, and central serous chorioretinopathy. For the latter, a thickening of the choroid is observed although it is not known whether this thickening comes with an increase or decrease of the local choroidal blood flow.

## 1.2 Imaging blood flow in the eye

We present here a non-exhaustive overview of the methods clinically used to image or measure the vasculature or blood flow in the eye. Non discussed techniques include the retinal vessel analyzer where the diameter of retinal vessels is measured along cardiac cycles to infer flow variations. As shown in Fig. 1.7, angiographic maps of the retinal vasculature can be obtained with SLO based on contrast of moving RBCs inside blood vessels, with a diffraction limited spatial resolution and confocal axial sectioning [45, 46]. These images can be used to measure the velocity of red blood cells in retinal capillary [47]. Several implementations of Doppler-OCT have been proposed with the idea of measuring blood flow from OCT data. The phase shift induced by the Doppler effect is measured in order to make quantitative flow measurements (in physical volume and velocity units); the measurement can be done with a good temporal resolution but only in single location [48].

### 1.2.1 Invasive optical methods: FA and ICG-A

In the past decades and still to this date, invasive methods such as fluorescein angiography (FA) and indocyanin-green angiography (ICG-A) have been popular to study the ocular circulation. Both of these methods are based on the use of a fluorescent contrast agent to reveal the vasculature. The particularity of these techniques is that the dye circulates first through the arteries and then through the veins, so it first reveals the arteries then the veins, as illustrated in Fig. 1.8. For FA, the excitation is made at 490 nm, and fluorescence images are made around 525 nm so it nicely reveals retinal vessels. For the Spectralis HRA from Heidelberg, ICG the excitation is made at 790 nm and images are performed with a filter at 830 nm (spectral values can vary from one instrument to another as the absorption and fluorescence spectra are quite wide). The excitation and fluorescence wavelengths of ICG further in the near-infrared spectrum allows for a better imaging of the choroid (as shown in Fig. 1.8), as light is less impeded by the optical barrier formed by the photoreceptors and RPE. ICG-A remains a popular method to image the choroid, and is the only commercialized instrument able to make a distinction between arteries and veins in the choroid. Choroidal arteries are however only revealed with difficulties because they are only briefly revealed by the dye. However FA is still used to this date to reveal leakage. Cases of diabetic retinopathy are especially interesting to study with FA, as leakage, neovascularization, and microaneurysms are efficiently revealed with the dye. FA reveals proliferation better than ICG because it is a contrast agents that binds to permeable particles whereas ICG is confined to the vasculature because it binds to large plasma proteins. Contrast agents can be used to measure mean arm-retina circulation time, and dye velocity within the retina, but these measurements do not allow for quantitative flow measurements. Some major downsides need to be considered for these methods. First the invasive nature of the examination is problematic: inconvenience for the patient, injection cost, and though very unlikely, risk of severe reaction to the dye. Most importantly, the contrast of the images is related to presence of fluorescent particles, and not really to the flow characteristics: it does not really provide any quantitative flow or velocity measurements.

### 1.2.2 OCT and OCT-A

Optical coherence tomography (OCT) was first demonstrated in 1991 [51], and has known a phenomenal success in ophthalmology because it was the first optical instrument able to perform cross-sectional images of the retina (see Fig. 1.9(a) for a B-scan example). OCT is a particularly well suited technique to image the development of retinal detachments occurring in AMD, as they are very well visible on cross-sectional cuts. Originally demonstrated in a time-domain configuration, OCT was then used in a spectral-domain mode for a better contrast, and later in a swept-source mode for faster acquisition which now allow en-face imaging of the choroid. Regarding the vascularization of the eye, OCT has been used extensively to study the choroidal thickness as a way to evaluate the role played by the choroid in health and disease [52]. However there are great inter-individual variations of choroidal thickness: a person can have a 20 or 700  $\mu\text{m}$  thick choroid and normal vision. Consequently, choroidal thickness is an incomplete assessment to understand the choroid, and en-face imaging of the choroid with ICG and with recently commercialized SS-OCT are very welcomed tools for clinicians. The limitation of OCT for en-face imaging of the choroid is that it does not allow for any sort of differentiation between arteries and veins, all vessels are entangled so images are hard to interpret (see Fig. 1.9(c)). The strong axial sectioning ability and volumetric imaging of OCT can come as a disadvantage to image the large choroidal vessels, because it does not provide a single image with a direct and simple overview of the choroid.

Later OCT-angiography (OCT-A) was introduced to produce images of the retinal

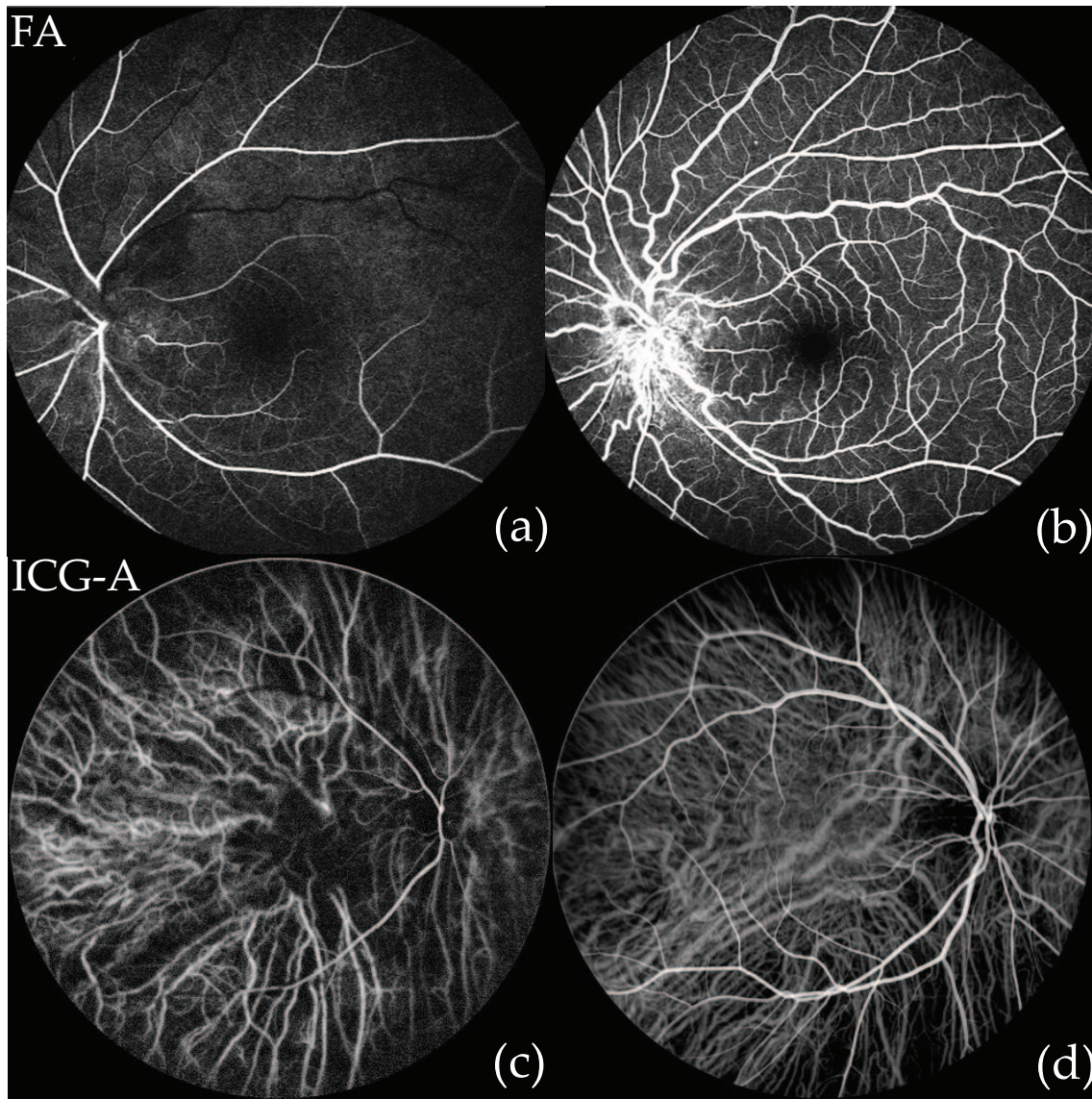


Figure 1.8: Fluorescein angiography (FA) and indocyanine-green angiography (ICG-A) progressively reveals arteries then veins as the contrast agent propagates into the vasculature. (a-b): FA reveals the retinal arteries then veins (images adapted from [49]). (c-d): ICG first efficiently reveals not only the retinal arteries but also the choroidal arteries. After a few seconds, the retinal and choroidal veins are then revealed. Finally, the retinal arteries remains visible whereas the choroidal arteries are no longer visible. The choroidal arteries are thus very briefly revealed by ICG which makes them more difficult to image than choroidal veins; typical ICG images thus usually only show choroidal veins (images provided by A. Gaudric).

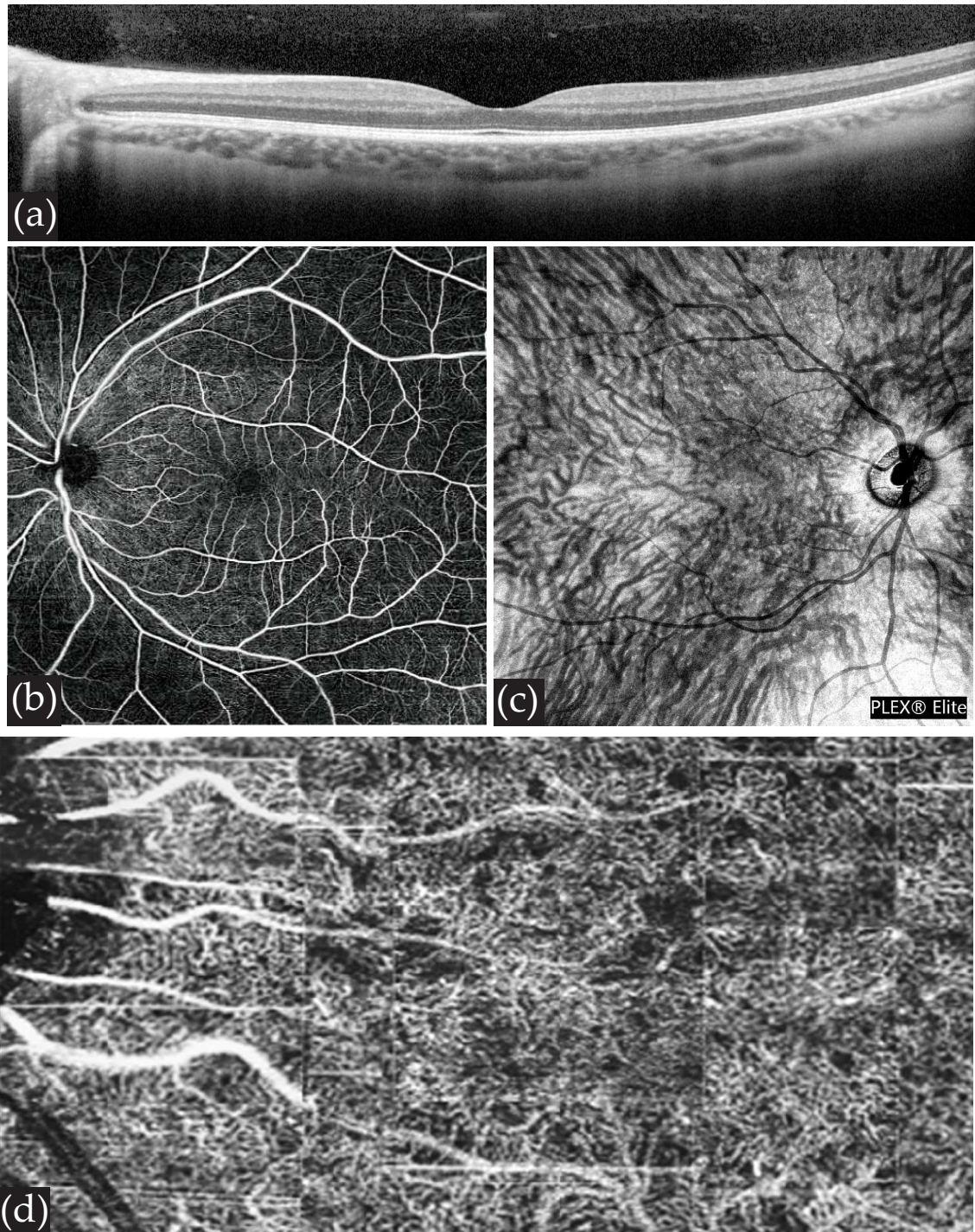


Figure 1.9: Imaging the eye with OCT and OCT-A. (a) an SD-OCT B-scan from a commercial instrument over 30 degrees of visual angle reveals the fundus layers: possible retinal detachments, the thickness of the choroidal compartment and NFL are especially studied. (b) en-face OCT-A revealing the retinal vasculature (adapted from Nidek website); the microvasculature density and extent of the foveal avascular zone are of particular interest. (c) en-face SS-OCT in the choroid revealing large choroidal vessels with a dark contrast (from another commercial instrument). (d) en-face SS-OCT-A reveals the choriocapillaris (adapted from [50]).

microvasculature based on the speckle fluctuations due to the circulation of RBCs (example shown in Fig. 1.9(b)). Several B-scans are acquired (typically two or four) and an algorithm based on a more or less sophisticated normalized standard deviation of the temporal

variations along the slow scanning axis reveals retinal capillaries. Structures such as blood vessels where rapidly moving RBCs generate a faster decorrelation time are very nicely revealed by OCT-A. Thus OCT-A produces blood flow contrasted images. The lateral resolution is limited by optical aberrations, but the spacing between retinal capillaries is large enough so that it is not necessary to have a diffraction limited spatial resolution to image the retinal microvasculature. OCT has found a second youth thanks to the spectacular images that can be produced with OCT-A, which can be used to measure the size of the foveal avascular zone, or the retinal microvascular density. In the last few years, promising images of the choriocapillaris have been obtained with OCT-A as shown in Fig. 1.9(d) [53, 50, 54], this should push even further the development of OCT-A as it opens new avenues to study the implication of the choriocapillaris in ocular diseases. Until now, the choriocapillaris was mostly studied post-mortem or in cases of retinal atrophy where RPE and photoreceptor are gone which makes it possible to image the possibly remaining choriocapillaris. The penetration depth of OCT-A is however still not good enough to allow for the imaging of the choroidal vessels beneath the choriocapillaris. But as we saw, OCT can produce nice images of large choroidal vessels thanks to the shadowing artefacts. So people have started using OCT images of the choroid with an inverted contrast to have choroidal vessel appear in bright tones instead of dark tones.

Part of the developments in OCT-A aim at addressing the problem of flow quantification. Currently, the microvascular maps generated in OCT-A are binarized and yield no information on blood volume or velocity. Another important limitation of OCT-A for the study of blood flow is that it has a very poor temporal resolution. It usually takes several seconds for commercial instruments to acquire a single OCT-A volume (or more if the subject has fixation issues), which is far from enough to study the blood changes transient to the cardiac cycle.

### 1.2.3 Laser speckle contrast

The principle of laser speckle flowgraphy was first described in 1981 by Fercher and Briers [55]. This method, like OCT-A, derives a blood flow contrast from the speckle pattern fluctuations. With an appropriate temporal sampling, areas where the speckle pattern is rapidly changing will be blurred accordingly with the local flow velocity. A velocity mapping can be obtained from the analysis of the local blurring. Fercher and Briers initially used a single-exposure photography with optical high-pass spatial filtering to produce blood flow contrasted images, all done analogically. In their 1981 paper, they mentioned that this method could be used to image retinal blood flow. Still based on single exposure images, the method was later adapted in a digitized version, allowing to use numerical computations to derive a more precise flow mapping [56]. Laser speckle contrast imaging has since been a very dynamic field of research especially to image cerebral microvascular blood flow [57, 58, 59, 60]. It remains the simplest technique to image blood flow over an extended field of view because it requires very simple equipment: contrarily to laser Doppler measurements where the sampling is done at least in the kHz range, the camera does not need to be that fast as the exposure time must be longer than the speckle decorrelation time (typically a few hundred Hz for retinal imaging).

In the field of ophthalmology, an instrument based on this concept has been commercialized (Softcare, NAVI, LSFSG), as shown in Fig. 1.10. This instrument can image retinal blood flow in real-time with a frame rate of about 30 Hz with a blood flow quantified in terms of mean blur rate (spatio-temporal blurring). The use of laser speckle flowgraphy in clinical research is only beginning, but the first results are promising [61, 62, 63, 64, 65, 66]. It is hard to comment on the limitations of this instrument without having access to it to compare results, but it seems that the potential to get quantitative flow measurements is not as good as with laser Doppler techniques. Indeed in the case of single exposure laser speckle contrast imaging, the dynamic range of flow imaged is limited [67], and multi

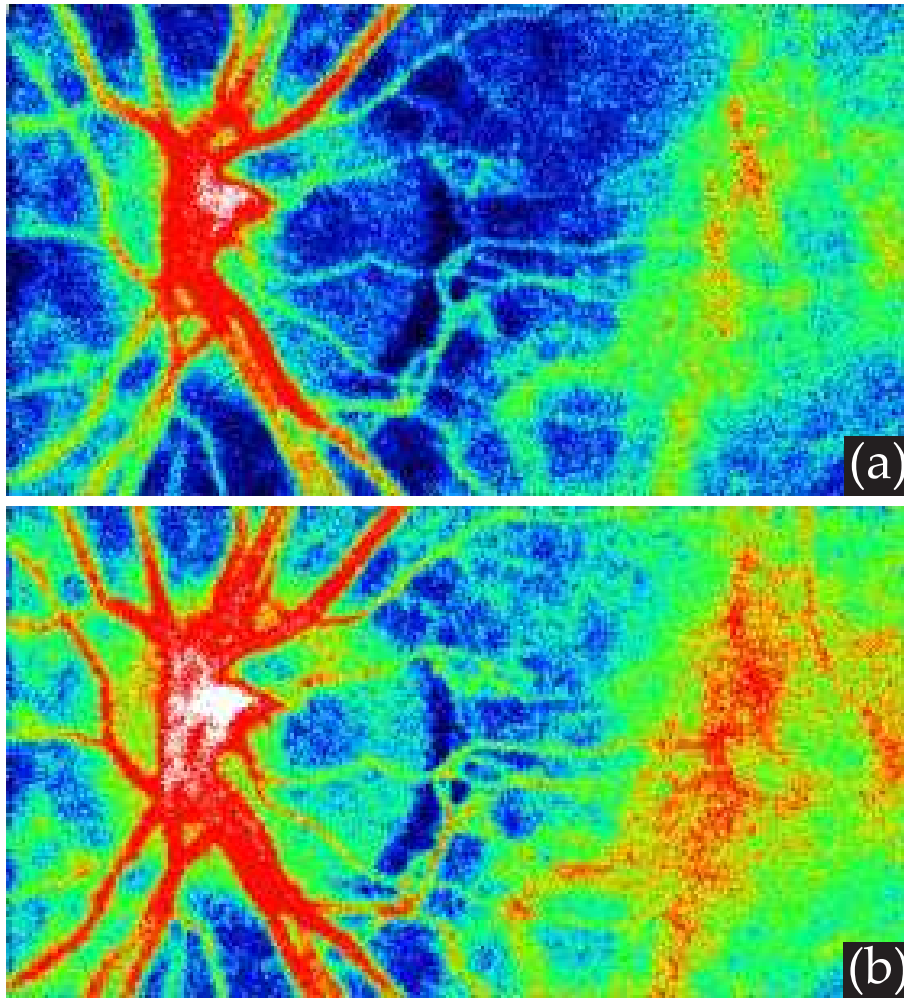


Figure 1.10: Laser speckle flowgraphy during (a) diastole, and (b) systole. As blood flow passes through the retinal vasculature, the speckle contrast signal is greater. Not only the blood vessels are brighter during systole but also their surroundings. The signal also increases outside the papilla. Images for the LSFNG NAVI instrument (Softcare Co., Ltd).

exposure speckle contrast imaging requires several frames with different exposure times which necessarily limits the temporal resolution. Finally, to my knowledge, the choroidal vasculature has so far only been poorly revealed by laser speckle flowgraphy.

#### 1.2.4 Doppler ultrasound

Color Doppler imaging (CDI) is an ultrasound technique where blood flow is measured from the Doppler effect induced by the ophthalmic vasculature on acoustic waves. Ultrasonography B-scans have a much better penetration depth than what is possible in optics, but on the other hand the spatial resolution is quite poor. Nonetheless CDI allows for quantitative and reproducible blood flow measurements in retrobulbar vessels [69, 70]. The flow in the ophthalmic artery, central retinal artery and vein, posterior ciliary arteries, and the superior ophthalmic vein can be measured with a good temporal resolution. Blood flow changes over cardiac cycles are clearly resolved, and the typical metrics used are peak-systolic velocity (PSV), end-diastolic velocity (EDV), mean velocity, and resistivity index (RI). Typical measurements are shown in Fig. 1.11. The examination is performed with the patient lying supine with eyes closed, and the transducer is applied to the closed upper eyelid using a thick layer of acoustic gel. The frequency of the Doppler probe is chosen as a compromise between resolution and penetration depth: it is usually higher

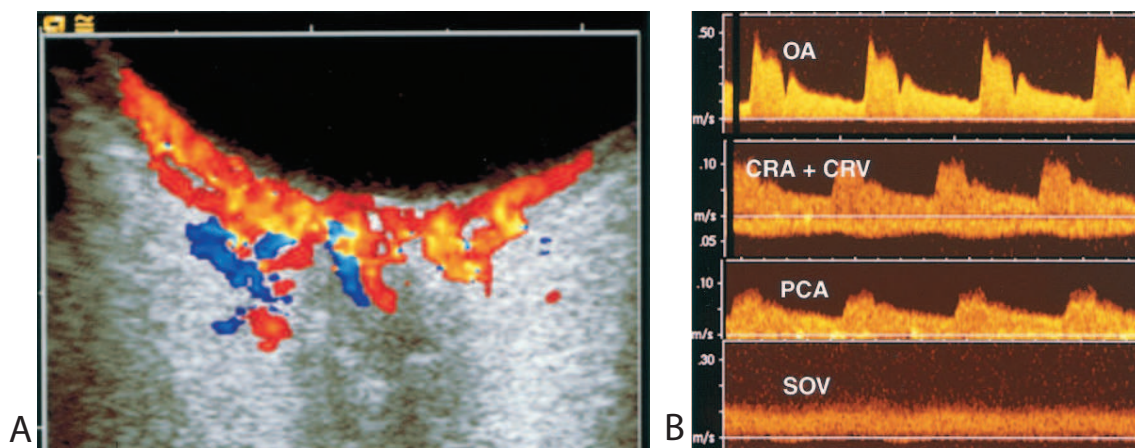


Figure 1.11: Typical images obtained with Doppler sonography, adapted from [68]. (A): Cross-sectional image of the fundus where can be observed the choroid, posterior ciliary arteries, the central retinal artery and vein. (B): Blood flow waveforms in the ophthalmic artery, central retinal artery and vein, posterior ciliary artery, and superior ophthalmic vein. The CRA and CRV, and PCA waveforms are of a particular interest to make a comparison with LDH.

than 7 MHz [68], some investigators having used up to 18 MHz in a plane-wave configuration [71]. The main limitation of CDI is that due to its very limited spatial resolution, it does not allow for the measurement of local blood flow in the retina or choroid. Moreover the examination is operator dependent and can be difficult because the probe needs to be very well positioned.

### 1.2.5 Laser Doppler flowmetry

Laser Doppler flowmetry is a technique where blood flow is measured from the self-interference of the light backscattered by the eye on a photodiode [72, 73, 74, 75, 76]. In this approach, it is considered that a part of the backscattered light is non Doppler shifted because it has been scattered by static diffusers, whereas another part of the light has been scattered by RBCs which induces Doppler frequency shifts in the kHz range. A short-time Fourier transform analysis is applied to extract a blood flow contrast, with a short-time window width of several hundreds points, recorded with a frequency in the kHz range (to have the Nyquist frequency greater than width of the Doppler power spectrum density). This technique is supported by theoretical developments that determined that from the Doppler power spectrum density measurement, it is possible to derive metrics such as the local velocity and volume of blood [77, 78]. Blood flow is unfortunately monitored only in a single point. In order to obtain an extended field of view, there has been demonstrations of scanning configurations and even a commercialized instrument (Heidelberg Retinal Flowmeter), but they have had limited success [79, 80]. Most likely because they were too slow to provide wide field images with a temporal resolution relevant with respect to the cardiac cycles blood flow variations. Secondly, these instruments seemed unable to isolate the retinal contribution from the choroidal contribution, as they failed to measure retinal hypoperfusion where it was expected [81]. Very recently, a line-scanning implementation of laser Doppler flowmetry has proven able to provide unique images (shown in Fig. 1.4(b)) of the choroidal vasculature non-invasively, and quantitatively [14]. However the authors have not shown any dynamic flow measurements with their method.

	ICG-A/FA	OCT-A	LSFG	Doppler US	LDF
invasive	yes	no	no	no	no
quantitative flow	no	no	yes	yes	yes
flow resolution	--	--	+	++	++
spatial resolution	+	++	+	--	-
temporal resolution	--	--	+	+	+
field of view	++	+	=	++	--
penetration depth	++	+	=	++	+
axial sectioning	no	yes	no	yes	no
shows leakage	yes	no	no	no	no

Table 1.2: Summary of the performances of the ophthalmic instrument presented in this section, subjectively appreciated.

## Conclusion

Laser Doppler holography can be described as a combination of the techniques presented here. It is a full-field instrument, as in speckle contrast imaging, where the blood flow contrast is obtained the same way as in laser Doppler flowmetry. In contrast with LDF, in LDH a reference arm is introduced so the system becomes an interferometer. The Doppler spectrum is not measured from the self-interference of the light scattered by RBCs and the light scattered by static diffusers, but from the interference between the light backscattered and the coherent reference beam. Working with this additional reference beam makes the technique holographic, and provides substantial advantages. First of all, it offers the possibility to make full-field measurements, while recording images at a very high frame rate by simply increasing the reference beam power. Secondly, it opens the door to all sort of post processing computational calculations such as numerical propagation, or digital adaptive optics.

From this overview of the different needs existing in ophthalmology, and the gaps there are despite the wide range of techniques to study ocular blood flow, there are two main applications where our instrument may have a relevant contribution. First in the field of imaging retinal blood flow with a higher temporal resolution and an improved ability to make quantitative measurements. The second use of LDH could be to image the choroid, non-invasively, and with a quantitative flow contrast.



## Chapter 2

# Holography and laser Doppler

### 2.1 Basic principles of holography

The term holography is generally used to denote the process of recording an interference pattern between a wave field scattered by an object and a reference wave. Whether the recording is done photographically or digitally, the object wave field can be retrieved by illuminating the recorded hologram now acting as a diffraction grating with the same reference field. Whether the re-illumination is carried out optically or computationally, the reconstructed object is identical to the original one, insofar as the spatial sampling of the hologram allows it. In other words, holography is a technique for recording and reconstructing the amplitude and phase of a wave field, instead of the mere intensity as in conventional non-coherent imaging techniques. The access to the phase of the wave field provided by holography opens up many possibilities, and the improvement in cameras, light sources, and computer technology, has allowed for the recent development of digital holography. Holographic methods can be seen as based on the time-reversal invariance of wave equations [82]. More conventionally, the diffraction of a wave field obeys Maxwell's equations. It is possible to use these equations to determine how light propagates in free space. Digital holography and numerical reconstruction rely on discretized solutions to the Helmholtz equation. In practice, depending on the experimental context different assumptions can be made, and therefore different approaches are used to numerically propagate the field. We evoke here the Fresnel transformation and the angular spectrum propagation as they are the two methods that were used in this thesis.

#### 2.1.1 Fresnel Domain

A first approach for holographic numerical reconstruction relies on the theory developed by Kirchhoff and the Fresnel-Huygens principle. It is used to reconstruct holograms which are recorded in specific experimental conditions corresponding to the Fresnel approximations later defined. In this situation, it is considered that the reference field used to record holograms is equal to a constant as we experimentally used a plane wave as reference field. The Fresnel-Kirchhoff formula gives the optical field  $E(x', y', z)$  diffracted by an aperture in a plane separated from the aperture by a distance  $z$  [83, 84, 85]:

$$E(x', y', z) = \frac{i}{\lambda} \iint E(x, y, z = 0) \frac{\exp(-ik\rho)}{\rho} dx dy \quad (2.1)$$

where  $E(x, y, z = 0)$  is the field to be propagated,  $\lambda$  is the optical wavelength, and  $k$  the corresponding wavenumber. Finally  $\rho$  is the distance between two points in the sensor and reconstruction planes:

$$\rho = \sqrt{z^2 + (x - x')^2 + (y - y')^2} \quad (2.2)$$

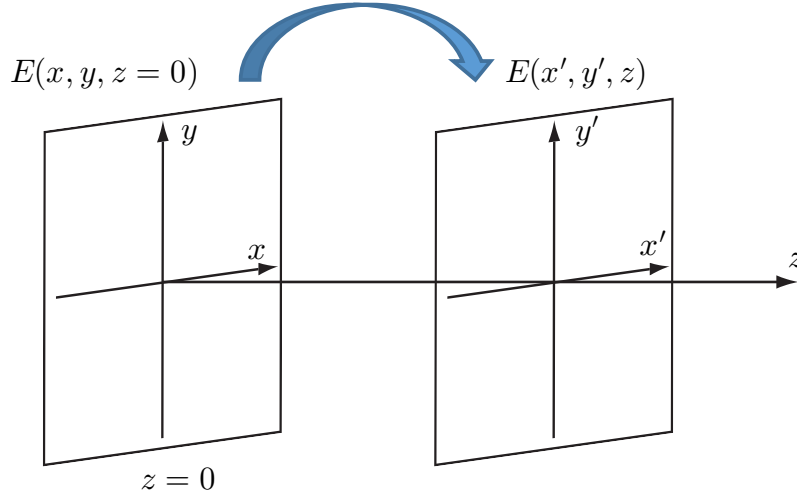


Figure 2.1: Numerical propagation between two parallel planes separated by a distance  $z$  and of coordinates  $(x, y)$  to  $(x', y')$ . The field  $E(x', y', z)$  in the plane  $z$  is determined by the field  $E(x, y, z=0)$  with Helmholtz equation.

Assuming the distance  $z$  separating the two planes can be considered greater than the sensor and object sizes, the term  $\rho$  can be expanded to a Taylor series:

$$\rho = z + \frac{(x - x')^2}{2z} + \frac{(y - y')^2}{2z} - \frac{[(x - x')^2 + (y - y')^2]^2}{8z^3} + \dots \quad (2.3)$$

The term  $\rho$  is present as the denominator in the integral, and in the phase of the exponential in the integral, which calls for different approximations. In the first case,  $\rho$  can simply be reduced to  $z$ , and in the second case  $\rho$  can be approximated to the second order of the Taylor series provided the third order is negligible compared to  $\pi$ , which amounts to the following approximation [83]:

$$z^3 \gg \frac{\pi}{4\lambda} [(x - x')^2 + (y - y')^2]^2 \quad (2.4)$$

As a result, the spherical phase term in the exponential in Eq. 2.1 is replaced by a parabolic phase term. This simplification constitutes the Fresnel approximation and calls for a large propagation distances with respect to the dimensions of the object and sensor. It allows to simplify the writing of the Fresnel-Kirchhoff diffraction equation:

$$E(x', y', z) = \frac{i}{\lambda z} \exp(-ikz) \iint E(x, y, 0) \exp\left(\frac{-ik}{2z} [(x - x')^2 + (y - y')^2]\right) dx dy \quad (2.5)$$

This equation can be further modified by expanding the quadratic phase term in the exponential which develops into: (i) an exponential phase term inside the integral, (ii) an exponential phase term outside the integral, (iii) a cross-product term that allows to reveal the underlying Fourier transform. The absolute phase terms (outside the integral, i.e. applied in the reconstruction plane) are not necessary when working with relative phase changes which is our case. After expansion and removal of this phase term, the Fresnel transform can be elegantly formulated with the discrete 2D Fourier operator  $\mathcal{F}$ :

$$E(z) \propto \mathcal{F}\{E(z=0) \times h_{m,n}(z)\} \quad (2.6)$$

where  $h_{m,n}(z)$  is the free-space propagation impulse response:

$$h_{m,n}(z) = \frac{1}{i\lambda z} \exp\left[\frac{2i\pi z}{\lambda} + \frac{i\pi}{\lambda z}(m^2 d^2 + n^2 d^2)\right] \quad (2.7)$$

In this discrete formulation of the equation, the optical field in the sensor plane is sampled over a matrix array of size  $N \times N$ , with steps corresponding to the camera pixel size  $\Delta x = \Delta y = d$ . The coordinates  $(x, y)$  are indexed by integers  $(m, n)$  such that:

$$x = md; \quad y = nd \quad (2.8)$$

The free-space propagation impulse response involves  $\lambda$ ,  $z$ , and  $d$ , which actually amount to a single parameter:

$$\frac{d^2}{\lambda z} \quad (2.9)$$

Therefore, in order to reconstruct the complex optical field, it is not really required to know the optical wavelength, camera sampling pitch, and propagation distance, because the optimal reconstruction parameter can be determined empirically.

The effect of the Fresnel transformation can be understood as the application of a parabola phase mask followed by a 2D Fourier transform of the field. Thanks to the properties of the Fourier transform operator, the coordinates in the sensor plane and reconstruction plane are related with the following equations:

$$\Delta x' = \Delta y' = \frac{\lambda z}{Nd} \quad (2.10)$$

It should be noticed here that with a Fresnel transformation, the pixel pitch in the reconstruction plane scales linearly with the propagation distance, as presented in Fig. 2.2.

### 2.1.2 Angular Spectrum domain

The diffraction of the optical field can also be viewed as the propagation of its angular spectrum, or linear space filter [83]. In this approach, the propagation of the wave field relies on the Fourier decomposition of the electrical field. The Fourier components provides an orthonormal basis of plane wave vectors. The incident wave field is decomposed on this basis in order to form what is denominated as the angular spectrum of the wave field:

$$\hat{E}(f_x, f_y, 0) = \iint E(x, y, 0) \exp[-2i\pi(f_x x + f_y y)] dx dy \quad (2.11)$$

where the hat operator designs the analytical Fourier transform. The optical field and its Fourier transform form Fourier pairs, the wave field can be re-obtained from the inverse Fourier transform of the angular spectrum:

$$E(x, y, 0) = \iint \hat{E}(f_x, f_y, 0) \exp[2i\pi(f_x x + f_y y)] df_x df_y \quad (2.12)$$

The wave field is written in its Fourier decomposition form and injected in the Helmholtz equation, which leads to the following constraint [83]:

$$\hat{E}(f_x, f_y, z) = \hat{E}(f_x, f_y, 0) \exp\left(2i\pi z \sqrt{1 - f_x^2 - f_y^2}\right) \quad (2.13)$$

This equation determines the angular spectrum of a wave field propagated of a distance  $z$ . Then by inverse Fourier transform of the propagated angular spectrum  $\hat{E}(f_x, f_y, z)$ , the optical field  $E(x, y, z)$  can be obtained. Numerically, the angular spectrum propagation is carried out on the discretized wave field using the following equation:

$$E(z) \propto \mathcal{F}^{-1}\{\mathcal{F}\{E(z=0)\} \times H(z)\} \quad (2.14)$$

where  $H(z) = H_{m,n}(z)$  is the angular spectrum propagation kernel defined as:

$$H_{m,n}(z) = \exp\left[\frac{2i\pi z}{\lambda} \sqrt{1 - \left(\frac{m\lambda}{Md}\right)^2 - \left(\frac{n\lambda}{Nd}\right)^2}\right] \quad (2.15)$$

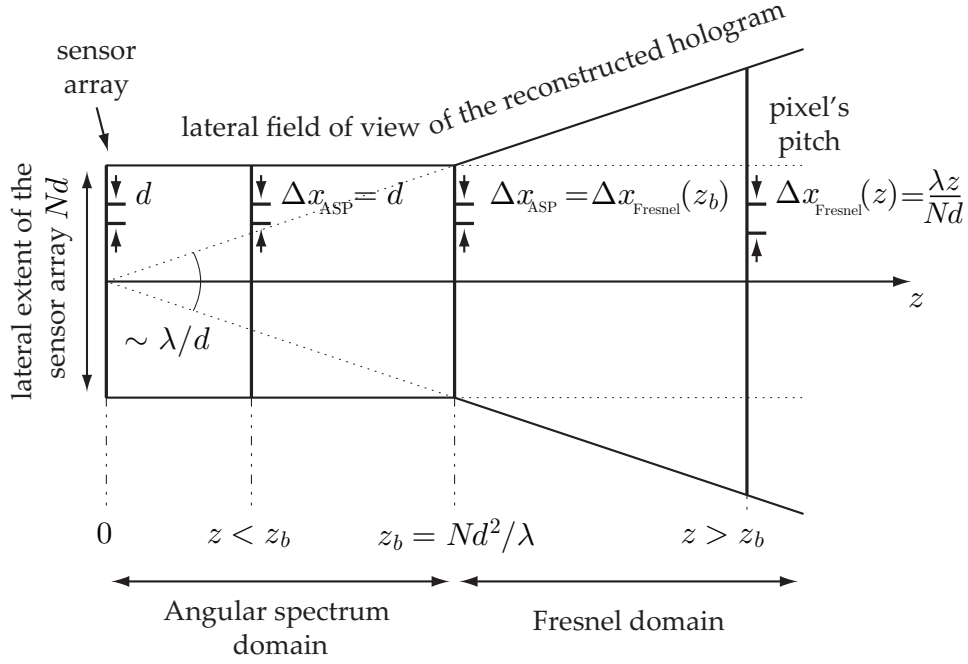


Figure 2.2: Appropriate reconstruction method according to the camera-object distance: for a propagation distance larger than  $z_b = \frac{Nd^2}{\lambda}$ , the Fresnel transform is better suited, and conversely for a distance inferior to  $z_b$  the propagation of the angular spectrum works better.

Propagating the wave field with the angular spectrum is thus done by (i) calculating the 2-D Fourier transform, (ii) applying a phase mask, and (iii) calculating the inverse Fourier transform. Physically, this approach can be understood as a linear spatial filter. The object wave is decomposed on the orthogonal plane waves basis, and each plane wave has a direction of propagation related to its spatial frequency. As the object wave propagates, the largest spatial frequencies corresponding to the most tilted plane waves are lost, and there remains the smallest spatial frequencies for which the propagation direction is close to the optical axis.

Writing mathematical operations of the angular spectrum propagation operator leads to the following observation: the phase mask greatly resembles the one in the Fresnel transformation, except the Fresnel approximation on the distance  $z$  is not made [83]. A major difference with the Fresnel transformation is that the sampling step is constant during the propagation: in any plane the lateral sampling step is the same as in the camera plane, i.e. equal to the camera pixel size  $d$ .

Because the angular spectrum propagation requires two Fourier transform to be implemented, it is sometimes referred to as '2 FFT' propagation, in contrast with the '1 FFT' Fresnel transform.

### 2.1.3 Boundary between reconstruction domains

As represented in Fig.2.2, the Fresnel approximation makes the Fresnel transform more suitable for larger distances, whereas the angular spectrum propagation works better for smaller distance. We evoke here the boundary that delimits the angular spectrum and the Fresnel domains, and present some basic mathematical developments to explain the origin and value of this boundary. Both reconstruction methods involve a phase mask determined by  $z$ , and the spatial discretization of the phase mask needs to be done so as to avoid any undersampling in case  $z$  is too large or too small.

### Fresnel domain

For the Fresnel transform, the key element to the numerical propagation is the lens applied in the Fresnel transform:

$$h_{m,n}(z) = \frac{1}{i\lambda z} \exp \left[ \frac{2i\pi z}{\lambda} + \frac{i\pi}{\lambda z} (m^2 d^2 + n^2 d^2) \right] \quad (2.16)$$

The phase mask values depend on both the reconstruction distance  $z$  and the array characteristics (pixel pitch  $d$ , and dimensions  $(M, N) = \max(m, n)$ ). At a given location on the sensor, the local interfringe of the phase mask decreases linearly with  $1/z$ . Conversely for a given  $z$ , the pixel to pixel phase variations will be greater when  $(m, n)$  is greater. Due to the spatial sampling of the phase mask by the discrete array, the phase variations from one pixel to another should be smaller than  $2\pi$ . If not the phase mask would be spatially undersampled, and aliasing would occur. The condition to be realized in order to avoid undersampling is to have  $z$  such that:

$$\forall(m, n), \Phi [h_{m,n}(z) - h_{m-1,n-1}(z)] \leq 2\pi \quad (2.17)$$

where  $\Phi(x)$  is the function that gives the phase of the variable  $x$ . For the sake of simplicity, we make the approximation to consider the sampling only along one of the two dimensions. The condition becomes:

$$\Phi [h_n(z) - h_{n-1}(z)] = \frac{\pi}{z\lambda} d^2 [n^2 - (n-1)^2] \quad (2.18)$$

Which amounts to:

$$\frac{\pi d^2}{z\lambda} (2n-1) \leq 2\pi \quad (2.19)$$

This quantity is maximal when  $n = N$ , i.e. on the edges of the lens. Then we make the approximation  $(2N-1) \sim 2N$ , so that the condition can finally be written after simplification:

$$\frac{Nd^2}{\lambda} \leq z \quad (2.20)$$

### Angular spectrum domain

In the angular spectrum propagation approach, there is also a phase mask which is a function of  $z$  that is applied to the wave field in the reconstruction process. We make the same kind of development as before to find the  $z$  limit so as to have the phase mask properly sampled by the discrete array. The impulse response is written as follows:

$$H_{m,n}(z) = \exp \left[ \frac{2i\pi z}{\lambda} \sqrt{1 - \left( \frac{m\lambda}{Md} \right)^2 - \left( \frac{n\lambda}{Nd} \right)^2} \right] \quad (2.21)$$

Similarly as before, in order to avoid aliasing we want to find  $z$  such that:

$$\forall(m, n), \Phi [H_{m,n}(z) - H_{m-1,n-1}(z)] \leq 2\pi \quad (2.22)$$

We again consider the problem along a single dimension, so for a given  $n$ , the phase variation between two adjacent pixels:

$$\frac{2\pi z}{\lambda} \left[ \sqrt{1 - \left( \frac{n\lambda}{Nd} \right)^2} - \sqrt{1 - \left( \frac{(n-1)\lambda}{Nd} \right)^2} \right] \leq 2\pi \quad (2.23)$$

After a Taylor expansion to the second order of the square root term, we have:

$$\frac{2\pi z}{\lambda} \left[ \frac{-1}{2} \frac{(1-2n)\lambda^2}{N^2 d^2} \right] \leq 2\pi \quad (2.24)$$

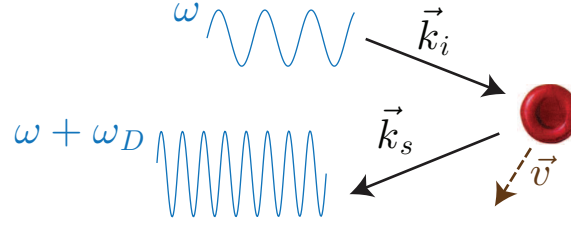


Figure 2.3: Doppler frequency shift of a wave field upon scattering by a moving particle: the frequency shift is proportional to the scatterer velocity.

Which amounts to:

$$\frac{(2n-1)\lambda}{2N^2d^2}z \leq 1 \quad (2.25)$$

And finally:

$$z \leq \frac{Nd^2}{\lambda} \quad (2.26)$$

The condition expressed in Eq. 2.26 is the exact reciprocal of that determined in Eq. 2.20. For a propagation distance greater than  $\frac{Nd^2}{\lambda}$ , it is necessary to favor the Fresnel reconstruction method. Conversely, for a propagation distance lower than  $\frac{Nd^2}{\lambda}$ , the angular spectrum propagation method should be used.

### Other holograms: Fraunhofer domain and image plane holography

Other holographic conditions include the Fraunhofer domain where the second order terms of the Taylor series decomposition in equation 2.3 are neglected. As the phase mask applied within the Fresnel transform is removed, the propagation equation becomes a simple Fourier transform instead of a Fresnel transform. The sensor is located in the Fraunhofer area of the object which can be done by placing the object in the focal plane of a lens or by collecting the light backscattered by the object in the far field.

Another configuration is the image plane holography, where the image of the object is directly formed on the sensor so no numerical propagation is required.

## 2.2 Laser Doppler measurements

### 2.2.1 Doppler broadening

Laser Doppler techniques aim at measuring the velocity of an object from the Doppler optical frequency shifts it induces on a coherent backscattered laser beam. In case of single scattering of light by a moving particle, the scattered light undergoes a Doppler frequency shift which is proportional to the particle velocity and scattering directions:

$$\omega_D = (\mathbf{k}_s - \mathbf{k}_i) \cdot \mathbf{v} \quad (2.27)$$

where  $\mathbf{k}_i$  is the incident wave vector,  $\mathbf{k}_s$  the scattered wave vector and  $\mathbf{v}$  the scatterer instantaneous velocity vector. Thus in this view, the optical frequency of the scattered light, which is inversely proportional to its wavelength, is changed. These individual frequency shifts can have a statistical effect when considering the whole spectrum of the laser beam scattered by the object. When the object probed by the laser beam is a biological tissue, light will be scattered by particles with a large distribution of velocity. This leads to a large distribution of Doppler frequency shifts; the effect on the power spectrum of the scattered light (initially monochromatic) is referred to as Doppler broadening.

In laser Doppler flowmetry, it is considered that some scatterers are relatively static, whereas others such as rapidly moving RBCs can induce large Doppler frequency shifts.

For the retina, only a small part of the total number of particles are RBCs, and according to the work from Bonner and Nossal [78, 77], it is likely that the light scattered by RBCs will also be scattered before or after by static diffusers. This multiple scattering situation implies some degree of randomization of the incident and scattered wave vectors, so the information it carries about blood flow direction is lost. In another words, measurements deriving blood flow contrast from the Doppler broadening are relatively angle independent (it is not entirely the case though, as experimentally studied in the next chapters).

With a Fourier analysis, it is possible to infer from the Doppler spectrum the average velocity of moving particles of the probed area, the local number of moving particles, and the product of these two quantities which yields the blood cells flux when considering a blood vessel. In practice these frequencies can be quite high: Doppler frequency shifts can be up to 30-40 kHz in large choroidal arteries or in retinal arteries close to the central retinal artery [86]. These frequencies can be easily sampled with a photodetector, but they are quite high relatively to the achievable sampling frequencies of current modern cameras. We have implemented two Fourier based techniques to perform blood flow imaging from the laser Doppler broadening entitled wideband and narrowband approaches. They allows for high quality measurements and low quality real-time monitoring, respectively. In the wideband approach, the camera Nyquist frequency allows to sample without any aliasing the whole Doppler spectrum, whereas in the narrowband approach only a small part of the Doppler spectrum is efficiently used, as illustrated in Fig. 2.4.

### 2.2.2 Wideband approach

We here describe the mathematical formalism used in our approach to form laser Doppler images with the wideband approach (i.e. with a very fast camera). It is the method that is used to produce almost all of the LDH images presented in this thesis. Let us consider two scalar electrical fields  $E$  and  $E_{LO}$  at optical angular frequency  $\omega_L$ .  $E$  and  $E_{LO}$  are the object (Doppler broadened) and reference beam (local oscillator), and are written the following way:

$$E(t) = \mathcal{E}(t) \exp(i\omega_L t) \quad (2.28)$$

$$E_{LO}(t) = \mathcal{E}_{LO} \exp(i\omega_L t) \quad (2.29)$$

where  $\mathcal{E}(t)$  is the term that carries the optical Doppler broadening, written in the form of a Fourier series decomposition:

$$\mathcal{E}(t) = \sum_n \tilde{\mathcal{E}}(\omega_n) \exp(i\omega_n t) \quad (2.30)$$

$\tilde{\mathcal{E}}(\omega_n)$  is the amplitude of the Doppler power spectrum density at angular frequency  $\omega_n$ . Assuming these two fields are coherent, they are able to interfere on a camera sensor. The irradiance of the interference pattern is obtained by the classical interferometry equation from the squared magnitude of the sum of the electrical fields in presence:

$$I(t) = \frac{1}{2} \epsilon_0 c \left( |E(t)|^2 + |E_{LO}(t)|^2 + E_{LO}(t) E^*(t) + E_{LO}^*(t) E(t) \right) \quad (2.31)$$

where  $\epsilon_0$  and  $c$  denote the permittivity and speed of light in vacuum, respectively. The first two terms are autocorrelation terms; they are not of interest to us and will be easily removed by the temporal filtering of the data processing that follows. The last two terms are cross-correlation terms which are the terms of interest. They are the holographic twin images (also called real and virtual images) that carry the same information. In the event where there is a numerical propagation to do in order to reconstruct the object field, these two terms are reconstructed in symmetrical reconstruction planes: one of them is reconstructed at  $+z_c$ , and the other one at  $-z_c$ . Thus after numerical propagation, we are only left with one of these two terms, that we here denote  $H(t)$ :

$$H(t) = E_{LO}^*(t) E(t) \quad (2.32)$$

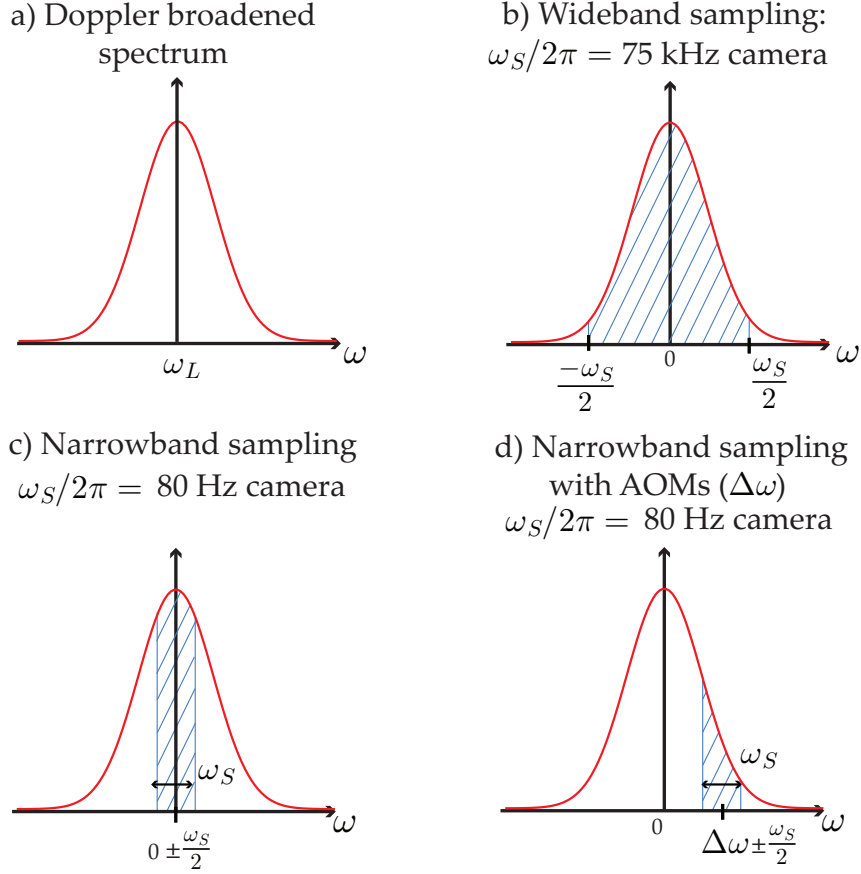


Figure 2.4: Illustration of the wideband and narrowband schemes to measure the Doppler spectrum. (a) Spectrum density of the light backscattered by the eye, centered on the laser optical frequency  $\omega_L$ . (b) Wideband approach: interferogram beat frequency spectrum as sampled by the fast camera. The whole spectrum can be sampled. (c) Narrowband approach without AOMs: interferogram beat frequency spectrum as sampled by the slow camera. Only a small part of the spectrum centered on the zero Doppler frequency shift is sampled without aliasing. (d) Narrowband approach with AOMs: still only a small part of the spectrum can be sampled, but the central frequency of the Doppler spectrum is now offset by the  $\Delta\omega$  frequency introduced by the AOMs.

When injecting the above expressions for  $E$  and  $E_{LO}$ , this leads to us to:

$$H(t) = \mathcal{E}_{LO} \sum_n \tilde{\mathcal{E}}(\omega_n) \exp(i\omega_n t) \quad (2.33)$$

This is the fundamental equation for laser Doppler holography. It gives two important information. First, this equation shows that the beat frequency spectrum of the interferogram yields exactly the Doppler spectrum. Thus as light undergoes Doppler frequency shifts in the retina in the kHz range, we find these same frequencies in the interference pattern beat frequency. Secondly, it shows that the signal of interest is proportional to the amplitude of the object and reference beam. This means that it is possible to some extent to improve the SNR of the laser Doppler measurements by increasing the reference beam power. indeed the coherence gain introduced by the reference arm power enables to achieve the shot-noise limited detection more easily. This is a considerable advantage for LDH compared to LDF where light is self-interfering, because the only way to increase the SNR is to increase the power of the laser beam sent into the eye. With LDH, it becomes possible to increase the frame rate to record interferograms with very high sampling frequencies such as 75 kHz or more (although higher than 75 kHz may not be that useful)

while keeping the same retinal illumination. Sampling the interference pattern at high frequency then allows to have the camera Nyquist frequency greater than the largest Doppler frequency shift and be able to capture the DPSD without aliasing (which corresponds to Fig. 2.4(b)).

### 2.2.3 Narrowband approach

The narrowband approach is used when working with the slow camera (maximum frame rate  $f_S = 80$  Hz) in conjunction with acousto-optic modulators (AOMs). The 80 Hz camera is not able to capture the Doppler broadening, so it can only capture the part of the signal in the frequency range  $[-f_S/2; f_S/2] = [-40\text{Hz}; 40\text{Hz}]$ . Inserting AOMs in the reference channel allows to introduce an optical frequency shift  $\Delta\omega$  in the reference beam, so the local oscillator electric field is now written:

$$E_{LO}(t) = \mathcal{E}_{LO} \exp(i(\omega_L + \Delta\omega)t) \quad (2.34)$$

The Doppler broadened field (same as before) and this new reference field interfere on the camera sensor, and we again select one of the twin images. When using the new expression for the reference field to write the cross-correlation term of interest, we now have:

$$H(t) = \mathcal{E}_{LO} \sum_n \tilde{\mathcal{E}}(\omega_n) \exp(i(\omega_n - \Delta\omega)t) \quad (2.35)$$

Thus the cross-correlation term is the same as before to the exception of the  $\Delta\omega = 2\pi\Delta f$  frequency shift, i.e. the frequency introduced by the AOMs. Instead of being centered on the zero Doppler frequency shift, the interferogram beat frequency is now offset by  $\Delta f$ . As a result, when setting the AOMs to have a frequency shift of  $\Delta f$ , we are able to measure the amplitude of the DPSD in the frequency range  $[\Delta f - \frac{f_S}{2}; \Delta f + \frac{f_S}{2}]$ . This frequency shift introduced by the AOMs can then be varied very easily: it is possible to sweep  $\Delta f$  between 0 Hz and the maximal Doppler frequency shift and measure the entire DPSD. However for every frequency to be estimated, it is required to record at least a few points to make a phase demodulation, and in an ideal case it would be better to have several hundred points to apply a Fourier analysis. But doing so with the 80 Hz camera takes too much time with respect to the speed at which the DPSD changes over cardiac cycles. Consequently, it is not possible to evaluate the entire DPSD with the slow camera with AOMs in the retina, although this could change in the future with faster cameras. So in practice, the AOMs are left at a fixed frequency, and by doing a two phase demodulation we are able to have a contrast somewhat related to blood flow, which is enough guidance for what we use it for (i.e. holographic alignments, and have a clue about the area being imaged on the retina). This method is not really discussed in the following chapters because we have not obtained compelling results to this date. An example is given in Fig. 2.5 and the associated movie.

### 2.2.4 Dual imaging channel laser Doppler holography

The fast camera works in a wideband mode and yields high quality LDH images because it is able to measure the entire Doppler spectrum at once. However the output of this fast camera is not available in real-time. A movie of interferogram is recorded on the on-board memory of the camera, and only 3.5 s of acquisition at 75 kHz is enough to generate 132 GB of data (for about 260.000  $512 \times 512$  frames). It then takes about 5 to 10 minutes to transfer the images on the computer, and a couple of hours to do all the image processing to retrieve the blood flow movie. A real-time display on the camera software is available with a reduced frame rate but it does not allow much more than to make some basic alignments procedures (adjust saturation, beam positions on the camera): it does not give information about the general information about the quality of the holograms and about

the retinal area being imaged. This absence of real-time information about the final image is very problematic to conduct experiments.

To address this issue, we added a second imaging channel which also performs LDH measurements but with a slow camera that works in a narrowband mode. The output of the slow camera is available in real-time and allows for real-time monitoring of the experiments. In reality, it still takes a very powerful software and lot of computations on GPUs to have real-time information as the computer receives about 0.33 GB per second ( $2048 \times 2048 \times 80 \times 1$  bytes) and has to compute many FFTs to obtain the final results (at least a two-dimensional FFT per  $2048 \times 2048$  image for the Fresnel transform). All of these calculations are carried out with Holovibes, a homemade software for real-time hologram rendering [87].

The sensors of the two cameras receive the exact same interferogram (schematic in next Chapter), but because they largely differ in temporal and spatial sampling characteristics, they call for different post-processing methods. The quality of the LDH images that we can have with the slow camera is considerably lower (see example at the end of the Chapter in Fig.2.6(b)), but they can still provide some information about the proper positioning of the subject eye in front of the device, the retinal area being imaged, possible vignetting, possible parasite reflections. This is all the information we need to trigger the acquisition of the fast camera once we have ensured proper recording conditions.

The following Table summarizes the spatial and temporal sampling characteristics of the two cameras:

	Slow camera	Fast camera
Model	Ximea - XiQ	Ametek - Phantom V2511
Frame rate	80 Hz	75 kHz
Pixel size	$5.5 \mu\text{m}$	$28 \mu\text{m}$
Format	$2048 \times 2048$	$512 \times 512$
Reconstruction	Fresnel transform	angular spectrum
Doppler processing	narrowband	wideband
Signal quality	low	high
Real-time	yes	no

Table 2.1: Sampling characteristics of the cameras, and corresponding processing.

In practice, working with these two cameras in order to make simultaneous LDH measurements implies a few complications that we need to address:

### Numerical propagation method

First of all, we need to use two different numerical propagation methods for each camera because of their different in sensor characteristics (pixel size and number of pixel). As we determined earlier in the Chapter the boundary between the angular spectrum domain and the Fresnel domain is set by:

$$z_b = \frac{Nd^2}{\lambda} \quad (2.36)$$

We have  $z_{b,\text{slowcamera}} = 0.07\text{m}$  and  $z_{b,\text{fastcamera}} = 0.51\text{m}$ . Thus we use the Fresnel transform method with the slow camera and the angular spectrum method with the fast camera.

### Illumination level

Besides the different Fourier analyses of the DPSD, we need to solve the problem of the different illumination level required by the two cameras and different reconstruction methods. Despite being very sensitive and having very large pixel ( $28 \mu\text{m}$ ), the fast

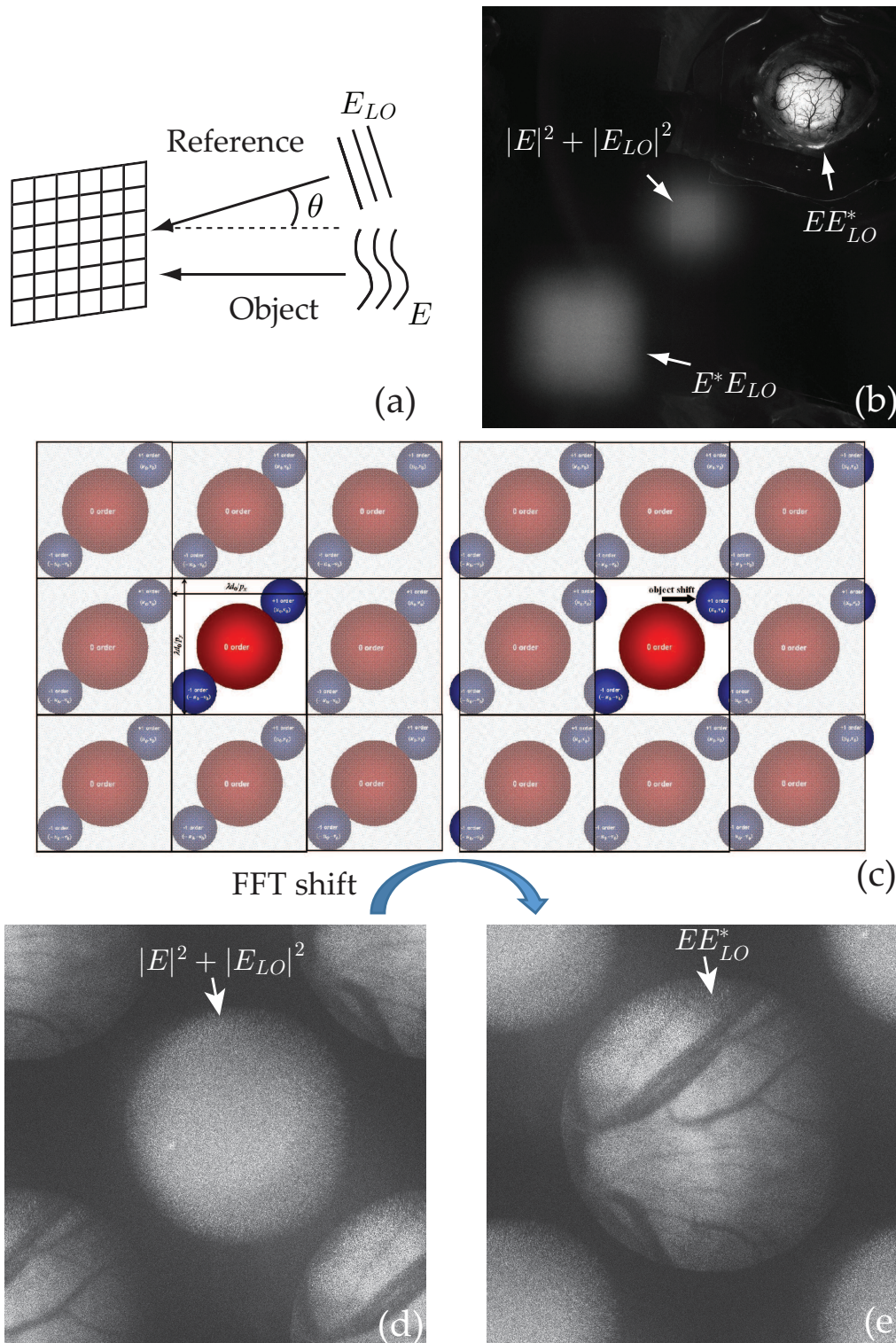


Figure 2.5: Off-axis laser Doppler holography. (a) Off-axis holography: a tilt is introduced in one of the two optical beams. (b) Off-axis LDH from previous experiments on mouse cerebral blood flow [88]: the twin images are separated from the autocorrelations terms in the Fresnel/Fourier plane. (c) Adapted from [89]: undersampling the off-axis carrier frequency in Fresnel digital holography leads to aliasing. (d-e) Off-axis LDH: one of the twin image is offset so that it is in the corner of the Fresnel plane, but the image can be complete with a quadrant shift operation.

camera requires a powerful reference beam in order to work at near saturation level. This

illumination level is too large for the slow camera, so we need to put a neutral density filter in front of the slow camera. Unfortunately, this neutral density also attenuates the light coming from the eye. A faster slow camera, or with a larger full well capacity would be more efficient as we would need a less powerful neutral density. This approach is currently under investigation.

### Off-axis angle and heterodyne measurements directivity

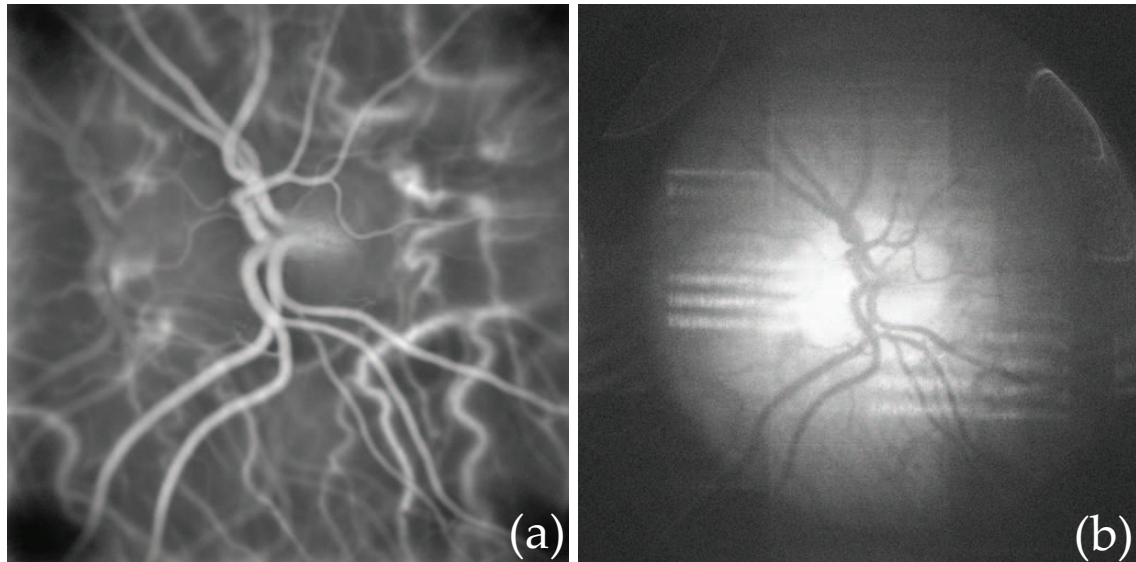
We originally intended to work in an off-axis configuration with the slow camera in order to benefit from the large number of pixel it has ( $2048 \times 2048$ ). The concept of off-axis holography is illustrated in Fig. 2.5: one of the two interfering beams is tilted in order to separate interferometric terms in the Fourier plane [90, 91]. Because the Fresnel transform is similar to the Fourier transform, the diffraction orders (auto and cross-correlation terms) can also be separated in the Fresnel reconstruction plane.

The location and area occupied by the off-axis term depend on the angle between the reference and object beams, and on the field of view of the hologram. In off-axis Fresnel digital holography, it is possible to benefit from an aliasing trick: if the spatial frequencies encoding the hologram exceed the Nyquist frequency they can be retrieved by fftshift thanks to the virtual periodicity of the reconstructed field (due to the discrete sampling being equivalent to a multiplication by a Dirac comb in Fourier space). This periodicity is illustrated in Fig. 2.5(c): when a part on the hologram exceeds the Nyquist frequency, the under-sampled part of the object is shifted out of the main window and reappears in the opposite corner. As it is studied in [89], the undersampled part is however attenuated by a sinc function. As illustrated in Fig. 2.5(d-e) with LDH images of human retina blood flow, a simple quadrant shift (fftshift) operation allows to reunite the separated pieces of the hologram. This operation allows to have a wider field of view, at the cost of having the out-of-focus twin image overlapping with the reconstructed image. However in a case where we are not making very phase sensitive measurements, it could be acceptable to lose in signal quality if it allows to expand the field of view.

However we ended up actually not using this configuration. Indeed, because the two cameras receive the same interferograms, this would also imply to be working in an off-axis configuration on the fast camera, which would conflict with the requirements set by the "antenna properties of a heterodyne receiver" [92, 93]. This theory states that when measuring a beat frequency between two beams of different optical frequencies and tilted by a given angle, the heterodyne sensitivity will decrease if the off-axis interfringe is smaller than the elementary sensor size (photodiode or pixel effective surface). As demonstrated by Siegman, in our case the angular directivity is given by  $\lambda/d$  where  $d$  is the pixel pitch. This is also the value of the angle corresponding to the maximum spatial frequency in the Fresnel space.

So on the one hand, an off-axis angle on the slow camera should be set to about 2-3 degrees in order to have the cross-correlation terms well separated from the autocorrelation term and fully benefit from the available place in the Fourier plane. But on the other hand, in order to make heterodyne measurements, the angular directivity is quite small for the fast camera: only 1.6 degree (0.8 for the half-angle). If we were to work in an off-axis configuration appropriate for the slow camera, the modulation fringes would be spatially undersampled by the fast camera, which would decrease the sensitivity of the heterodyne measurements. Besides, the peak sensitivity for heterodyne measurements is reached when the reference and object waves share the same optical axis, i.e. in a perfectly on-axis configuration.

Consequently, the holographic configuration is on-axis for both cameras, which produces good results on the fast camera but not so good on the slow camera, as illustrated



Angular directivity for heterodyne measurements:

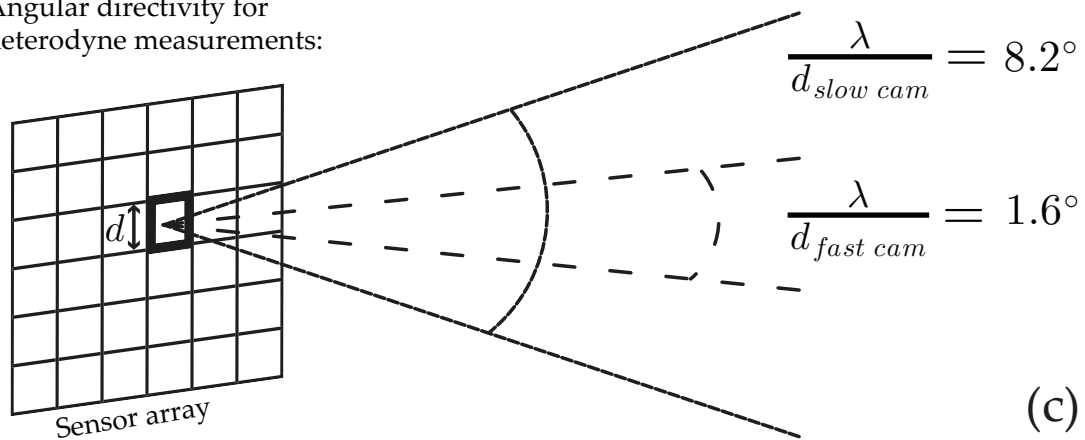


Figure 2.6: Example of LDH images with the two methods. (a) LDH in wideband mode (fast camera) yields high quality blood flow image, but not in real-time (movie fast camera). (b) LDH in narrowband (slow camera) can provide low quality but real-time blood flow images (movie slow camera). The hologram is on-axis (zero frequency at the center of the image) because introducing an off-axis angle reduces the signal quality for the fast camera. (c) Antenna properties of a heterodyne receiver [92]: the directivity of the sensitivity is  $\lambda/d$ ; because the pixel size of the fast camera is very large, the directivity is reduced to a smaller angle than for the slow camera, which calls for an on-axis configuration.

in Fig. 2.6 and associated videos. The same field of view is being imaged with the two imaging channels: the real-time available information is shown in Fig. 2.6(b), whereas the offline results from the fast camera is shown in Fig. 2.6(a). The angular acceptance of both receivers is illustrated in Fig. 2.6(c). The image quality on the slow camera is just enough to know the retinal area being imaged, and to see if the subject pupil is well positioned with respect to the optical axis. However as can be seen in the video, the dynamic signal is of terrible quality with occasional parasite signal, and it is not even possible to see the blood pulsatility.

## Chapter 3

# Imaging retinal blood flow

### 3.1 Article: In-vivo laser Doppler holography of the human retina

In this chapter are presented the results published in *Biomedical Optics Express* for the first application of laser Doppler holography in the human eye. This article introduces the framework of the application of LDH for in vivo imaging in human subject eyes. The setup is presented in detail, as well as the data processing to obtain the blood flow images and movies. Among other points, the temporal resolution, the meaning of the contrast, requirement in terms of sampling frequency, and sensitivity to eye motion are discussed in this article. In this same chapter is then discussed the ocular safety analysis, and some additional results concerning the adaptability of the field of view, and possibility to compensate for the eye aberrations.



# In vivo laser Doppler holography of the human retina

L. PUYO,<sup>1,\*</sup> M. PAQUES,<sup>2,3</sup> M. FINK,<sup>1</sup> J.-A. SAHEL,<sup>2,3</sup> AND M. ATLAN<sup>1</sup>

<sup>1</sup>Institut Langevin, Centre National de la Recherche Scientifique (CNRS), Paris Sciences & Lettres (PSL Research University), École Supérieure de Physique et de Chimie Industrielles (ESPCI Paris) - 1 rue Jussieu, 75005 Paris, France

<sup>2</sup>Institut de la Vision, INSERM UMR-S 968, CNRS UMR 7210, UPMC, 17 rue Moreau, 75012 Paris, France

<sup>3</sup>Centre d'Investigation Clinique (CIC) Centre Hospitalier National d'Ophthalmologie des Quinze-Vingts, INSERM, 28 rue de Charenton, 75012 Paris, France

\*gl.puyo@gmail.com

**Abstract:** The eye offers a unique opportunity for the non-invasive exploration of cardiovascular diseases. Optical angiography in the retina requires sensitive measurements, which hinders conventional full-field laser Doppler imaging schemes. To overcome this limitation, we used digital holography to perform laser Doppler perfusion imaging of human retina with near-infrared light. Two imaging channels with a slow and a fast CMOS camera were used simultaneously for real-time narrowband measurements, and offline wideband measurements, respectively. The beat frequency spectrum of optical interferograms recorded with the fast (up to 75 kHz) CMOS camera was analyzed by short-time Fourier transformation. Power Doppler images drawn from the Doppler power spectrum density qualitatively revealed blood flow in retinal vessels over  $512 \times 512$  pixels covering  $2.4 \times 2.4 \text{ mm}^2$  on the retina with a temporal resolution down to 1.6 ms. The sensitivity to lateral motion as well as the requirements in terms of sampling frequency are discussed.

© 2018 Optical Society of America under the terms of the [OSA Open Access Publishing Agreement](#)

**OCIS codes:** (090.0090) Holography; (170.4460) Ophthalmic optics and devices; (170.3340) Laser Doppler velocimetry.

## References and links

1. S. H. Hardarson and E. Stefánsson, "Retinal oxygen saturation is altered in diabetic retinopathy," *Br. J. Ophthalmol.* **96**, 560–563 (2012).
2. B. Pemp and L. Schmetterer, "Ocular blood flow in diabetes and age-related macular degeneration," *Can. J. Ophthalmol. Can. d'Ophthalmologie* **43**, 295–301 (2008).
3. A. P. Cherecheanu, G. Garhofer, D. Schmidl, R. Werkmeister, and L. Schmetterer, "Ocular perfusion pressure and ocular blood flow in glaucoma," *Curr. Opin. Pharmacol.* **13**, 36–42 (2013).
4. J. A. Briers and S. Webster, "Quasi real-time digital version of single-exposure speckle photography for full-field monitoring of velocity or flow fields," *Opt. Comm.* **116**, 36–42 (1995).
5. A. H. Kashani, C.-L. Chen, J. K. Gahm, F. Zheng, G. M. Richter, P. J. Rosenfeld, Y. Shi, and R. K. Wang, "Optical coherence tomography angiography: A comprehensive review of current methods and clinical applications," *Prog. Retin. Eye Res.* (2017).
6. R. K. Wang, L. An, P. Francis, and D. J. Wilson, "Depth-resolved imaging of capillary networks in retina and choroid using ultrahigh sensitive optical microangiography," *Opt. Lett.* **35**, 1467–1469 (2010).
7. Y. Jia, J. C. Morrison, J. Tokayer, O. Tan, L. Lombardi, B. Baumann, C. D. Lu, W. Choi, J. G. Fujimoto, and D. Huang, "Quantitative OCT angiography of optic nerve head blood flow," *Biomed. Opt. Express* **3**, 3127–3137 (2012).
8. W. Choi, K. J. Mohler, B. Potsaid, C. D. Lu, J. J. Liu, V. Jayaraman, A. E. Cable, J. S. Duker, R. Huber, and J. G. Fujimoto, "Choriocapillaris and choroidal microvasculature imaging with ultrahigh speed OCT angiography," *PloS One* **8**, e81499 (2013).
9. Y. Jia, S. T. Bailey, T. S. Hwang, S. M. McClintic, S. S. Gao, M. E. Pennesi, C. J. Flaxel, A. K. Lauer, D. J. Wilson, J. Hornegger, J. G. Fujimoto, and D. Huang, "Quantitative optical coherence tomography angiography of vascular abnormalities in the living human eye," *Proc. Natl. Acad. Sci.* **112**, E2395–E2402 (2015).
10. Z. Chen, T. E. Milner, S. Srinivas, X. Wang, A. Malekafzali, M. J. van Gemert, and J. S. Nelson, "Non-invasive imaging of in vivo blood flow velocity using optical Doppler tomography," *Opt. Lett.* **22**, 1119–1121 (1997).
11. J. A. Izatt, M. D. Kulkarni, S. Yazdanfar, J. K. Barton, and A. J. Welch, "In vivo bidirectional color Doppler flow imaging of picoliter blood volumes using optical coherence tomography," *Opt. Lett.* **22**, 1439–1441 (1997).

12. Y. Zhao, Z. Chen, C. Saxer, S. Xiang, J. F. de Boer, and J. S. Nelson, "Phase-resolved optical coherence tomography and optical Doppler tomography for imaging blood flow in human skin with fast scanning speed and high velocity sensitivity," *Opt. Lett.* **25**, 114–116 (2000).
13. R. A. Leitgeb, R. M. Werkmeister, C. Blatter, and L. Schmetterer, "Doppler Optical Coherence Tomography," *Prog. Retin. Eye Res.* **41**, 26–43 (2014).
14. H. Fujii, "Visualisation of retinal blood flow by laser speckle flowgraphy," *Med. Biol. Eng. Comput.* **32**, 302–304 (1994).
15. T. Sugiyama, M. Araie, C. E. Riva, L. Schmetterer, and S. Orgul, "Use of laser speckle flowgraphy in ocular blood flow research," *Acta Ophthalmol.* **88**, 723–729 (2010).
16. C. Riva, S. Harino, B. Petrig, and R. Shonat, "Laser Doppler flowmetry in the optic nerve," *Exp. Eye Res.* **55**, 499–506 (1992).
17. M. Leahy, F. De Mul, G. Nilsson, and R. Maniewski, "Principles and practice of the laser-Doppler perfusion technique," *Technol. Heal. Care* **7**, 143–162 (1999).
18. C. E. Riva, M. Geiser, and B. L. Petrig, "Ocular blood flow assessment using continuous laser Doppler flowmetry," *Acta Ophthalmol.* **88**, 622–629 (2009).
19. V. Rajan, B. Varghese, T. G. van Leeuwen, and W. Steenbergen, "Review of methodological developments in laser Doppler flowmetry," *Lasers Med. Sci.* **24**, 269–283 (2009).
20. G. Michelson, B. Schmauss, M. Langhans, J. Harazny, and M. Groh, "Principle, validity, and reliability of scanning laser Doppler flowmetry," *J. Glaucoma.* **5**, 99–105 (1996).
21. L. Schmetterer and G. Garhofer, "How can blood flow be measured?" *Surv. Ophthalmol.* **52**, S134–S138 (2007).
22. A. Serov, W. Steenbergen, and F. de Mul, "Laser Doppler perfusion imaging with complementary metal oxide semiconductor image sensor," *Opt. Lett.* **27**, 300–302 (2002).
23. H. Spahr, D. Hillmann, C. Hain, C. Pfäffle, H. Sudkamp, G. Franke, and G. Hüttmann, "Imaging pulse wave propagation in human retinal vessels using full-field swept-source optical coherence tomography," *Opt. letters* **40**, 4771–4774 (2015).
24. H. Sudkamp, P. Koch, H. Spahr, D. Hillmann, G. Franke, M. Müntz, F. Reinholz, R. Birngruber, and G. Hüttmann, "In-vivo retinal imaging with off-axis full-field time-domain optical coherence tomography," *Opt. Lett.* **41**, 4987–4990 (2016).
25. D. J. Fechtig, B. Grajciar, T. Schmoll, C. Blatter, R. M. Werkmeister, W. Drexler, and R. A. Leitgeb, "Line-field parallel swept source MHz OCT for structural and functional retinal imaging," *Biomed. Opt. Express* **6**, 716–735 (2015).
26. D. Hillmann, H. Spahr, C. Hain, H. Sudkamp, G. Franke, C. Pfäffle, C. Winter, and G. Hüttmann, "Aberration-free volumetric high-speed imaging of in vivo retina," *Sci. Reports* **6**, 35209 (2016).
27. L. Ginner, T. Schmoll, A. Kumar, M. Salas, N. Pricoupenko, L. M. Wurster, and R. A. Leitgeb, "Holographic line field en-face OCT with digital adaptive optics in the retina in vivo," *Biomed. Opt. Express* **9**, 472–485 (2018).
28. M. Pellizzari, M. Simonutti, J. Degardin, J.-A. Sahel, M. Fink, M. Paques, and M. Atlan, "High speed optical holography of retinal blood flow," *Opt. letters* **41**, 3503–3506 (2016).
29. H. Albrecht, M. Borys, N. Damaschke, and C. Tropea, *Laser Doppler and Phase Doppler Measurement Techniques* (Springer, 2003).
30. C. E. Riva, J. E. Grunwald, S. H. Sinclair, and B. Petrig, "Blood velocity and volumetric flow rate in human retinal vessels," *Investig. Ophthalmol. & Vis. Sci.* **26**, 1124–1132 (1985).
31. C. Magnain, A. Castel, T. Boucneau, M. Simonutti, I. Ferezou, A. Rancillac, T. Vitalis, J.-A. Sahel, M. Paques, and M. Atlan, "Holographic laser Doppler imaging of microvascular blood flow," *JOSA A* **31**, 2723–2735 (2014).
32. J. W. Goodman, *Introduction to Fourier Optics* (Roberts and Company Publishers, 2005).
33. M. Guizar-Sicairos, S. T. Thurman, and J. R. Fienup, "Efficient subpixel image registration algorithms," *Opt. Lett.* **33**, 156–158 (2008).
34. B. R. White, M. C. Pierce, N. Nassif, B. Cense, B. H. Park, G. J. Tearney, B. E. Bouma, T. C. Chen, and J. F. de Boer, "In vivo dynamic human retinal blood flow imaging using ultra-high-speed spectral domain optical Doppler tomography," *Opt. Express* **11**, 3490–3497 (2003).
35. H. N. Sabbah and P. D. Stein, "Valve origin of the aortic incisura," *Am. J. Cardiol.* **41**, 32–38 (1978).
36. M. Stern, D. Lappe, P. Bowen, J. Chimosky, G. Holloway, H. Keiser, and R. Bowman, "Continuous measurement of tissue blood flow by laser-Doppler spectroscopy," *Am. J. Physiol.* **232**, H441–H448 (1977).
37. J. F. Polak, J. M. Alessi-Chinetti, A. R. Patel, and J. M. Estes, "Association of common carotid artery Doppler-determined dicrotic notch velocity with the left ventricular ejection fraction," *J. Ultrasound Medicine* **34**, 461–467 (2015).
38. V. Doblhoff-Dier, L. Schmetterer, W. Vilser, G. Garhofer, M. Gröschl, R. A. Leitgeb, and R. M. Werkmeister, "Measurement of the total retinal blood flow using dual beam Fourier-domain Doppler optical coherence tomography with orthogonal detection planes," *Biomed. Opt. Express* **5**, 630–642 (2014).
39. Z. Zhong, B. L. Petrig, X. Qi, and S. A. Burns, "In vivo measurement of erythrocyte velocity and retinal blood flow using adaptive optics scanning laser ophthalmoscopy," *Opt. Express* **16**, 12746–12756 (2008).
40. R. Bonner and R. Nossal, "Model for laser Doppler measurements of blood flow in tissue," *Appl. Opt.* **20**, 2097–2107 (1981).
41. R. F. Bonner and R. Nossal, "Principles of laser-Doppler flowmetry," in "Laser-Doppler Blood Flowmetry," (Springer,

1990), pp. 17–45.

42. J. Schmitt, A. Gandjbakhche, and R. Bonner, "Use of polarized light to discriminate short-path photons in a multiply scattering medium," *Appl. Opt.* **31**, 6535 (1992).
43. L. F. Rojas-Ochoa, D. Lacoste, R. Lenke, P. Schurtenberger, and F. Scheffold, "Depolarization of backscattered linearly polarized light," *JOSA A* **21**, 1799–1804 (2004).

## 1. Introduction

The implication of vascular disorders has been questioned for major diseases affecting the retina such as diabetic retinopathy [1], age-related macular deneneration [2] and glaucoma [3]. Monitoring retinal blood flow appears crucial to understand the pathophysiology of these diseases. Most state of the art non-invasive instruments used for ocular blood flow assessment rely on speckle contrast analysis or laser Doppler methods. Both of these approaches use the intensity fluctuations of coherent light caused by moving objects in order to measure blood flow [4]. Nowadays, Optical Coherence Tomography Angiography (OCT-A) has emerged as a powerful vascular imaging technique [5]. OCT-A makes use of the speckle variations in the OCT signal caused by moving scatterers to generate an angiographic contrast by calculating the local variance of speckle realizations over a few repeated measurements [6, 7]. OCT-A instruments can map the retinal micro-vascular network with a micrometer axial resolution [8] and can be used to measure metrics relevant to the development of diabetic retinopathy such as the size and distribution of capillaries and the extent of the foveal avascular zone [9]. However, as it is necessary to reconstruct a full volume to obtain en-face images, the temporal resolution for swept-source OCT-A is of the order of a second, which is too slow for blood flow monitoring during a single cardiac cycle. Doppler OCT is a technique based on OCT that measures the Doppler frequency [10, 11] or phase [12] shift caused by the flow. The phase shift can be calculated between two consecutive measurements to extract a dynamic signal and reveal blood flow. However large flows causing a modulation higher than  $2\pi$  rad cannot be unambiguously calculated [13]. Another limitation is that it cannot detect flow in vessels perpendicular to the incident OCT beam and only the axial component of the flow can be easily retrieved. Laser speckle flowgraphy is another technique based on speckle contrast whose purpose is to image retinal blood flow quantitatively, although in arbitrary units [14, 15]. En-face images of the retina are formed on the sensor and several images are combined to extract an angiographic contrast; this allows for full-field blood flow measurements with a high temporal resolution. Indeed a commercialized ophthalmic instrument based on this technology (LSFG NAVI, Softcare Ltd, Fukuoka, Japan) is able to image pulsatile flow in real-time with a temporal resolution of 33 ms. In contrast with OCT-A, laser speckle flowgraphy has no depth sectioning ability so the influence of choroidal flow is unclear. Inter-eye comparisons are not possible but intraindividual measurements are highly reproducible [15], which makes it an appropriate instrument to investigate ocular blood flow changes upon physiological or pharmacological stimuli. Laser Doppler flowmetry is based on measuring the Doppler broadening of coherent light induced by moving red blood cells in vascularized tissues [16–19]. The frequency shift is measured by means of interference between Doppler shifted light and non shifted light. This method allows monitoring of blood flow only in a single area, but it has been implemented on scanning systems to monitor blood flow over a full-field [20]. Blood flow and mean velocity in relatives units can be derived from calculations based on the first moments of the power spectrum density. As for laser speckle flowgraphy, interindividual comparisons are difficult whereas intraindividual measurements are reproducible [21]. Laser Doppler flowmetry was used in a direct image detection scheme [22] but this method is too slow for retinal imaging due ocular safety limits.

Lately, holographic detection schemes such as full-field swept-source OCT [23], off-axis full-field time-domain OCT [24] or off-axis holographic line-field en-face OCT [25] have emerged. These techniques allow parallelized imaging and have been demonstrated for *in vivo* human

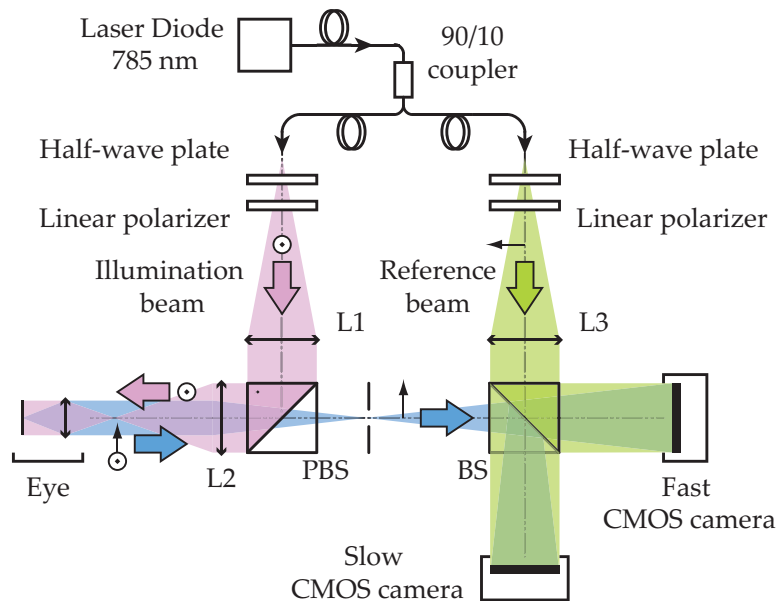


Fig. 1. Optical setup. L1, L2 and L3 are converging lenses. PBS: Polarizing Beam Splitter. BS: Beam Splitter. The light source is a single wavelength laser diode (SWL-7513-H-P, Newport). The 90% output of the fiber coupler is used for the object arm. The Doppler broadened light backscattered by the retina is combined with the reference field and interferograms are recorded on the two imaging channels to study the Doppler beat frequency. The data from the fast CMOS camera is processed offline while the the 80 Hz camera is used for real-time monitoring.

retinal imaging; they have been made possible by technological progress made by the camera industry which now allows for higher acquisition speed, and they seem to have opened the way for new possibilities especially in the realm of offline numerical processing [26, 27]. The laser Doppler holography technique we present here is conceptually close to laser Doppler flowmetry, but like the aforementioned methods it is derived from holography which allows for full-field imaging. In laser Doppler holography, the optical field serving as non-Doppler shifted light is a separate reference beam beating against the Doppler shifted optical field backscattered by the retina. This allows to increase as much as needed the power of the reference field impinging on the sensor and thus be able to work with very low exposure time. Interferograms are recorded with a high throughput camera and wideband measurements of the beat frequency of digitally reconstructed holograms are performed. The angiographic contrast is drawn from the Doppler spectral broadening of light backscattered by the retina and blood flow changes during cardiac cycles are revealed using a short-time Fourier transform analysis. We report here on the implementation of laser Doppler holographic perfusion imaging in the human retina. In contrast with previous attempts on rodent eyes [28], the holographic configuration is on-axis in order to maximize the field of view.

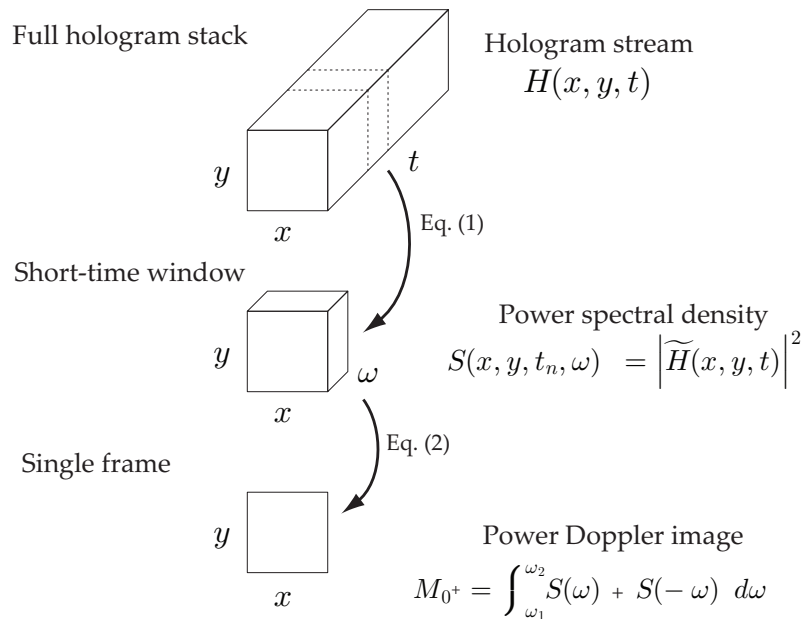


Fig. 2. Short-Time Fourier Transform analysis. A 3D sliding window of consecutive holograms is moved along the full hologram stack; for each window, the Doppler Power Spectral Density (DPSD) is estimated from the squared magnitude of the Fourier Transform in Eq. (3). A single image with blood flow contrast is obtained by integrating the DPSD over  $[\omega_1, \omega_2]$  in Eq. (4), and the resulting image  $M_{0^+}$  is referred to as power Doppler image. Examples of non-averaged power Doppler images are shown in Fig. 5, and examples of averaged power Doppler images are shown in Fig. 3(c) and Fig. 4(c).

## 2. Methods

### 2.1. Optical setup

The optical setup designed and used for this study, shown in Fig. 1, consists of a fiber Mach-Zehnder optical interferometer. The light source used for the experiments is a 45 mW, single-mode, fiber diode laser (Newport SWL-7513-H-P) at wavelength  $\lambda = 785$  nm. The retina is illuminated with a 1.5 mW constant exposure over  $2.4 \times 2.4$  mm<sup>2</sup> area. Informed consent was obtained for each subject and experimental procedures adhered to the tenets of the Declaration of Helsinki. The laser beam is focused in the front focal plane of the eye so that the light is collimated inside the eye and illuminates the retina on an extended area. This irradiation level is compliant with the exposure levels of the international standard for ophthalmic instruments ISO 15004-2:2007.

A Polarizing Beam Splitter (PBS) cube is used in the object arm to illuminate the eye and collect the light backscattered by the retina. The PBS separates linear polarizations: it fully reflects the illumination beam and only the cross-polarized component of the light backscattered by the retina is transmitted to the camera. The reference beam  $E_{LO}$  is collimated and considered to be monochromatic and stable. The object and reference waves are combined using a non-polarizing beam splitter cube and they interfere on the sensor plane. The polarization of the reference wave is adjusted with a half-wave plate and a polarizer to optimize fringe contrast.

The interference pattern is recorded simultaneously on two imaging channels: a slow CMOS camera (Ximea - xiQ, frame rate 80 Hz,  $2048 \times 2048$  pixels, 8 bit pixel depth, pixel size  $5.5 \mu\text{m}$ )

for real-time monitoring and a fast CMOS camera (Ametek - Phantom V2511, frame rate, up to 75 kHz for a  $512 \times 512$  format, quantum efficiency 40%, 12-bit pixel depth, pixel size  $28 \mu\text{m}$ ) for offline processing.

## 2.2. Laser Doppler measurements

In laser Doppler measurement techniques, the Doppler effect is treated as a frequency shift of the optical field itself [29]; here the optical field  $E$  backscattered by the retina is considered to be the sum of the Doppler frequency shifted contributions. The interference pattern on the sensor is  $I = |E_{LO} + E|^2$ . In the cross-beating terms, the optical field frequencies cancel out: the interferogram beat frequency spectrum carries the optical Doppler broadening. Doppler frequency shifts for biological tissues are small compared to the laser optical frequency  $3.8 \times 10^{14}$  Hz as the typical Doppler shift frequency spectra width for retinal vessels has been reported to be around 15-20 kHz [30]. However, as the spectral width corresponds to the Nyquist frequency of the fast camera, a major part of the Doppler broadening can be measured within the camera bandwidth in the interferogram beat frequency.

Acousto-optics modulators (not shown on the schematic) are used in conjunction with the slow camera to introduce a 40 Hz frequency shift in order to perform stroboscopic and narrowband signal measurements in time-averaging conditions [31]. However due to eye motion the quality of the signal is limited and this channel is mostly used for alignment purposes. As both methods are based on holography, the slow camera gives indications on the quality of the holographic reconstruction that are also valid for the fast camera; moreover it is able to yield a contrast related to blood flow that allows visualizing the retinal area being imaged during the acquisition, which is not possible on the fast camera. The real-time hologram rendering is done with our software (Holovibes) that runs calculations on graphics processing units; for this purpose a personal computer equipped with a Nvidia GeForce GTX Titan graphics card is used.

The fast camera is used for wideband measurements of the Doppler spectral broadening. Interferograms from this camera are recorded on its on-board memory and the data are processed offline using Matlab. Interferograms are recorded on the  $512 \times 512$  pixel sensor with an acquisition rate of  $f_s = 39$  kHz (except in section 4 where experiments are made to explore the effect of the sampling frequency), and a frame exposure time of  $25.6 \mu\text{s}$ . Image rendering of complex-valued holograms  $H(x, y)$  is performed using the angular spectrum propagation of the recorded interferograms  $I(x, y)$ , appropriate for near-field reconstructions [32]:

$$H(x, y, z) \approx \iint \hat{I}(k_x, k_y) \exp(ik_z z) \exp(ik_x x + ik_y y) dk_x dk_y \quad (1)$$

where  $\hat{I}(k_x, k_y)$  is the two-dimensional Fourier transform of the interferogram  $I(x, y)$ . The optical axis is  $z$ , and  $k_x$ ,  $k_y$ , and  $k_z = \sqrt{k^2 - k_x^2 - k_y^2}$  are the wave vectors projections along  $x$ ,  $y$ , and  $z$ , respectively. The lateral field of view of the reconstructed holograms of  $512 \times 512$  pixels extends over  $2.4 \times 2.4 \text{ mm}^2$  on the retina.

## 2.3. Data processing

Data processing consists of measuring the local optical fluctuations of the holograms recorded with the high-speed CMOS camera. A Short-Time Fourier Transform (STFT) method is used to analyze the changes in blood flow over time through the changes in the Doppler broadened spectrum. The variations over time of the Doppler Power Spectrum Density (DPSD) are resolved with a sliding short time window constituted of  $j_{\text{win}}$  consecutive holograms  $H$ . Given a sampling

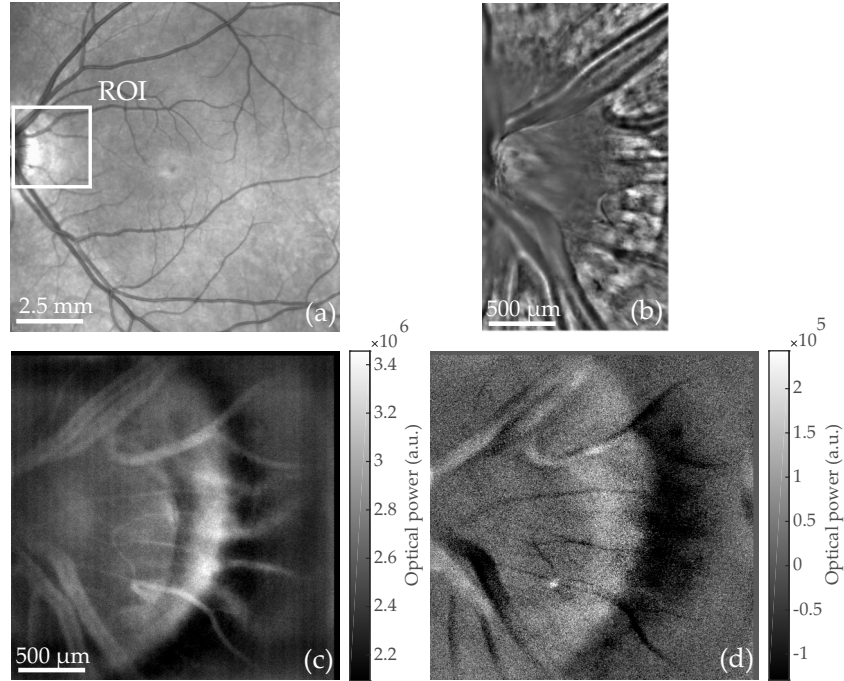


Fig. 3. Optic Nerve Head (ONH) region imaged with commercialized instruments and Laser Doppler holography. (a) Scanning laser ophthalmoscope (Spectralis, Heidelberg). (b) Adaptive optics flood illumination (rtx1, Imagine Eyes). (c) Power Doppler images  $M_{0+}$  calculated from holograms recorded at  $f_S = 39$  kHz;  $S(\omega)$  is integrated over  $[f_1, f_2] = 4-19.5$  kHz. Multiple power Doppler images  $M_{0+}$  are averaged over a total time of 80 ms (see Visualization 1 for blood flow movie). The peri-papillary crescent is visible on the edge of the ONH. (d) Asymmetry of the DPSD  $M_{0-}$  (averaged over the same period of time) illustrating the resultant flow direction with respect to the optical axis.

frequency  $f_S$ , the duration of the short-time window is thus:

$$\sigma_{\text{win}} = \frac{j_{\text{win}}}{f_S} \quad (2)$$

For each short-time window, a single image with a blood flow contrast is formed using the process illustrated in Fig. 2. First, the short-time window is fast Fourier transformed along the temporal dimension, then the power spectral density is estimated from the squared magnitude of the Fourier transform:

$$S(x, y, t_n, \omega) = \left| \int_{t_n}^{t_n + \sigma_{\text{win}}} H(x, y, \tau) \exp(-i\omega\tau) d\tau \right|^2 \quad (3)$$

Finally the quantity  $M_{0\pm}$  is calculated from the integration of the DPSD:

$$M_{0\pm}(x, y, t_n) = \int_{\omega_1}^{\omega_2} S(x, y, t_n, \omega) \pm S(x, y, t_n, -\omega) d\omega \quad (4)$$

$M_{0+}$  is the zeroth moment of the bandpass filtered DPSD; it is a single image corresponding to the area under the curve of the DPSD over the frequency interval  $[f_1, f_2] = (2\pi)^{-1} \times [\omega_1, \omega_2]$ .  $M_{0-}$  images reveal the asymmetry of the DPSD and are discussed in detail in section 3.4. Temporal

frequencies in this article are referred to indifferently as  $f$  or  $\omega = 2\pi f$ .  $M_{0+}$  images are referred to as Power Doppler images (PDIs) and reveal the local blood flow. The frequency band  $[f_1, f_2]$  is typically a high-pass filter (i.e.  $f_2 = f_S/2$ ). The lower boundary  $f_1$  is set between 4 kHz and 7 kHz in order to filter off the contributions that are not due to pulsatile flow in the vessels. The effect of the frequency band  $[f_1, f_2]$  is explored in subsection 4.1. Once the  $M_{0+}$  image has been calculated, the sliding window is moved along the temporal dimension of the hologram stack. In this way, a sequence of PDIs revealing the blood flow for each moment of the cardiac cycle is made.

### 3. Results

#### 3.1. Blood flow contrast

Output images of the STFT analysis  $M_{0+}$  are displayed in Fig. 3(c) and Fig. 4(c) and associated visualizations linked in corresponding captions. These images reveal the tissue perfusion occurring during the duration of the short-time window  $\sigma_{\text{win}}$ . Indeed the Doppler frequency shift is greater when the velocity of the scattering particle is greater. When integrating the whole high-pass filtered DPSD, the pixels where the Doppler broadening is the greatest have the brightest intensity on  $M_{0+}$  images. Thus areas of the retina where the local flow is greater are directly revealed in the intensity of PDIs.

As a result, the most noticeable features of the PDIs are the retinal vessels, due to the considerable flow of red blood cells moving at high speed. Blood vessels are clearly visible on PDIs and give a stronger signal than background tissues because of the larger flow in the vessels. Other features such as the nerve fiber layer are visible on reflectance images obtained with an adaptive optics flood illumination instrument (rtx1, Imagine Eyes, Orsay, France) in Fig. 3(b) and in Fig. 4(b), but these features are not visible on  $M_{0+}$  images.

#### 3.2. STFT parameter $\sigma_{\text{win}}$

The chosen width of the short-time window  $\sigma_{\text{win}}$  results from a trade-off between temporal resolution and Signal-to-Noise Ratio (SNR). Integrating the signal over a longer time period improves the SNR insofar as the amplitude of lateral displacements stays limited during the duration of the short-time window. For excessively long short-time windows, involuntary eye movements limit the improvement in SNR. More importantly, as two events happening during the same short-time window cannot be separated, the sliding window duration  $\sigma_{\text{win}}$  defines the temporal resolution of the instrument. In Fig. 5 and Fig. 6, a comparison is made to evaluate the importance of  $\sigma_{\text{win}}$  on the SNR. The STFT analysis was carried out two times on the same dataset by using different parameters with an approximate tenfold increase in temporal resolution;  $j_{\text{win}} = 64$  ( $\sigma_{\text{win}} = 1.6$  ms) in the first case and  $j_{\text{win}} = 512$  ( $\sigma_{\text{win}} = 13.1$  ms) in the second case. As can be observed on individual PDIs in Fig. 5, the SNR greatly improves when increasing  $\sigma_{\text{win}}$ . Nonetheless the vasculature is already visible with  $\sigma_{\text{win}} = 1.6$  ms. Besides when looking at pulsatile flow, the shape of the power Doppler signal with  $j_{\text{win}} = 64$  can show cardiac cycle signal the with a lower SNR than for  $j_{\text{win}} = 512$ .

For the STFT analysis conducted with  $\sigma_{\text{win}} = 13.1$  ms, a smaller ROI is required to spatially average the results to have a better SNR which illustrates as the SNR in the case where  $j_{\text{win}} = 64$  is lower. Finally, it is interesting to notice that when averaging power Doppler images made with a STFT analysis performed with  $j_{\text{win}} = 64$  and  $j_{\text{win}} = 512$ , the averaged image in the end are virtually the same as long as the total time on which PDIs are averaged is the same. This results are illustrated in images visible in Fig. 6: in this case, 800 PDIs with  $j_{\text{win}} = 64$  and 100 PDIs with  $j_{\text{win}} = 512$  over the same period of time, and the two averaged PDIs show the same features with an equal SNR.

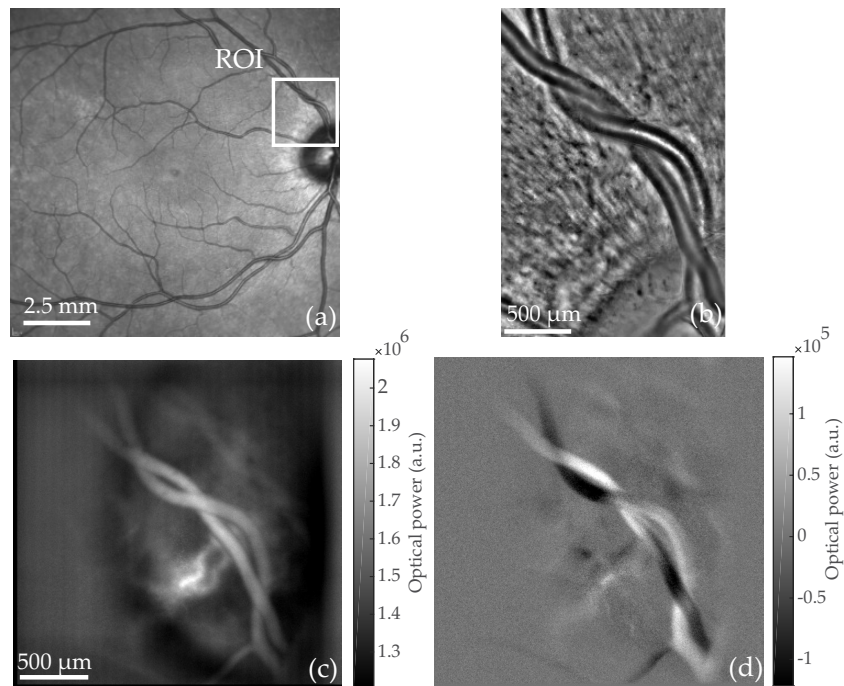


Fig. 4. An artery intertwined with a vein is imaged with commercialized instruments and Laser Doppler holography. (a) Scanning laser ophthalmoscope (Spectralis, Heidelberg). (b) Adaptive optics flood illumination (rtx1, Imagine Eyes). (c) Power Doppler images  $M_{0+}$  calculated from holograms recorded at  $f_S = 39$  kHz;  $S(\omega)$  is integrated over  $[f_1, f_2] = 7-19.5$  kHz. Multiple power Doppler images  $M_{0+}$  are averaged over a total time of 0.66 s (see [Visualization 2](#) for blood flow movie). (d) Asymmetry of the DPSD  $M_{0-}$  (averaged over the same period of time) illustrating the resultant flow direction with respect to the optical axis.

### 3.3. Pulsatile flow

The temporal resolution of the instrument is short enough to observe the changes in blood flow within cardiac cycles. When a heartbeat occurs, the increased speed and concentration of particles in vessels causes momentarily a larger Doppler spectral broadening of the optical field scattered in these structures, which is revealed by the STFT analysis. In Fig. 6, the changes in blood flow throughout cardiac cycles can be observed in a retinal artery and vein. The power Doppler signal is spatially averaged in regions of interest corresponding to an artery, a vein, and background tissues; PDIs have been registered to compensate for lateral eye movements using [33]. During systole (when the cardiac muscles contract and blood pressure is maximum) and diastole (when the cardiac muscles relax and the blood pressure is the lowest) the intensity of both vessels vary with the flow pulsatility. The artery gives a stronger signal than the vein during systole, because of the higher speed of circulating red blood cells which is in agreement with results reported in the literature [34]. The artery also shows a larger modulation depth of the flow than the vein.

Interestingly, for each cardiac cycle, a first peak is reached at the time where the perfusion is maximum, and is followed by a second one of lower amplitude. This second peak corresponds to the dicrotic notch which is thought to be due to the stretch and recoil of the aorta [35]. This waveform has previously been observed in various blood flow monitoring systems such as laser Doppler spectroscopy [36], Doppler sonography [37], Doppler OCT [38], or adaptive optics scanning laser ophthalmoscopy [39]. It should be noted that the background tissue also exhibits a

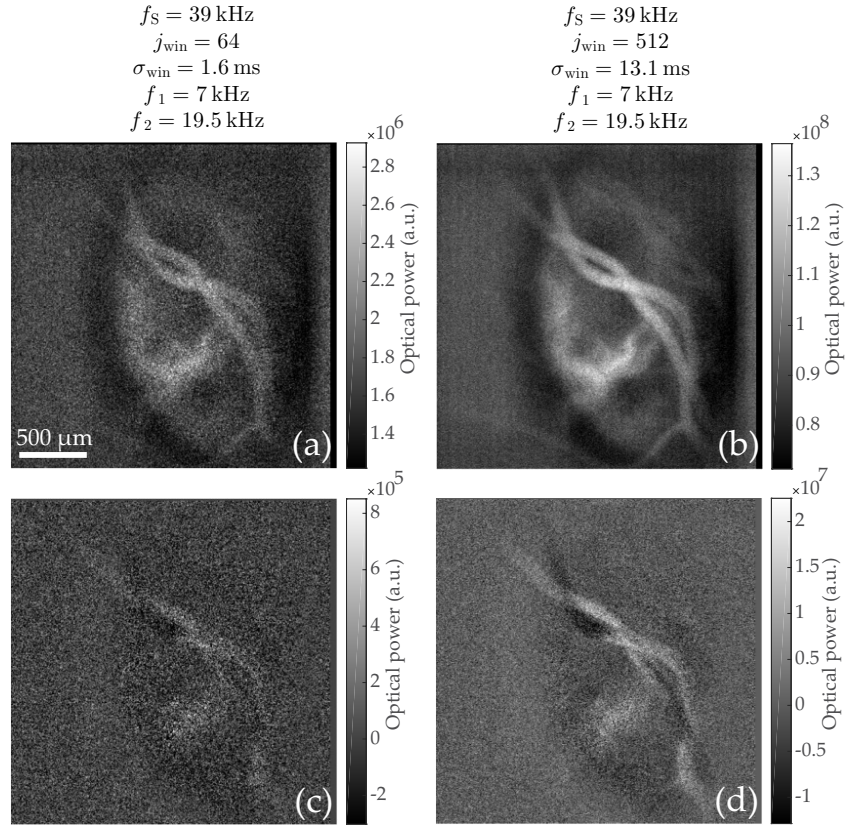


Fig. 5. Comparison in Signal to Noise Ratio (SNR) of power Doppler images  $M_{0+}$  and  $M_{0-}$  calculated with  $j_{\text{win}} = 64$  and 512 holograms (i.e.  $\sigma_{\text{win}} = 1.6 \text{ ms}$  and  $13.1 \text{ ms}$ , respectively). The four images are non-averaged power Doppler images calculated from raw holograms acquired at 39 kHz: (a)  $M_{0+}$ ,  $j_{\text{win}} = 64$ . (b)  $M_{0+}$ ,  $j_{\text{win}} = 512$ . (c)  $M_{0-}$ ,  $j_{\text{win}} = 64$ . (d)  $M_{0-}$ ,  $j_{\text{win}} = 512$ . The SNR dramatically improves with the duration of the short-time window.

flow behavior that we assume to be due to unresolved retinal or choroidal capillaries.

### 3.4. Laser Doppler spectral asymmetry

In the full-field CMOS Doppler imaging scheme proposed by Serov et al. [22], the light backscattered by the sample was not combined with a reference beam but was self-interfering. With this method, the non Doppler shifted light played the role of reference field to perform heterodyne measurements. In this configuration, a negative or positive Doppler frequency shift generates the same intensity fluctuations on the sensor: the signal recorded is real so its spectrum is exactly symmetric and the sign of the frequency shift cannot be recovered. In our case, as the reconstructed holograms are complex-valued and the phase of the optical field is known, the spectrum is no longer symmetric and it becomes possible to distinguish positive and negative frequency shifts. It can be observed that the difference between the negative and positive part of the DPSD contains information about the resultant flow direction when calculating the following quantity:

$$M_{0-}(x, y, t_n) = \int_{\omega_1}^{\omega_2} S(x, y, t_n, \omega) - S(x, y, t_n, -\omega) d\omega \quad (5)$$

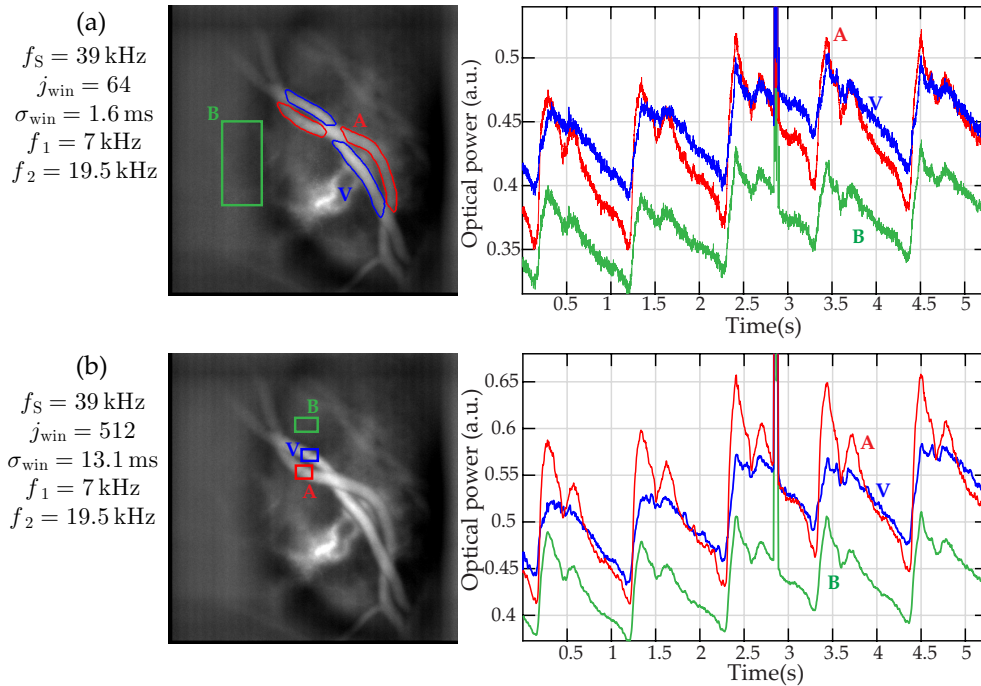


Fig. 6. Comparison of pulsatile flow measurements in a vein and an artery for two STFT analysis performed on the same dataset with (a)  $j_{\text{win}} = 64$  and (b)  $j_{\text{win}} = 512$  holograms. For each analysis, a time averaged power Doppler images  $M_{0+}$  is displayed on the left hand side and shows a red, blue and green ROI which mark an artery (A), a vein (V), and the background tissues (B), respectively. These regions are used to spatially average the power Doppler signal for the plots on the right hand side. Although noisier, the pulsatility signal is already well visible when using  $j_{\text{win}} = 64$ .

The asymmetry of the spectrum is in agreement with the vessel geometry (cf. Fig. 3(d) and Fig. 4(d) considering the expected sign of the Doppler shift. Indeed the Doppler frequency shift  $\omega_D$  occurring when the field is scattered by a moving object is calculated using the following formula:

$$\omega_D = (\vec{k}_s - \vec{k}_i) \cdot \vec{v} \quad (6)$$

where  $\vec{v}$  is the velocity vector of the scattering particle and  $\vec{k}_i$  and  $\vec{k}_s$  are the incoming and scattered optical wave vectors, respectively. According to the direction of the particle with respect to the optical axis, the frequency shift can be positive or negative as schematized in Fig. 7(a) and Fig. 7(b).  $M_{0-}$  thus reveals the predominant direction of the flow with respect to the optical axis. If the vessels are not perpendicular to the optical axis, the projection of the velocity vector on the optical axis is non-null and the sign of the DPSD asymmetry varies accordingly with vessel directions. This is well visible in Fig. 7(d) and Fig. 7(e). The power spectrum density has been calculated according to Eq.(3) in two regions that differ from the direction of the local flow. In the first case the vessel is going slightly upward with respect to the optical axis and  $S(\omega) > S(-\omega)$  over the frequency band  $[f_1, f_2]$  which is used to integrate DPSD when calculating the PDIs. In the second case, the vessel is going downward and  $S(\omega) < S(-\omega)$  over the frequency band of interest. This discrepancy between negative and positive parts of the DPSD is imputable to the directly backscattered light. It can also be noticed that for lower frequencies (for example the peak occurring at about  $\approx 1 \text{ kHz}$ ), this inversion cannot be observed in two different regions as

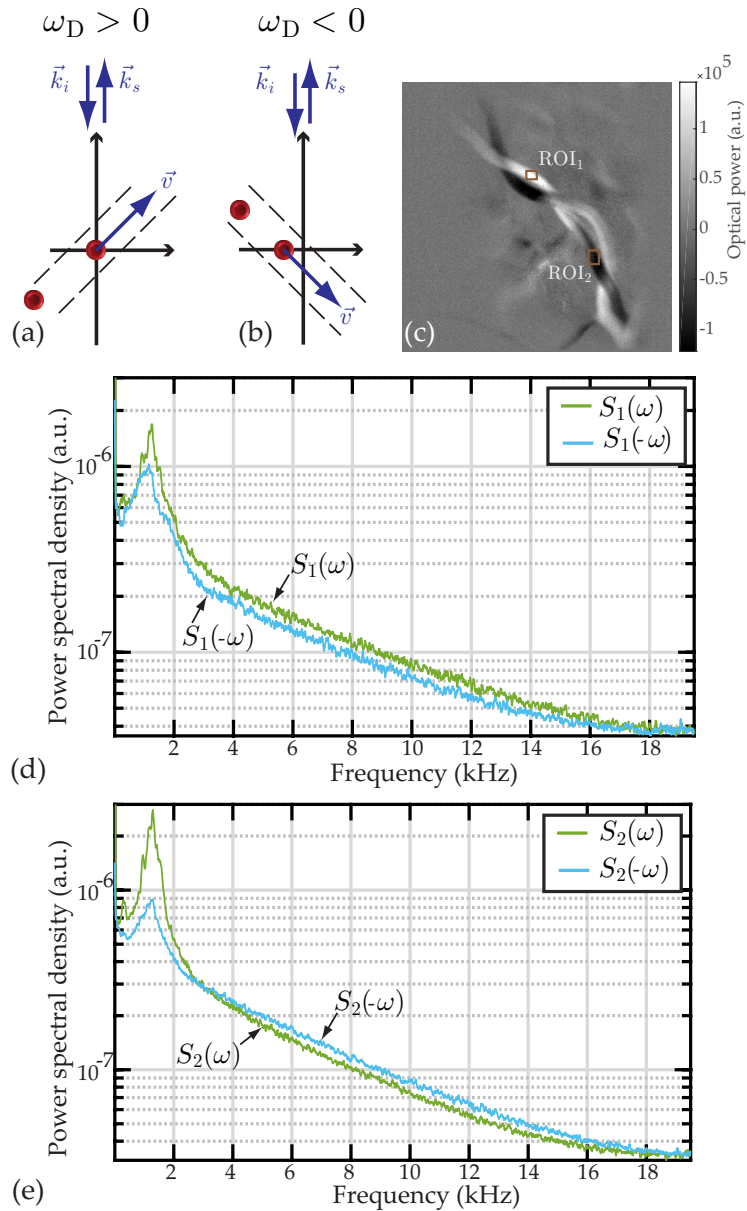


Fig. 7. Cases of spectral asymmetry between the positive and negative parts of the DPSD calculated according to Eq. (3). (a, b) Schematic illustrating the sign of the Doppler frequency shift for the direct backscatter (cf. Eq. (6)). (c)  $M_0$ - showing the two regions where the spectra are calculated. (d) Negative and positive part of the DPSD measured in the ROI 1. (e) Negative and positive part of the DPSD measured in the ROI 2. For the range of frequencies 4-19.5 kHz used to calculate PDIs,  $S_1(\omega) > S_1(-\omega)$  and on the contrary  $S_2(\omega) < S_2(-\omega)$  depending on the vessel geometry.

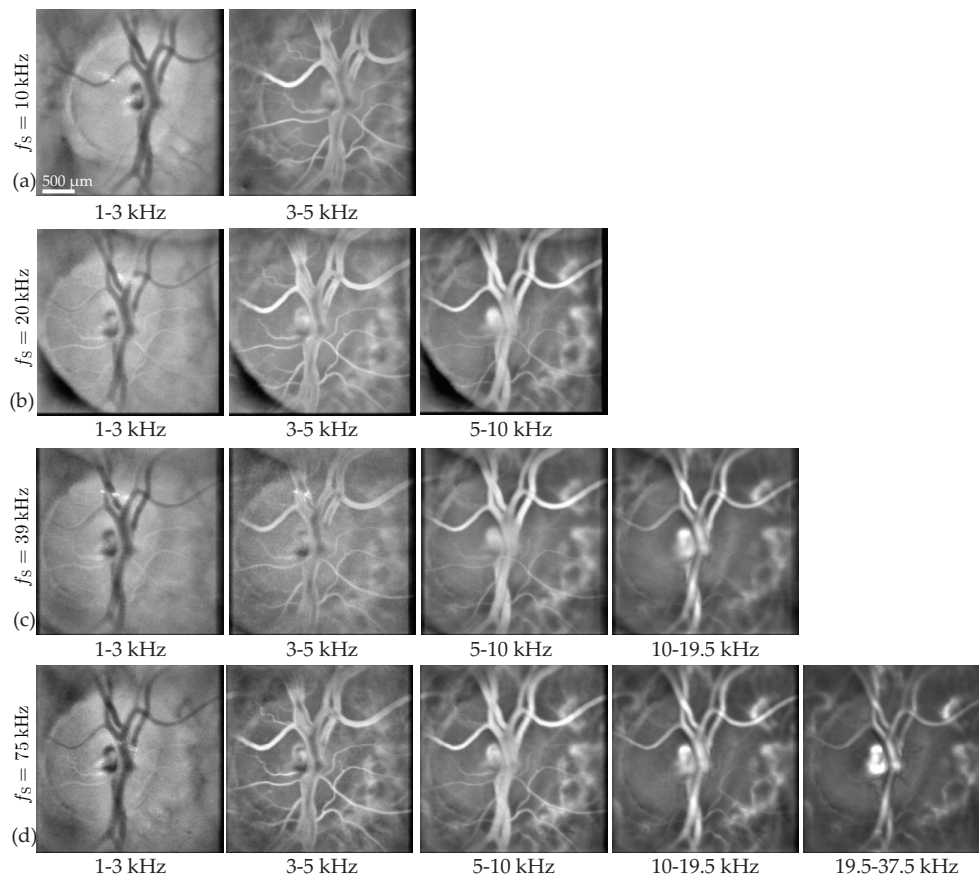


Fig. 8. Multiple laser Doppler holography measurements of a same region are made with different sampling frequencies. For each of these sampling frequencies, PDIs  $M_{0+}$  are calculated for different frequency bands indicated below the images. (a)  $f_s = 10$  kHz. (b)  $f_s = 20$  kHz. (c)  $f_s = 39$  kHz. (d)  $f_s = 75$  kHz.

these frequencies correspond to Doppler shifts induced by global movements.

#### 4. Role of the frequency band $[f_1, f_2]$ and sampling frequency $f_s$

In this section, results from several measurements performed at the same retinal location using different sampling frequencies (10, 20, 39, 75 kHz) are exploited to investigate on the effect of the frequency band  $[f_1, f_2]$  and sampling frequency  $f_s$  on the resulting power Doppler images  $M_{0+}$ . All measurements were done with the Phantom V2511 camera; the exposure time of the camera was set to the maximum for each acquisition (i.e. 100, 50, 25.6, 13.3  $\mu$ s, respectively). The retina of a young and healthy subject was illuminated with the same exposure for all acquisitions, only the power of the reference arm was adjusted using neutral densities so that the camera was filled with the same amount of light (near saturation of the brightest pixels). The region imaged in these acquisitions is centered on the optic disc. The field of view is close to  $3 \times 3$  mm<sup>2</sup>, slightly larger than for the results shown in previous Figs. because we used a different combination of lenses.

#### 4.1. Choice for $[f_1, f_2]$

The frequency band  $[f_1, f_2]$  used to integrate the DPSD in Eq. (4) is chosen so as to filter off the DC and autocorrelation terms as well as the signals due to global eye movements while keeping the contribution of Doppler shifted light due to pulsatile flow in the vessels. The lower boundary is generally set between 4 and 7 kHz depending on the retinal region being imaged while the upper boundary is set to the camera Nyquist frequency  $f_s/2$ . In Fig. 8, the displayed PDIs are calculated for different frequency bands for each sampling frequency. Each row of the Fig. corresponds to a sampling frequency,  $f_s = 10, 20, 39,$  and  $75$  kHz, for the rows (a), (b), (c), and (d), respectively. For each column,  $M_{0+}$  are calculated for several bandpass interval:  $[f_1, f_2] = 1-3$  kHz,  $3-5$  kHz,  $5-10$  kHz,  $10-19.5$  kHz and  $19.5-37.5$  kHz from left to right. Except for the acquisition with the highest sampling frequency, some intervals are above the Nyquist frequency of some sampling frequencies and consequently PDIs cannot be calculated for these frequencies. The visualization linked in caption Fig. 8 shows PDIs for a more precise range of frequencies in the case of the acquisition at 75 kHz.

It can be observed in Fig. 8 that for the lowest frequency band 1-3 kHz, the background tissue DPSD is greater than the vessels DPSD, so the vessels appear darker than the tissue on the PDIs. For the frequency band 3-5 kHz, the edges of the large retinal vessel appear brighter than the lumen, as the latter remains dark. That is because the flow is greater at the center of the vessels and the Doppler broadening occurring in these structures is still undersampled. However, for this frequency band, the Doppler broadening caused by the flow in smaller retinal vessels seems adequately sampled as they appear brightly. For frequencies superior to 10 kHz, the DPSD in the lumen seems adequately sampled. Thus integrating lower frequencies allows us to get the signal from smaller retinal vessels, although it also increases the contribution of global axial and lateral movements. It can be noticed that PDIs calculated using a certain frequency band look alike independently from the sampling frequency. For example PDIs calculated with the frequency band 1-3 kHz are virtually the same with the sampling frequencies 10 kHz and 75 kHz. So in the former case, all the signal above 5 kHz (Nyquist frequency for  $f_s = 10$  kHz) which is aliased has no visible effect on the resulting  $M_{0+}$  image.

This leads to the conclusion that to make a simple image of the vasculature, the aliased part of the DPSD does not make significant change on PDIs. It is also possible to conclude that the DPSD corresponding to the contributions of pulsatile flow in large vessels lies in frequency bands that are above 5 – 10 kHz and up to 37.5 kHz depending on the size of the vessel.

#### 4.2. Sampling frequency $f_s$

In Fig. 9, the requirements in terms of sampling frequency to perform laser Doppler holography in the human retina are investigated. For this purpose, both the vasculature images of the retina  $M_{0+}$  and the changes in power Doppler signal during the cardiac cycles are considered. STFT analysis are performed with  $j_{win} = 128, 256, 512, 1024$  holograms for the acquisitions at  $f_s = 10, 20, 39,$  and  $75$  kHz respectively. In this way the temporal resolutions of the STFT analyses are approximately the same for all acquisitions ( $\sigma_{win} \approx 13$  ms). Power Doppler images  $M_{0+}$  are calculated using the highest possible frequency bands according to the sampling frequency:  $[f_1, f_2] = 3-5$  kHz,  $5-10$  kHz,  $10-19.5$  and  $19.5-37.5$  kHz, for  $f_s = 10, 20, 39,$  and  $75$  kHz, respectively. For each sampling frequency, an image calculated from PDIs averaged over time is displayed on the left, and the plots on the right correspond to the signal over time of  $M_{0+}$  averaged in the region indicated on the associated image. This ROI is centered on the arterial bifurcation of the central retinal artery where the flow is expected to be the greatest in the retina.

As observed in the previous subsection 4.1, PDIs of the vasculature at lower frequencies show a weaker signal inside the vessel lumen because the Doppler broadening is undersampled. The curve for the lowest frequency band 3-5 kHz displayed on the right side on the Fig. does not show a pattern related to the cardiac cycle. However for the frequency band above (5-10 kHz), the

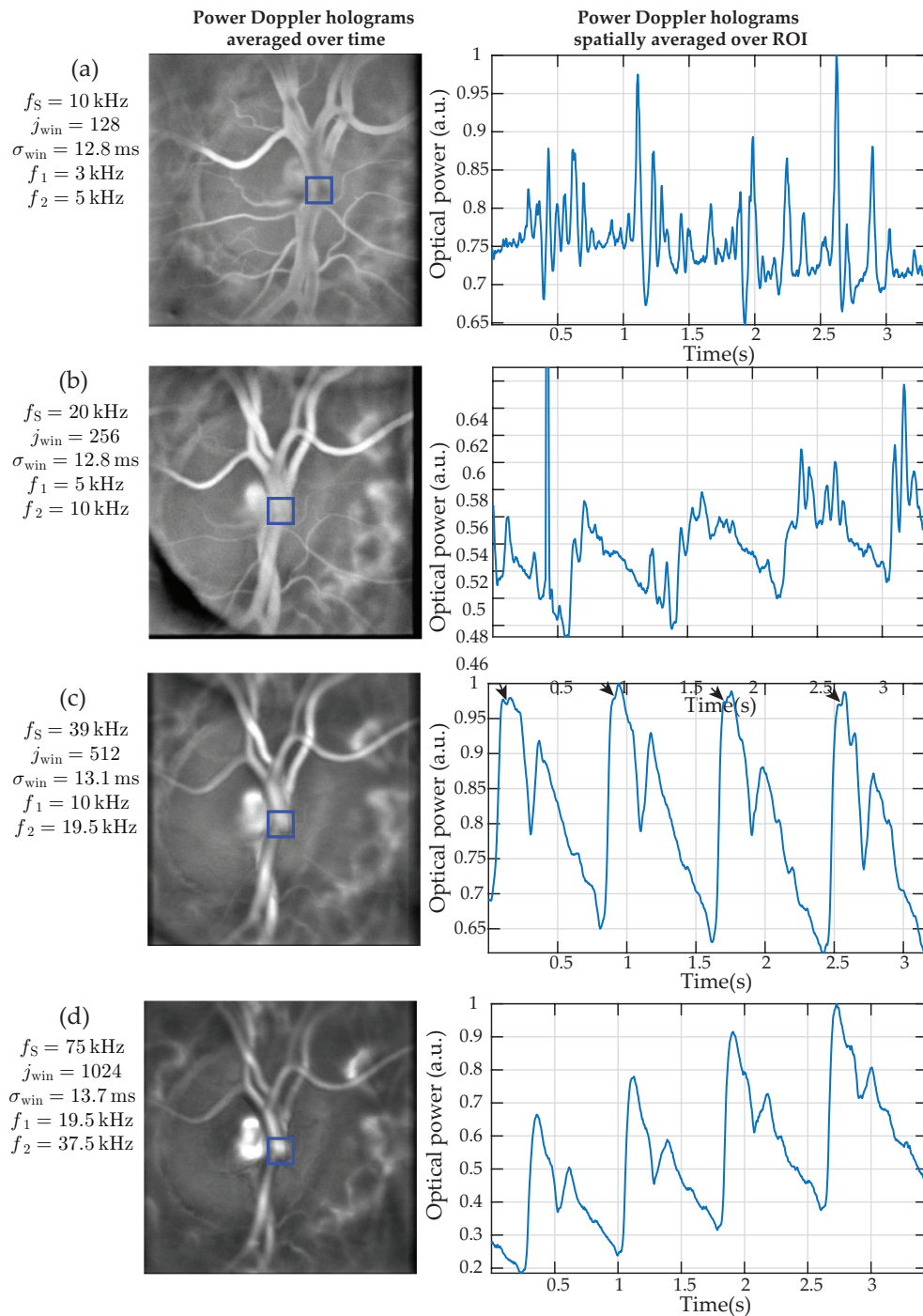


Fig. 9. Requirements in terms of sampling frequency for laser Doppler holography in the central retinal artery. For each sampling frequency, power Doppler images are spatially averaged over the depicted ROIs on the left hand side and the result is displayed in the associated plot. The STFT parameters used for each acquisition are displayed on the left and have been chosen to have  $\sigma_{win} \approx 13$  ms for all acquisitions. (a)  $f_S = 10$  kHz, (b)  $f_S = 20$  kHz, (c)  $f_S = 39$  kHz, (d)  $f_S = 75$  kHz. [Visualization 3](#) shows PDIs as a function of the frequency for the acquisition with  $f_S = 75$  kHz.

typical curve of flow over time in the vessels is recognizable. Then for the two highest frequency bands, the difference is minor. Indeed when looking closely it is possible to see that around the maximum of the systolic peak for the 10-19.5 kHz plot, the curve is not well rounded and shows an abrupt decrease (indicated by the arrows) that is not visible for 19.5-37.5 kHz plots. We assume that a minor undersampling briefly occurs at this moment for large systolic flows. In Fig. 9(d), an overall increase over time of the power Doppler signal can be noticed: it is due to an involuntary eye movement which progressively shifts the pupil position.

Hence Fig. 9 shows that the Doppler shifted light corresponding to the pulsatile flow in large vessels is located further along the power spectrum density. Considering these results, performing measurements with a sampling frequency above 30 to 40 kHz seems to be a requirement for large retinal vessels. Otherwise, the part of the DPSD corresponding to the pulsatile flow is undersampled, aliased, and mixed with low frequencies of greater amplitude and is therefore not retrievable. However, for vessels of smaller size it is possible to use a smaller sampling frequency and have a properly sampled Doppler signal but there is a risk that this signal might be too weak due to the low number of circulating red cells especially compared to the Doppler shifts induced by global eye movements.

## 5. Discussion and conclusion

It is possible to record up to 259,329 frames in a  $512 \times 512$  format on the on-board memory of the Phantom V2511 camera. This corresponds to approximately 6.6 s of acquisition at  $f_s = 39$  kHz or 3.5 s of acquisition at  $f_s = 75$  kHz. We showed in the previous section that with  $f_s = 39$  kHz the Doppler broadening caused by pulsatile flow seems somewhat undersampled only when imaging the central retinal artery during systole. As a result, when imaging other retinal regions where the flow is weaker, this sampling frequency yields negligible aliasing. Consequently, for this work the sampling frequency was usually set to 39 kHz to be able to record longer acquisitions and maximize our chances to measure consecutive cardiac cycles unaffected by micro-saccades. Indeed, as with most ophthalmic instruments, the ability of laser Doppler holography to perform retinal imaging during micro-saccades is limited. The Doppler broadening induced by global movements is greater than the one induced by local pulsatile flows (for example the strong peak occurring at 2.8 s in Fig. 6 is a micro-saccade). Consequently, during a micro-saccade, the intensity of the PDIs is predominated by global movements. However drifts and tremor do not prevent blood flow imaging, as can be observed in movies because slow movements generate low frequency Doppler shifts that are removed when high pass filtering the DPSD. It should be noted that this process also filters off the Doppler signal due to the flow in small retinal vessels.

The technique presented in this article makes use of the backscattered light that has been highly Doppler shifted. This part of the light is selected when high-pass filtering the DPSD in Eq.(3). One of the assumptions of the theory used for laser Doppler flowmetry is that photons scattered by red blood cells (i.e. highly Doppler shifted photons) have been scattered by static diffusers before they impinge on erythrocytes [40, 41]. The result of this is a randomization of the wave vectors involved in the scalar product in Eq. (6) yielding the Doppler frequency shift: the situation is comparable to red blood cells being illuminated from all directions. Thus, selecting highly Doppler shifted light implies selecting multiply scattered light. Yet multiply scattered light loses the original linear polarization of the incident beam because light is depolarized in the multiple scattering regime [42, 43]. Consequently, it is possible to carry out laser Doppler holography with cross-polarized light because we work with the backscattered light that is highly Doppler shifted, thus multiply scattered and depolarized. For this reason we used a polarizing beam splitter cube which allows us to filter off the specular reflection occurring on the cornea. Indeed this reflection conserves the original linear polarization of the incident beam and is reflected by the polarizing beam splitter cube instead of being transmitted to the camera.

An important aspect of working with multiply scattered light is that the instrument is sensitive to

lateral motion. For conventional blood flow monitoring methods based on Doppler approaches, the flow is assessed in a simple manner only in vessels parallel to the optical axis. The flow in vessels perpendicular to the optical axis cannot be assessed as the Doppler shift is minimum, and for vessels with intermediate inclinations, the geometry must be known to calculate the corresponding flow. In our case, because we select multiply scattered light, vessels with any inclinations with respect to the optical axis contribute to the Doppler broadening of the backscattered light. Consequently the instrument is sensitive to lateral motion and able to image blood vessels in en-face planes as can be seen in the PDIs shown in Figs. 3, 4, and 8.

However in laser Doppler flowmetry, the retinal area where the blood flow is monitored is not a large blood vessel but tissues that are mainly vascularized by capillaries. In this medium the randomization of the light is a safer assumption because small vessels are oriented in all directions and are surrounded by a dense matrix of static diffusers. However in our case it can be argued that the multiple scattering assumption is less valid as the vessel walls and other structures around large vessels may not diffuse the incident beam sufficiently, and the limits of this assumption can be seen in the asymmetry of the DPSD  $M_{0-}$ . Indeed in a situation of purely multiple scattered light there should not be any difference between the positive and negative parts of the spectrum despite the vessels geometry since the asymmetry exists because of the signed Doppler shifts of the directly backscattered light. However, as explained in section 3.4, a mild asymmetry does exist in the DPSD depending on the vessel geometry (less than 10 to 15% in the example shown). This asymmetry may cause a bias of flow sensitivity according to the vessels orientation with respect to the optical axis. However the impact seems limited and is mitigated by the process of averaging the positive and negative parts of the spectrum. Moreover in the parts of vessels where the flow direction is perpendicular to the optical axis (i.e. the areas where  $M_{0-} = 0$ ), the flow sensitivity does not seem to be affected by the local inclination of the vessel with respect to the optical axis.

In conclusion, wideband laser Doppler holography can reveal retinal blood flow pulsatility in humans over a full-field with a temporal resolution of only 1.6 ms while keeping the retinal exposure under 1.5 mW at 785 nm. The angiographic contrast which is sensitive to local dynamics, including lateral motion, is drawn from the Doppler power spectrum density using a short-time Fourier transform analysis. Thanks to its high temporal resolution, laser Doppler holography could provide new insight in the dynamics of the vascular system as well as potential new ways to diagnose and follow-up major retinal or cardio-vascular diseases.

## Funding

LABEX WIFI (Laboratory of Excellence ANR-10-LABX-24) within the French Program Investments for the Future under Reference ANR-10-IDEX-0001-02 PSL; and European Research Council (ERC Synergy HELMHOLTZ, grant agreement #610110).

## Acknowledgments

The authors would like to thank S. Meimon, K. Grieve and J-P. Huignard for helpful discussions.

The Titan Xp used for this research was donated by the NVIDIA Corporation.

## Disclosures

The authors declare that there are no conflicts of interest related to this article.

### 3.2 Ocular safety: ISO 15004-2 (2007)

The laser safety analysis for our instrument is based on the European standard ISO 15004-2:2007 which sets the fundamental requirements and test methods for light hazard protection in ophthalmic instruments. Our instrument sends a single laser beam into the eye over an extended area of the cornea and retina in a full-field configuration. The laser diode provides a beam of constant power to near-infrared light. It is not scanned over time which considerably simplifies eye safety calculations. In the experiments made in the context of this thesis, a monochromatic light source at 785 nm was used, with a power incident at the cornea lower or equal to 1.5 mW.

The ISO 15004-2 standard sets maximal permissible exposure (MPE) limits for ophthalmic instruments. Instruments are classified into two categories: group 1 for instruments that do not present any potential radiation hazard, and group 2 instruments which present a potential hazard related to radiation. We have kept with the group 1 category in order to minimize any risks and to obtain more easily the authorizations to make clinical experiments.

5.4.1.4	Unweighted corneal and lenticular infrared radiation irradiance, $E_{\text{IR-CL}}$	770 to 2 500	$E_{\text{IR-CL}} = \sum_{770}^{2500} E_{\lambda} \times \Delta\lambda$	20 mW/cm <sup>2</sup>
The corneal irradiance shall be evaluated by averaging the highest localized radiant power incident upon a circular area at the corneal plane with a diameter of 1 mm ( $7,9 \times 10^{-3}$ cm <sup>2</sup> ).				
5.4.1.6	Retinal visible and infrared radiation thermal hazard  The limit values given in a) and b) are equivalent. It is only necessary to evaluate the retinal visible and infrared radiation thermal hazard with <b>either a) or b)</b> below.			
a)	Weighted retinal visible and infrared radiation thermal irradiance, $E_{\text{VIR-R}}$	380 to 1 400	$E_{\text{VIR-R}} = \sum_{380}^{1400} E_{\lambda} \times R(\lambda) \times \Delta\lambda$	0,7 W/cm <sup>2</sup>
The position of the highest irradiance found in the irradiated retinal area shall be found. The weighted retinal visible and infrared radiation irradiance value, $E_{\text{VIR-R}}$ , shall then be calculated by dividing the spectral radiant power, $\Phi_{\text{VIR-R}}$ , in watts, incident on the retina in a 0,03 mm circular disc centred on the position of highest irradiance by the area of this disc ( $7,07 \times 10^{-6}$ cm <sup>2</sup> ). See Annex D for instructions on the way to make this calculation.				

Figure 3.1: Maximum permissible exposure (MPE) limits set by ISO 15004-2 (2007): a limit is set for the retina and cornea illumination. For an equal surface exposition of the cornea and retina, the corneal MPE is the more limiting in the near-infrared because photoreceptor become less sensitive and the cornea becomes more absorbent than in the visible spectrum.

In Fig. 3.1 are shown the retinal an corneal MPE for a constant power in the near-infrared sprectrum, as stated by ISO 15004-2 (2007). There is an MPE for both the retinal and corneal surfaces which take into consideration the laser wavelength, the size of illumination beam, and the ray focusing geometry. In general, the limit comes from the MPE on the retina (thermal danger), but in our case it comes from the cornea. This is most likely because the iris is thought to absorb infrared light whereas the photoreceptor are not very sensitive in the near-infrared light. Indeed according to ISO 15004-2 (2007), the corneal MPE is 20 mW/cm<sup>2</sup> whereas the MPE on the retina is given by the following formula:

$$\int_{380}^{1400} E(\lambda)R(\lambda) d\lambda \leq 700 \text{ mW/cm}^2 \quad (3.1)$$

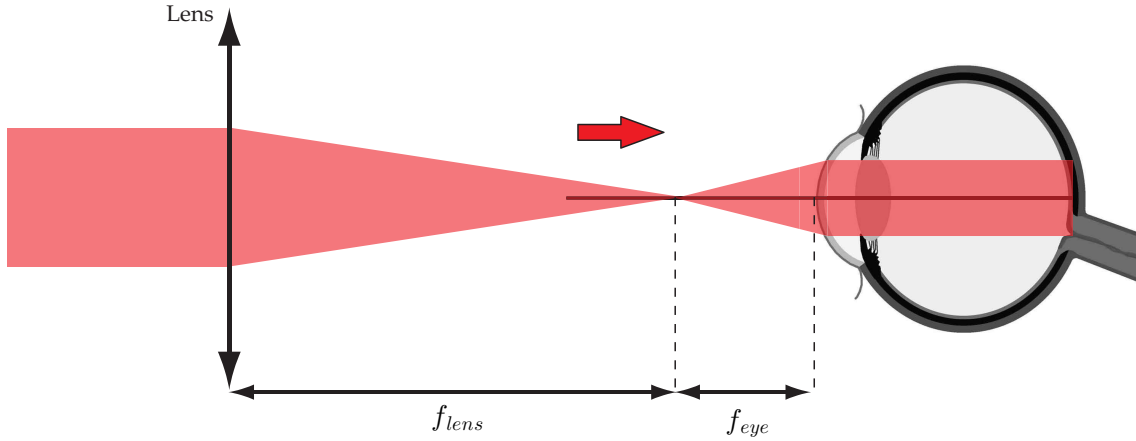


Figure 3.2: Position of the eye in front of the instrument: the subject is placed so that the laser beam is focused in the front focal plane of the eye. The laser beam is collimated within the eye and the corneal and retinal surface exposed are about equal.

with  $E(\lambda)$  and  $R(\lambda)$  the spectral illumination and the weighting factor of the thermal hazard, respectively. We consider that our source is monochromatic, so the limitation becomes:

$$E_{source}R(\lambda) \leq 700 \text{ mW/cm}^2 \quad (3.2)$$

leading to:

$$E_{source} \leq \frac{700 \text{ mW/cm}^2}{R(\lambda)} \quad (3.3)$$

When  $\lambda$  varies between 770 and 1400 nm,  $R(\lambda)$  varies monotonously between  $R(\lambda = 770 \text{ nm}) = 0.72$  and  $R(\lambda = 1400 \text{ nm}) = 0.2$ . If we consider the most constraining value of  $R(\lambda)$  reached for  $\lambda = 770 \text{ nm}$ , i.e. 0.72, this leads to a retinal MPE of  $970 \text{ mW/cm}^2$ , which is 48.5 times higher than the  $20 \text{ mW/cm}^2$  corneal MPE

As shown in Fig. 3.2, the laser beam is focused in front of the eye at the focal plane of the optical system of the eye and the light within the eye is collimated. Consequently, the retinal and corneal surfaces exposed to the light beam are about equal. For a laser beam power of 2 mW, and spread over a disc of diameter 4 mm, the irradiance is therefore  $12.5 \text{ mW/cm}^2$  on both the cornea and the retina, which represents 62.5% and 1.3% of MPE for the cornea and retina, respectively. In these calculations, the Gaussian distribution of energy is not considered. The ISO standard that the limitation level should be verified by checking that the MPE stays under the limit for 1 mm pinhole placed in the expected plane of the cornea (as stated in the annex E of ISO 15004-2 (2007)).

### 3.3 Adaptability of the field of view

In Fig. 3.4 are shown power Doppler images of a same region of interest acquired with different optical configurations. The lens placed in front of the eye was changed in order to modify the size of the field of view. The position of the subject was also changed to keep the laser beam focused in the front focal plane of the eye. A lens with a shorter focal length allows to expand the field of view on the retina. The small, intermediate, and large field of view shown here were obtained with a 100, 75, and 50 mm lens, respectively ( $L_2$  lens in the schematic in Fig. 1 of the article). Unfortunately, in the full-field imaging configuration that we use, there is a limit to the maximum field of view set by the size of the pupil. Although for some subject with a large pupil it is possible to use a lens with a shorter focal length without having too much vignetting, for most the work we have kept with the 50 mm lens.

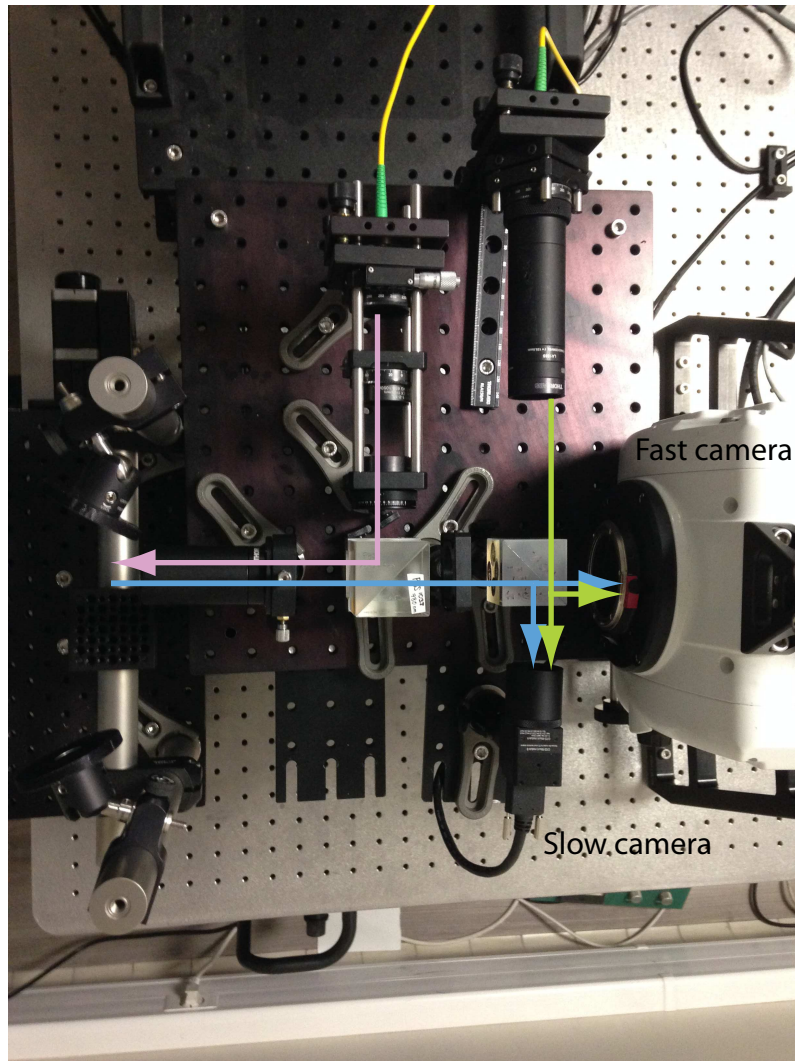


Figure 3.3: Photo of the exposed setup. The color code is the same as in the setup schematic in Fig. 1 of the article.

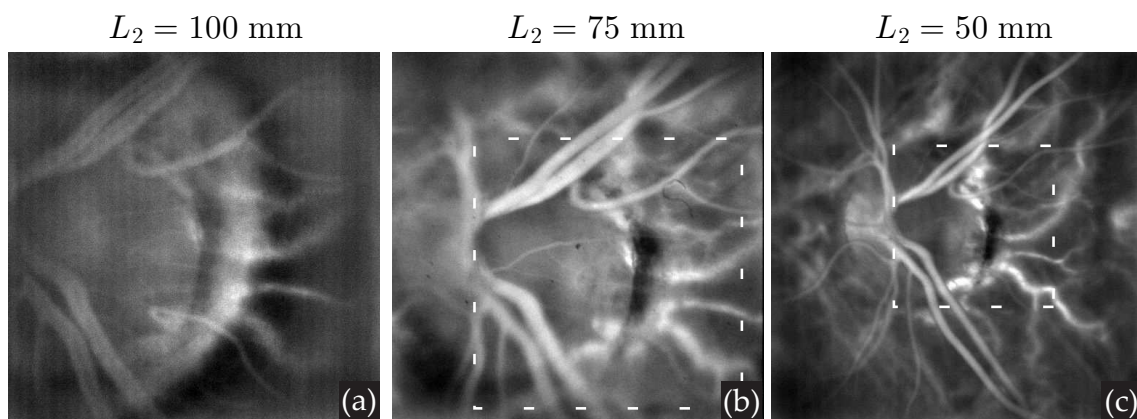


Figure 3.4: Different acquisitions of the same region of interest while changing the lens placed in front of the eye. With a lens of longer focal length, it is possible to image a smaller field of view. In the first article, we used a 100 mm lens, and then we used a 50 or 75 mm lens because a larger field of view is appreciated by medical doctors.

### 3.4 Aberrations correction

With digital holography, it is possible to numerically correct aberrations of the wave field introduced by a refractive error from the cornea and lens. Several groups have recently demonstrated it in case of digital holographic imaging of the retina [94, 95, 96]. These methods are either based on iterative optimizations of the image quality through a metric such as entropy, or on non-iterative measurements of the wavefront shape with a digital equivalent of a Shack-Hartmann wavefront sensor. In both cases, a wavefront correction is applied in a reciprocal plane of the image.

We have made some preliminary experiments in order to study the possibility and relevance of correcting for the aberration in our LDH setup. The smallest feature that we would usually see in the retina would be about  $20 - 30 \mu\text{m}$ , which is well above the limit set by aberrations in an emmetropic eye (generally closer to 10 microns, although there are large inter-individual variations). It seems that it is clearly the resolution of flow (sensitivity to small flow) that determines the smallest features that we can see. Thus the use of aberrations correction can seem very limited. However our hope was that correcting for optical aberration would help reveal smaller features anyway. Besides it could be useful to have the possibility to image ametropic eyes with our instrument without introducing any dispensable optical elements.

Some preliminary results are shown in Fig. 3.5. For this experiment, we made images on a subject when wearing and when not wearing contact lenses, and the power Doppler images were reconstructed in the expected retinal plane (at a set reconstruction distance). Then an iterative algorithm was used in order to determine a phase mask to apply in the Fourier plane of the image that would maximize entropy (while limiting the optimization to the first few Zernike polynomial functions). The development of the iterative optimization algorithm was carried out by Thomas Andal and Armand Touminet during their internships at the Institut Langevin.

In Fig. 3.5(a) is shown the image on the eye wearing contact lens (i.e. emmetropic), and in Fig. 3.5(b) the image after running the optimization procedure. The two images are identical which shows that using a Zernike polynomial of higher order than a defocus does not help improve the spatial resolution, possibly because the optimization procedure has failed to converge to the optimal solution, but most likely because the spatial resolution is limited by flow sensitivity. In Fig. 3.5(c) the subject was not wearing contact lenses (about 3 diopters of myopia) and the image is blurred, and in Fig. 3.5(d) the optimization algorithm has found the proper phase mask to retrieve an image as sharp as originally.

The holographic reconstruction is based on the angular spectrum propagation: a parabolic phase mask is applied in the Fourier space of the image. This parabolic phase function is equivalent to the defocus Zernike polynomial. If we don't take into consideration anisoplanatism, in both cases the 2D Fourier transform is calculated, a quadratic phase mask is applied and then the inverse 2D Fourier transform is calculated. In practice the algorithm converges towards the same image as if we had manually selected the best reconstruction distance, so it does not provide better results than an autofocus. The optimization for higher Zernike polynomials than the defocus (e.g. with spherical aberration of order 3 or astigmatism) does not further improve the image quality in this case.

Correcting for the spherical aberration does not improve the image quality because the features we can resolve (due to the sensitivity to small flows) are already retrieved by correcting for the defocus. For subjects with a strong astigmatism, because it is not a symmetrical aberration, it cannot be simply corrected with a defocus, so a numerical correction should be able to improve the image quality. However we have not yet encountered a subject with an astigmatic refractive error strong enough that the deterioration of the spatial resolution on LDH images could be improved by numerical correction.

In conclusion, the possibility to correct for aberration is hereby demonstrated by this

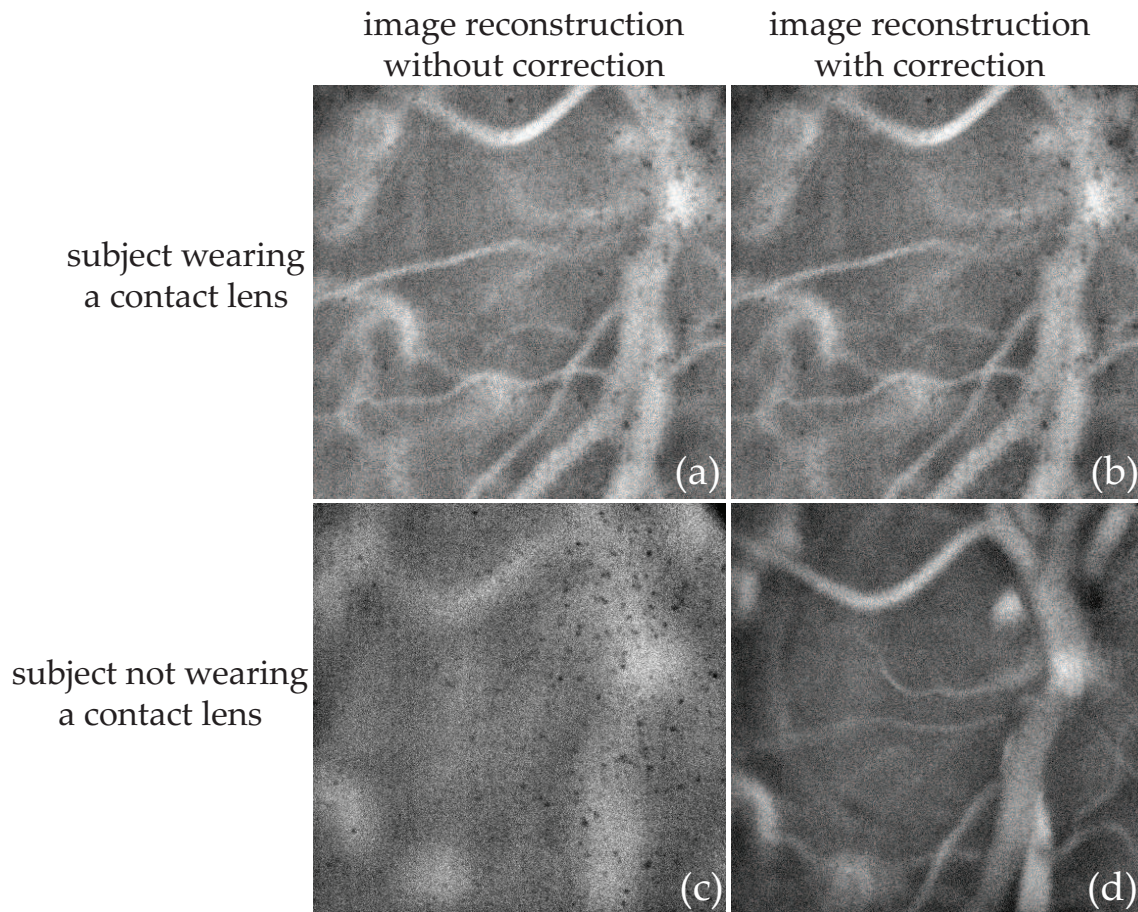


Figure 3.5: Digital compensation of defocus for 3 diopter of myopia with/without contact lens. (a) Regular power Doppler image where the subject is wearing a contact lens (thus the eye is effectively emmetropic). (b) The iterative optimization procedure does not improve the image quality. (c) The subject is no longer wearing a contact lens, when the image reconstructed at the same reconstruction plane as before is blurred. (d) The optimization procedure allows to retrieve an image with a similar quality as before. This demonstrates the feasibility of aberration digital correction with LDH, although the use of it seems rather limited.

simple experiment with/without contact lens, but it does not seem to improve the image quality, which could be expected because of the limited flow sensitivity, but it may also be imputable to a failure from the algorithm in finding the best Zernike polynomial coefficients. This work is currently being pursued.



## Chapter 4

# Imaging the choroid

### 4.1 Article: Choroidal vasculature imaging with laser Doppler holography

In this chapter is presented the possibility to image the choroidal vasculature with LDH. The choroid is a tissue that is both crucial for the retinal health and poorly understood as of yet because of the obstacles to direct and easy optical imaging: scattering and absorption in the RPE and photoreceptor cells, and melanin of the choroid itself, and large blood flow in choroidal vessels. The results we obtained with LDH are presented in the form of an article published in *Biomedical Optics Express*. This article explores what structures are revealed by LDH and how to make use of the quantitative flow measurements to perform an arteriovenous differentiation in the choroid. We made extensive comparisons with commercial instruments that helped us better understand the physiology of the choroid. To the best of my knowledge, this article demonstrates the first non-invasive imaging of the choroid with arteriovenous differentiation capability. The method used to position the subject in front of the instrument is discussed in this Chapter, as well as some complimentary results: color composite LDH montages, and montages based on the Doppler spectrum asymmetry.



# Choroidal vasculature imaging with laser Doppler holography

LÉO PUYO,<sup>1,2,\*</sup> MICHEL PAQUES,<sup>2,3,4</sup> MATHIAS FINK,<sup>1,2</sup>  
JOSÉ-ALAIN SAHEL,<sup>2,3,4</sup> AND MICHAEL ATLAN<sup>1,2</sup>

<sup>1</sup>*Institut Langevin, Centre National de la Recherche Scientifique (CNRS), Paris Sciences & Lettres (PSL University), École Supérieure de Physique et de Chimie Industrielles (ESPCI Paris), 1 rue Jussieu, 75005 Paris, France*

<sup>2</sup>*Paris Adaptive Optics, Retinal Imaging, and Surgery, (PARIS) Group, France*

<sup>3</sup>*Centre Hospitalier National d'Ophthalmologie des Quinze-Vingts, INSERM-DHOS CIC 1423, 28 rue de Charenton, 75012 Paris, France*

<sup>4</sup>*Institut de la Vision-Sorbonne Universités, 17 rue Moreau, 75012 Paris, France*

\**gl.puyo@gmail.com*

**Abstract:** The choroid is a highly vascularized tissue supplying the retinal pigment epithelium and photoreceptors. Its implication in retinal diseases is gaining increasing interest. However, investigating the anatomy and flow of the choroid remains challenging. Here we show that laser Doppler holography provides high-contrast imaging of choroidal vessels in humans, with a spatial resolution comparable to state-of-the-art indocyanine green angiography and optical coherence tomography. Additionally, laser Doppler holography contributes to sort out choroidal arteries and veins by using a power Doppler spectral analysis. We thus demonstrate the potential of laser Doppler holography to improve our understanding of the anatomy and flow of the choroidal vascular network.

© 2019 Optical Society of America under the terms of the [OSA Open Access Publishing Agreement](#)

## 1. Introduction

The choroid is a highly vascularized tissue supplying the retinal pigment epithelium (RPE) and photoreceptors which carries a notably higher blood flow than the retina itself [1]. It is gaining interest as a potential driver of a number of retinal diseases, a role which has been documented by indocyanine green angiography (ICG-A) [2] and optical coherence tomography (OCT) [3, 4]. Evidence indeed suggests that the choroid is involved in the pathogenesis of diseases such as central serous chorioretinopathy, myopic chorioretinal atrophy, and chorioretinal inflammatory diseases [5]. Additionally, the implication of choroidal vascular abnormalities has been suggested in age-related macular degeneration (AMD) [6]. Thus, a better insight into the choroid physiology in normal and pathological conditions appears to be crucial to improve our understanding of many ocular diseases.

The choroid is a very remarkable tissue, with the vascular compartment accounting for most of its volume. The normal choroidal circulation originates from the posterior ciliary arteries (PCAs), branching into short PCAs (SPCAs) that penetrate the sclera usually in the posterior pole [7]. The distribution of flow within the choroid itself is rather poorly known because the anatomical disposition of choroidal vessels remains difficult to document in patients. ICG-A enables imaging of choroidal vessels thanks to the penetration of infrared light through the optical barrier formed by the photoreceptor and epithelial cells. Although the clinical use of ICG-A has been recommended for a few highly selective chorioretinal disorders [8], it is an invasive method that allows limited insights into the arteriovenous distinction in most eyes and does not allow flow analysis. Non-invasive optical methods include OCT which allows visualization of the choroid on cross-sections with a high signal to noise ratio and study of the choroidal thickness [9]. OCT-angiography (OCT-A) is a speckle contrast imaging method based on OCT that allows for

the volumetric imaging quality of OCT with a functional contrast sensitive to blood flow, and it has allowed to image the retinal vascular tissue with high spatial resolution [10]. This led to the finding that many retinal diseases are related to an increased choroidal thickness, with vascular dilation being the primary cause of such increased thickness [5]. OCT based methods have been used with the purpose of imaging the choroid en-face [11–14] but the technique faces issues including fringe washout due to the large choroidal blood flow and recent work suggests that a higher acquisition rate improves the quality of choroidal images [15]. Laser speckle flowgraphy also allows en-face imaging of the choroid but details of choroidal vessels are rather limited [16, 17]. Ultimately, none of the above-mentioned techniques allows a robust arteriovenous differentiation and quantitative flow measurements. Very recently, line-scanning laser Doppler flowmetry was used successfully to reveal the choroidal vasculature [18], but no arteriovenous differentiation was investigated.

Laser Doppler holography (LDH) is a digital holographic method that relies on analyzing the beat frequency spectrum between a Doppler broadened beam and a monochromatic reference beam to extract a blood flow contrast [19–21]. We have shown in humans that LDH can reveal blood flow in retinal vessels over an extended field of view with a temporal resolution down to a few milliseconds [22]. Because digital holography allows for the reference beam to be the main source of light on the camera, ultrahigh speed measurements of the Doppler power spectral density (DPSD) can be performed over a full field. This allows to separate weakly Doppler shifted photon (from dynamic scattering and global eye movements) and strongly Doppler shifted photon (from pulsatile flow in blood vessels). Low-frequency shift contributions are discarded in a temporal Fourier transform analysis thus producing an effective selection of the photons that have been scattered by high velocity red cells. Owing to this ability to select strongly Doppler shifted light, we were able to reveal choroidal vessels where the flow is even greater than in the retina, resulting in even greater Doppler frequency shifts. In this work, we found that LDH was able to reveal choroidal vascular structures that were not observed with state of the art ICG-A and OCT instruments. Besides, we show that an additional Fourier analysis of the DPSD in choroidal vessels offers a robust segregation of vessels based on their blood flow which leads to an arteriovenous differentiation.

## 2. Methods

### 2.1. Laser Doppler holography

We used the laser Doppler holography setup sketched in Fig. 1 and presented in [22]. Briefly, it consists of a fiber Mach-Zehnder optical interferometer where the light source used for the experiments is a 45 mW and 785 nm single-mode fiber diode laser (Newport SWL-7513-H-P), spatially and temporally coherent. In contrast with our previous work, we did not use acousto-optic modulators and real-time monitoring channel which further simplifies the optical setup. The power of the laser beam incident at the cornea was 1.5 mW of constant exposure and covered the retina over approximately  $4 \times 4 \text{ mm}^2$ . This irradiation level is compliant with the exposure levels of the international standard for ophthalmic instruments ISO 15004-2:2007. The images presented in this manuscript were obtained in the left and right eye of the same subject that were healthy except for moderate myopia. The eye used in Fig. 7 has a -3.5 diopters myopia and the eye used for all the other figures has -5.5 diopters myopia. Informed consent was obtained for the subject and experimental procedures adhered to the tenets of the Declaration of Helsinki.

The wave backscattered by the retina, which bears a Doppler broadened spectrum, is combined with the reference wave using a non-polarizing beamsplitter cube. The polarization of the reference wave is adjusted with a half-wave plate and a polarizer to optimize fringe contrast. The interferograms formed in the sensor plane are recorded using a CMOS camera (Ametek - Phantom V2511, quantum efficiency 40%, 12-bit pixel depth, pixel size  $28 \mu\text{m}$ ) with a  $f_S = 60 \text{ kHz}$  frame rate in a  $512 \times 512$  format; the exposure time for each frame was set to  $16.215 \mu\text{s}$ .

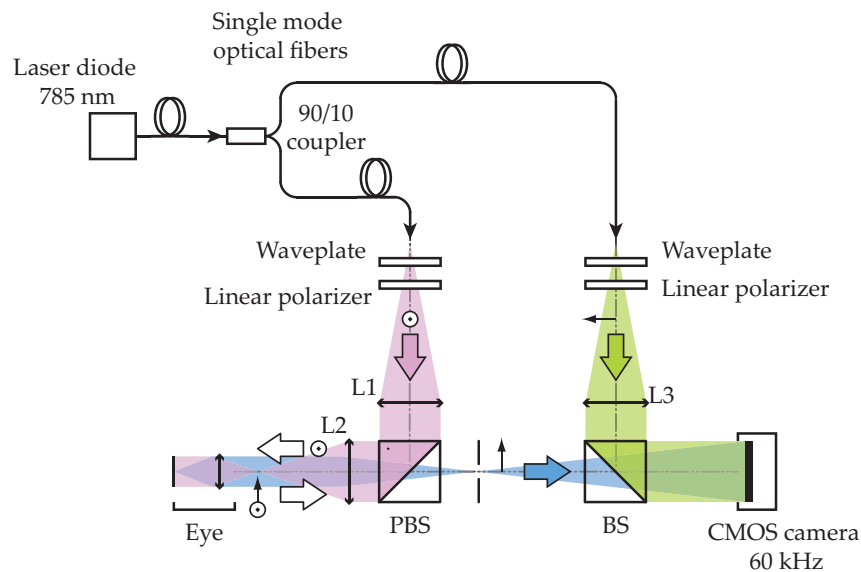


Fig. 1. Laser Doppler holography optical setup. L1, L2 and L3 are converging lenses. PBS: Polarizing Beam-Splitter. BS: Beam-Splitter. The light source is a single wavelength laser diode (SWL-7513-H-P, Newport). The Doppler broadened light backscattered by the retina and choroid is combined with the reference field and interferograms are recorded on the CMOS camera (Ametek - Phantom V2511) running at 60 kHz.

The diffracted speckle pattern is numerically propagated to the retinal plane using the angular spectrum propagation. The holographic configuration is on-axis and the reconstruction distance ( $z \approx 0.19$  m) is large enough so that the twin image energy is spread over the reconstructed hologram and has no appreciable effect on the resulting image. After numerical propagation, the beat frequency spectrum of the reconstructed holograms is analyzed by short-time Fourier transform which naturally removes the interferometric zero-order term. In this approach, it is considered that the cross-beating terms of the holograms carry the Doppler broadening caused by the passage of red cells and the data processing consists of measuring the local optical temporal fluctuations. Power Doppler images are calculated by integration of the DPSD over the frequency interval  $[f_1, f_2]$ . Power Doppler images quantitatively measure blood flow in arbitrary units that depend on both the local blood volume and blood velocity.

## 2.2. Hyperspectral flow analysis

In our previous work, we analyzed the retinal blood flow changes of power Doppler images throughout cardiac cycles. In this article, we present vasculature maps obtained by averaging power Doppler images over time, and we introduce a temporal analysis method based on a segmentation of the DPSD. The chosen frequency range  $[f_1, f_2]$  over which the DPSD is integrated to produce power Doppler images determines the blood vessels that are revealed according to their flow [22]. Integrating lower Doppler frequency shifts reveal vessels with a lower blood flow while large frequency shifts reveals vessels with greater flows. When separating the low and high frequency power Doppler images and combining them into a single composite color image, we can simultaneously display vessels with a wide range of flows and qualitatively encode the flow information in the image color, as shown in subsection 3.4.

### 2.3. *Stitching process*

The field of view of an individual power Doppler image is about  $4 \times 4 \text{ mm}^2$ , so in order to cover a wider field of view, we stitched together power Doppler images of multiple locations of the eye fundus. This process was used to create images displayed in subsection 3.2 and 3.4. For each location, power Doppler images were averaged for a period of time approximately equal to the cardiac cycle period although for a few acquisitions, the averaging time was slightly under this duration as some frames affected by micro-saccades were discarded. The open source software Hugin was used to create the full panorama by stitching together all the individual power Doppler images. To proceed with the alignment procedure, the images were manually placed in the correct position and control points were automatically detected in manually indicated regions of interest using Hugin's CPFind native function. Hugin optimization changes the images position parameters so as to minimize the separation of the control points and improve the overall image alignment in the overlapping areas. Finally, Hugin's built-in blender compensated for the mismatches of intensity on the edges of individual images.

## 3. Results

### 3.1. *Choroidal vasculature around the optic nerve head*

In Fig. 2, we compare different angiographic instruments by imaging the optic nerve head (ONH) region in the same eye. A power Doppler image is presented in Fig. 2(a), and Fig. 2(b) shows the equivalent ICG angiogram (Heidelberg - Spectralis HRA). Figures 2(c) and 2(d) show respectively an OCT-A image of the retinal layer and an OCT image of the choroid without the choriocapillaris (Optovue, RTVue XR Avanti with AngioVue). The RTVue XR Avanti that was used is a spectral-domain OCT that can acquire up to 70,000 A-Scan/s with an operating wavelength centered on 840 nm.

The power Doppler image in Fig. 2(a) reveals the retinal vessels with a bright contrast due to LDH blood flow sensitivity. Other vascular structures around the ONH can be noticed such as choroidal arteries originating from paraoptic SPCAs in the surroundings of the optic disc (arrows). We assume the vascular structure revealed by LDH around the ONH is the peripapillary choroidal arcade, possibly made more visible by a local photoreceptor atrophy. With ICG-A, the retinal vessels and the two cilioretinal arteries are clearly revealed, but the choroidal arteries cannot be observed. The timing of the acquisition of the ICG angiogram presented in this figure was late enough that the dye had reached the venous retinal vasculature. However, as discussed, in the ICG-angiogram of the arterial timing in the same eye shown in subsection 3.3, the choroidal arteries are still not revealed close to the ONH. OCT-A reveals retinal vessels with a very good sensitivity to small blood flows and allows to effectively identify to which layers belong the blood vessels. For the part of the choroid that is below the choriocapillaris, we show an OCT image instead of OCT-A as we found it revealed more efficiently the larger choroidal vessels. However even with OCT the imaging quality of these vessels is rather limited.

Hence in the images presented, LDH is able to reveal retinal vascular structures and also other deeper vascular structures that were not observed with ICG-A or with difficulty with OCT (Optovue, RTVue XR Avanti).

### 3.2. *Choroidal vasculature in the posterior pole*

In Fig. 3 a wide-field LDH panorama is compared to SLO and ICG-A. The power Doppler image shown in Fig. 3(a) was made out of  $5 \times 5$  individual images that were stitched together following the process described in subsection 2.3. The power Doppler images were calculated using the frequency range  $[f_1, f_2] = 5 - 30 \text{ kHz}$ . To help with the registration all images overlapped and the total field of view is estimated at 12 mm. Figures 3(b) and 3(c) show the same region imaged with the SLO and ICG-A modules of a Spectralis-HRA (Heidelberg).

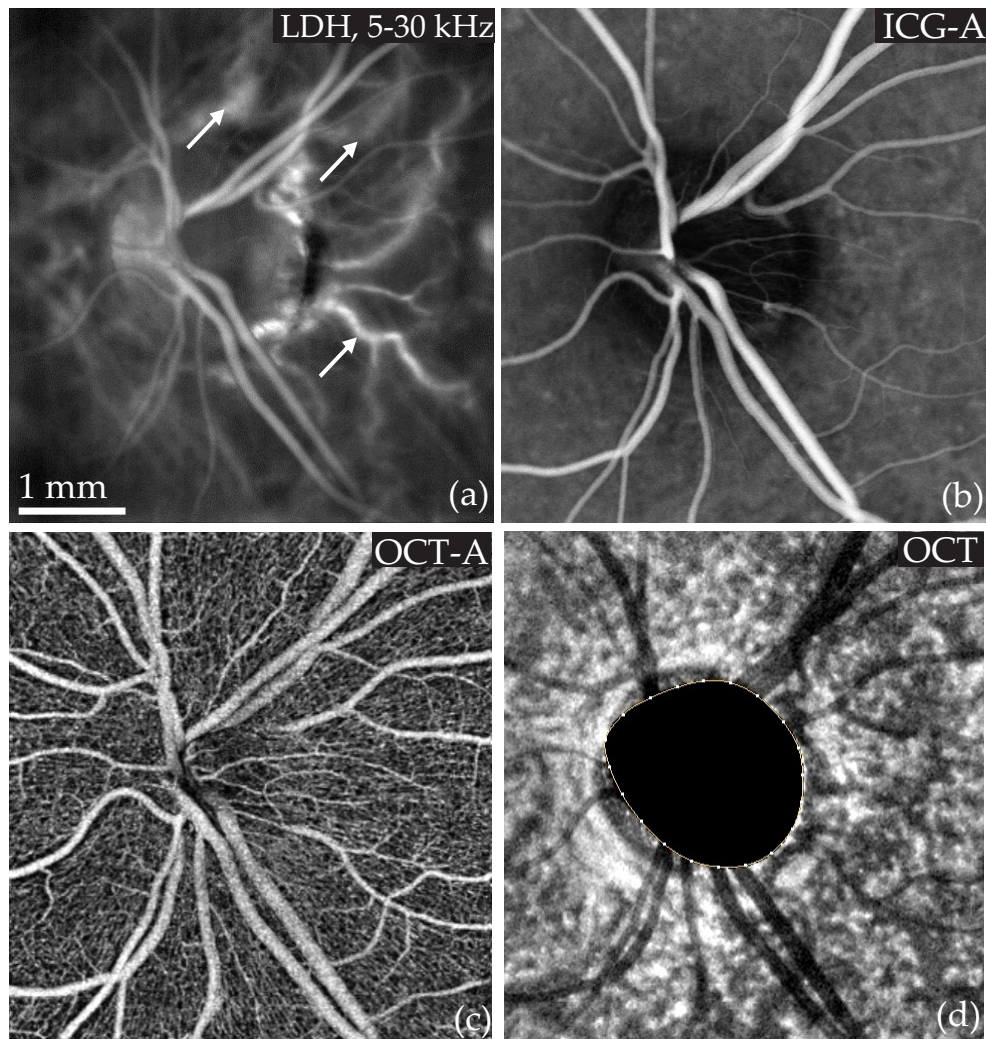


Fig. 2. Angiographic images of the optic nerve head (ONH) with different instruments. (a) LDH reveals the retinal vasculature and choroidal arteries (arrows) originating from paraoptic SPCAs. (b) A late ICG-A (Heidelberg - Spectralis) reveals the retinal vessels. (c) and (d): OCT-A image of the retinal layer and OCT image of the choroid without the choriocapillaris (Optovue, Avanti with AngioVue), respectively.

SLO reveals the vessels that belong to the retina, so when comparing images obtained with SLO and LDH, it is manifest that the vast majority of the vessels revealed by the latter instrument belongs to the choroid. ICG-A also reveals some choroidal vessels as well as retinal vessels, but when comparing LDH with ICG-A it is apparent that these two angiograms do not consistently show the same choroidal vessels. For example close to the macular region, ICG-A does not reveal any vessel whereas LDH shows several very large choroidal vessels. Conversely, some vessels apparent with ICG-A are not visible on this LDH panorama.

In the posterior pole, the choroidal vessels visible on power Doppler images calculated with high frequency shifts tend to be choroidal arteries while the choroidal vessels visible with this ICG angiogram are mostly veins. This conjecture is consistent with the known anatomy of the

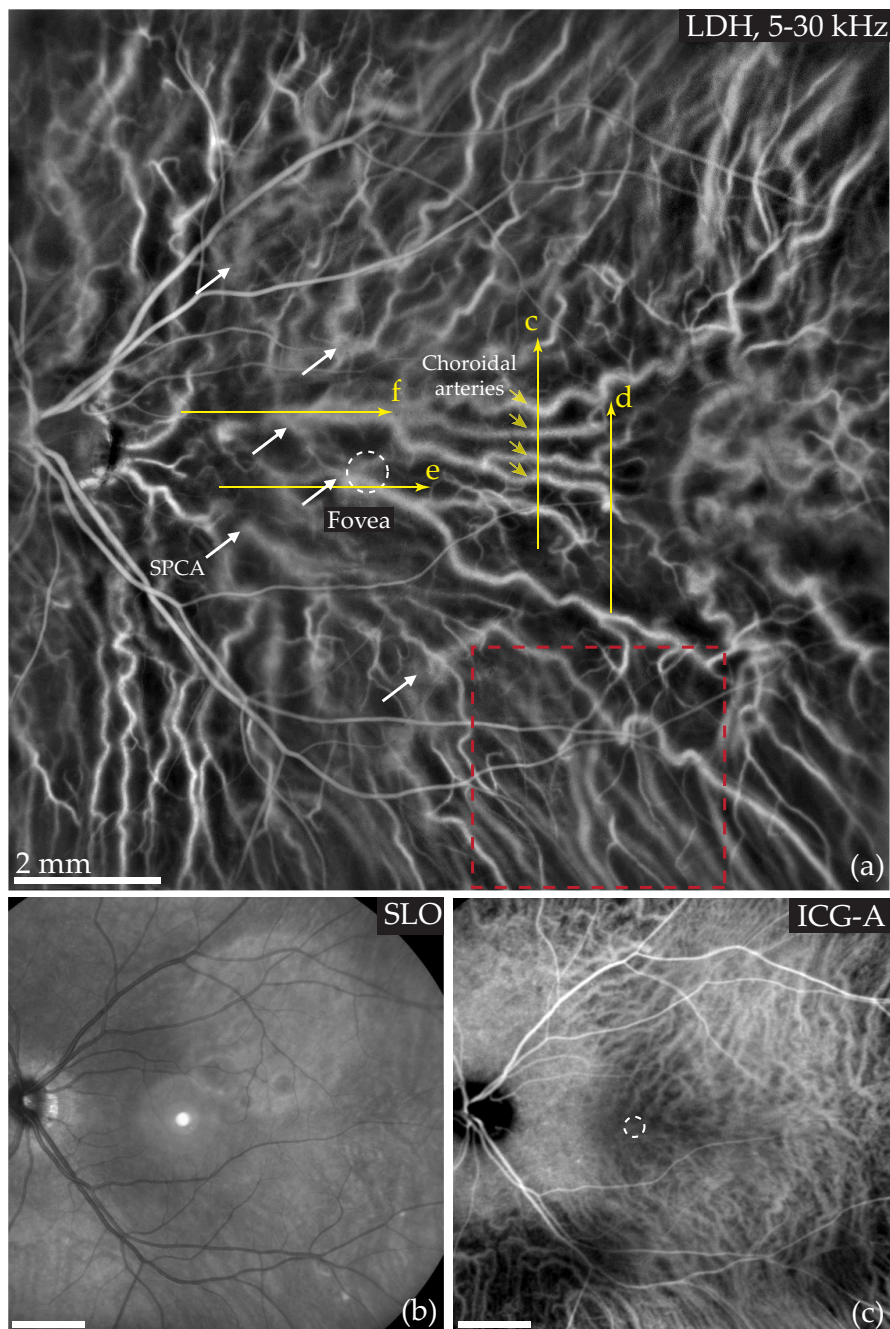


Fig. 3. LDH, SLO and ICG-A in the same eye. (a)  $5 \times 5$  power Doppler images calculated over 5 – 30 kHz are stitched to produce a panorama on which retinal and choroidal vessels can be observed. The white circle indicates the fovea; the white arrows mark temporal distal SPCAs; the yellow lines shows the location of the B-scans presented in Fig. 4 and the yellow arrows mark the position of the deep choroidal arteries identified in Fig. 4(c). Finally, the red square indicates the location of the images in Fig. 6. (b) SLO (Heidelberg - Spectralis) image of the retina. (c) Late ICG angiogram (Heidelberg - Spectralis) image showing retinal and choroidal vessels (mostly veins).

choroid, as approximately 10-20 SPCAs from the sclera penetrate the choroid around the ONH and macular region and run radially towards the equator [23,24]. The SPCAs then branch into choroidal arteries that supply the RPE and photoreceptors in a segmented organization [25].

The type of vessels that are revealed with LDH is determined by the frequency range used to compute power Doppler images. As demonstrated in subsection 3.4, to some extent it is possible to produce power Doppler images more similar to late phase ICG-A when using a lower frequency range. To make this panorama, the DPSD was integrated over the frequencies 5 – 30 kHz which gives more importance to larger flows as the total power Doppler signal is naturally greater in areas with a greater flow such as arteries. However as explained in subsections 3.4 and 3.5, outside the posterior pole, choroidal arteries tend to stay visible during the late phase ICG-A while choroidal veins become visible at high Doppler frequency shifts. It can also be noticed in the bottom right part of this LDH panorama that some choroidal veins can already be observed with LDH.

To some extent there might have been variations of quality between individual acquisitions (eye position etc) which may explain the differences in contrast that can be noticed between some parts of the panorama. It is also likely that the variations in density of photoreceptors and epithelial cells has an impact on the imaging quality of the underlying vessels. In particular, in the macular region where the density of photoreceptor and epithelial cells is the highest, it seems the quality of the power Doppler images is slightly lower compared to the rest of the panorama.

We used state of the art OCT instruments in the same eye as the one used to make the images presented in Fig. 3 in order to give another insight of the same choroidal structures. A swept-source OCT (Zeiss - Plex Elite 9000) was used to produce en-face images shown in Figs. 4(a) and 4(b). This instrument can acquire  $12 \times 12$  mm images with a relatively high A-scan rate (100 kHz) and wavelength of operation (1050 nm) which allow a better penetration depth into the choroid. We also used a spectral-domain OCT (Heidelberg - Spectralis) to make cross-sectional images in areas where we identified specific choroidal structures with LDH. We present the structural rather than the OCT-A images obtained by swept-source and spectral-domain OCT (SS-OCT and SD-OCT, respectively) as we found they revealed the deeper choroidal vasculature more efficiently. Figures 4(a) and 4(b) show en-face SS-OCT images of the deep choroid and sclera, and Figs. 4(c)–4(f) are SD-OCT B-scans. The positions of all B-scans are indicated in Fig. 3, those presented in Fig. 4(c) and 4(d) are also indicated in Fig. 4(a), while those in Fig. 4(e) and 4(f) are indicated in Fig. 4(b).

Although OCT images do not provide any quantitative flow measurements and no arteriovenous differentiation of vessels, they give accurate 3D information about the deep choroidal vasculature. Indeed the choroidal vessels leave very contrasted dark projections underneath them which helps locating them, and especially, the cross-sectional OCT images provide information that can help interpret the LDH panorama.

Figure 4(a) allows to reconcile the information obtained with LDH, ICG-A and OCT. For example, in the bottom right of the image shown in Fig. 3(a), one can find the same choroidal veins than with ICG-A and LDH. On the bottom left, SS-OCT reveals the same choroidal veins as ICG-A, but not the choroidal arteries visible with LDH. In this figure, we also show the remarkable positions of four choroidal arteries very noticeable with LDH in Fig. 3(a), and also visible with en-face SS-OCT in Fig. 4(a), and on the SD-OCT B-scan shown in Fig. 4(c). Although these arteries give a very strong signal with LDH, OCT data reveals that they are lying at the bottom of the choroid. This shows that the depth of field of the instrument allows to have both choroidal and retinal vessels simultaneously in focus despite the distance between them as measured with OCT being close to  $400 \mu\text{m}$ . Finally, the value of the information brought by LDH comparatively with OCT in this case is explicit, as whereas OCT does not provide clear information on the type of the detected choroidal vessels, as shown in subsection 3.4 in this same region of interest, LDH can identify these vessels as choroidal arteries.

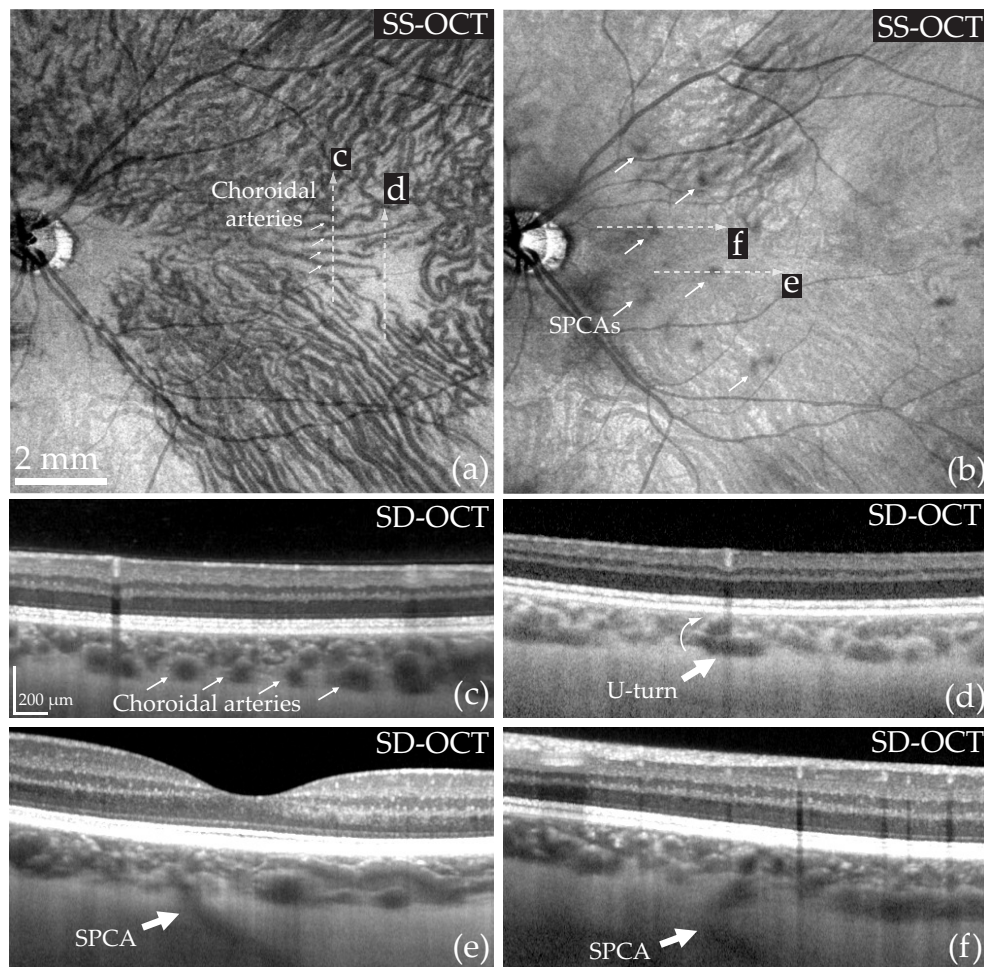


Fig. 4. Structural OCT images of the same eye as in Fig. 3. (a) and (b): en-face SS-OCT images (Zeiss - Plex Elite 9000) showing the deep choroid and the sclera, respectively. The arrows indicate choroidal arteries in (a) and SPCAs in (b). (c-f): SD-OCT B-scans (Heidelberg - Spectralis). (c) Cross-section showing the position of four choroidal arteries in the choroid (arrows). (d) A choroidal artery makes a U-turn to approach Bruch's membrane. (e-f) The entry points of SPCAs visible with LDH are also revealed with OCT.

In Fig. 4(b), we show an en-face SS-OCT image that was averaged over  $70\ \mu\text{m}$ , approximately  $30\ \mu\text{m}$  below the choroid. At this depth, it is possible to see the entry points of some temporal distal SPCAs from the sclera into the choroid as they appear as dark spots (arrows) with SS-OCT. With LDH, these SPCAs can be detected as they carry a very large flow, but they appear as white and blurred spots, probably because of the strong intrasceral scattering. We marked with arrows some same SPCAs that were detected with LDH and SS-OCT in Fig. 3(a) and in Fig. 4(b), respectively. Additionally, we provide two examples of SD-OCT cross-section views of SPCAs identified with both LDH and SS-OCT in Fig. 4(e) and 4(f). The course of these SPCAs is not straightforward as in both cases they are slightly tilted with respect to the optical axis. When looking closely at the LDH panorama in Fig. 3(a), it is possible to see how some of these SPCAs branch into choroidal arteries. For example, when following the course of the SPCA examined in

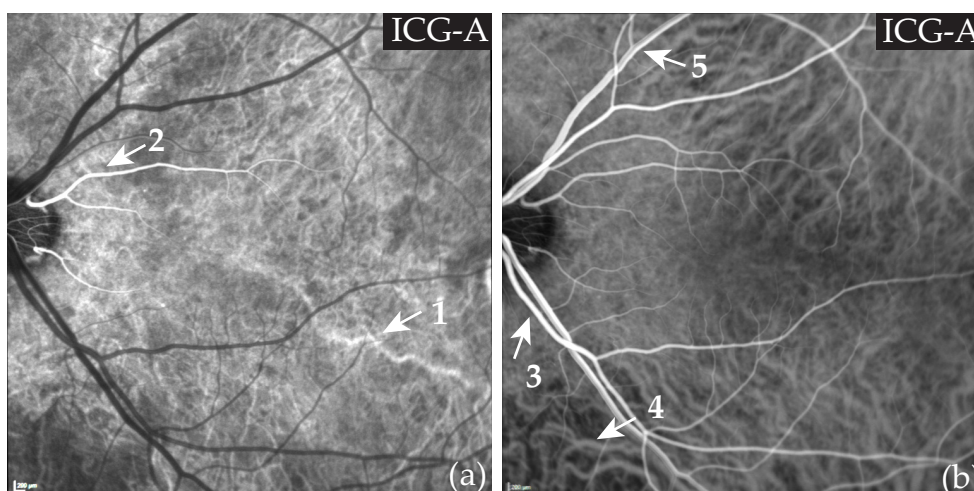


Fig. 5. Circulation of the ICG in the fundus vasculature. (a) Choroidal arteries and cilioretinal arteries are revealed by the contrast agent. (b) The contrast agent has reached the retinal arteries, the choroidal veins, and the retinal veins whereas choroidal arteries cannot be observed anymore. See [Visualization 1](#) for the injection movie.

Fig. 4(e), it is possible to see it branch into two large choroidal arteries.

Finally, in Fig. 4(d), we present a case of a choroidal artery making a U-turn to approach Bruch's membrane. We identified the same vessel with LDH where the upright part of the artery is very bright because the direction of its flow maximizes the Doppler sensitivity. Around this bright spot, it is possible to see with LDH this choroidal artery branch into smaller arteries in a vascular pattern that resembles a star. Although LDH is sensitive to lateral motion which allows to image vessels in en-face planes [22], the sensitivity of the instrument appears greater for flows with a direction parallel to the optical axis. This explains why the upright part of SPCAs and choroidal arteries approaching Bruch's membrane produce a greater power Doppler signal.

As choroidal vessels are entangled in multiple planes of the 3D choroid and the vertical summation of vessels makes it somewhat non trivial to interpret OCT images. The task of isolating any vessel in a particular en-face plane is complicated by the fact that averaging too many layers makes the resulting image unintelligible. However we have shown here that the information LDH and OCT can provide about the choroidal vasculature can complete one another to provide a better understanding of the overall choroidal anatomy. For example, we have demonstrated here that it is possible to follow a choroidal artery from the scleral SPCA to the location where it branches into arterioles.

### 3.3. Stages of the indocyanine green injection

ICG-A unfolds in several stages corresponding to the filling pattern of the dye inside the vascular circuit of the eye [26], which gives a certain insight into the choroid and helps identify arteries and veins. We performed an ICG-A in the same subject on whom we made the power Doppler panorama presented in Fig. 3 and we present in Fig. 5 the stages of the ICG circulation in the fundus vasculature that we observed experimentally. The vascular structures progressively appearing are marked by arrows. The general pattern is that following the natural course of blood through the vessels, the dye reveals arteries before veins, and the choroidal circuit is revealed slightly before the retinal circuit [27]. At the initial time of the injection (see [Visualization 1](#)), no features are yet visible. Then Fig. 5(a) shows that following the injection, the choroidal arteries

and two cilioretinal arteries coursing towards the fovea are the first structures to be revealed. Subsequently the contrast agent reaches the retinal arteries, the choroidal veins, and finally the retinal veins as shown in Fig. 5(b). At this stage, the cilioretinal arterial branches are still visible while the choroidal arteries no longer are.

Although they contribute to the retinal capillary bed like other retinal vessels, the cilioretinal arteries are branches from the PCAs. Consequently, they become visible concomitantly with choroidal arteries as they all originate from the PCA circulation. It can also be noticed that the first vessels revealed by ICG-A tend to be the ones that are the most visible with the LDH panorama shown in the previous section. For example, the large vessel marked by the arrow "1" in Fig. 5(a) is also very visible in Fig. 3(a) which is another indication that high frequency power Doppler images preferentially reveal choroidal arteries.

With ICG video-angiography, a movie is recorded throughout the injection so the gain is set to a higher value to allow for a better temporal resolution, which diminishes the signal to noise ratio of the images. It is possible to obtain higher quality ICG angiograms of the choroidal arterial phase by using a lower gain. For example, analog photographic cameras have been very successfully used to image the choroidal arteries [28]. However the choroidal arterial phase only lasts for a few seconds which makes the task challenging. This illustrates that ICG-A is a technique that is operator-dependent, especially when it is used with the intention to capture the moment when the arterial vasculature of the choroid is revealed.

#### 3.4. Power Doppler spectral analysis

We present here the results we obtained by using the process described in subsection 2.2. We applied this process in a single power Doppler image in Fig. 6, and in two stitched areas to demonstrate the reproducibility of the method. In Fig. 7, we show power Doppler panoramas for the whole spectrum of the DPSD, and in Fig. 8 we show the result of the process for part of the same dataset used in Fig. 3 to show how the data can be processed otherwise to reveal different information about the choroid.

In Fig. 6, the temporal Fourier transform was calculated over 8192 holograms (i.e. 0.14 s), and two power Doppler images calculated for the frequency ranges 2.5 – 6 kHz and 10 – 30 kHz are shown in Fig. 6(a) and 6(b), respectively. A composite color image was obtained by merging these two images in Fig. 6(c) where low and high frequencies are encoded in the cyan and red channels, respectively. In Fig. 6(d), an ICG angiogram of the same region of interest is shown. Finally in Fig. 6(e) are plotted the DPSD measured in the regions of interest drawn in Fig. 6(c). These spectra were calculated as the squared magnitude of the temporal Fourier transform of the reconstructed holograms amplitude.

Noticeably, the power Doppler images made with the frequency ranges 2.5 – 6 kHz and 10 – 30 kHz do not reveal exactly the same vessels. In this example, the 2.5 – 6 kHz power Doppler image is very similar to the ICG-angiogram, whereas the 10 – 30 kHz power Doppler image reveals vessels that cannot be observed with ICG-A; the largest vessel revealed with LDH (arrow) in Fig. 6(b) even seems to leave a shadow on the ICG angiogram. The frequency range at which the vessels appear is not determined by the size of the vessels, as proven by the fact that the vessels revealed with the high frequency power Doppler image can be of both bigger or smaller size than those revealed by the low frequency power Doppler image. Figure 6(c) offers an effective segregation of vessels based on the blood flow they carry: vessels appearing in red have a larger blood flow whereas vessels in blue have a lower blood flow. The spectra in Fig. 6(e) were calculated in vessels of comparable sizes for "A" and "V" and in a third area "B" where although no vessels can be observed, there are unresolved retinal and choroidal capillaries. These spectra can be segmented into three parts. In the first range of frequency 0 – 2 kHz, the DPSD in vessels "A" and "V" is smaller than that of the background "B". Then for 2 – 6 kHz, the DPSD is greater in the area "V" and finally, for large frequencies such as 10 – 30 kHz, the DPSD is clearly greater

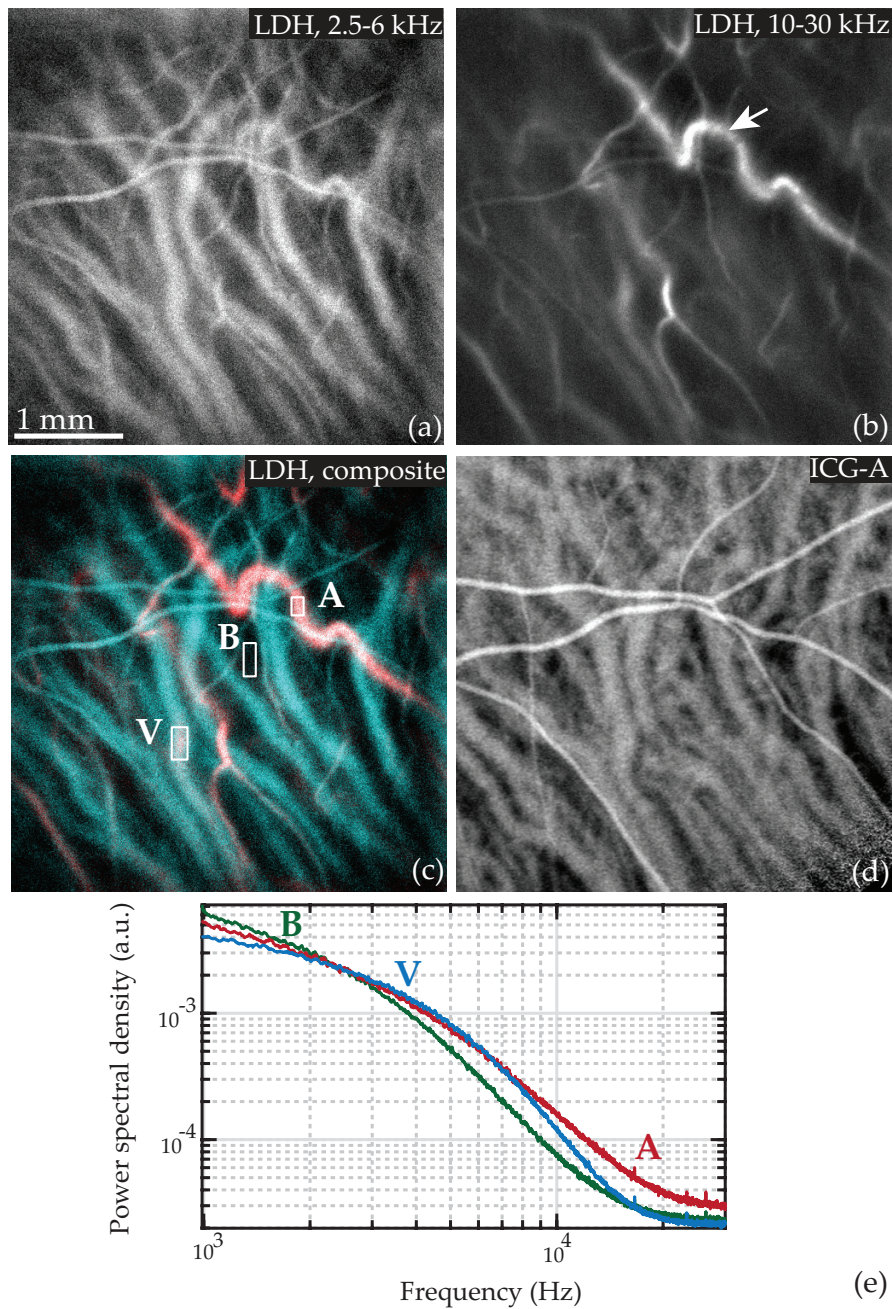


Fig. 6. Power Doppler spectral images and ICG-A. (a) Power Doppler image where the DPSD is integrated over 2.5 – 6 kHz which reveals vessels with smaller flows. (b) Power Doppler image integrated over 10 – 30 kHz revealing vessels with larger flows. (c) Composite color image of (a) and (b) encoded in the cyan and red channels, respectively. (d) ICG-A in the same region. (e) Power spectral density spatially averaged over the regions indicated in (c). See [Visualization 2](#) for the power Doppler spectral movie.

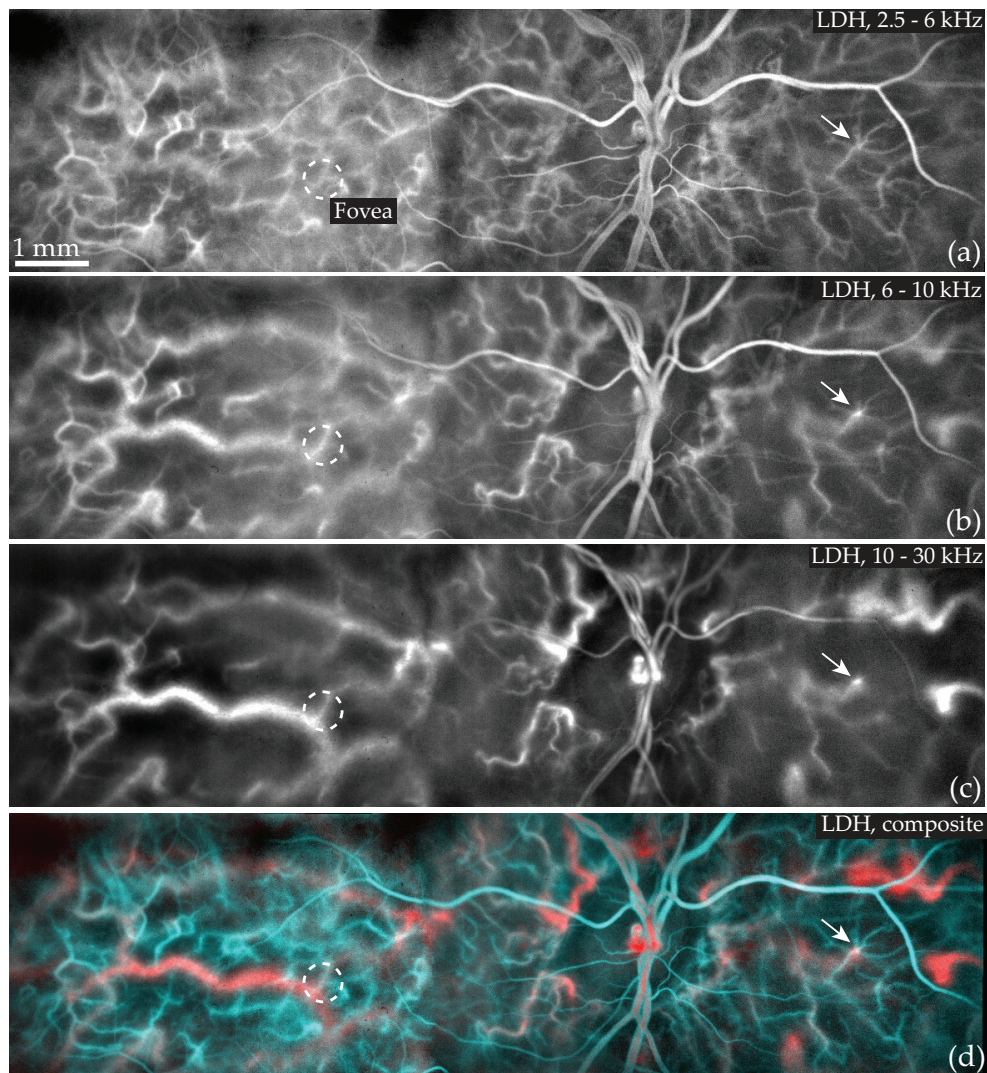


Fig. 7. Power Doppler spectral panoramas calculated using the frequency ranges (a) 2.5 – 6 kHz, (b) 6 – 10 kHz, 10 – 30 kHz. (d) Composite color panorama of (a) and (c) encoded in the cyan and red channels, respectively.

in the vessel "A".

This information is enough to determine that "A" and "V" actually mark an artery and a vein, respectively. First, whereas all the surrounding vessels were seen in the late phase ICG-angiogram, the "A" vessel was not observed, and as we saw in subsection 3.3, this is typical of choroidal arteries. Secondly, this "A" vessel appears with very high Doppler frequency shifts which reveal very large flows, and choroidal arteries are known to have large flows. Other vessels appear at high Doppler frequency shifts despite being of a smaller caliber than the typical vessels appearing at low frequencies; these vessels were also not observed with ICG-A so we can assume they are choroidal arterioles that carry a comparable flow than choroidal veins of a greater size.

In Fig. 7, power Doppler spectral images from five lateral adjacent locations were stitched following the process described in subsection 2.3 to reveal the choroidal vasculature over a

wider field of view. Figures 7(a)–7(c) show power Doppler panoramas for the frequency ranges 2.5 – 6 kHz, 6 – 10 kHz, and 10 – 30 kHz, respectively. Figure 7(d) is the composite color panorama that was obtained by fusing power Doppler spectral images for the frequency ranges 2.5 – 6 kHz and 10 – 30 kHz (encoded in the cyan and red channels, respectively).

In Fig. 7(a) is shown the power spectral image with the lowest frequency range that reveals the smallest detected flows. It is possible to observe large retinal vessels with the lumen of the vessels that appears dark because the local optical Doppler broadening occurs for higher frequency shifts than 2.5 – 6 kHz. It is also possible to observe many choroidal vessels with small and intermediate sizes (see white arrow for example). In Fig. 7(b), it is possible to notice choroidal arteries and retinal vessels of intermediate size are well visible. Finally, in Fig. 7(c), it is possible to observe the largest choroidal arteries and other large choroidal structures temporally around the ONH with an improved contrast. The apparent diameter of retinal vessels is reduced when compared to the low frequency power Doppler image. Once again the color composite image in Fig. 7(d) offers an effective segregation of vessels based on their blood flow that facilitates an arteriovenous differentiation of the choroidal vessels. The red vascular structures that stand out the most in Fig. 7(d) are large choroidal arteries originating from temporal and nasal distal SPCAs and paraoptic SPCAs. Conversely, the vascular structures with a low blood flow that stand out in blue in Fig. 7(d) are the small choroidal vessels.

In Figs. 8(a) and 8(b), images from four lateral locations have been stitched for the frequency ranges 2.5 – 6 kHz and 10 – 30 kHz, respectively. Figure 8(c) is the composite color panorama that was obtained by fusing power Doppler spectral images for low and high frequencies encoded in the cyan and red channels, respectively. Finally, Fig. 8(d) offers a comparison with ICG-A in the same region of interest.

In the low frequency power Doppler panorama shown in Fig. 8(a), large retinal vessels with their lumen in dark as well as smaller vessels can be observed. Especially, about 2 mm temporally from the fovea, a network of choroidal vessels of relatively small caliber (about 40  $\mu\text{m}$ ) is visible. In Fig. 8(b), the small choroidal vessels cannot be observed anymore and instead very large choroidal vessels can be observed. Finally, Fig. 8(c) shows again a segregation of vessels based on their flow that leads to an arteriovenous differentiation: the large choroidal vessels that appear in red are arteries, whereas the large vessels in blue are mostly veins and the smaller ones are arterioles.

In the two power Doppler stitched images presented in Figs. 7 and 8, we have shown that despite the high density of RPE and photoreceptor cells in the central retina, LDH allows us to reveal the underlying choroidal vasculature. Large choroidal arteries lying in the deepest layer of the choroid can be revealed and in both examples it could be noticed that the fovea lied right over a very large choroidal artery. Some other interesting vasculature structures revealed by LDH are the smaller choroidal vessels which have the size of choroidal arterioles or venules. These vessels are arterioles following this reasoning: as the choroidal veins are not visible at their starting points with LDH, choroidal venules should also not be observable with LDH as their flow is even lower. Interestingly, Fig. 8(d) shows that during the venous filling, ICG-A reveals neither the choroidal arterioles visible in the low frequency power Doppler image, nor the large choroidal arteries visible in the high frequency power Doppler image.

The comparative ICG angiogram we show in Fig. 8 does not reveal any of these arterial choroidal structures of the macular region because the ICG angiogram is made at a late stage of the dye injection so choroidal arteries are no longer visible. However even in the early stage (cf Fig. 5(b)), the structures revealed by LDH could here hardly be discerned with ICG video-angiography.

The power Doppler spectral analysis that we present here led to a clear discrimination of vessels according to their flows; in the posterior pole, this process allowed us to differentiate the choroidal arteries from the choroidal veins. The validity of this segregation is further discussed

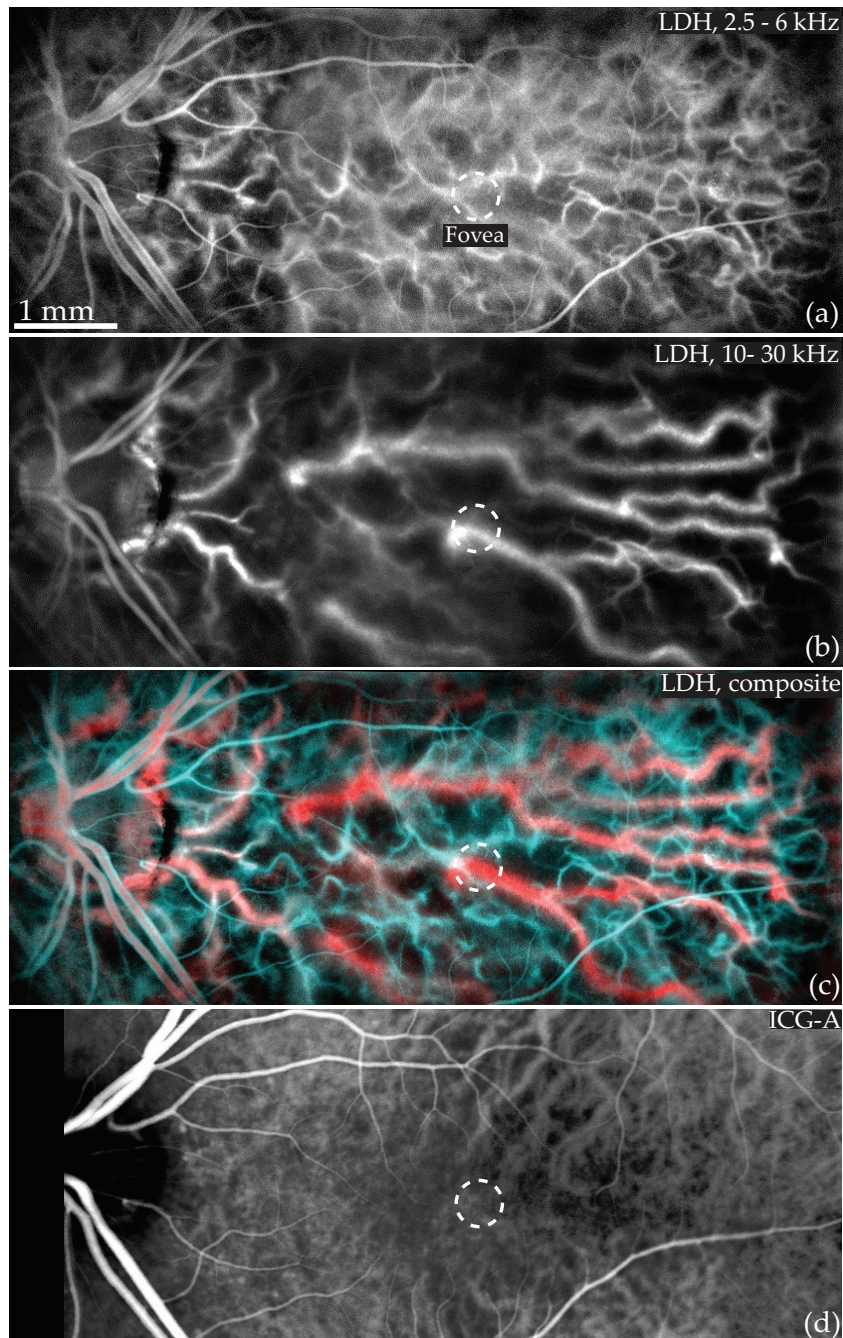


Fig. 8. Power Doppler spectral panoramas and ICG-A. (a) Low frequency (2.5 – 6 kHz) power Doppler panorama which reveals small flows. (b) High frequency (10 – 30 kHz) power Doppler panorama revealing vessels with larger flows. (c) Composite color panorama of (a) and (b), encoded in the cyan and red channels, respectively. (d) ICG angiogram of the same region. See [Visualization 3](#) for a power Doppler spectral movie in one of the area. .

in section 4.

### 3.5. Vortex veins

The density of epithelial and photoreceptor cells decreases with the eccentricity from the fovea, so as these cells contribute to the scattering and absorption of light, a decrease in their density benefits the contrast of choroidal images. Imaging at a greater eccentricity seems to improve the visibility of choroidal vessels with both ICG-A and LDH. In the example presented in Fig. 9(b), LDH was used at about 45 degrees of eccentricity in the superior temporal choroid; the region of interest is delineated by the rectangle drawn in the ICG angiogram presented in Fig. 9(a). The power Doppler image, calculated by integrating the DPSD over 10 – 30 kHz, reveals a vortex vein with a contrast and spatial resolution comparable to ICG-A. The arrow marks a choroidal artery visible with both ICG-A and LDH with a different contrast: with ICG-A this artery does not appear as bright as the surrounding vessels whereas with laser Doppler holography this artery appears brighter than the surrounding vessels. Considering these surrounding vessels are converging towards the vortex vein, they can be identified as choroidal veins.

In the previously shown example in Fig. 6, the choroidal veins were visible for the frequency range 2.5 – 6 kHz whereas the veins close to the vortex veins are visible for the frequency range 10 – 30 kHz. This large difference of flow can be explained by the fact that the flow in choroidal veins is expected to be considerably larger close to the vortex veins due to their large caliber and because they also drain the iris and ciliary body circulation which further increase the flow they carry. Conversely, in Fig. 8, some choroidal veins visible with ICG-A could not be observed with LDH. It can be assumed that it is because in this region of interest the choroidal veins are too close to their starting points so their flow might be too weak and goes undetected by LDH.

This example shows that outside the posterior pole, ICG-A is able to reveal choroidal arteries in the late injection phase, while on the other hand, choroidal veins become visible on high frequency power Doppler images. Nonetheless, the greater power Doppler signal of the artery compared to the other vessels despite its smaller diameter still allows us to identify it as a choroidal artery.

## 4. Discussion and conclusion

In the present optical configuration, the depth of field of the instrument is large enough so that both retinal and choroidal vessels come into focus at the same reconstruction distance. This allows for the simultaneous visualization of flow in vessels from both of these vascular circuits. However, care should be taken when comparing flows between retinal and choroidal vessels as the layers lying in-between the retina and the choroid may have a non-trivial effect on the spectrum of the transmitted light. Power Doppler images are calculated from the high-pass filtered DPSD: this quantity depends on both the number of Doppler shifted photons (amplitude of the spectrum) and their frequency shifts (spectral distribution of the energy). The photoreceptor and RPE layers between the retina and the choroid are known for their scattering and absorption properties which may alter the Doppler spectrum of the transmitted light. Consequently, although these layers possibly have only a negligible effect on the spectrum, without further investigation it is not possible to compare the power Doppler values for the retina and the choroid.

Still, the results we obtained are consistent with what can be expected: the flow rate through the retinal vessels is known to be significantly slower than the blood flow through the choroidal vasculature [1]. In our results, the signal of the retinal arteries lies in a lower frequency range than the frequency range for the choroidal arteries (cf Figs. 6–8). Additionally, comparisons of flow in inter-choroidal vessels should be legitimate as the light backscattered by these structures goes through the same layers. Finally and most importantly, although the results are not quantitative for velocities, they still allow for a visualization of the architecture of the choroidal vasculature.

Recording interferograms with a high-speed camera is essential to the purpose of LDH.

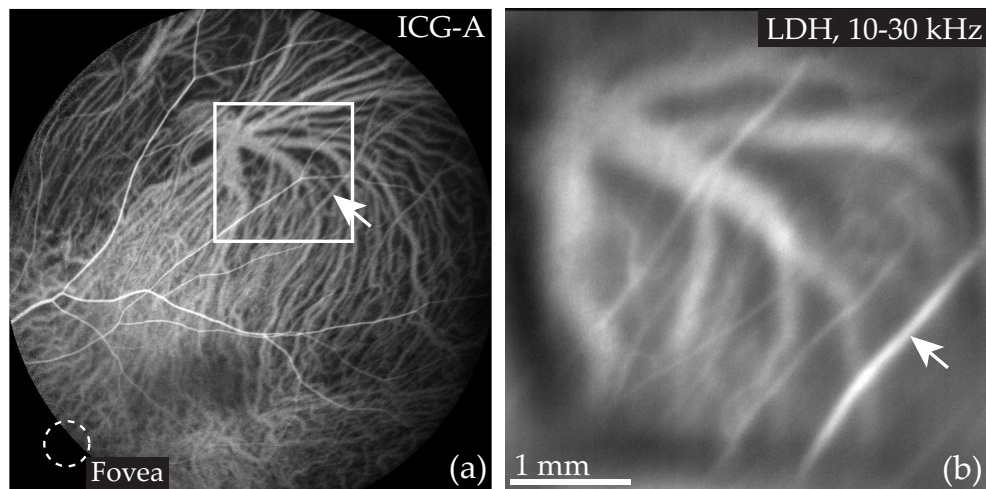


Fig. 9. Vortex vein imaged with ICG-A and LDH (a) ICG angiogram; the vortex vein is located at about 45 degrees of eccentricity; the fovea is indicated by the white circle and the rectangular box indicates the area covered by the power Doppler image (b) Power Doppler image integrated over the frequency range 10 – 30 kHz. The arrow marks a choroidal artery visible with a bright contrast with LDH, and a darker contrast with ICG.

Wideband measurements must be performed with a Nyquist-Shannon frequency above the frequency of the signal to be sampled [22]. As shown in the spectra calculated in Fig. 6, the Doppler broadening in choroidal arteries can reach 30 kHz or more (as visible in [Visualization 2](#) and [Visualization 3](#)), and a major part of the Doppler signal for these vessels with a large flow lies in frequencies above 10 kHz. Consequently, in this configuration it is necessary to be working with a camera that has a framerate of several tens of kHz to obtain a better signal-to-noise ratio. Using a powerful reference beam allows to dramatically increase the framerate in comparison with optical configuration where the images on the camera are formed only with the light backscattered by the retina, which is why digital holography is convenient to make wideband laser Doppler measurements. We had previously shown that the pulsatile signal in retinal blood vessels can be separated from the signal of global eye motion [22]. In the case of choroidal vessels, not only the Fourier filtering helps removing the Doppler contribution of global eye motion, but it also helps to select the photons backscattered to the sensor despite the strongly scattering layers lying in-between. Finally, as was also discussed in [22], working with highly Doppler shifted photons also means working with multiply scattered light, which allows the angiographic contrast to be sensitive to lateral motion. This property of power Doppler images is yet again ascertainable as in all the images presented in this manuscript, the vast majority of the vessels are oriented perpendicularly to the optical axis.

As demonstrated in subsection 3.4, a power Doppler spectral analysis allows to discriminate vessels according to the intensity of their flow. In Fig. 6 this approach allowed to reveal choroidal veins with a low frequency power Doppler image while large choroidal arteries were revealed with a high frequency power Doppler image. In the other example considered in Fig. 8, choroidal arteries can be seen once again at high frequencies, but on the other hand choroidal arterioles can be seen at low frequencies with choroidal veins. And finally, in the example presented in Fig. 9, choroidal veins near a large vortex vein can be seen at high Doppler frequency shifts. Thus, the separation that can be made with this spectral analysis is based on the flow of the vessels and not whether they are arteries or veins. However we identified with certainty as arteries some vessels such as those that appear at high frequencies in the macular region for several

reasons: (i) they appear at an early stage of ICG-A, (ii) they can be seen with LDH for strong Doppler frequency shifts, and (iii) they have a geometry consistent with the expected disposition of choroidal arteries.

Because the fovea has the highest needs for oxygen and nutrients and because numerous ocular diseases tend to form primarily in this area, the choroidal vasculature in the submacular region is of paramount importance. We have shown that comparatively with other ophthalmic instruments, LDH gives new insights about choroid, especially in the submacular area. Even operating at 785 nm LDH can provide high contrast imaging of choroidal vessels in human, with a resolution at least equivalent to state of the art ICG-A and OCT instruments. LDH preferentially reveals the choroidal arterial structures due to their greater blood flow, and provides the opportunity to discriminate arteries from veins in the posterior pole of the choroid based on a power Doppler spectral analysis. Combined with the accurate volumetric information accessible with OCT, LDH offers the possibility to gain major insights about the physiology of the choroid non-invasively.

### Funding

LABEX WIFI (Laboratory of Excellence ANR-10-LABX-24) within the French Program Investments for the Future (ANR-10-IDEX-0001-02 PSL); European Research Council (ERC Synergy HELMHOLTZ (610110)).

### Acknowledgments

The authors would like to thank Céline Chaumette, Carlo Lavia, Alain Gaudric, and Sarah Mrejen for data acquisition and helpful discussions, and Kate Grieve for advice and language corrections. The Titan Xp used for this research was donated by the NVIDIA Corporation.

### Disclosures

The authors declare that there are no conflicts of interest related to this article.

### References

1. A. Alm and A. Bill, "Ocular and optic nerve blood flow at normal and increased intraocular pressures in monkeys (macaca irus): a study with radioactively labelled microspheres including flow determinations in brain and some other tissues," *Exp. Eye Res.* **15**, 15–29 (1973).
2. P. M. Bischoff and R. W. Flower, "Ten years experience with choroidal angiography using indocyanine green dye: a new routine examination or an epilogue?" *Documenta Ophthalmol.* **60**, 235–291 (1985).
3. H. Lavers and H. Zambarakji, "Enhanced depth imaging-OCT of the choroid: a review of the current literature," *Graefe's Arch. for Clin. Exp. Ophthalmol.* **252**, 1871–1883 (2014).
4. D. Ferrara, N. K. Waheed, and J. S. Duker, "Investigating the choriocapillaris and choroidal vasculature with new optical coherence tomography technologies," *Prog. Retin. Eye Res.* **52**, 130–155 (2016).
5. S. Mrejen and R. F. Spaide, "Optical coherence tomography: imaging of the choroid and beyond," *Surv. Ophthalmol.* **58**, 387–429 (2013).
6. D. S. McLeod, R. Grebe, I. Bhutto, C. Merges, T. Baba, and G. A. Luty, "Relationship between RPE and choriocapillaris in age-related macular degeneration," *Investig. Ophthalmol. & Vis. Sci.* **50**, 4982–4991 (2009).
7. S. S. Hayreh, "Blood Supply of the Optic Nerve," in *Ischemic Optic Neuropathies*, (Springer, 2011), pp. 35–78.
8. L. A. Yannuzzi, "Indocyanine green angiography: a perspective on use in the clinical setting," *Am. J. Ophthalmol.* **151**, 745–751 (2011).
9. R. F. Spaide, H. Koizumi, and M. C. Pozzoni, "Enhanced depth imaging spectral-domain optical coherence tomography," *Am. J. Ophthalmol.* **146**, 496–500 (2008).
10. R. F. Spaide, J. G. Fujimoto, N. K. Waheed, S. R. Sadda, and G. Staurengi, "Optical coherence tomography angiography," *Prog. Retin. Eye Res.* **64**, 1–55 (2018).
11. W. Choi, K. J. Mohler, B. Potsaid, C. D. Lu, J. J. Liu, V. Jayaraman, A. E. Cable, J. S. Duker, R. Huber, and J. G. Fujimoto, "Choriocapillaris and choroidal microvasculature imaging with ultrahigh speed OCT angiography," *PLoS One* **8**, e81499 (2013).
12. R. Poddar, D. Y. Kim, J. S. Werner, and R. J. Zawadzki, "In vivo imaging of human vasculature in the chorioretinal complex using phase-variance contrast method with phase-stabilized 1- $\mu$ m swept-source optical coherence tomography," *J. Biomed. Opt.* **19**, 126010 (2014).

13. I. Gorczynska, J. V. Migacz, R. J. Zawadzki, A. G. Capps, and J. S. Werner, "Comparison of amplitude-decorrelation, speckle-variance and phase-variance OCT angiography methods for imaging the human retina and choroid," *Biomed. Opt. Express* **7**, 911–942 (2016).
14. K. Kurokawa, Z. Liu, and D. T. Miller, "Adaptive optics optical coherence tomography angiography for morphometric analysis of choriocapillaris," *Biomed. Opt. Express* **8**, 1803–1822 (2017).
15. J. V. Migacz, I. Gorczynska, M. Azimipour, R. Jonnal, R. J. Zawadzki, and J. S. Werner, "Megahertz-rate optical coherence tomography angiography improves the contrast of the choriocapillaris and choroid in human retinal imaging," *Biomed. Opt. Express* **10**, 50–65 (2019).
16. T. Sugiyama, M. Araie, C. E. Riva, L. Schmetterer, and S. Orgul, "Use of laser speckle flowgraphy in ocular blood flow research," *Acta Ophthalmol.* **88**, 723–729 (2010).
17. G. Calzetti, K. Fondi, A. M. Bata, N. Luft, P. A. Wozniak, K. J. Witkowska, M. Bolz, A. Popa-Cherecheanu, R. M. Werkmeister, D. Schmidl, G. Garhofer, and L. Schmetterer, "Assessment of choroidal blood flow using laser speckle flowgraphy," *Br. J. Ophthalmol.* pp. bjophthalmol–2017 (2018).
18. M. Mujat, Y. Lu, G. Maguluri, Y. Zhao, N. Iftimia, and R. D. Ferguson, "Visualizing the vasculature of the entire human eye posterior hemisphere without a contrast agent," *Biomed. Opt. Express* **10**, 167–180 (2019).
19. C. Magnain, A. Castel, T. Boucneau, M. Simonutti, I. Ferezou, A. Rancillac, T. Vitalis, J.-A. Sahel, M. Paques, and M. Atlan, "Holographic laser Doppler imaging of microvascular blood flow," *JOSA A* **31**, 2723–2735 (2014).
20. M. Pellizzari, M. Simonutti, J. Degardin, J.-A. Sahel, M. Fink, M. Paques, and M. Atlan, "High speed optical holography of retinal blood flow," *Opt. Lett.* **41**, 3503–3506 (2016).
21. D. Donnarumma, A. Brodoline, D. Alexandre, and M. Gross, "4D holographic microscopy of zebrafish larvae microcirculation," *Opt. Express* **24**, 26887–26900 (2016).
22. L. Puyo, M. Paques, M. Fink, J.-A. Sahel, and M. Atlan, "In vivo laser Doppler holography of the human retina," *Biomed. Opt. Express* **9**, 4113–4129 (2018).
23. S. S. Hayreh, "Posterior ciliary artery circulation in health and disease the Weisenfeld lecture," *Investig. Ophthalmol. & Vis. Sci.* **45**, 749–757 (2004).
24. C. V. Network, "Developmental anatomy of the retinal and choroidal vasculature," *The Retin. Its Disord.* **179** (2011).
25. S. S. Hayreh, "Segmental nature of the choroidal vasculature," *Br. J. Ophthalmol.* **59**, 631–648 (1975).
26. K. Hayashi and J. De Laey, "Indocyanine green angiography of submacular choroidal vessels in the human eye," *Ophthalmologica* **190**, 20–29 (1985).
27. F. G. Bottoni, A. L. Aandekerck, and A. F. Deutman, "Clinical application of digital indocyanine green videoangiography in senile macular degeneration," *Graefe's Arch. for Clin. Exp. Ophthalmol.* **232**, 458–468 (1994).
28. P. Amalric, "The choriocapillaris in the macular area," *Int. Ophthalmol.* **6**, 149–153 (1983).

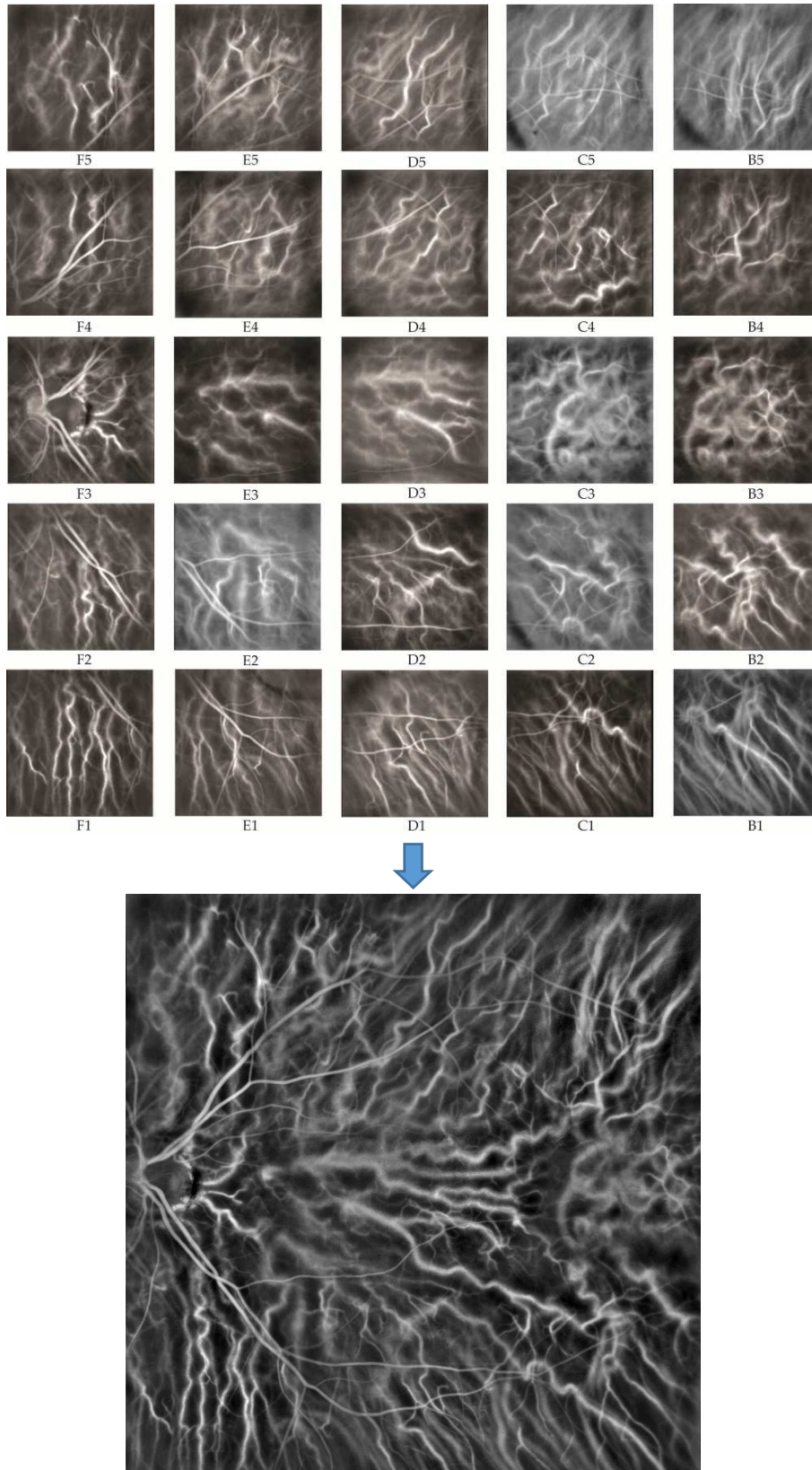


Figure 4.1: Making of an LDH montage. Multiple images from several areas of the fundus are stitched together to obtain a field of view relevant to the size of the choroid. Individual images suffer from vignetting but the software used for the montage (Hugin) is able to compensate the mismatch of intensity in the areas where images overlap.

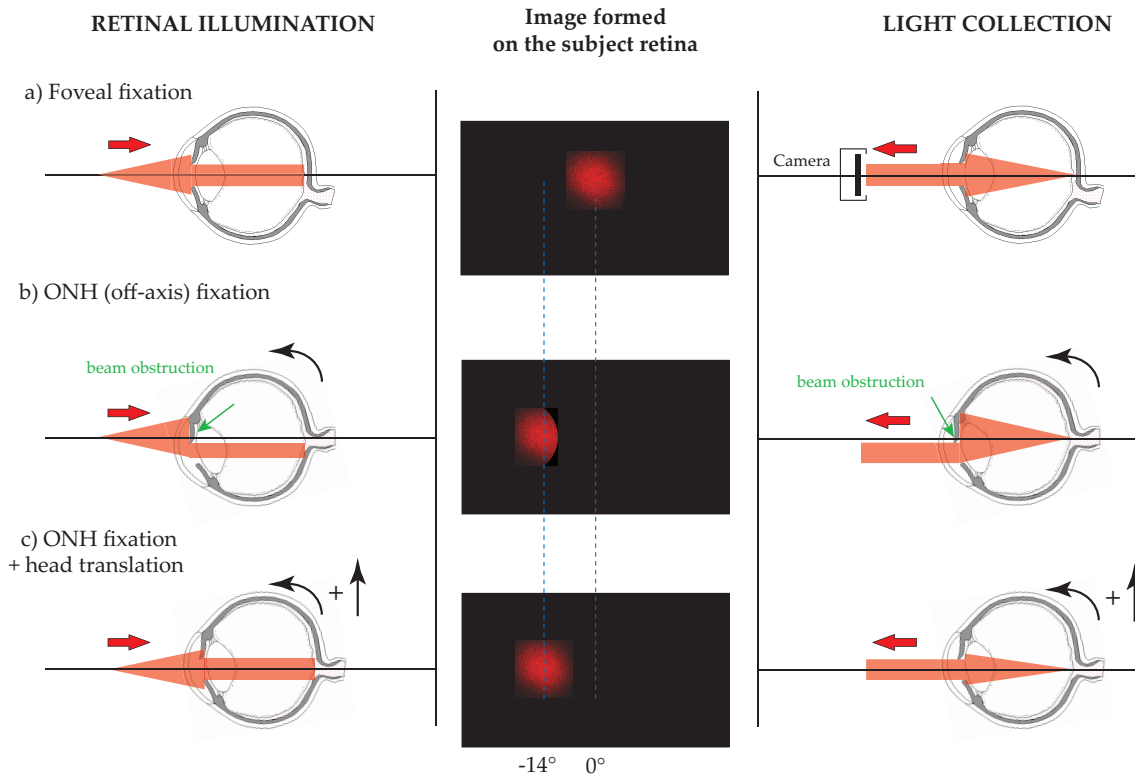


Figure 4.2: Self-positioning of the subject in front of the device, as is necessary in case of absence of real-time monitoring channel, or when the operator wants to acquire images on himself. (a) When the ROI is the fovea, the subject simply needs to stare at the center of the laser beam and the eye would be optically well aligned. (b) However if the ROI is the ONH, if the subject only changes his fixation direction to have the laser beam illuminate the ONH, there is an obstruction of the beam for the illumination and collection. (c) When both changing the fixation direction and translating the head, the optical axis of the eye is better aligned and the beam obstruction is minimized. This basic positioning can be carried out by the subject himself by checking how he perceives the laser beam in his peripheral vision.

## 4.2 Placement of the subject eye

Compared to some other retinal imaging techniques (let's say time-domain full-field OCT with a spatially incoherent illumination [97]), LDH does not require a very precise positioning of the subject pupil to be able to produce images. As the source of light is very coherent spatially and temporally, a mispositioning of the subject pupil that modifies the local optical path length does not prevent interference. However in order not to obstruct the field of view, and to optimize the illumination and collection, a basic alignment is required, especially because we are looking at off-axis locations of the fundus. As illustrated in Fig 4.2 the optical alignment can be performed by the subject himself. Imaging an area close to the fovea does not pose any particular problem: the subject can position himself by making sure he is fixating well into the laser beam, and in that case the subject sees the laser spot in the center of his vision. The complications come when imaging an area on the retina that is off-axis with regards to the eye optical axis. For example the ONH region is very interesting to us, and it is about 14 degrees off axis in the visual field. If the subject positions himself in front of the laser beam and simply looks away at 14 degrees (i.e. operates a rotation) to have the ONH illuminated by the laser, there will be an obstruction of the laser beam for the illumination and collection. Thus the subject must look away and then a translation must be operated in order to have the center of

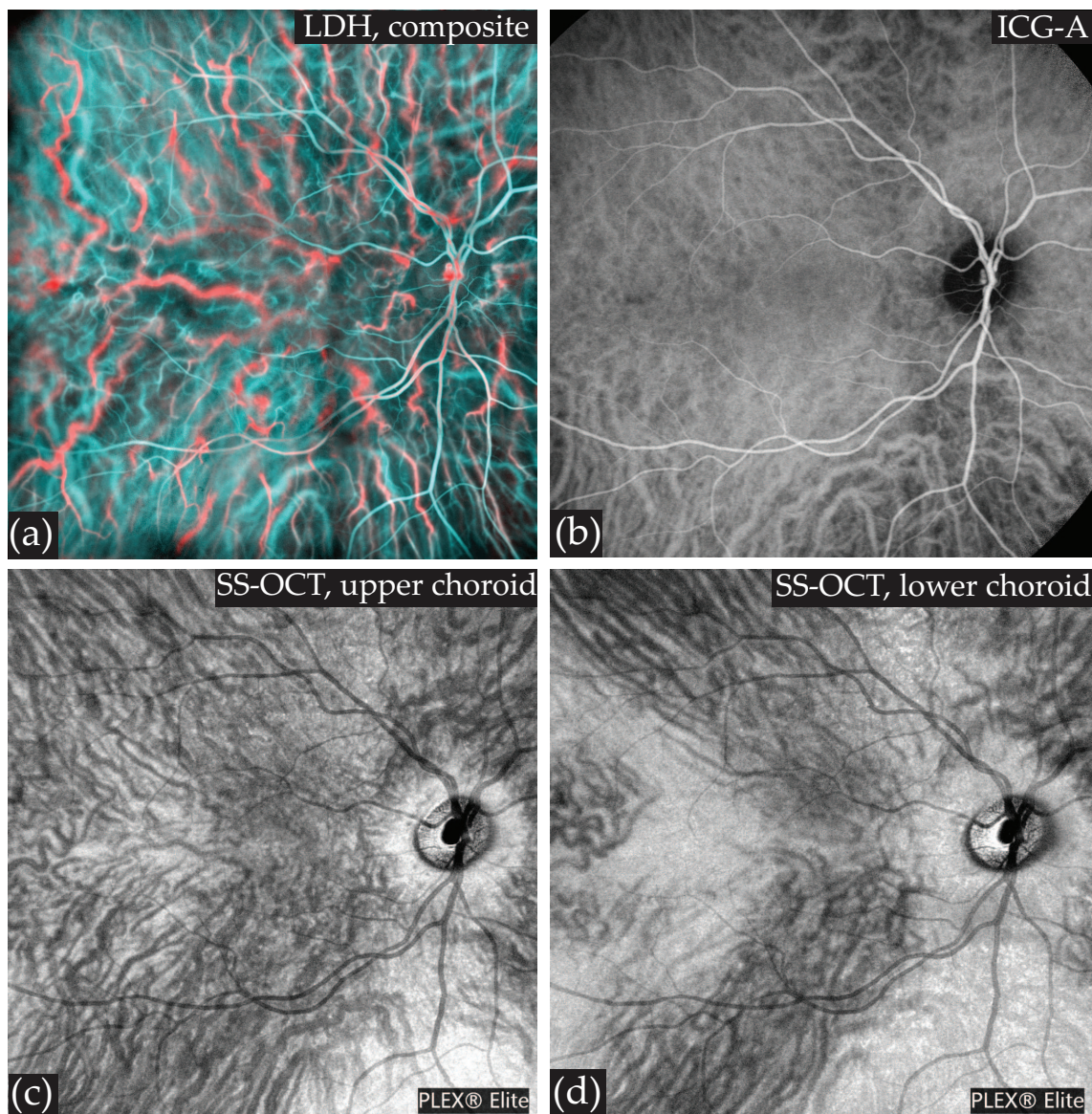


Figure 4.3: Multimodal imaging in an OD eye. (a) LDH composite color image (2.5-6 kHz in cyan and 10-30 kHz in red) where both arteries and veins from the choroid can be revealed with a different contrast; arteries tend to be in red and veins in blue because of the flow differences. (b): ICG-A during the venous phase where the choroidal vessels revealed are mostly veins. (c) and (d): SS-OCT (Plex Elite 9000 - Zeiss) of the deep and superficial choroid, respectively. With OCT, the choroidal vessels best revealed are the largest, or those located on top of the choroid.

the subject pupil on the optical axis. This procedure was used in the early days of the instrument. There is now an additional pupil camera that allows to position the laser beam on the pupil, and then precisely monitor the pupil position with the second imaging channel that relies on LDH. This new configuration has allowed to have untrained subjects have their eye successfully examined with our instrument.

### 4.3 Large LDH color montage

In Fig. 4.3 is shown an example of a LDH montage with color composite images, and two other examples are shown in the Supplementary Materials section at the end of the manuscript. These large field LDH images of the choroidal vasculature fully demonstrate

the potential of LDH to bring a new insight into the choroid: the ability to have a signal with an intensity related to the flow is a great advantage. When comparing the LDH and SS-OCT images, it can be observed that SS-OCT seems to reveal more efficiently the choroidal veins than the choroidal arteries

#### 4.4 Depth of field

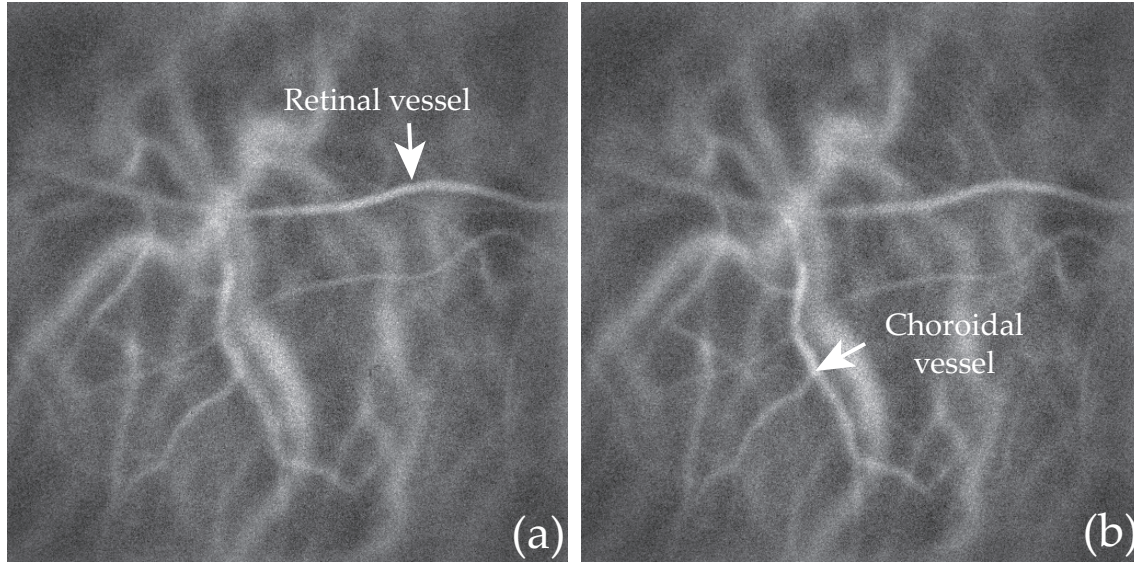


Figure 4.4: Focus difference between the retina and choroid. (a) The numerical propagation is carried out to have the retinal vessel in focus. (b) The choroidal vessel are now in focus.

The example provided in Fig. 4.4 is here to illustrate that in some cases, the depth of field is not large enough to have both the retinal and choroidal layers in focus in the same reconstruction plane. In Fig. 4.4(a) the focus is done on the retinal layer whereas in Fig. 4.4(b) the focus is done on the choroidal layer. The position of retinal blood vessels in the retina varies a lot over the fundus, and the thickness of the choroid varies even more. Overall the choroid and retina are usually thickest around the fovea. The distance between retinal and choroidal vessels can then be around  $300 \mu\text{m}$  in normal subjects, which would be above our expected depth of focus for a subject with a fully dilated pupil (that could be roughly estimated to  $100 \mu\text{m}$  based on a numerical aperture close to 0.1).

#### 4.5 Difference of spectrum panorama

In Fig. 4.5 is shown the equivalent of the montage presented in the Fig. 8 of the article when calculating:

$$M_{0-}(x, y, t_n) = \int_{\omega_1}^{\omega_2} S(x, y, t_n, \omega) - S(x, y, t_n, -\omega) d\omega \quad (4.1)$$

instead of:

$$M_{0+}(x, y, t_n) = \int_{\omega_1}^{\omega_2} S(x, y, t_n, \omega) + S(x, y, t_n, -\omega) d\omega \quad (4.2)$$

As it was presented in the Fig. 7 of the first article,  $M_{0-}$  provides a signal related to the geometry of vessel: a residue of single-scattering leaves a signed Doppler contribution, i.e. this contributions lies only on the positive or negative side of the spectrum depending on the flow direction with respect to the optical axis. This type of images, as illustrated in

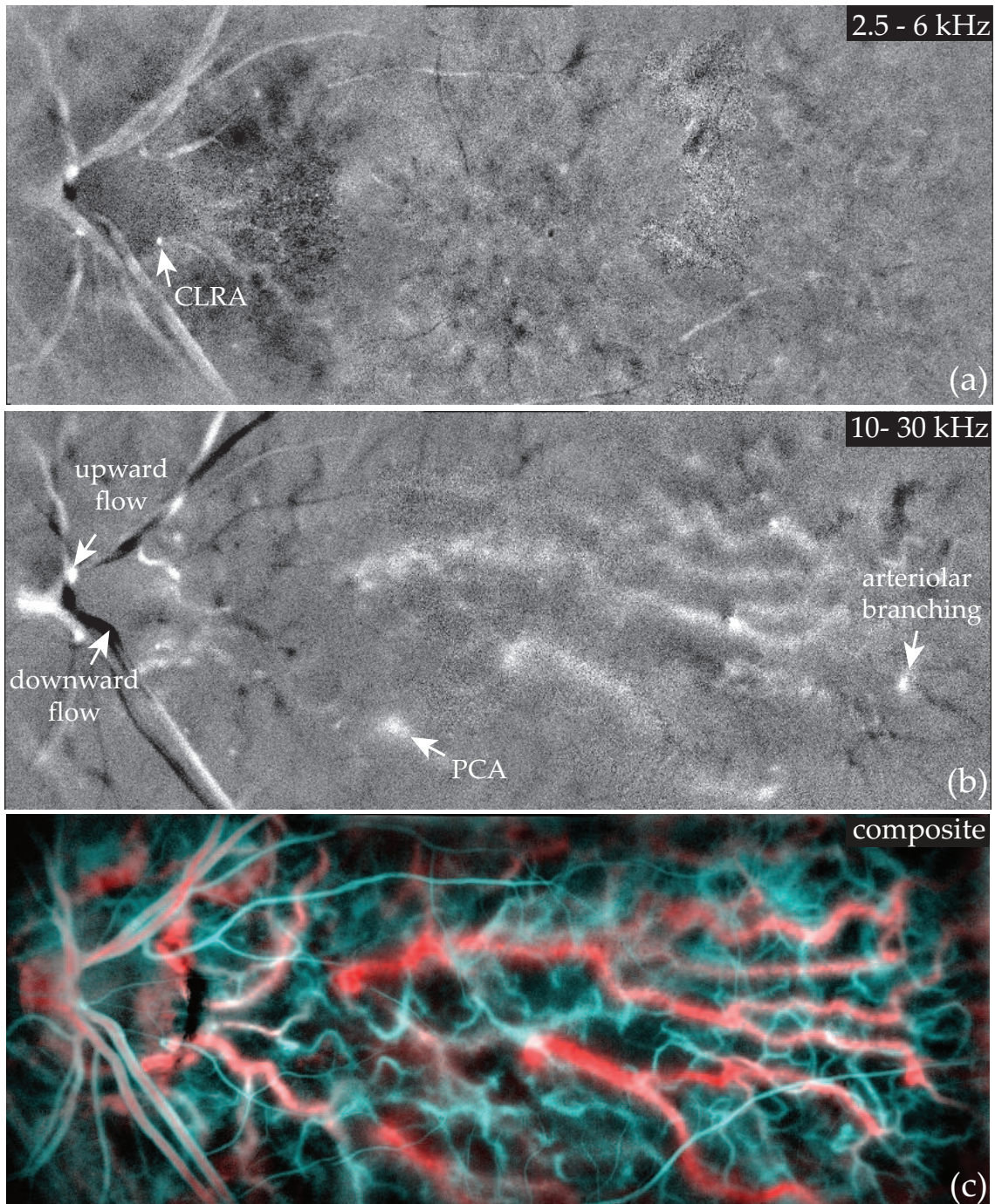


Figure 4.5: LDH montage using the spectrum difference  $M_{0-}$  instead of  $M_{0+}$ . (a) and (b) are  $M_{0-}$  montage for the 2.5-6 and 10-30 kHz frequency ranges. The white and black areas indicate the upward and downward flow directions, respectively. Contrasted parts of vessels reveal when they are not exactly contained in a plane perpendicular to the optical axis. Brights white and dark spots may indicate arterioles and venules. (c) same color composite montage as shown in the article to serve as a comparison.

Fig. 4.5 allows to see the direction of the flow according to the color (bright is towards the camera and dark outward from the camera).

## Chapter 5

# Blood flow waveform analysis

### 5.1 Article: Waveform analysis of retinal and choroidal blood flow with laser Doppler holography

The last article that constitutes this thesis was also published in *Biomedical Optics Express*, and aims at understanding better what are the different contributions to the power Doppler, and try to isolate them. A spatio-temporal filtering is applied to data obtained with the same experimental setup as before, allowing to extract the blood flow waveform in retinal vessels. The flow waveform in retinal arteries and veins can be measured and provides results more consistent with what is expected than before. Additionally, we demonstrate the use of a resistivity index (RI) mapping to characterize the flow waveform in arteries and veins (although vascular resistance only holds a real meaning for arteries). Finally, we explore the possibility to monitor blood flow variations over cardiac cycle simultaneously in the choroid and retina.

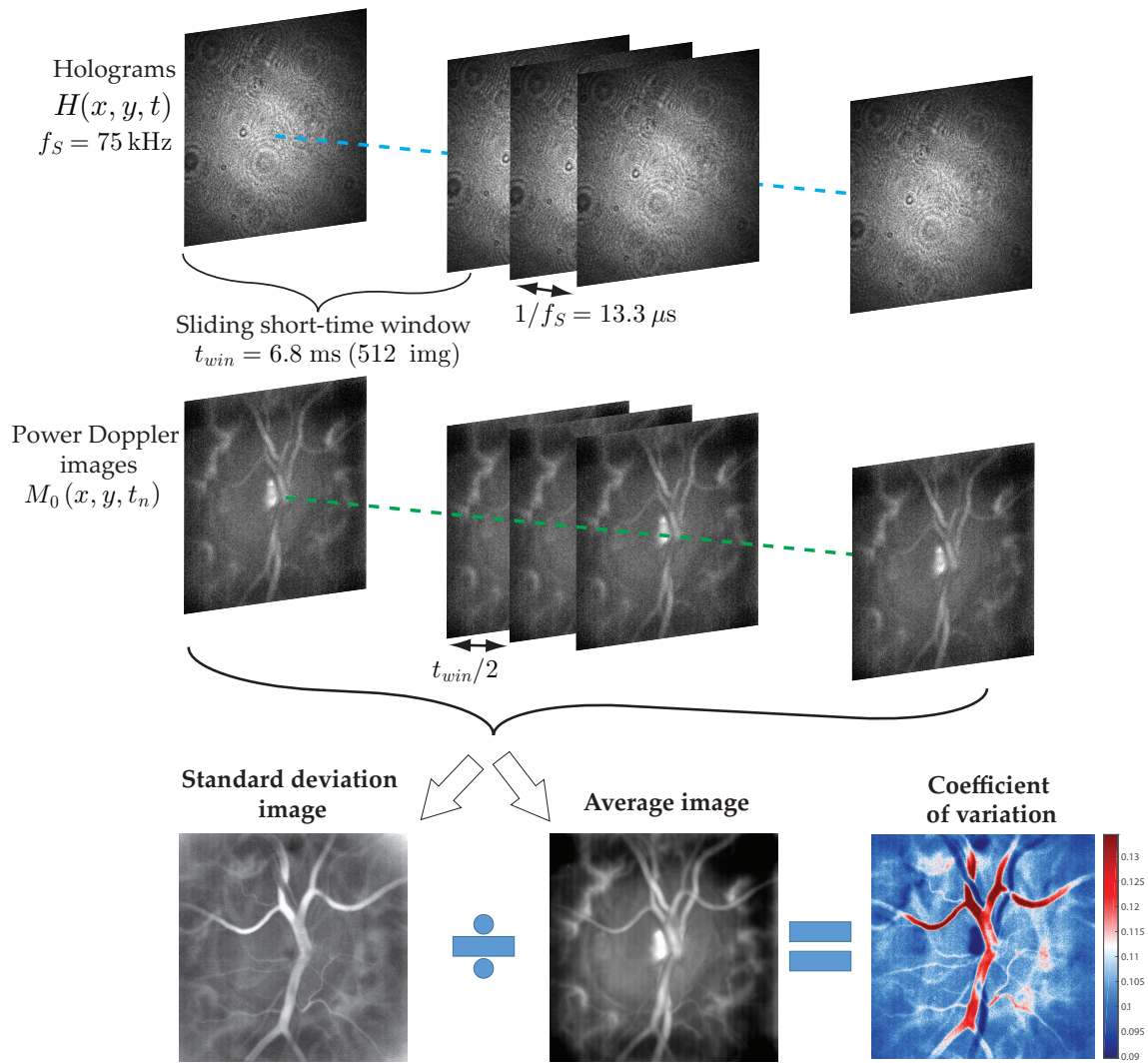


Figure 5.1: Data processing chart. A STFT analysis is performed with a  $t_{win}$  window size on holograms acquired at a  $f_S$  rate. This produces a power Doppler image sequence, over which we calculate pixel-wise the temporal standard deviation and average images. The ratio of these two images gives the coefficient of variation map which allows to clearly discriminate retinal arteries and veins due to their differences of systolodiastolic blood flow variations.

# Waveform analysis of human retinal and choroidal blood flow with laser Doppler holography

LÉO PUYO,<sup>1,2,\*</sup> MICHEL PAQUES,<sup>2,3,4</sup> MATHIAS FINK,<sup>1,2</sup>  
JOSÉ-ALAIN SAHEL,<sup>2,3,4</sup> AND MICHAEL ATLAN<sup>1,2</sup>

<sup>1</sup>Institut Langevin, Centre National de la Recherche Scientifique (CNRS), Paris Sciences & Lettres (PSL University), École Supérieure de Physique et de Chimie Industrielles (ESPCI Paris) - 1 rue Jussieu, 75005 Paris, France

<sup>2</sup>Paris Adaptive Optics, Retinal Imaging, and Surgery, Paris, France

<sup>3</sup>Centre Hospitalier National d'Ophthalmologie des Quinze-Vingts, INSERM-DHOS CIC 1423, 28 rue de Charenton, 75012 Paris, France

<sup>4</sup>Institut de la Vision-Sorbonne Universités, 17 rue Moreau, 75012 Paris, France

\*[gl.puyo@gmail.com](mailto:gl.puyo@gmail.com)

**Abstract:** Laser Doppler holography was introduced as a full-field imaging technique to measure blood flow in the retina and choroid with an as yet unrivaled temporal resolution. We here investigate separating the different contributions to the power Doppler signal in order to isolate the flow waveforms of vessels in the posterior pole of the human eye. Distinct flow behaviors are found in retinal arteries and veins with seemingly interrelated waveforms. We demonstrate a full field mapping of the local resistivity index, and the possibility to perform unambiguous identification of retinal arteries and veins on the basis of their systolodiastolic variations. Finally we investigate the arterial flow waveforms in the retina and choroid and find synchronous and similar waveforms, although with a lower pulsatility in choroidal arteries. This work demonstrates the potential held by laser Doppler holography to study ocular hemodynamics in healthy and diseased eyes.

© 2019 Optical Society of America under the terms of the [OSA Open Access Publishing Agreement](#)

## 1. Introduction

The ocular circulation is of major interest for the study of increasingly prevalent diseases such as diabetic retinopathy, glaucoma, and hypertension. Other fundus diseases such as retinal vein occlusion and central serous chorioretinopathy are even more directly linked with the fundus perfusion. For the purposes of screening these diseases early on, understanding their pathophysiologies, and monitoring the efficiency of administrated treatments, measuring blood flow in the retina and choroid is of great importance. In the last decade, the irruption and development of optical coherence tomography (OCT) and subsequently of OCT-angiography (OCT-A) has allowed for a comprehensive study of the relationship between diseases affecting the eye and the fundus vasculature anatomy by its ability to resolve the retinal microvasculature [1, 2], and the thickness of the vascular choroidal compartment [3]. Another approach to investigate the ocular circulation is the study of the blood flow dynamics, which requires a temporal resolution currently not in the reach of present day OCT-A systems [4]. First, blood flow monitoring is important to evidence retinal hypoperfusion inherent to many ocular diseases. For example laser speckle flowgraphy can measure abnormal perfusion in some types of glaucoma [5, 6], and Doppler ultrasound is able to detect decrease of the ocular circulation [7]. Going further into the study of blood flow dynamics, a time-resolved analysis of blood flow changes contains a wealth of information as the arterial waveform profile is influenced by the arterial compliance and peripheral resistance [8–10]. Several approaches are used to investigate the Doppler waveform

profiles such as the study of the arterial peak systolic and end diastolic blood flow velocity [11, 12], which can be combined to produce indices to characterize the pulsatility [13]. Another approach is to derive mathematical metrics from the pulse waveform curve such as skew, blowout time, rising rate and falling rate [14–16]. A wave decomposition analysis of ultrasonic Doppler flow velocity waveforms has also proven able to identify microvascular hemodynamic abnormalities in the ophthalmic and carotid artery in cases of diabetic retinopathy [17]. Another factor to take into consideration for the shape and amplitude of the arterial flow profile is the site of measurement of the waveform. As reflection flow and pressure waves superimpose with the forward waves, they modify the incident arterial flow profile on a predictable basis with ageing and diseases [18–20]. Reflection waves are rapidly dissipated when propagating, thus it would be of great interest to measure the flow waveforms as close as possible from the arteriolar branching as it is considered to be the main sites of wave reflections [21]. This flow waveform is all the more interesting as measurements of an impaired pulsatile arterial flow could provide more information regarding potential microvascular damages provoked by an overly high perfusion pressure.

For the purpose of measuring blood flow directly in the retina, optic nerve head (ONH), and choroid, laser Doppler flowmetry (LDF) makes use of the time profile characteristics of the Doppler power spectrum density (DPSD) [22–24]. Determining the Doppler broadening induced by the distribution of velocities and scattering angles allows to measure blood flow parameters such as volume and velocity. A short-time Fourier transform method is carried out to analyze the self-interfering light backscattered by the fundus, and blood flow variations are measured with a temporal resolution sufficient to observe the DPSD changes transient to cardiac cycles. However, this technique is performed only at a single location, and although full-field alternatives have been proposed [25], they have not been implemented in the retina as they require more illumination than permissible. Scanning implementation with the aim of imaging a two dimensional (2-D) field of view face a dilemma between temporal resolution and the spatial extent of the investigated area. Thus so far flying spot and line-scanning LDF have not demonstrated hemodynamic measurements over a 2-D field of view [26, 27]. Laser Doppler holography (LDH) is a digital holographic method that relies on measuring the DPSD from the interference between a Doppler broadened beam and a holographic reference beam, allowing to extract a blood flow contrast similar to LDF [28–30]. The additional reference beam is a plane or spherical wave and provides two advantages: it allows to use a higher camera frame rate by simply increasing the reference beam power, and it opens the door to all sorts of numerical manipulation of the wave field, such as numerical refocusing and digital adaptive optics [31, 32], or synthetic subaperture Doppler measurements [33–35]. This way it becomes possible to perform a pixel wise parallel estimation of the DPSD in the human retina, which leads to simultaneous measurements of Doppler broadening over the 2-D field of view. We have previously used LDH to make full-field non-directional blood flow measurements in the retina with a few milliseconds of temporal resolution [36]. We have then shown that the depth of field of a few hundreds microns provided by LDH allows to encompass both the retinal and choroidal vessels in a single imaging plane, and LDH is able to reveal non-invasively the choroidal vasculature while providing quantitative Doppler frequency shift measurements [37]. We have used this feature to show the large differences of blood flow existing between arteries and veins in the choroid, and proposed an arteriovenous differentiation of choroidal vessels based on a flow analysis. In this article, we more carefully examine the waveform profiles that can be measured in retinal arteries and veins after spatio-temporal filtering, and show that the flow behavior is very different according to the vessel type. We then demonstrate the use of indices to characterize power Doppler waveforms: 2-D maps of the local vascular resistivity index (RI) and coefficient of variation (CV) are shown. These metrics can be calculated over a few cardiac cycles and provide clear discrimination of arterial and venous flow in the retina. Finally, we analyze the dynamic flow in the choroid and demonstrate that the spatially averaged baseline signal (dominant signal)

in laser Doppler measurements is close to the choroidal arterial waveform.

## 2. Methods

### 2.1. Optical setup

We use the laser Doppler holographic setup presented in [36]. Briefly, it consists of a fiber Mach-Zehnder optical interferometer where the light source is a 45 mW and 785 nm single frequency laser diode (Newport SWL-7513-H-P). It is an external cavity laser diode that is spatially and temporally coherent, with a 200 kHz spectral linewidth which is favorable for laser speckle contrast measurements [38]. The power of the laser beam incident at the cornea is 1.5 mW of constant exposure and covers the retina over a disk with a radius of 3 to 4 mm. This irradiation level is compliant with the exposure levels of the international standard for ophthalmic instruments ISO 15004-2:2007. Informed consent was obtained from the subjects, experimental procedures adhered to the tenets of the Declaration of Helsinki, and study authorization was sought from the appropriate local ethics review boards (CPP and ANSM, IDRCB number: 2019-A00942-5). The results shown were obtained from 7 eyes of 5 different subjects, with ages ranging from 24 to 33.

The wave backscattered by the retina is combined with the reference wave using a non-polarizing beamsplitter cube. The polarization of the reference wave is adjusted with a half-wave plate and a polarizer to optimize fringe contrast. The interferograms formed in the sensor plane are recorded using a CMOS camera (Ametek - Phantom V2511, quantum efficiency 40%, 12-bit pixel depth, pixel size 28  $\mu\text{m}$ ) with a frame rate  $f_S$  of typically 60 or 75 kHz in a  $512 \times 512$  format. The diffracted speckle pattern is numerically propagated to the retinal plane using the angular spectrum propagation method [39]. The configuration is on-axis and the reconstruction distance is large enough so that the holographic twin image energy is spread over the reconstructed hologram and has no appreciable effect on the resulting image. The following data processing consists of measuring the local optical temporal fluctuations of the holograms cross-beating terms in order to make quantitative measurements from the DPSD.

### 2.2. Doppler processing

After numerical propagation of the recorded interferograms, the beat frequency spectrum of the reconstructed holograms is analyzed pixel-wise by short-time Fourier transform:

$$S(x, y, t_n, f) = \left| \int_{t_n}^{t_n+t_{\text{win}}} H(x, y, \tau) \exp(-2i\pi f\tau) d\tau \right|^2 \quad (1)$$

Where  $H(x, y, \tau)$  is the hologram complex amplitude at pixel indexes  $(x, y)$  and time  $\tau$ , and  $t_{\text{win}}$  is the integration time of the sliding window which determines the temporal resolution of the system. In order to optimize the trade-off between signal-to-noise ratio (SNR) and temporal resolution ( $t_{\text{win}}$ ), we typically use a short-time window with 512 images (6.8 ms with a 75 kHz frame rate) and an overlap between two consecutive windows of 256 images.

The Doppler spectrum contains a lot of hemodynamic information that can be retrieved through the changes over time of amplitude and frequency of the spectrum. In the conventional data processing for optical [22], and ultrasound Doppler measurements [40, 41], the zeroth moment, first moment, and normalized first moment of the DPSD reveal local blood volume, blood flow, and blood velocity, respectively. The zeroth and first moment of the DPSD are here denoted  $M_0(x, y, t_n)$  and  $M_1(x, y, t_n)$ , and are calculated in the following way:

$$M_0(x, y, t_n) = \int S(x, y, t_n, f) df \quad (2)$$

$$M_1(x, y, t_n) = \int S(x, y, t_n, f) f df \quad (3)$$

In the rest of the article, the zeroth moment is also referred to as "power Doppler"; it is computed as the area under the power spectrum curve so it represents the number of scatterers traveling at any speed above the frequency threshold. Consequently it depends on the quantity of moving red blood cells, i.e. the blood volume in a given pixel. The frequency content of the spectrum reflects the velocity of the sampled area; it is analyzed using the normalization of the first moment by the zeroth moment, which mathematically yields the mean Doppler frequency shift:

$$f_{\text{mean}}(x, y, t_n) = \frac{\int S(x, y, t_n, f) f df}{\int S(x, y, t_n, f) df} = \frac{M_1(x, y, t_n)}{M_0(x, y, t_n)} \quad (4)$$

We have empirically determined that for  $f_{\text{mean}}$  the best results were obtained when removing the first term of the Fourier spectrum, i.e. with a frequency range of  $[0.5 \text{ kHz} - f_S/2]$ . The interferometric zero-order term is naturally removed by the spectrum analysis which gives more weight to higher frequencies. As for  $M_0$ , the upper integration boundary is also generally set to  $f_S/2$ , but a higher low cut-off frequency is used so as to remove bulk motion noise. This low cut-off frequency is typically set to 6 kHz to obtain a power Doppler image where smaller vessels can be revealed, or 10 kHz if the aim is to measure a waveform without any contribution from ocular movement in the signal (except for micro-saccades). The result of this high-pass filtering is that  $M_0$  not only depends on blood volume but also on blood velocity as when the flow speed increases, a part of the spectrum reaches the frequency threshold and becomes integrated in  $M_0$ . This effect is analyzed in section 3.2.

Finally  $M_0(x, y, t_n)$  and  $M_1(x, y, t_n)$  images are compensated for the non-uniform illumination of the retina and vignetting. To do so, each image is divided by its spatially filtered (blurred) self. A conservation of the image energy (calculated as the sum of all pixel intensity) is used so that each image has the same energy before and after division. Only the spatial distribution of energy is changed while the total energy is conserved.

### 2.3. Indices to characterize the Doppler waveform

Several indices quantitatively characterizing Doppler waveform profiles have been introduced so as to study circulatory parameters [13]. In this approach, the vascular circulation is described as an alternative current circuit, where the blood flow in the arterial system is a pulsatile phenomenon driven by periodic myocardial contractions, and whose waveform profile is shaped by both upstream and downstream circulatory parameters [42,43]. The higher compliance at the level of the large elastic arteries helps buffering the intermittent inflow in order to convert it into a steadier flow. The end of the vascular tree also plays an important role by offering a vascular resistance to the incoming flow at the arteriolar level. The opposition to blood flow due to friction on the vessel walls encompasses parameters such as blood viscosity, vessel length, and total cross-sectional area of the arterial bed. In the analogy with electrical circuits, the arterial compliance plays a capacitive role and the downstream opposition to flow acts as a resistance. Therefore, the flow wave is shaped by fundamental properties of the vasculature, and analyzing the Doppler waveform is of great interest as a surrogate means to assess these properties. The indices used for the purpose of studying the hemodynamic modulation of the Doppler waveform have various discriminatory performances and abilities to reflect different circulatory parameters; their use has become standard in Doppler ultrasound [13,44,45]. In this work, we used two of these metrics: the first one is known as the Pourcelot or resistivity index (RI) [46]. For a given function  $g$ , the RI is calculated pixel-wise using the following formula:

$$RI_g(x, y) = \frac{g(x, y, t_{\text{syst}}) - g(x, y, t_{\text{diast}})}{g(x, y, t_{\text{syst}})} \quad (5)$$

Where  $g(x, y, t)_{\text{syst}}$  and  $g(x, y, t)_{\text{diast}}$  are the values of the function  $g$  at the peak systolic and end diastolic time points, which are manually determined. In a compliant vasculature, the resistivity

index increases with the vascular resistance peripheral to the measurement site [47–49]. However it is also subject to changes of arterial compliance as a reduced upstream arterial compliance produces an impaired pulsatile flow with abnormally high systolic flow and lower than normal diastolic flow. Therefore it has been suggested to name it impedance index instead [47, 50]. The second metric we used is a simple estimation of the local coefficient of variation of the power Doppler temporal fluctuations, calculated as the local standard deviation normalized by the local average.

$$CV_g(x, y) = \frac{\sigma_{g(x,y)}}{\mu_{g(x,y)}} \quad (6)$$

Where  $\sigma_{g(x,y)}$  and  $\mu_{g(x,y)}$  denote the standard deviation and average of temporal fluctuations calculated pixel-wise over a few cardiac cycles. With both the *RI* and *CV* metrics, the areas where the systolodiastolic variations are greater come out with greater values, whereas areas with lower variations have lower values.

### 3. Results in the retina

#### 3.1. Pulsatile flow in retinal arteries and veins

In Fig. 1, we analyze the temporal changes in power Doppler  $M_0(x, y, t_n)$  and mean Doppler frequency shift  $f_{\text{mean}}(x, y, t_n)$  in different regions of interest (ROIs). The LDH acquisition was performed close to the optic nerve head, at 75 kHz, and  $M_0$  was integrated over the frequency range [10-37 kHz] to fulfill Nyquist requirement, while we used the frequency range [0.5-37 kHz] for the calculation of  $f_{\text{mean}}$ . In Fig. 1(a) and (b), we show the power Doppler, and mean Doppler frequency shift images averaged over time. In Fig. 1(a-b) are shown the ROIs used to measure the local pulsatile flow; the red, blue, and green boxes mark an artery, a vein, and an area in the background devoid of any large vessels. In Fig. 1(c) and (d), we have plotted the local dynamic power Doppler and mean frequency shift variations in the depicted ROIs and found very similar variations in all areas. So, in Fig. 1(e) and (f), the baseline signal (spatially averaged over the entire field of view, also referred to as dominant signal), is subtracted from the same measurements, i.e. we measure  $M_0 - \langle M_0 \rangle_{x,y}$ , and  $f_{\text{mean}} - \langle f_{\text{mean}} \rangle_{x,y}$ . The difference between the raw movie and the movie corrected from the spatial average are shown in [Visualization 1](#) and [Visualization 2](#), for  $M_0$  and  $f_{\text{mean}}$ .

The power Doppler and mean Doppler frequency shift images are similar but some difference of contrast can be noticed in certain features, especially the optic disc appears darker with the mean frequency image than with the power Doppler image. As mentioned in section 2, the power Doppler supposedly reflects the local blood volume while the mean frequency shift is related to the local blood velocity;  $f_{\text{mean}}$  is measured in absolute frequency units (kHz) whereas  $M_0$  is measured in arbitrary units (a.u.). A first observation on the signal dynamic changes that can be made from Fig. 1(c) and (d), is that the raw measurements performed with LDH are very correlated between all the ROIs. For both the power Doppler and mean frequency shift, all measured waveforms have very similar profiles. The systolic and diastolic times are very well visible, and the dicrotic notch is also noticeable, in the artery, vein and background. When subtracting  $\langle M_0 \rangle_{x,y}$  and  $\langle f_{\text{mean}} \rangle_{x,y}$  from the dynamic signal as shown in Fig. 1(e) and (f), significantly different behaviors can be observed accordingly with the probed feature. Indeed, with this process, the signal in the retinal artery shows considerably larger systolodiastolic variations whereas the signal in the retinal vein appears to be more constant, almost cycloidal; the dicrotic notch becomes clearly visible only in the artery and not in the vein. In the arterial profile, the systolic upward slope is very steep while the diastolic downward slope is gentle. Finally, for both the power Doppler and mean frequency shift, the arterial systolic peak maximum coincides with the minimum of flow in the retinal vein.

Subtracting the baseline signal allows to reveal flow behaviors specific to the probed features. This operations aims at removing the contribution of underneath features such as multiple

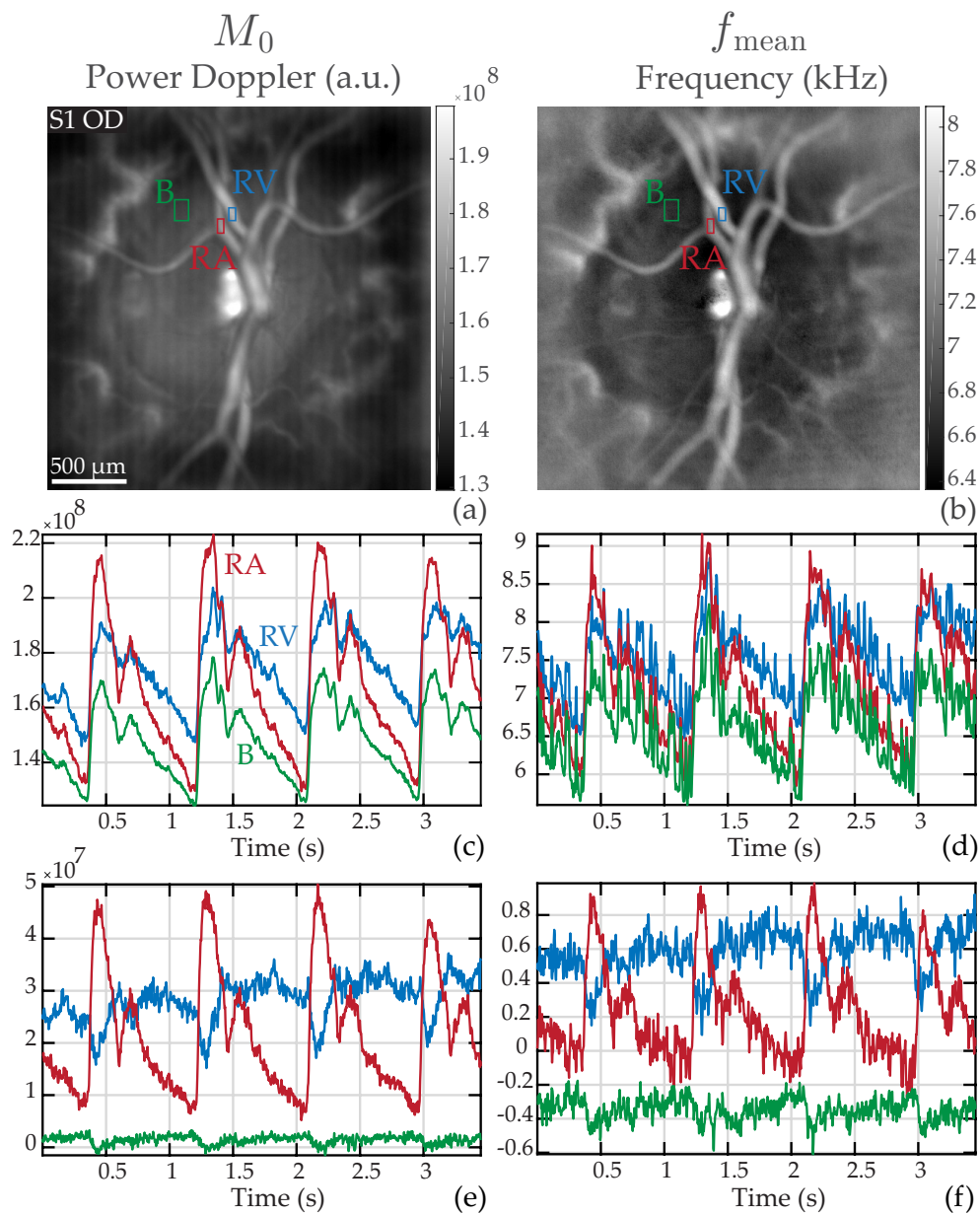


Fig. 1. Analysis of the dynamic changes in power Doppler signal and mean Doppler frequency shift, which supposedly yield volume and velocity, respectively. (a) and (b): power Doppler image  $M_0(x, y)$  and mean frequency shift  $f_{\text{mean}}(x, y)$  temporally averaged; the red, blue, and green ROIs mark a retinal artery (RA), a retinal vein (RV), and the background (B), respectively. (c) and (d) temporal traces of  $M_0$  and  $f_{\text{mean}}$  in the depicted ROIs. (e) and (f): temporal traces in the same ROIs when subtracting the spatially averaged signal over the entire image, i.e.  $M_0 - \langle M_0 \rangle_{x,y}$ , and  $f_{\text{mean}} - \langle f_{\text{mean}} \rangle_{x,y}$ . See [Visualization 1](#) and [Visualization 2](#) for the juxtaposed movies of  $M_0$  and  $f_{\text{mean}}$  corrected and not-corrected from the spatial average. Removing the spatial average allows to reveal the retinal flow waveforms.

scattering from the choroid. The spatially averaged signal subtracted from the dynamic data also has an effect on the images by adding an offset value to the power and mean frequency shift maps. A calibration should be done to derive the actual physical units [22]. The variations over time measured in terms of power Doppler and mean frequency shift are quite similar, although  $f_{\text{mean}}$  is more noisy. This is because unlike for  $M_0$ , the low frequency range [0.5-10 kHz] is used in the calculations of  $f_{\text{mean}}$ , and this frequency range carries a contribution from global eye movements. However the time-averaged mean frequency image seems of slightly better quality than the power Doppler image. In the rest of the article we represent images mostly with the mean frequency shift metric, and temporal line plots of the hemodynamic with the power Doppler metric.

### 3.2. Dependence of the waveform profile upon the frequency range

In Fig. 2, we analyze the arterial waveform profile as a function of the frequency range used for the power Doppler calculation. Figure 2(a) and (b) show the dynamic raw power Doppler and power Doppler corrected from the spatial average in an artery for three frequency ranges: 6-10 kHz in the pink solid line, 10-20 kHz in the red dashed line, and 20-37 kHz in the deep red dotted line. In Fig. 2(c) and (d), we show the corresponding waveform profiles averaged over three cardiac cycles with variation normalized between 0 and 1.

A first observation is that the waveform profile calculated with frequencies under 10 kHz resembles the pulse waveform, but with additional noise. This is presumably because this lowest frequency range contains a mix of spectral contributions from bulk motion and pulsatile blood flow. Thus even though a part of the investigated flow signal lies in the frequency range 6-10 kHz, it seems best not to use this frequency range because it is tainted by global eye movements. In order to obtain a waveform purely representative of pulsatile blood flow, in the rest of the article we work with a 10 kHz lower frequency threshold for the calculation of  $M_0$ . The second observation is that the very high Doppler frequency shifts normalized arterial waveform exhibits a steeper profile as visible from the difference between the 10-20 and 20-37 kHz profiles in Fig. 2(d). This is the result of the high-pass frequency filtering which acts as a velocity threshold. This thresholding removes the contribution of the lower speed constant flow as the velocity limit is exceeded mostly during systole and dicrotic notch. This leads to a sharper peak during systole and dicrotic notch, which amplifies the pulsatile shape of the blood flow waveform.

### 3.3. Phase relationship between the arterial and venous waveforms

We applied the waveform normalization process in Fig. 3 to investigate how the retinal arterial and venous waveform timings are linked. To this end, we compare waveform profiles normalized between 0 and 1, and corrected from the spatial average in a retinal artery 'RA' (red) and a retinal vein 'RV' (blue), and the normalized waveform of the spatially averaged dominant signal 'D' (black). It should be kept in mind that the amplitude of venous flow variations is in reality considerably lower than the amplitude of arterial flow variations, as was shown in Fig. 1. The measurements were performed in three different subjects, and averaged over two to four cardiac cycles.

In all the examples shown in Fig. 3, the spatially averaged power Doppler and the power Doppler in the retinal artery follow similar variations, but the systolic peak is earlier by a few tens of milliseconds in the retinal artery with a few inter-individual variations. The arterial and venous waveforms also vary from one person to another but some common features can be observed: right before the systolic peak, a venous drop is synchronous with a rapid arterial increase up to the arterial systolic peak which coincides with the venous minimum flow. After the systole, the arterial flow drops then increases a little at the dicrotic notch (when present), and then slowly decreases until the end of diastole. For its part the venous flow increases after the systole and reaches its maximum a few hundreds milliseconds after the systole, then slowly decreases till the diastole end. When looking more closely, it can be seen that the venous minimum is

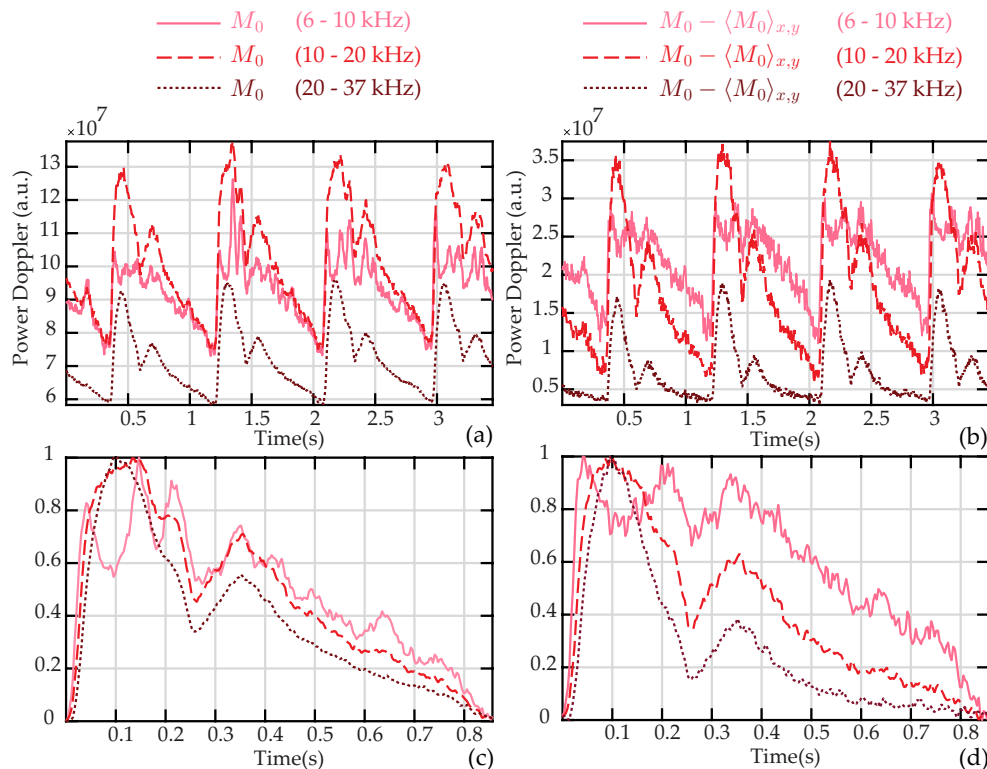


Fig. 2. Dependence of the retinal arterial waveform profile upon the Doppler frequency range. All curves are obtained from the same LDH measurements, only with different processing. (a) and (b): dynamic raw power Doppler and power Doppler corrected from the spatial average for three frequency ranges: 6-10 kHz in the pink solid line, 10-20 kHz in the red dashed line, and 20-37 kHz in the deep red dotted line. (c) and (d): waveform profile averaged over three cardiac cycle with variations normalized between 0 and 1. The waveform profile calculated with the frequency band 6-10 kHz shows a pulsatile signal tainted by bulk motion (attributed by unexpected oscillations); the normalized arterial waveform calculated with the very high frequency range appears steeper due to the velocity thresholding effect.

more contemporary with the arterial maximum than with the dominant signal maximum. In the first example shown in [Visualization 3](#), it can also be observed that the arterial increase is contemporary with a venous decrease during the diastolic notch. In [Visualization 4](#), the lower hemivessel swells and retracts in a timing consistent with the power Doppler curve: the vessel retracts until the flow is minimum, and reaches its maximum swelling when the measured power Doppler is maximum.

The dominant signal is subtracted from the dynamic signal, thus it is possible that there is an overcompensation of this signal which could introduce artifacts in the shape of the venous profile. However it seems that the venous minimum contemporary of the arterial maximum is not an artifact. Indeed in case of an overcompensation, the venous minimum would have been synchronous with the maximum of the dominant signal 'D'. The fact that it is instead synchronous with the arterial signal indicates that it likely truthfully reflects the retinal venous blood flow waveform. Moreover, the caliber of the vein in [Visualization 4](#) changes in a pattern consistent with the flow measurements. This vein's behavior may be particular to that subject due to a specific vascular branching, as one of the vein branches makes an acute angle with the larger vein

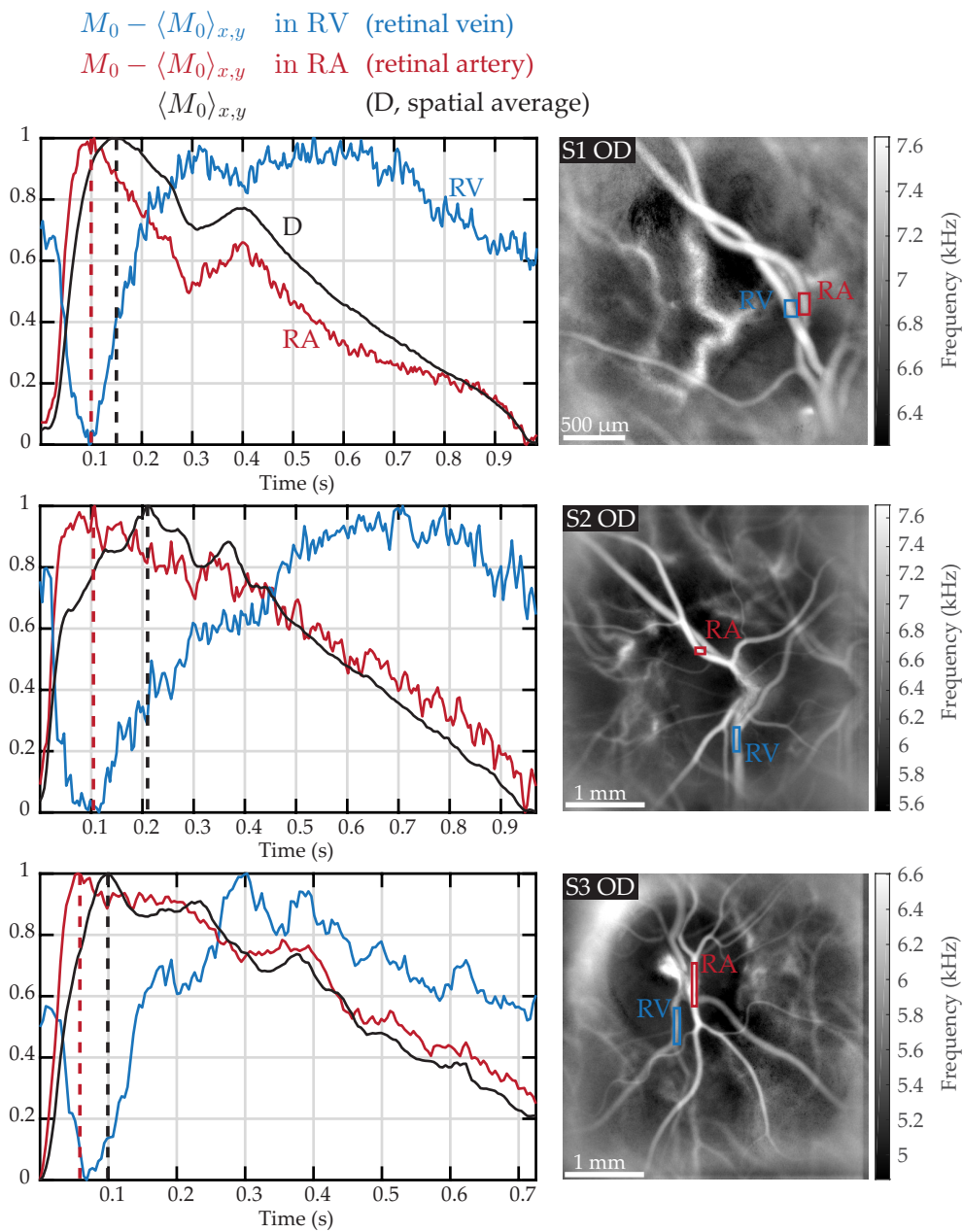


Fig. 3. Venous and arterial retinal waveforms compared to the spatial average in three examples close to the ONH. Left column: normalized waveform in a retinal vein and artery ('RV' in blue, and 'RA' in red), and normalized waveform of the spatial average (over the entire image) in black. As seen from the red and black dashed lines indicating the end of systole, the venous minimum is more contemporary with the retinal arterial flow maximum than with the maximum of the spatial average. See [Visualization 3](#) and [Visualization 4](#).

which might complicate the convergence of venous inflow. Nonetheless, the arterial and venous waveforms measured in these vessels are representative of those we measured in all other eyes.

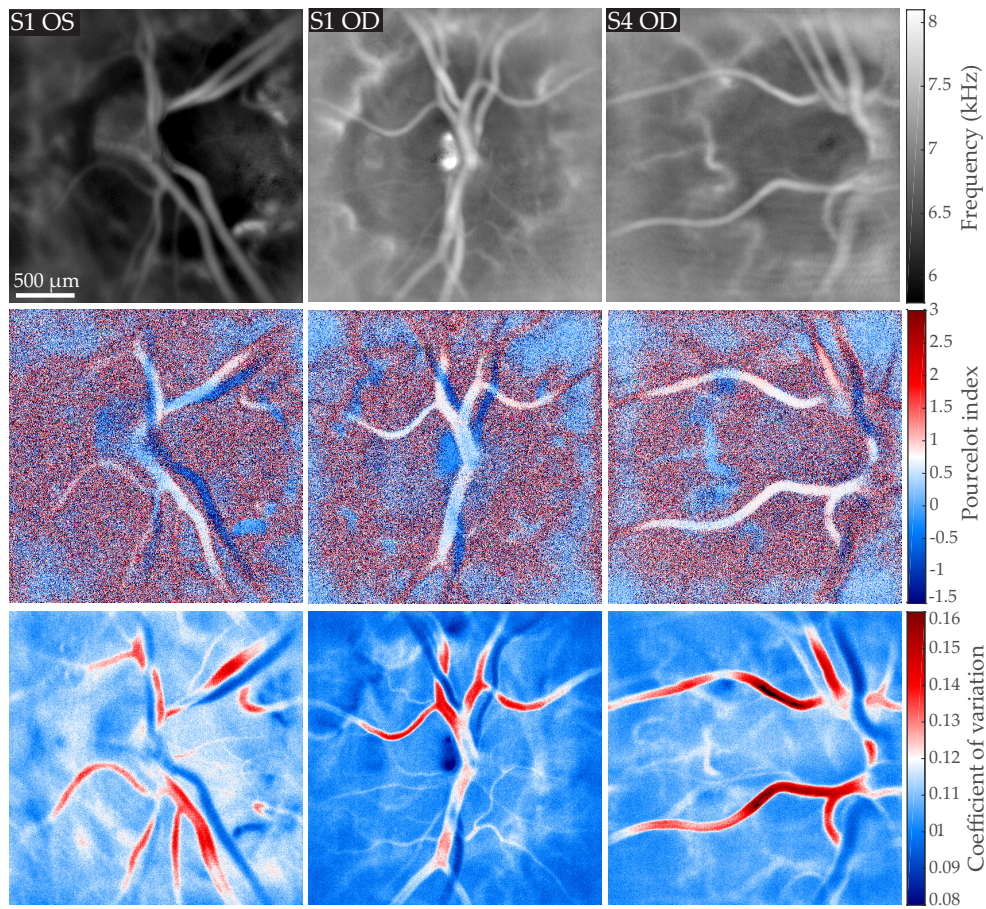


Fig. 4. Mapping in three different eyes of the local blood velocity, RI, and CV indices; all images are displayed on the same gray/color scale. First row: mean Doppler frequency shift  $f_{\text{mean}}(x, y)$ . Second row: resistivity map calculated according to the Pourcelot index on the flow variations corrected from the baseline signal  $RI_{M_0 - \langle M_0 \rangle_{x,y}}$ ; the RI value in the arteries is around 0.7. Third row: coefficient of variation map of the raw signal  $CV_{M_0}$ .

### 3.4. Blood flow resistivity mapping

In Fig. 4, we show in three different eyes examples of mapping of the local blood velocity, RI, and CV indices. For each eye, the measurement was performed in the vicinity of the optic disc, and the camera sampling frequency was set to  $f_S = 75\text{kHz}$ . The first row of Fig. 4 shows the local mean Doppler frequency shift  $f_{\text{mean}}(x, y)$  calculated over the frequency range [0.5-37 kHz]. The second row shows the resistivity map calculated according to the Pourcelot index  $RI_{M_0 - \langle M_0 \rangle_{x,y}}$  from power Doppler movies corrected from the background. Finally, the third row shows the local coefficient of variation  $CV_{M_0}$  calculated from the raw power Doppler variations.

On the time-averaged frequency maps  $f_{\text{mean}}(x, y)$ , the mean Doppler frequency shift is greater in greater vessels: the value measured within large retinal vessels is around 7-8 kHz, and 6-6.5 kHz in the optic disc where there are no visible vessels but there should be unresolved capillaries. All  $f_{\text{mean}}$  images were averaged over 3.5s, so it is not possible to distinguish arteries from veins based on the value of the mean frequency shift because when averaged over cardiac cycles these values are too similar in the two types of vessels. With the resistivity maps shown below in Fig. 4,

a difference of contrast between veins and arteries appears: with the Pourcelot index, it is possible to see large retinal arteries in white, and large retinal veins in blue. The resistivity index value measured in these examples is approximately 0.7 for arteries, which is consistent with the values measured with Doppler sonography in the central retinal artery [44]. The coefficient of variations maps calculated on the raw power Doppler signal show similar contrast but with a much better signal to noise ratio. Arteries come out in red with values around 0.12 - 0.16, veins come out in blue with values in the range of 0.08 - 0.11, and the value in the background is around 0.10.

This difference of contrast between veins and arteries in the RI and CV maps can be easily understood in the light of the information shown in Fig. 1. Whether the maps are computed using the raw signals or on the signal corrected from the spatial average, the amplitude of systolodiastolic variations is larger in arteries than in veins, thus a difference of contrast appears. The systolodiastolic variations are slightly greater in the veins than in the background, but the variations normalized by the mean value are greater in the background. Consequently the veins come out as the features with the lowest RI and CV values. The most striking difference between  $CV_{M_0}$  and  $RI_{M_0-(M_0)_{x,y}}$  is an improvement of the SNR, which is due to the fact that the coefficient of variation calculation uses all the data points of the cardiac cycles, whereas the Pourcelot index is solely based on two time measurements made at peak systolic and end diastolic time points. Only the Pourcelot index holds a real physical sense, as the values of the coefficient of variations are based on raw power Doppler which are figurative of the background signal variations. However as these two types of maps yield similar contrasts, we used the coefficient of variation in the rest of the manuscript to provide high SNR arteriovenous mapping. Interestingly, with the LDH technique we used in this work, the Doppler contrast is not quite equally sensitive to in-plane motion as it is to out of plane motion [36]. This may result in overestimation of blood volume and velocity in out of plane vessels. The resistivity maps are predicted to be relatively independent of the flow geometry given that the angular Doppler sensitivity is expected to be compensated in the ratio. Finally it can be noticed that resistivity values in arteries are corrupted when there is a vein beneath. This is due to the relative transparency of blood vessels and the large depth of field of the instrument; it can be also be noticed on flow images that when vessels overlap their intensity is cumulated.

### 3.5. Comparative CV mapping with $f_{\text{mean}}$ and $M_0$

In Fig. 5, we compare the coefficient of variation maps that can be obtained on the basis of the pixel-wise variations of  $f_{\text{mean}}$ , and compare them to the maps calculated from the variations of  $M_0$  as those that were shown in Fig. 4. The two corresponding maps are denoted  $CV_{f_{\text{mean}}}(x, y)$  and  $CV_{M_0}(x, y)$ . The two columns in Fig. 5 show these images for the right and left eye of the same subject; both measurements were performed with a camera frame rate of 60 kHz. The frequency ranges used for the calculations of  $f_{\text{mean}}$  and  $M_0$  are 0.5-30 kHz and 6-30 kHz, respectively.

With both the  $CV_{f_{\text{mean}}}$  and  $CV_{M_0}$  maps, a difference of contrast is visible between arteries and veins, and the values found in  $CV_{M_0}(x, y)$  are very close to those of  $CV_{f_{\text{mean}}}(x, y)$ . The most visible difference is that in  $CV_{f_{\text{mean}}}(x, y)$  maps, the coefficient of variation is greater in the optic disc than in almost any other feature, except for arteries in the optic disc because they benefit from the signal of the optic disc underneath. As a result, unlike with the  $CV_{M_0}(x, y)$  map, retinal arteries are not the structures where the coefficient of variation is the greatest. Compared to the rest of the visible features, the optic disc area appears darker with  $f_{\text{mean}}(x, y)$  than with  $M_0(x, y)$ . As  $CV_{f_{\text{mean}}}(x, y)$  is calculated as the division of the standard deviation image by the time-averaged image, this explains why this region appears redder than the rest of the image in the coefficient of variation maps. As for the retinal veins, they are the structures with the lowest coefficient of variation with the two types of maps. It can also be noticed that the apparent diameter of retinal vessels is larger with images based on  $f_{\text{mean}}$  than with images based on  $M_0$ . A likely explanation is that because the 0.5-6 kHz frequency range is not used in  $M_0$  images, the contribution of higher

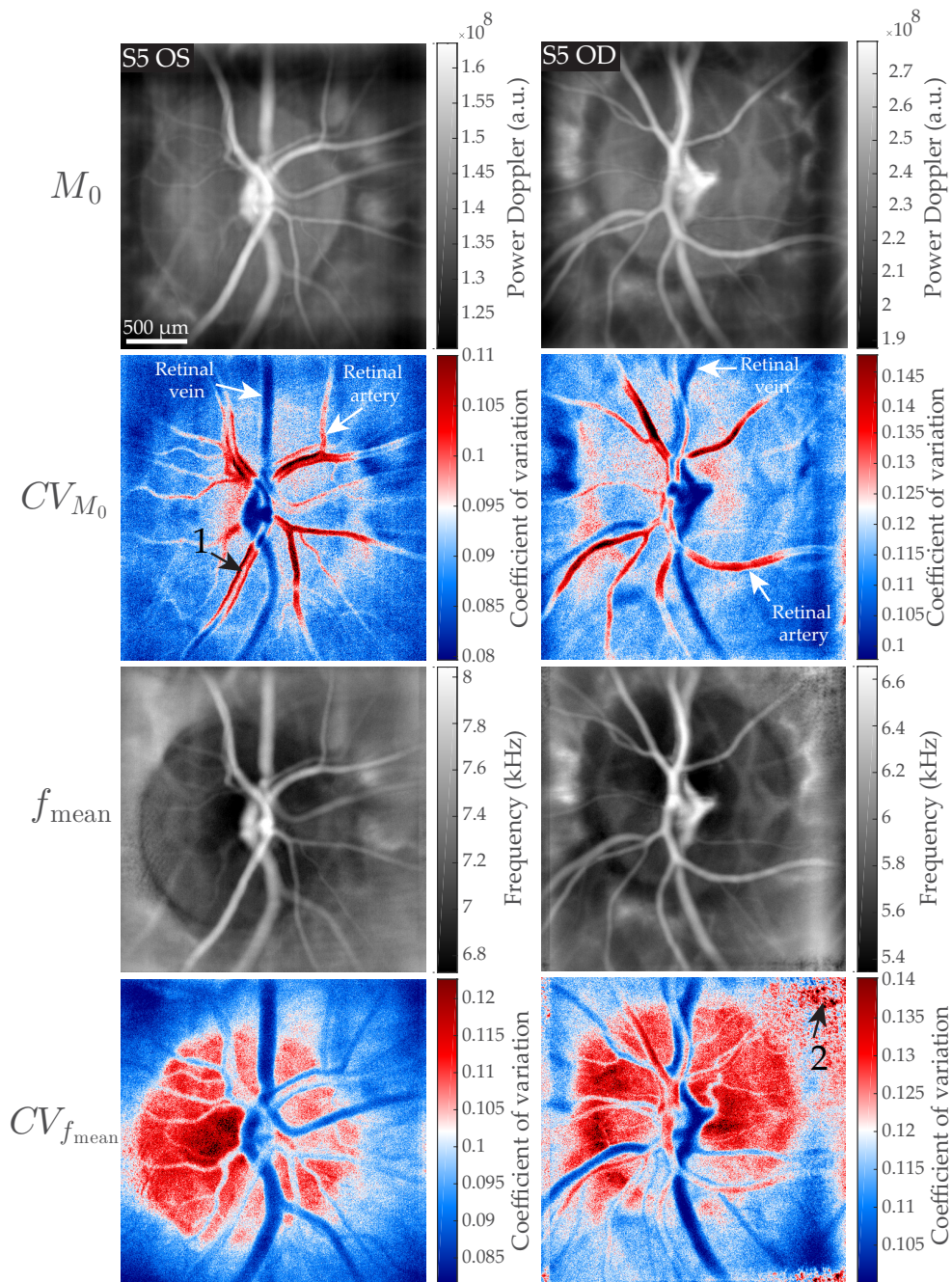


Fig. 5. Comparison of CV maps obtained from the variation of  $M_0$  and  $f_{\text{mean}}$  in the right and left eye of the same subject. From top to down:  $M_0(x, y)$ ,  $CV_{M_0}(x, y)$ ,  $f_{\text{mean}}(x, y)$ , and  $CV_{f_{\text{mean}}}(x, y)$ . The coefficient of variation in the optic disc differs significantly between the two methods. The arrow '1' and '2' point to areas where the Doppler broadening is undersampled and to low frequency noise, respectively.

frequencies (which reveal greater blood flow) is more important, so vessels show a weaker signal closer to the edges.

It can be noted that the lumen of some large retinal arteries in  $CV_{M_0}(x, y)$  (arrow '1') has a lower coefficient of variation than closer to the vessel walls. As we fail to see any physical explanation of this phenomenon, we suppose it is caused by an aliasing of the Doppler spectrum during systole in the area where the velocity is the greatest, which would result in a lower than normal systolic power Doppler flow measurement, and thus in lower systolodiastolic variations. We had already noticed that at 60 kHz this sort of Doppler undersampling could occur in branches of the central retinal artery [36]. An interesting feature of  $CV_{f_{\text{mean}}}(x, y)$  maps, is that as  $f_{\text{mean}}$  itself, they are more prone to low frequency noise (arrow '2'), and require a careful instrumentation that minimizes specular reflections.

#### 4. Results in the choroid

The blood flow supply to the retina is carried out by two independent vasculatures originating from the ophthalmic artery that differ in organization and function. The retinal vessels are branches of the central retinal artery and supply the neural retina and the prelaminar region of the ONH, whereas the choroidal vessels originate from the posterior ciliary arteries (PCAs) which supply the photoreceptor and epithelial cells. These two vascular systems especially differ at the capillary bed level as choroidal capillaries are considerably bigger than retinal capillaries [51], resulting in a lower vascular resistance in the choroid. Therefore, because they share a common inflow source but differ in outflow, the retinal and choroidal circulation are interesting to study the ocular circulation. The difficulty about the choroid is that it lies beneath the photoreceptor and RPE layers which have a non-trivial effect on the light. We previously demonstrated that LDH is able to reveal the deep choroidal vasculature, and that this difference of organization allows to discriminate arteries from veins in the choroid on the basis of the flow they carry [37]. Here we investigate the blood flow dynamics in the choroid.

##### 4.1. Choroidal arterial waveform in different regions

In Fig. 6, we explore how the photoreceptor density affects the laser Doppler measurements in choroidal arteries. To that end, we imaged two areas in the fundus, in the macular region and in a peripheral region at approximately 40 degrees of foveal eccentricity where the density of photoreceptor and RPE cells is expected to be considerably lower. In Fig. 6(a) and (b), we show the mean frequency images of the two imaged areas, and the ROIs placed on a choroidal artery ('CA', purple) and an area devoid of any large vessels ('B', green). In Fig. 6(c) and (d), we show the raw power Doppler measured in the ROIs, i.e.  $M_0$ . Then in Fig. 6(e) and (f), we show the power Doppler in the same ROIs when subtracting the spatially averaged dynamic signal, i.e.  $M_0 - \langle M_0 \rangle_{x,y}$ .

Similarly to the results shown in Fig. 1, the raw power Doppler variations in the two ROIs have very correlated variations. When subtracting the baseline dynamic value, a pulsatile arterial signal remains in the choroidal artery in the peripheral region, whereas in the macular region the signal measured in the choroidal artery only shows noise. We presume it is the higher density of photoreceptor and RPE cells in the macular region that prevents us from making measurements in choroidal arteries in the same way as in the periphery. A plausible explanation is that the choroidal arterial signal in the macular region is exactly the dominant signal, which explains why it is totally suppressed when subtracting the spatially averaged signal. This particularity had already been demonstrated in laser Doppler flowmetry as the absence of retinal vasculature in the fovea was already used to make choroidal blood flow measurements [23].

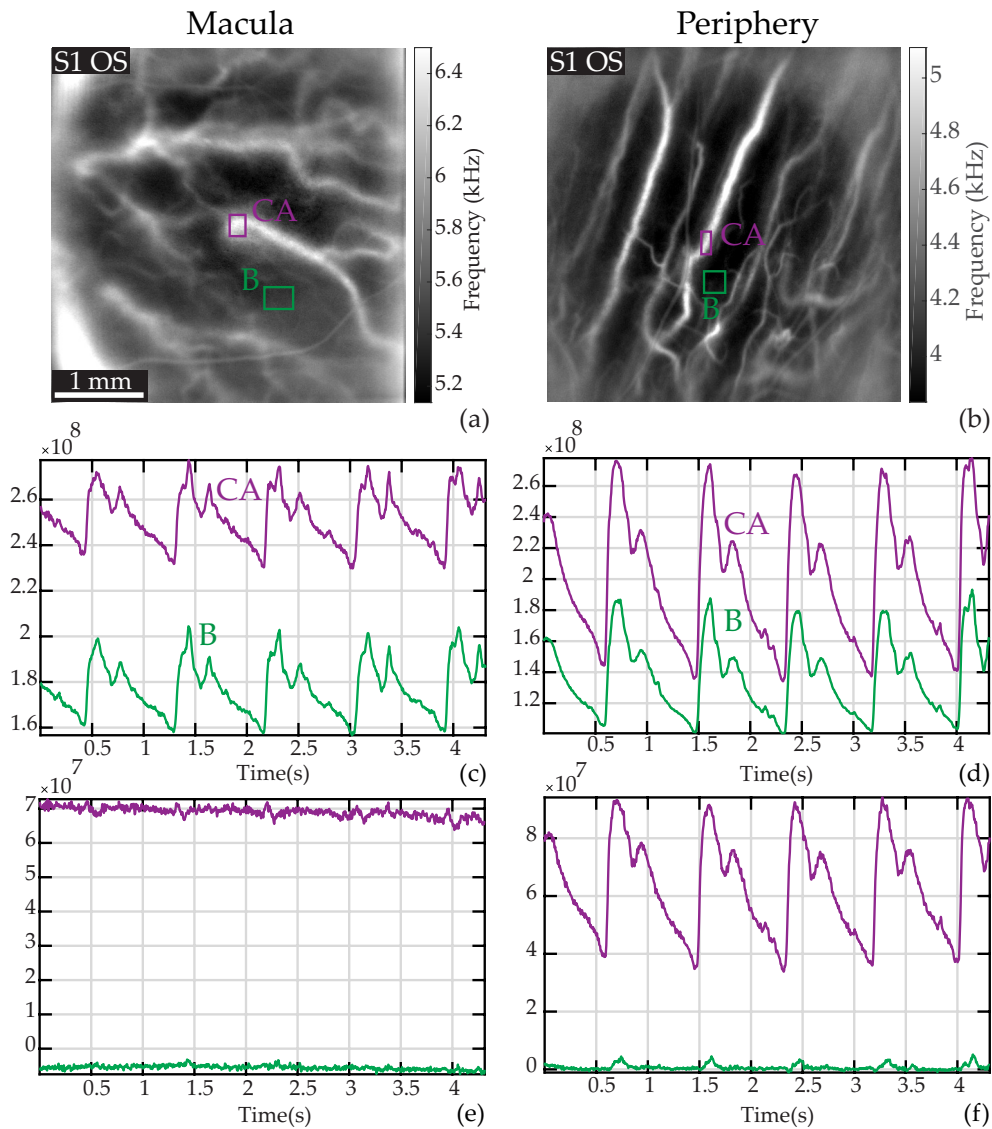


Fig. 6. Laser Doppler measurements in choroidal arteries in the macular and peripheral regions. (a) and (b): Mean frequency images with ROIs on a large choroidal artery ('CA', purple) and the background ('B', green). (c) and (d): Raw power Doppler signal  $M_0$  in the ROIs. (e) and (f): Power Doppler signal in the same ROIs when subtracting the spatially averaged dynamic value, i.e.,  $M_0 - \langle M_0 \rangle_{x,y}$ . In the peripheral region the power Doppler signal in 'CA' corrected from the dominant signal yields an arterial-like waveform whereas the power Doppler signal measured in 'CA' in the macular region shows only noise. This is probably because of the higher photoreceptors/RPE density, and because the dynamic signal measured in 'CA' in the macula is exactly like the spatial average signal.

#### 4.2. Simultaneous blood flow measurements in the retina and choroid

In Fig. 7, we provide an example of a CV map in an area close to the ONH with visible choroidal arteries that are branches of paraoptic short PCAs. The camera sampling frequency was set to

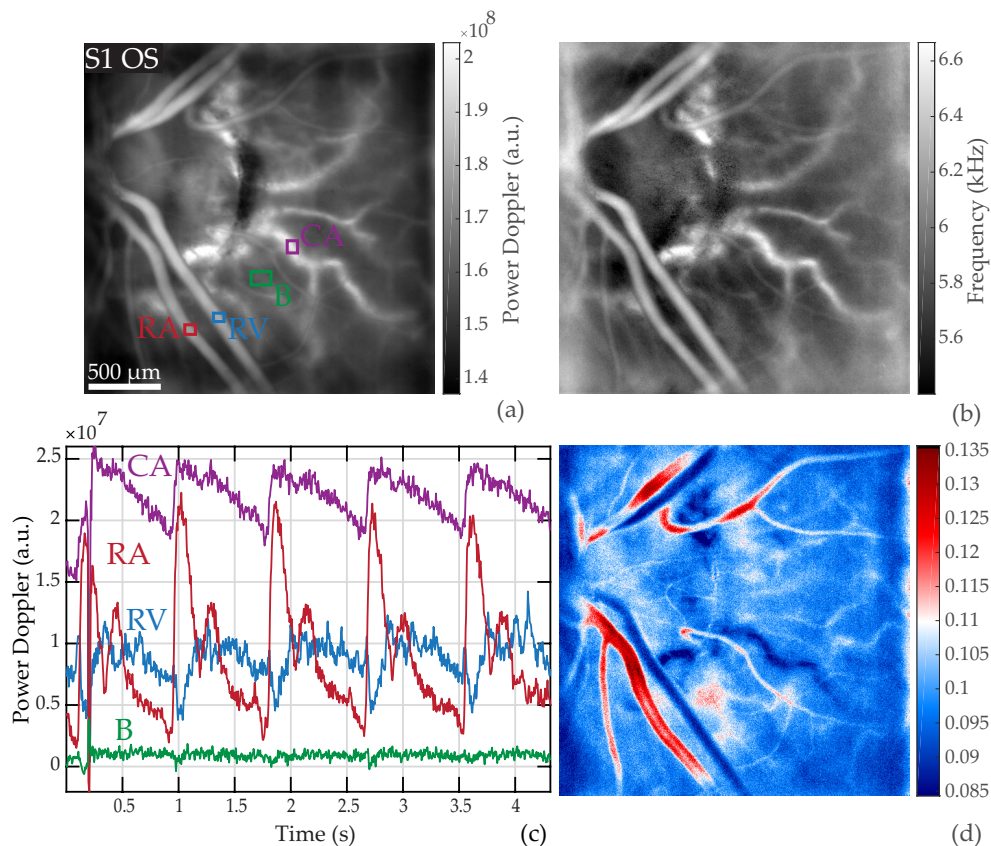


Fig. 7. Pulsatile flow in the retina and choroid. (a) Power Doppler image  $M_0(x, y)$  indicating the ROIs; the red, blue, green, purple boxes mark a retinal artery and vein, the background, and a choroidal artery, respectively. (b) Mean frequency shift image  $f_{\text{mean}}(x, y)$ . (c) Waveform of  $M_0 - \langle M_0 \rangle_{x,y}$  in the ROIs. (d) Coefficient of variation map  $CV_{M_0}(x, y)$ : the choroidal artery has a coefficient of variation close to the values found in retinal veins, despite exhibiting an arterial waveform profile. See the power Doppler movie in [Visualization 5](#).

60 kHz. In Fig. 7(a) and (b) are respectively shown the time-averaged power Doppler image  $M_0(x, y)$  and mean Doppler frequency shift image  $f_{\text{mean}}(x, y)$ . The power Doppler waveforms in the ROIs corrected from the spatial average are plotted in Fig. 7(c), and finally Fig. 7(d) shows the coefficient of variation map  $CV_{M_0}(x, y)$ . The corresponding power Doppler movie corrected from the spatial average is shown in [Visualization 5](#).

We see here the same distinct flow behaviors in the retinal artery and vein as before, leading to similar contrast on the CV map. The choroid artery 'CA' appears on the power Doppler and mean frequency images with a Doppler signal greater than in any other feature. The blood flow measured in this vessel in Fig. 7(c) exhibits an arterial-like waveform with very reduced systolodiastolic variations compared to the retinal artery, and slightly more noisy; it seems to have an offset value compared to the retinal vessel. It is apparent in [Visualization 5](#) that the measured pulsatility in the choroidal artery is very reduced compared to that of the retinal artery. Finally in the CV map displayed in Fig. 7(d), the choroidal artery 'CA' can be seen with a similar contrast to that of retinal veins.

This lower modulation depth combined with the high average value explains why this choroidal

artery appears in blue in the coefficient of variation map. Although reduced systolodiastolic variations are expected in the choroid because of the lower vascular resistance compared to the retina, the photoreceptor and RPE could also be playing a role in reducing the amplitude due the multiple scattering and absorption they introduce. This makes it impossible to compare the raw power Doppler value between the retinal and choroidal layers. To circumvent this issue, we here limit the study to the comparisons of shapes and timings of choroidal and retinal arteries flow waveforms in Fig. 8 by normalizing the waveform profiles.

#### 4.3. Comparison of the waveform of retinal arteries, choroidal arteries, and of the spatial average

In Fig. 8, we compare the waveform profiles of retinal and choroidal arteries, and of the dominant signal. In three examples, we measured the power Doppler signal corrected from the spatial average in a retinal and a choroidal artery ('RA' and 'CA'), and averaged the waveform profiles over several cardiac cycles (typically 2 to 4). We then compared these waveforms to the spatial average waveform 'D', i.e. to  $\langle M_0 \rangle_{x,y}$ . All waveforms were normalized to have variations between 0 and 1. For each example, we show the ROIs on the mean frequency shift image on the right, and the corresponding curves on the left. The retinal artery is marked 'RA' in red, and the choroidal artery 'CA' in purple.

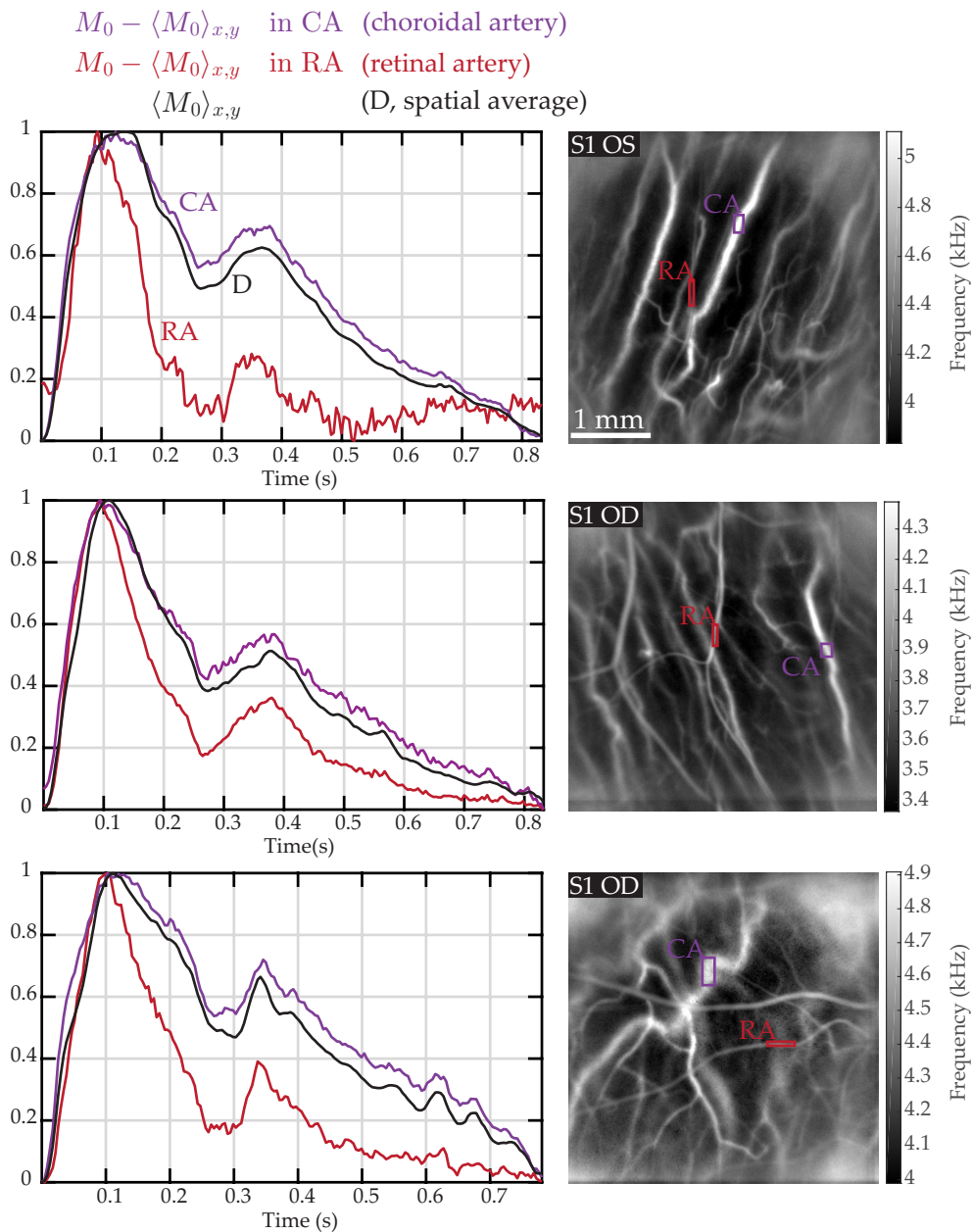
In the three examples, all waveforms exhibit an arterial profile: the systolic, diastolic, and dicrotic times are visible. No difference of synchronicity for the start of the systole and dicrotic notch can be observed between the different waveforms, but the systolic peak is slightly delayed in 'D' and 'CA'. A dominant contribution to the spatial average of light scattered in the choroid seems likely.

#### 4.4. Arteriovenous differentiation in the retina and choroid

In Fig. 9, we demonstrate the ability of LDH to perform an arteriovenous differentiation in the retina and choroid using a method adapted to each vasculature. In Fig. 9(a) and (b) we show images of the local mean Doppler frequency shift  $f_{\text{mean}}(x, y)$ . Then in Fig. 9(c) and (d), we show the mapping of the local coefficient of variation  $CV_{M_0}(x, y)$ . Finally, in Fig. 9(e) and (f), we show the composite color images obtained by merging low and high frequency power Doppler images (calculated with the frequency ranges 2.5-6, and 10-30 kHz, respectively) in cyan and red, following the process we previously demonstrated [37].

In the mean frequency shift images, all vessels from both the retinal and choroidal layers are visible except the choroidal veins. Although one can distinguish the retinal from the choroidal vessels as the latter are slightly larger, identifying the type of each vessel on the basis on the mean frequency shift is not possible. In the coefficient of variation maps, a difference of contrast appears between retinal arteries and veins and they can be clearly identified: as we have shown before, arteries come out in bright red and veins in deep blue. However on *CV* maps, the vessels of the choroid cannot be clearly identified: choroidal arteries have the same contrast as retinal veins, and choroidal veins have the same contrast as the background. Finally in the composite color images, while the retinal vessels appear with a neutral contrast, large differences can be noticed among choroidal vessels: choroidal arteries clearly stand out in red because they carry a larger flow, while choroidal veins can be seen in cyan. A final observation regarding Fig. 9, is that in these peripheral regions, the mean frequency shift is lower than in regions close to the ONH, while the average coefficient of variation index is greater.

LDH is able to carry out an arteriovenous differentiation of all vessels because it is able to make quantitative measurements of power Doppler in both the retina and choroid, and this quantity is related to the flow. For the retinal vasculature the discrimination is made on the basis of the respective hemodynamics of arteries and veins using *CV* maps. In the choroid, the arteriovenous segregation relies on the ability to analyze the flow in choroidal vessels. Choroidal



venous vessels are the hardest vessels to image in laser Doppler because they carry a smaller flow. We had found that in regions of eccentricity smaller than approximately 30-40 degrees,

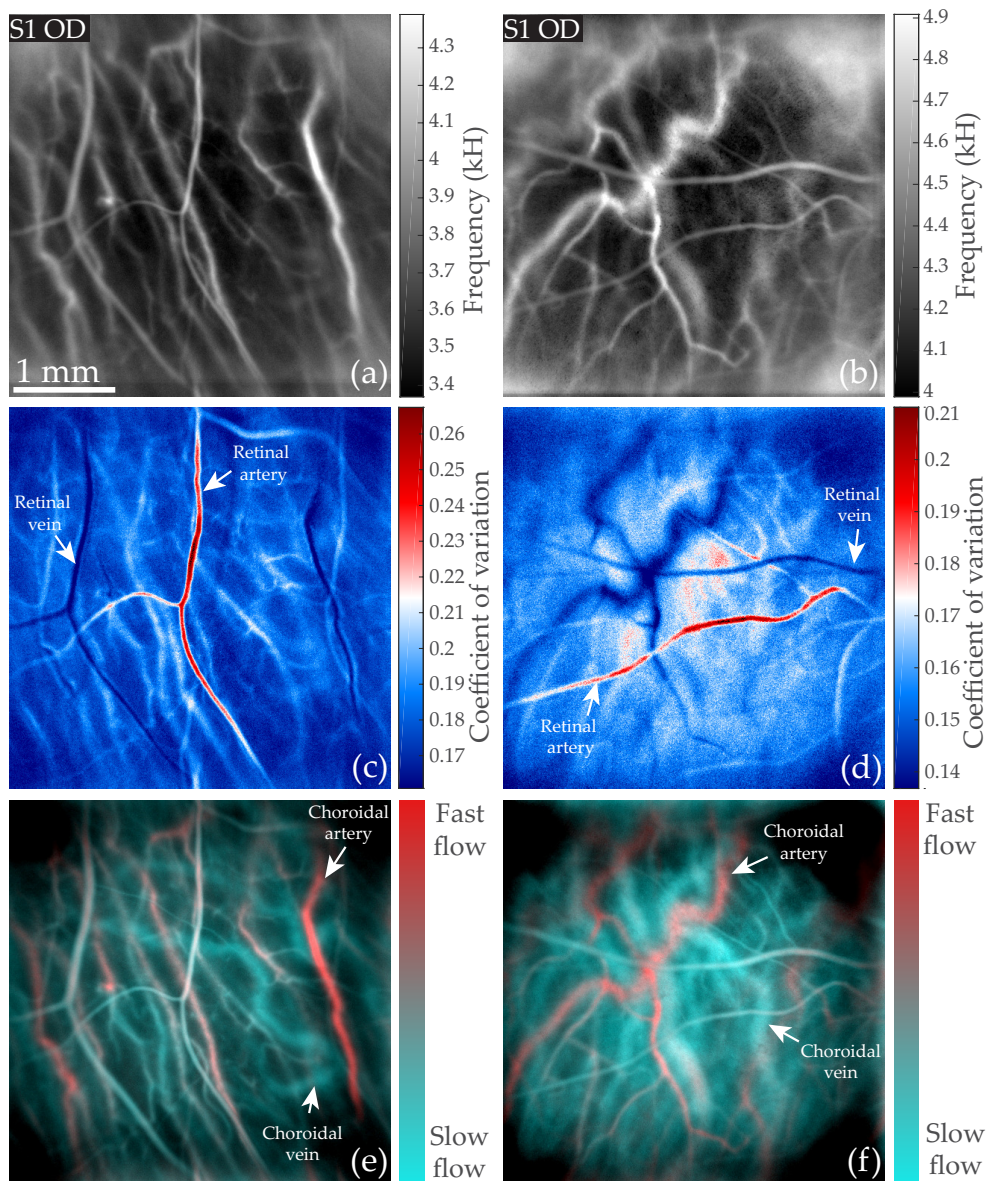


Fig. 9. Arteriovenous differentiation in the retina and choroid. (a) and (b): mean Doppler frequency  $f_{\text{mean}}(x, y)$ . (c) and (d): coefficient of variation  $CV_{M_0}$  revealing retinal arteries and veins. (e) and (f): color composite images obtained by merging low frequency and high (2.5-6 kHz, 10-30 kHz) power Doppler images in cyan and red, allowing identification of choroidal arteries and veins (colorbars are only indicative).

the Doppler broadening due to blood flow in choroidal veins lies in the frequency range 2.5-6 kHz [37]. However in this same range of frequency there are strong contributions of involuntary eye movements and fundus pulsations, which prevents us from measuring a dynamic signal. This is why so far we have not managed to measure the blood flow waveform in choroidal veins.

## 5. Discussion and conclusion

Our results indicate that the choroid constitutes the predominant contribution to the high frequency laser Doppler signal in all reported areas of the fundus. It is however possible to circumvent its influence by subtracting the spatially averaged baseline signal. Similar conclusions have been reached with other blood flow monitoring methods. In laser speckle flowgraphy, the spatially averaged value of MBR (mean blur rate) which is used to assess blood flow is subtracted in order to correct for the background pulsatile signal due to the choroid [52–54]. In scanning LDF, it was found that the measured perfusion maps did not give an accurate description of the retinal circulation alone as they failed to predict retinal hypoperfusion where expected [55]. The conclusion reached was that despite confocal gating, laser Doppler measurements represented the combined circulations of the retina and choriocapillaris. The ability to make full-field laser Doppler measurements thus appears as crucial as it allows to filter this dominant contribution from the choroid through the subtraction of the spatial average. This overall signal is most likely due to the scattering of the light backscattered by the choroid by the intermediate layers, with a likely Doppler broadening contribution from the choroidal precapillary sphincter or choriocapillaris that would explain why the spatially averaged signal reaches its systolic peak later than the retinal arteries.

In Fig. 8, we observed different waveform profiles in retinal and choroidal vessels. These measurements could potentially reflect a difference of arterial waveforms between these two vasculatures, but the important bias introduced by the high-pass frequency filtering of the power Doppler prevents any direct conclusion. As we saw in Fig. 2, the spectral contribution of global eye movements overlaps with the Doppler broadening due to pulsatile blood flow in the 6–10 kHz frequency range, especially in the periphery where retinal vessels are smaller and carry slower flows. We performed these measurements shown in Fig. 8 in the periphery to make measurement in choroidal vessels with a higher SNR, but the retinal arteries are smaller thus strongly impacted by the high-pass Doppler frequency filter set at 10 kHz. The frequency thresholding acts as a high-pass velocity filter which leads to a sharper waveform profile as the contribution of the constant flow is removed. Thus the pulsatile shape of the retinal arteries waveform profiles in Fig. 8 is amplified. Another doubt can be retained regarding the exactitude of the measured choroidal arterial waveform as it is possible that there remains a residual contribution of the dominant signal. Thus any interpretation based on the comparison of retinal and choroidal arterial waveforms should be made cautiously. Nonetheless these results stand in good agreement with the profiles measured with Doppler sonography measurements [44, 56], as it was found that the flow in PCAs exhibits lower systolodiastolic variations than in the central retinal artery, as it is typical in case of a lower downstream vascular resistance. LDH may be a useful technique to further study how the distal vascular resistance alters the arterial waveform.

We observed pulsatile blood flow changes in retinal veins in all investigated eyes. [Visualization 4](#) shows spontaneous retinal venous pulsation (SRVP). This is commonly observed in normal veins close to the disc, and probably results from interactions between intraocular and intracranial pressure (ICP), although the exact mechanism is uncertain [57, 58]. Our data suggests that the peak venous diameter is associated with the maximum of flow. Given the interest of such phenomenon for probing ICP, further research are warranted to better understand the flow behavior in cases of SRVP. Venous pulsation is rather uncommon in the human body, and there has been controversial reports regarding the phase of the flow and caliber pulsatile behavior of retinal veins [59–62]. In this work we have found the arterial blood flow systolic peak to be coincident with the venous minimum flow in all investigated eyes. In the past decades, several modern ophthalmic instruments have experimentally confirmed the coincidence of arterial maximum flow and venous minimum flow such as Doppler-OCT [63, 64], Doppler sonography [44, 65], or dynamic angiography in cases of retinal vein occlusion [66].

In conclusion, we have shown that thanks to its high temporal resolution and full-field imaging

capability, LDH is able to measure blood flow in retinal arteries and veins, and exhibit their specifically interrelated waveforms. Further we show that despite the absence of sectioning ability in LDH which results in having the retinal and choroidal layers reconstructed in a single plane, by spatio-temporal filtering it seems possible to isolate the contributions of each vasculature. We also demonstrate the use of the resistivity index which leads to a clear arteriovenous differentiation in the retina that complements the ability of LDH to differentiate arteries from veins in the choroid that we had previously demonstrated. The ability to characterize retinal and choroidal hemodynamic in the normal physiological state with LDH lays the foundation for studying altered blood flow in pathological conditions.

### Funding

LABEX WIFI (Laboratory of Excellence ANR-10-LABX-24) within the French Program Investments for the Future (ANR-10-IDEX-0001-02 PSL); European Research Council (ERC Synergy HELMHOLTZ, #610110).

### Acknowledgments

The authors would like to thank Sarah Mrejen, and Philippe Bonnin for helpful discussions, Kate Grieve for language corrections and her help in obtaining safety authorizations, and reviewers for their helpful comments.

The Titan Xp used for this research was donated by the NVIDIA Corporation.

### Disclosures

The authors declare that there are no conflicts of interest related to this article.

### References

1. A. H. Kashani, C.-L. Chen, J. K. Gahm, F. Zheng, G. M. Richter, P. J. Rosenfeld, Y. Shi, and R. K. Wang, "Optical coherence tomography angiography: A comprehensive review of current methods and clinical applications," *Prog. Retin. Eye Res.* (2017).
2. J. Chua, C. W. L. Chin, J. Hong, M. L. Chee, T.-T. Le, D. S. W. Ting, T. Y. Wong, and L. Schmetterer, "Impact of hypertension on retinal capillary microvasculature using optical coherence tomographic angiography," *J. Hypertens.* **37**, 572–580 (2019).
3. S. Mrejen and R. F. Spaide, "Optical coherence tomography: imaging of the choroid and beyond," *Surv. Ophthalmol.* **58**, 387–429 (2013).
4. P. J. Rosenfeld, M. K. Durbin, L. Roisman, F. Zheng, A. Miller, G. Robbins, K. B. Schaal, and G. Gregori, "Zeiss angioplex spectral domain optical coherence tomography angiography: technical aspects," in *OCT Angiography in Retinal and Macular Diseases*, vol. 56 (Karger Publishers, 2016), pp. 18–29.
5. Y. Shiga, H. Kunikata, N. Aizawa, N. Kiyota, Y. Maiya, Y. Yokoyama, K. Omodaka, H. Takahashi, T. Yasui, K. Kato *et al.*, "Optic nerve head blood flow, as measured by laser speckle flowgraphy, is significantly reduced in preperimetric glaucoma," *Curr. Eye Res.* **41**, 1447–1453 (2016).
6. A. S. Mursch-Edlmayr, N. Luft, D. Podkowinski, M. Ring, L. Schmetterer, and M. Bolz, "Laser speckle flowgraphy derived characteristics of optic nerve head perfusion in normal tension glaucoma and healthy individuals: a pilot study," *Sci. Reports* **8**, 5343 (2018).
7. P. Bonnin, J.-A. C. Pournaras, K. Makowiecka, V. Krivosic, A. W. Kedra, J.-F. Le Gargasson, A. Gaudric, B. I. Levy, Y. S. Cohen, R. Tadayoni *et al.*, "Ultrasound assessment of ocular vascular effects of repeated intravitreal injections of ranibizumab for wet age-related macular degeneration," *Acta Ophthalmol.* **92**, e382–e387 (2014).
8. G. E. McVeigh, A. J. Bank, and J. N. Cohn, "Arterial compliance," in *Cardiovascular Medicine* (Springer, 2007), pp. 1811–1831.
9. A. P. Avolio, M. Butlin, and A. Walsh, "Arterial blood pressure measurement and pulse wave analysis: their role in enhancing cardiovascular assessment," *Physiol. Meas.* **31**, R1 (2009).
10. D. Rosenbaum, N. Kachenoura, E. Koch, M. Paques, P. Cluzel, A. Redheuil, and X. Girerd, "Relationships between retinal arteriole anatomy and aortic geometry and function and peripheral resistance in hypertensives," *Hypertens. Res.* **39**, 536 (2016).
11. H. S. Brar and L. D. Platt, "Reverse end-diastolic flow velocity on umbilical artery velocimetry in high-risk pregnancies: an ominous finding with adverse pregnancy outcome," *Am. J. Obstet. Gynecol.* **159**, 559–561 (1988).
12. W. W. Nichols and D. G. Edwards, "Arterial elastance and wave reflection augmentation of systolic blood pressure: deleterious effects and implications for therapy," *J. Cardiovasc. Pharmacol. Ther.* **6**, 5–21 (2001).

13. D. Maulik, "Spectral Doppler sonography: waveform analysis and hemodynamic interpretation," in *Doppler Ultrasound in Obstetrics and Gynecology* (Springer, 2005), pp. 35–56.
14. S. Tsuda, H. Kunikata, M. Shimura, N. Aizawa, K. Omodaka, Y. Shiga, M. Yasuda, Y. Yokoyama, and T. Nakazawa, "Pulse-waveform analysis of normal population using laser speckle flowgraphy," *Curr. Eye Res.* **39**, 1207–1215 (2014).
15. N. Luft, P. A. Wozniak, G. C. Aschinger, K. Fondi, A. M. Bata, R. M. Werkmeister, D. Schmidl, K. J. Witkowska, M. Bolz, G. Garhöfer *et al.*, "Ocular blood flow measurements in healthy white subjects using laser speckle flowgraphy," *PLoS One* **11**, e0168190 (2016).
16. B. Gu, X. Wang, M. D. Twa, J. Tam, C. A. Girkin, and Y. Zhang, "Non-invasive in vivo characterization of erythrocyte motion in human retinal capillaries using high-speed adaptive optics near-confocal imaging," *Biomed. Opt. Express* **9**, 3653–3677 (2018).
17. R. D. Plumb, P. K. Hamilton, D. J. Rea, S. A. Wright, S. M. Hughes, R. C. McGivern, and G. E. McVeigh, "Wave reflection signatures: identifying early microvascular abnormalities in type 2 diabetes," *The Br. J. Diabetes & Vasc. Dis.* **11**, 243–248 (2011).
18. G. E. McVeigh, P. K. Hamilton, and D. R. Morgan, "Evaluation of mechanical arterial properties: clinical, experimental and therapeutic aspects," *Clin. Sci.* **102**, 51–67 (2002).
19. S. Laurent, J. Cockcroft, L. Van Bortel, P. Boutouyrie, C. Giannattasio, D. Hayoz, B. Pannier, C. Vlachopoulos, I. Wilkinson, and H. Struijker-Boudier, "Expert consensus document on arterial stiffness: methodological issues and clinical applications," *Eur. Hear. J.* **27**, 2588–2605 (2006).
20. M. E. Safar, "Arterial stiffness as a risk factor for clinical hypertension," *Nat. Rev. Cardiol.* **15**, 97 (2018).
21. M. E. Safar and P. Lacolley, "Disturbance of macro-and microcirculation: relations with pulse pressure and cardiac organ damage," *Am. J. Physiol. Circ. Physiol.* **293**, H1–H7 (2007).
22. R. F. Bonner and R. Nossal, "Principles of laser-Doppler flowmetry," in *Laser-Doppler Blood Flowmetry* (Springer, 1990), pp. 17–45.
23. C. Riva, S. Cranstoun, J. Grunwald, and B. Petrig, "Choroidal blood flow in the foveal region of the human ocular fundus," *Invest. Ophthalmol. Vis. Sci.* **35**, 4273–4281 (1994).
24. C. E. Riva, M. Geiser, and B. L. Petrig, "Ocular blood flow assessment using continuous laser Doppler flowmetry," *Acta Ophthalmol.* **88**, 622–629 (2010).
25. A. Serov and T. Lasser, "High-speed laser Doppler perfusion imaging using an integrating CMOS image sensor," *Opt. Express* **13**, 6416–6428 (2005).
26. G. Michelson, B. Schmauss, M. Langhans, J. Harazny, and M. Groh, "Principle, validity, and reliability of scanning laser Doppler flowmetry," *J. Glaucoma.* **5**, 99–105 (1996).
27. M. Mujat, Y. Lu, G. Maguluri, Y. Zhao, N. Iftimia, and R. D. Ferguson, "Visualizing the vasculature of the entire human eye posterior hemisphere without a contrast agent," *Biomed. Opt. Express* **10**, 167–180 (2019).
28. C. Magnain, A. Castel, T. Boucneau, M. Simonutti, I. Ferezou, A. Rancillac, T. Vitalis, J.-A. Sahel, M. Paques, and M. Atlan, "Holographic laser Doppler imaging of microvascular blood flow," *JOSA A* **31**, 2723–2735 (2014).
29. M. Pellizzari, M. Simonutti, J. Degardin, J.-A. Sahel, M. Fink, M. Paques, and M. Atlan, "High speed optical holography of retinal blood flow," *Opt. Lett.* **41**, 3503–3506 (2016).
30. D. Donnarumma, A. Brodoline, D. Alexandre, and M. Gross, "4d holographic microscopy of zebrafish larvae microcirculation," *Opt. Express* **24**, 26887–26900 (2016).
31. D. Hillmann, H. Spahr, C. Hain, H. Sudkamp, G. Franke, C. Pfäffle, C. Winter, and G. Hüttmann, "Aberration-free volumetric high-speed imaging of in vivo retina," *Sci. reports* **6**, 35209 (2016).
32. L. Ginner, T. Schmoll, A. Kumar, M. Salas, N. Pricoupenko, L. M. Wurster, and R. A. Leitgeb, "Holographic line field en-face OCT with digital adaptive optics in the retina in vivo," *Biomed. Opt. Express* **9**, 472–485 (2018).
33. H. Spahr, C. Pfäffle, P. Koch, H. Sudkamp, G. Hüttmann, and D. Hillmann, "Interferometric detection of 3D motion using computational subapertures in optical coherence tomography," *Opt. express* **26**, 18803–18816 (2018).
34. L. Ginner, A. Wartak, M. Salas, M. Augustin, M. Niederleithner, L. M. Wurster, and R. A. Leitgeb, "Synthetic subaperture-based angle-independent Doppler flow measurements using single-beam line field optical coherence tomography in vivo," *Opt. Lett.* **44**, 967–970 (2019).
35. A. Brodoline, N. Rawat, D. Alexandre, N. Cubedo, and M. Gross, "4d compressive sensing holographic microscopy imaging of small moving objects," *Opt. Lett.* **44**, 2827–2830 (2019).
36. L. Puyo, M. Paques, M. Fink, J.-A. Sahel, and M. Atlan, "In vivo laser Doppler holography of the human retina," *Biomed. Opt. Express* **9**, 4113–4129 (2018).
37. L. Puyo, M. Paques, M. Fink, J.-A. Sahel, and M. Atlan, "Choroidal vasculature imaging with laser Doppler holography," *Biomed. Opt. Express* **10**, 995–1012 (2019).
38. D. D. Postnov, X. Cheng, S. E. Erdener, and D. A. Boas, "Choosing a laser for laser speckle contrast imaging," *Sci. Reports* **9**, 2542 (2019).
39. J. W. Goodman, *Introduction to Fourier Optics* (Roberts and Company Publishers, 2005).
40. D. H. Evans, *Doppler Ultrasound: Physics, Instrumentation, and Clinical Applications* (John Wiley & Sons, 1989).
41. E. Macé, G. Montaldo, I. Cohen, M. Baulac, M. Fink, and M. Tanter, "Functional ultrasound imaging of the brain," *Nat. Methods* **8**, 662 (2011).
42. W. Nichols, C. Pepine, E. Geiser, and C. Conti, "Vascular load defined by the aortic input impedance spectrum," in *Federation Proceedings*, vol. 39 (1980), pp. 196–201.

43. S. M. Toy, J. Melbin, and A. Noordergraaf, "Reduced models of arterial systems," *IEEE Transactions on Biomed. Eng.* pp. 174–176 (1985).
44. F. Tranquart, O. Bergès, P. Koskas, S. Arsene, C. Rossazza, P.-J. Pisella, and L. Pourcelot, "Color Doppler imaging of orbital vessels: personal experience and literature review," *J. Clin. Ultrasound* **31**, 258–273 (2003).
45. C. Demené, M. Pernot, V. Biran, M. Alison, M. Fink, O. Baud, and M. Tanter, "Ultrafast Doppler reveals the mapping of cerebral vascular resistivity in neonates," *J. Cereb. Blood Flow & Metab.* **34**, 1009–1017 (2014).
46. L. Pourcelot, "Applications cliniques de l'examen Doppler transcutané," *Velocim. Ultrason. Doppler* **34**, 780–785 (1974).
47. R. O. Bude and J. M. Rubin, "Relationship between the resistive index and vascular compliance and resistance," *Radiology* **211**, 411–417 (1999).
48. R. O. Bude and J. M. Rubin, "Effect of downstream cross-sectional area of an arterial bed on the resistive index and the early systolic acceleration," *Radiology* **212**, 732–738 (1999).
49. E. J. Halpern, D. A. Merton, and F. Forsberg, "Effect of distal resistance on Doppler US flow patterns," *Radiology* **206**, 761–766 (1998).
50. E. Polska, K. Kircher, P. Ehrlich, P. V. Vecsei, and L. Schmetterer, "RI in central retinal artery as assessed by CDI does not correspond to retinal vascular resistance," *Am. J. Physiol. Circ. Physiol.* **280**, H1442–H1447 (2001).
51. C. V. Network, "Developmental anatomy of the retinal and choroidal vasculature," *The Retin. Its Disord.* **179** (2011).
52. H. Isono, S. Kishi, Y. Kimura, N. Hagiwara, N. Konishi, and H. Fujii, "Observation of choroidal circulation using index of erythrocytic velocity," *Arch. Ophthalmol.* **121**, 225–231 (2003).
53. T. Iwase, K. Yamamoto, E. Ra, K. Murotani, S. Matsui, and H. Terasaki, "Diurnal variations in blood flow at optic nerve head and choroid in healthy eyes: diurnal variations in blood flow," *Medicine* **94** (2015).
54. K. Fondi, A. M. Bata, N. Luft, K. J. Witkowska, R. M. Werkmeister, D. Schmidl, M. Bolz, L. Schmetterer, and G. Garhöfer, "Evaluation of flicker induced hyperemia in the retina and optic nerve head measured by laser speckle flowgraphy," *PloS One* **13**, e0207525 (2018).
55. D. Squirrell, A. Watts, D. Evans, C. Mody, and J. Talbot, "A prospective evaluation of the heidelberg retina flowmeter in diagnosing ischaemia following branch retinal vein occlusion: a masked, controlled comparison with fluorescein angiography," *Eye* **15**, 261 (2001).
56. W. E. Lieb, S. M. Cohen, D. A. Merton, J. A. Shields, D. G. Mitchell, and B. B. Goldberg, "Color Doppler imaging of the eye and orbit: technique and normal vascular anatomy," *Arch. Ophthalmol.* **109**, 527–531 (1991).
57. W. H. Morgan, M. L. Hazelton, and D.-Y. Yu, "Retinal venous pulsation: Expanding our understanding and use of this enigmatic phenomenon," *Prog. In Retin. And Eye Res.* **55**, 82–107 (2016).
58. A. Wartak, F. Beer, S. Desissaire, B. Baumann, M. Pircher, and C. K. Hitzenberger, "Investigating spontaneous retinal venous pulsation using Doppler optical coherence tomography," *Sci. Reports* **9**, 4237 (2019).
59. S. Kain, W. H. Morgan, and D.-Y. Yu, "New observations concerning the nature of central retinal vein pulsation," *Br. J. Ophthalmol.* **94**, 854–857 (2010).
60. W. H. Morgan, C. R. Lind, S. Kain, N. Fatehee, A. Bala, and D.-Y. Yu, "Retinal vein pulsation is in phase with intracranial pressure and not intraocular pressure," *Investig. Ophthalmol. & Vis. Sci.* **53**, 4676–4681 (2012).
61. W. H. Morgan, M. L. Hazelton, B. D. Betz-Stablein, D.-Y. Yu, C. R. Lind, V. Ravichandran, and P. H. House, "Photoplethysmographic measurement of various retinal vascular pulsation parameters and measurement of the venous phase delay," *Investig. Ophthalmol. & Vis. Sci.* **55**, 5998–6006 (2014).
62. F. Moret, C. M. Reiff, W. A. Lagreze, and M. Bach, "Quantitative analysis of fundus-image sequences reveals phase of spontaneous venous pulsations," *Transl. Vis. Sci. & Technol.* **4**, 3–3 (2015).
63. O. Tan, G. Liu, L. Liang, S. S. Gao, A. D. Pechauer, Y. Jia, and D. Huang, "En face Doppler total retinal blood flow measurement with 70 kHz spectral optical coherence tomography," *J. Of Biomed. Opt.* **20**, 066004 (2015).
64. V. Doblhoff-Dier, L. Schmetterer, W. Vilser, G. Garhöfer, M. Gröschl, R. A. Leitgeb, and R. M. Werkmeister, "Measurement of the total retinal blood flow using dual beam fourier-domain Doppler optical coherence tomography with orthogonal detection planes," *Biomed. Opt. Express* **5**, 630–642 (2014).
65. G. Michelson and J. Harazny, "Relationship between ocular pulse pressures and retinal vessel velocities," *Ophthalmology* **104**, 664–671 (1997).
66. M. Paques, O. Baillart, O. Genevois, A. Gaudric, B. Lévy, and J. Sahel, "Systolodiastolic variations of blood flow during central retinal vein occlusion: exploration by dynamic angiography," *Br. J. Ophthalmol.* **89**, 1036–1040 (2005).

## 5.2 Retinal, cilio-retinal, and choroidal arterial waveforms

In addition to the retinal and choroidal blood flow measurements, we also investigated the flow waveform in a cilio-retinal artery (CLRA) in Fig. 5.2. As mentioned before, the retinal arteries are supplied by the central retinal artery and supply the neural retina, whereas the choroidal arteries are supplied by posterior ciliary arteries while supplying the outer retina. The cilio-retinal arteries are also supplied by the posterior ciliary circulation, and yet they supply the neural retina through the retinal capillaries as do other retinal vessels. The cilioretinal arteries emerge in the ONH region and run towards the fovea, they are present in about 18% of eyes [12].

In Fig. 5.2(a) we show the normalized curves of the retinal, cilioretinal, and choroidal arterial waveforms, marked by the boxes 'RA' in red, 'CLRA' in orange, and 'CA' in purple on the corresponding image Fig. 5.2(b). What can be observed is that the cilioretinal waveform closely resembles that of other retinal arteries. Both the retinal and cilioretinal waveforms show a briefer systole and a steeper downward slope after the systolic peak. The CLRA make the connection between the two supplying vasculatures (CRA and PCAs) and two supplied vascular beds of the posterior pole; as such they might be of interest to further study how the downstream vascular resistance affects the upstream flow waveform.

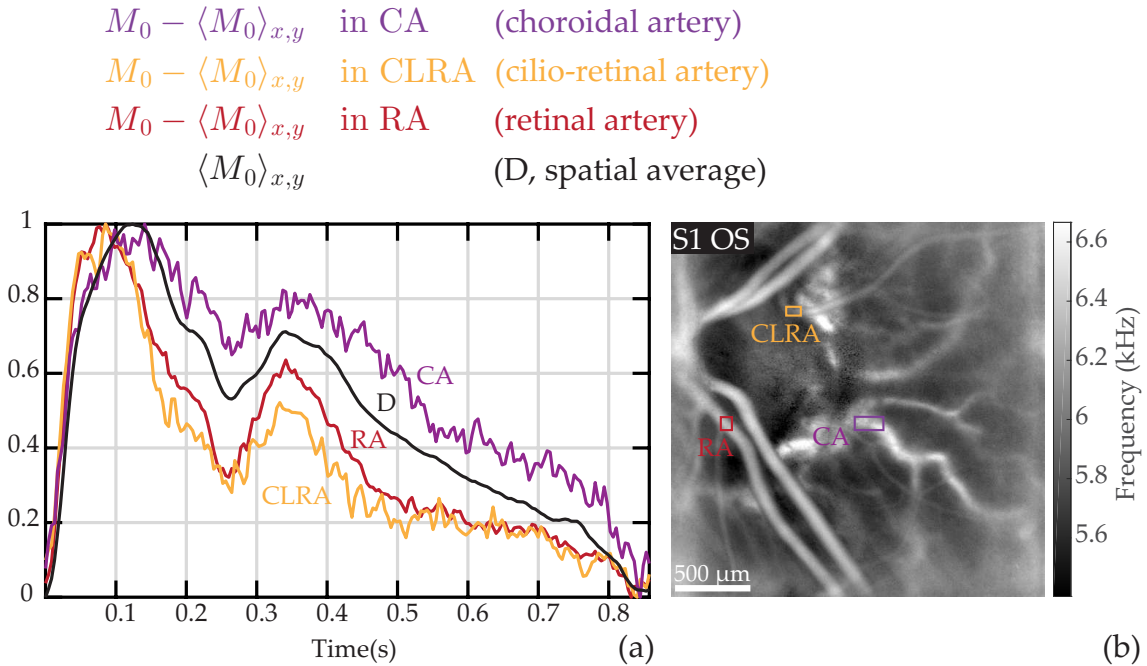


Figure 5.2: Measurements of the retinal, cilioretinal, and choroidal arterial waveforms. (a): Normalized power Doppler waveform in a retinal, cilioretinal and choroidal artery corrected from the dominant signal ('RA' in red, 'CLRA' in orange, and 'CA' in purple), and normalized waveform of the spatial average over the entire image ('D' in black). Despite being supplied by two separate vasculatures, the cilioretinal and retinal arteries have the same waveform.

## 5.3 Polarization: PBS - BS comparison

For the three articles presented in this thesis manuscript, all experiments were done with polarized light: the eye is illuminated with a linear polarization, and thanks to the PBS only the cross-polarized component is collected and able to reach the sensor. This is a feature of the instrument actually inherited from the time when it was used to make experiments on exposed tissues such as rodents brains [9, 88]. When imaging directly

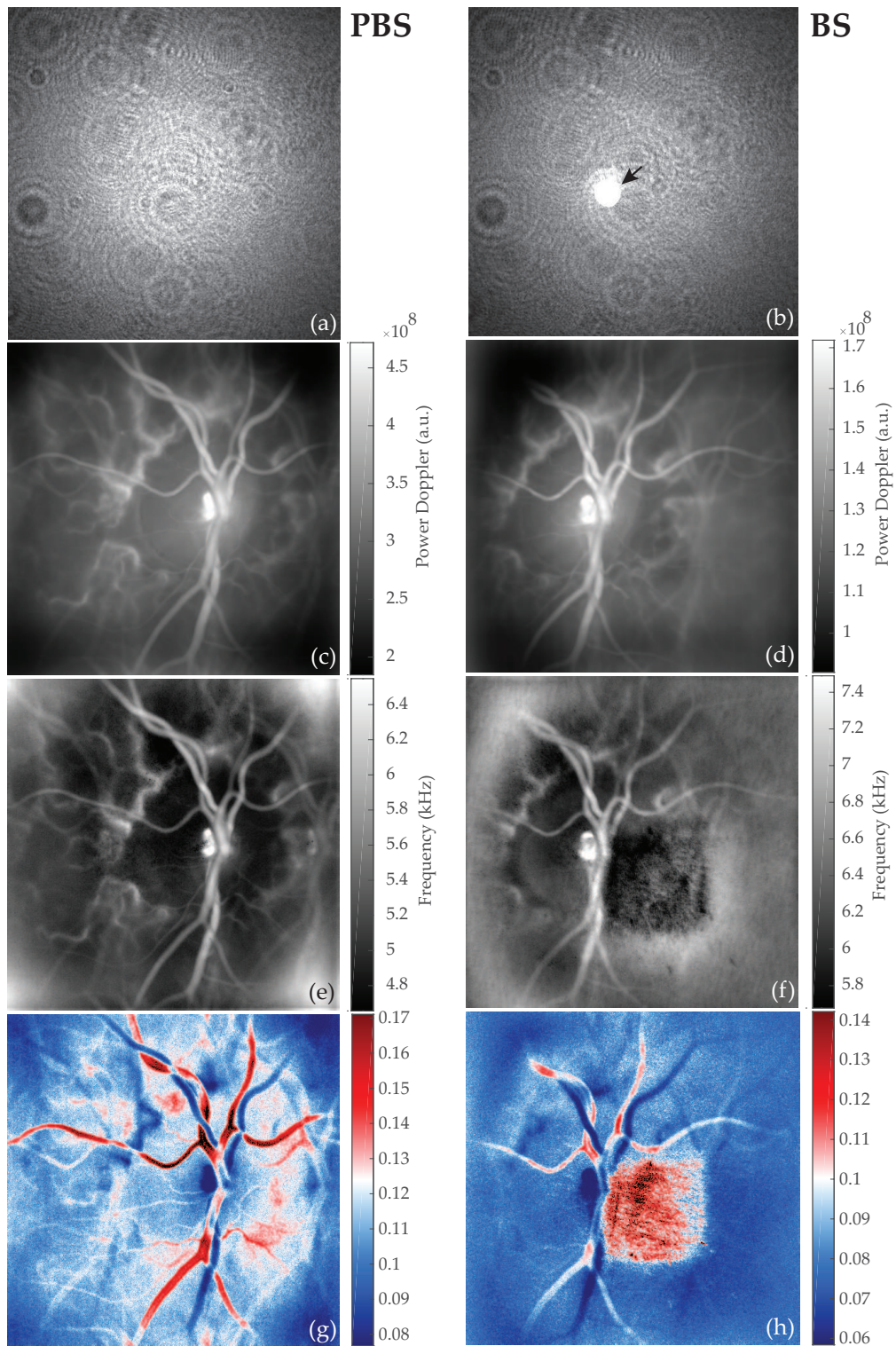


Figure 5.3: Experiments when using a BS (right column) instead of a PBS (left column) to collect the light backscattered by the eye. (a-b): raw interferograms: an area on the camera is saturated by the corneal specular reflection (arrow). (c-d): the averaged power Doppler images look fairly similar with both kinds of beamsplitter. (e-f): however when using a BS the mean frequency shift image is affected by a large stain. (g-h): the same stain is also visible on COV maps based on power Doppler movies; it seems to be due to the out of focus corneal specular reflection. See Visualization for the camera-retina refocus.

exposed tissues, the specular reflections has the same polarization state as the illumination beam whereas the Doppler shifted light tends to be depolarized because it is likely to have been multiply scattered. Thus, using a PBS is very efficient to suppress the specular reflections occurring on the tissue or on the glass put on top of the exposed tissue. However when it comes to retinal imaging the situation is slightly different because the cornea introduces a birefringence [98, 99]: the light that reaches the retina has lost its polarization state. Nonetheless this polarization scheme stays efficient to filter the corneal specular reflection which keeps the initial polarization state.

To investigate the relevance of using a PBS instead of a regular BS, we replaced the PBS by a BS and performed experiments in the same conditions. These results are presented in Fig. 5.3 where the left and right column of images show the results obtained with a PBS and BS, respectively. From top to bottom, the images are: (a-b) raw interferogram, (c-d) power Doppler images (6-30 kHz), (e-f) mean frequency shift images (0.5-30 kHz), coefficient of variation map (from the 6-30 kHz power Doppler movie). On the one hand, no large difference can be seen on the averaged power Doppler image, but all the other images present significant differences. On the interferogram, it can be seen that the corneal specular reflection saturates the camera images over a disc (arrow). It is very likely that this same specular reflection leaves an out of focus stain on the mean frequency shift image and even on the coefficient of variation map. This Visualization shows the mean frequency shift image reconstructed for different positions between the camera and the retina planes. This movie indicates that the saturated spot on the camera and the stain on the COV map share the same position, which suggests that it is the corneal reflection that causes this large stain in Fig. 5.3(f) and (h). Besides, the fact that the stain is visible when considering the mean frequency shift image and not the averaged power Doppler image shows that this contribution lies in the low frequencies of the Doppler broadening, which is consistent with what is expected of a specular reflection.

In conclusion, these results indicate that using a PBS remains efficient to remove the corneal reflection that is otherwise troublesome in LDH. However other approaches could be thought of to remove the corneal reflection, such as adding a pupil in a plane conjugate to the retinal plane.

## 5.4 Influence of $g_w$ parameter on the results

In the article integrated in this Chapter (end of subsection 2.2), is mentioned the fact that power Doppler images are corrected for a non-uniform illumination. This problem is probably due to vignetting as well as potentially the Gaussian shape of the illuminating beam. The numerical process to correct for it that was used in this thesis was to divide power Doppler images by a Gaussian filtered version of themselves. As illustrated in Fig. 5.4, the width of the Gaussian filter has an influence on the resulting images. Here we used the "imgaussfilt" function from Matlab, with a width  $g_w = 20, 40, \text{ and } 60$  (from top to bottom). A smaller value helps revealing smaller features, but an excessively small value can generate artifacts.

## 5.5 Subtraction of baseline signal

The subtraction of the baseline signal (spatial average) allows to reveal specific flow behaviors in retinal veins and arteries: we here discuss the validity of this subtraction. To do so we have plotted in Fig. 5.5 the variations of  $M_0 - a\langle M_0 \rangle_{x,y}$  in the usual ROIs ('RA', 'RV', and 'B') for different values of  $a$ . A value of 0 is no compensation at all, and a value of 1 is a total compensation.

The instrument has a depth of field integrating the contribution from the retina to the choroid, thus a pixel placed on a blood vessel will receive contributions from both

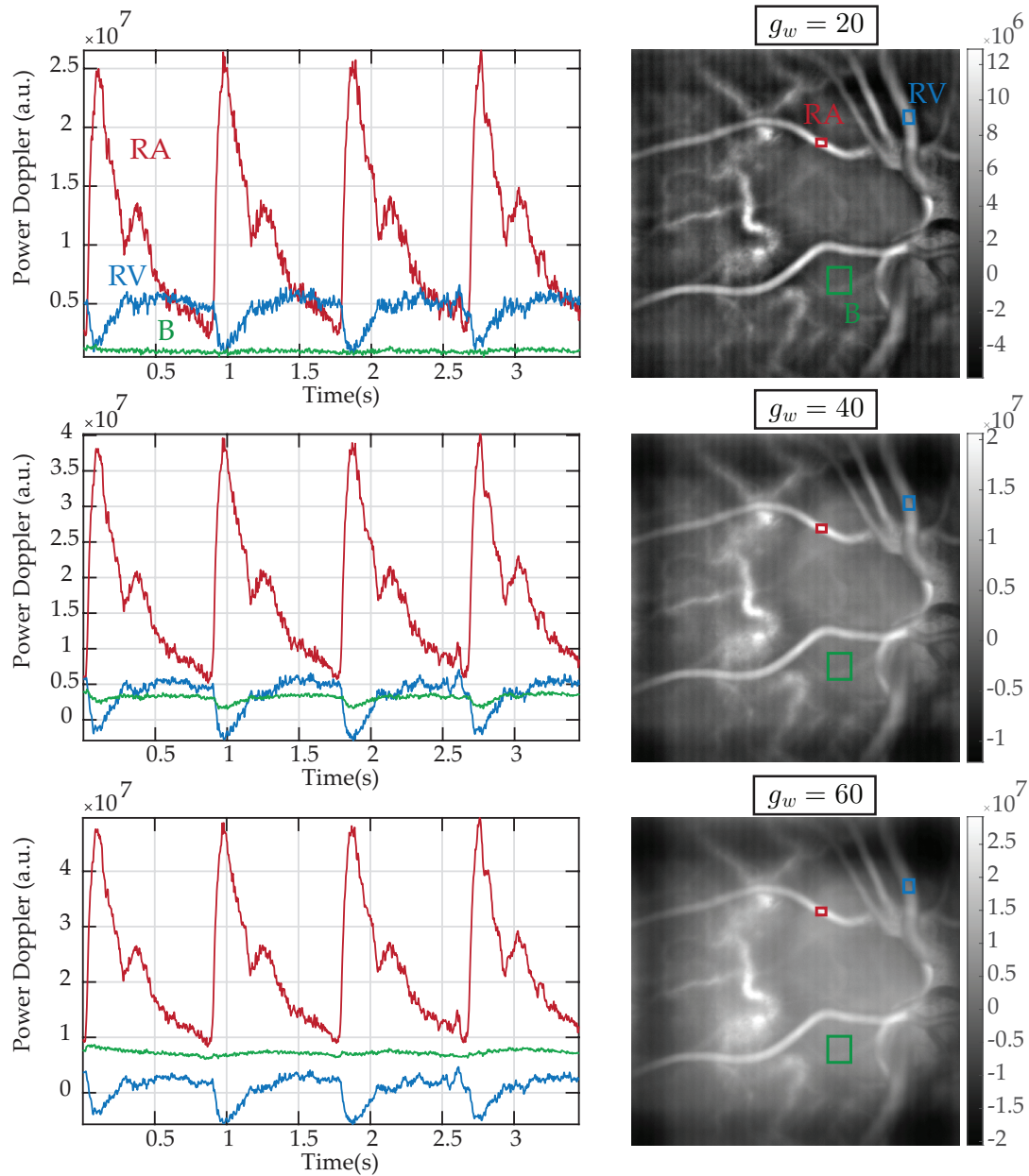


Figure 5.4: Illustration of the process to compensate for the non-uniform illumination: power Doppler images are divided by a Gaussian filtered version of themselves, and the width of the Gaussian filter is a parameter of importance. We show here for three different values of Gaussian width filter the power Doppler images and associated variations over time. We used "imgaussfilt" on Matlab with values of 20, 40, and 60 (from top to bottom). A smaller value helps revealing smaller features.

light scattered by the blood vessel but also from other layers. Removing the baseline signal should remove these contributions. It also allows to remove the contribution of global movements (axial or lateral motion of the ocular globe). However a value of  $a = 1$  implicitly makes the assumption that blood vessels are fully transparent (at least for a low numerical aperture), and that a pixel on a blood vessel will receive as much multiply scattered light from the choroid as if there was no blood vessel. Therefore a value of  $a = 1$  may be an excessive correction.

When using a coefficient of  $a = 1$ , we measure a sharper systolic peak in the artery, and reduced variations in the vein, which is what we would expect. It is also only with a coefficient of 1 that we can suppress the signal in 'B' so that we do not measure any

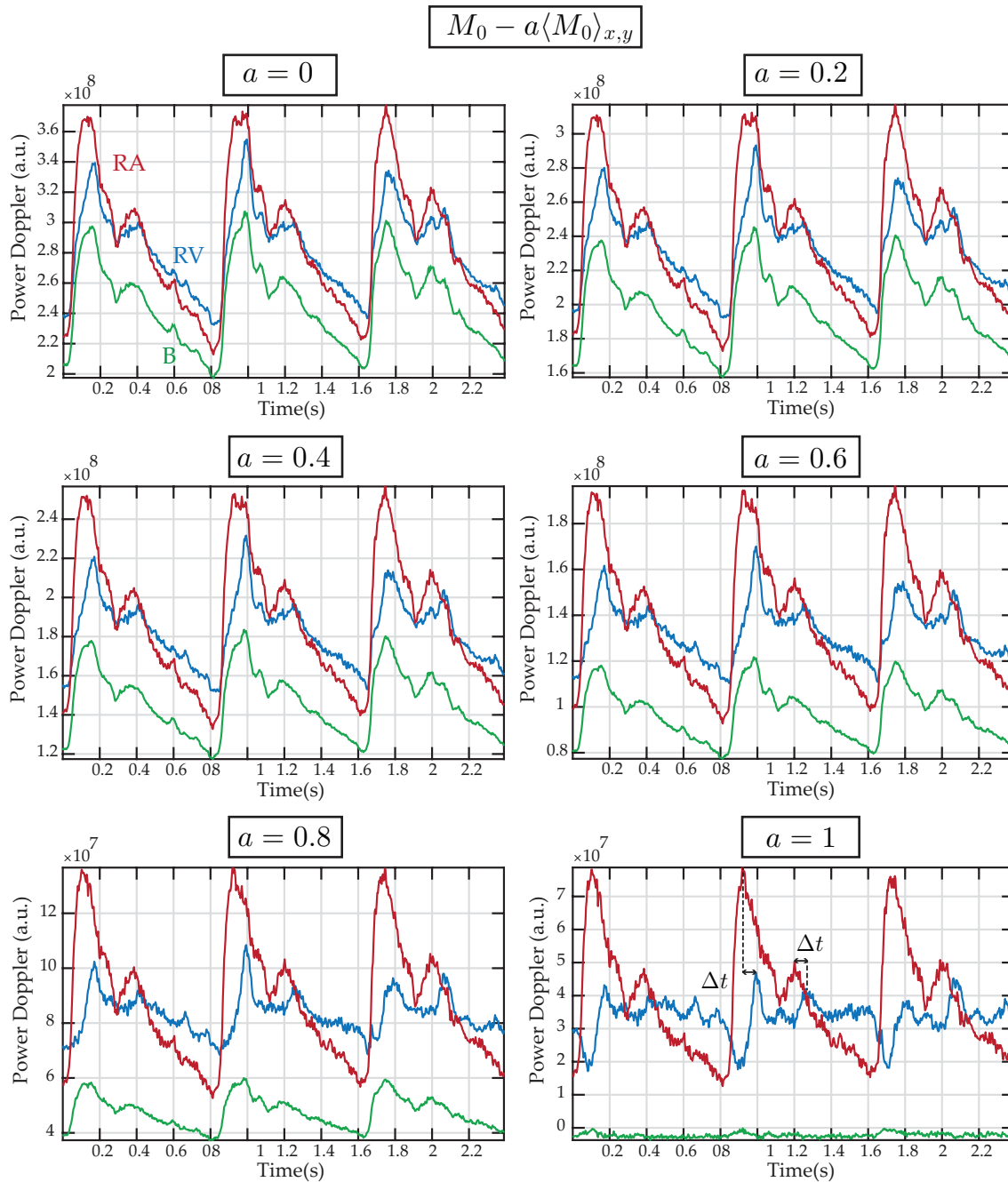


Figure 5.5: Waveform profile in a retinal artery, vein and background corrected from the baseline signal  $M_0 - a\langle M_0 \rangle_{x,y}$  for different values of the coefficient  $a$ . For  $a$  close to 0, little difference can be seen in the three ROIs, but for  $a$  close to 1, each retinal feature exhibit a specific flow behavior. A delay between the two arterial peaks and subsequent venous peaks can be observed of approximately  $\Delta t = 40$  ms.

variations anymore. Interestingly when doing so we can note a delay between the two arterial peaks (systole and diastolic notch), and then two peaks in the venous signal that follow with a delay of approximately  $\Delta t = 40$  ms.

## 5.6 Measurements with Doppler ultrasound

The blood flow waveform profiles vary significantly from one person to another, which comforts the hypothesis that it is an interesting measurement to assess properties of the

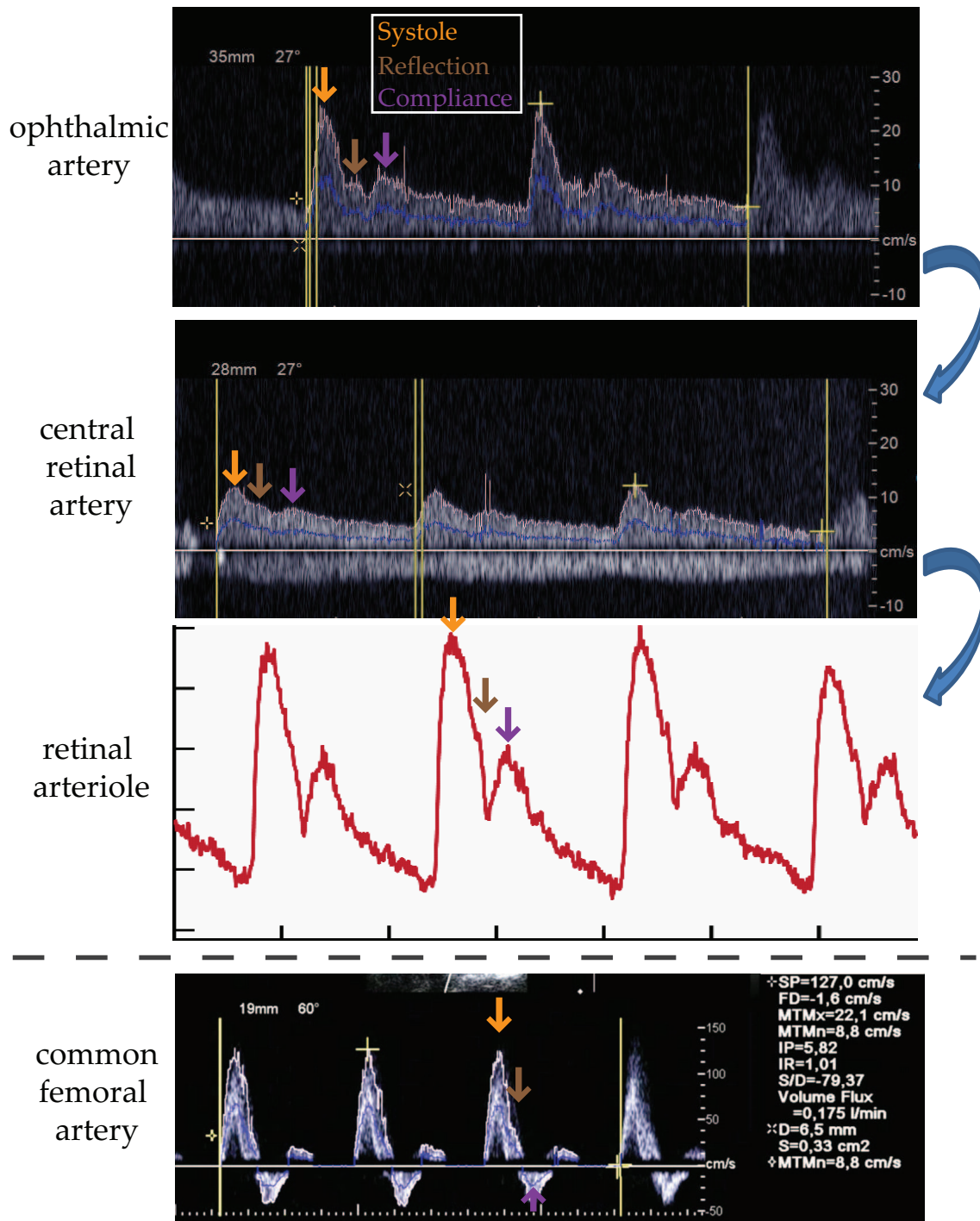


Figure 5.6: Blood flow as measured with Doppler ultrasound and LDH in a same eye. (a) Ophthalmic artery (Doppler ultrasound). (b) Central retinal artery (Doppler ultrasound). (c) Retinal arteriole (LDH). (d) Common femoral artery (in another person). Different phenomena play a role in shaping the waveform.

vasculature. In Fig. 5.6 we present our current understanding of the variations of the waveform (elaborated by Philippe Bonnin to which I express all my gratitude for his kind help). In Fig. 5.6(a-c) are presented flow measurements in a same eye, with Doppler ultrasound and with LDH. The interest of using both methods is that we can measure the flow in the successive arteries in which the blood circulates: with Doppler ultrasound we have access to the flow in the ophthalmic artery and CRA, and with LDH we can measure the flow in retinal arterioles.

For each of these flow waveforms, the orange arrows point to the systolic peak which mark the beginning of the cardiac cycle. The brown arrows point to what we think is the contribution of waves reflection that occur in arteriole bifurcations (cf first Chapter 1.1.3). In retinal arterioles, there is very little delay between the systole and the peak due to the reflection waves so they cannot be told apart, but in the CRA and ophthalmic artery, this contribution is separated from the systole because of the longer travel time.

Finally comes the case of the secondary peak, here called "compliance" contribution, that was termed dicrotic notch in this manuscript. This type of notch is often encountered in Doppler measurements, but different explanations can be found in the literature, partly because the explanation depends on where the measurement is performed:

- Some convincing evidence has shown that the closing of the aortic valves generates such type of notch [100]. This explanation holds very well for the flow in the aorta, but the aorta is quite far from the eye, and the flow waveform is very likely to be have been modified when it has reached the ophthalmic artery.
- It could also be possible that pulse wave reflections are actually at the origin of this secondary peak, and that another phenomenon causes the other notch found in the CRA and OA marked by the brown arrows. However we would expect the reflected pressure waves to propagate faster so that the peak they induce would be close to synchronized with the systolic peak.
- The stretch and recoil due to the compliance of the aorta and other large elastic arteries induces a redistribution of the flow (Windkessel effect), but it occurs over longer periods of time as the systolic energy is redistributed until the diastole end; this phenomena does not create a brief peak in the cardiac cycle.
- Finally, the most convincing explanation of the phenomena uses concepts of arterial compliance and vascular resistance, which is why it is termed "compliance" in Fig. 5.6(a). The different vascular territories of the body have each their own vascular resistance, and the cerebral vascular resistance is lower than that of the lower limbs for example. During systole, the flow is successfully pushed into all branches of the arterial vasculature because the systolic pressure is large enough to overcome all vascular resistance. In subjects with compliant arteries, the arterial vasculature expands during systole (not only large elastic arteries but also smaller arteries), so this energy is redistributed when the arteries recoil in the early diastole. However the pressure may not be enough for the flow to penetrate territories with a high vascular resistance. Thus in these territories it is possible to observe a reflux of the flow, for example it is the case in the common femoral artery as shown in Fig. 5.6(d). This reflux (retrograde flow) is then redistributed in territories with a low vascular resistance in the normal circulation direction (anterograde flow). Because the retina and choroid (and more generally the whole cerebral circulation) have a low vascular resistance, it is possible that the secondary notch we observe is a reflux of flow that was supposed to supply territories with a higher vascular resistance.

Whatever the reason of this notch, its presence seems to be a marker of arterial elasticity. The understanding of the flow waveform is rendered complicated by the fact that at two different points of the vascular tree, the flow waveform may have a similar shape but for different reasons: for example this secondary notch is present close to the aorta because of the closing of the valves (first hypothesis), and our hypothesis is that it is present in the eye because of a compliant reflux. This explanation has not been proven yet. In order to prove these theories and better understand this flow waveform, measurements on large cohorts of healthy and diseased eyes will be of a great help. For example it would be interesting to see if the delay between the systole and dicrotic notch depends on the height of the subject: if it is caused by a reflux that comes from the lower limbs, the travel time

would be greater, and because our instrument has a good temporal resolution it would be possible to measure this delay with sufficient precision to see a difference depending on the subject height.

# Chapter 6

## Conclusions and perspectives

### 6.1 Conclusion

In conclusion, the work carried out in this thesis demonstrates a high clinical potential in ophthalmology for LDH because of its simplicity, robustness, and comfort for the subject. Two major field of applications stand out for the instrument. First we have demonstrated its ability to make full-field retinal blood flow measurements with a very good combination of spatial/temporal/flow resolution, over a field of view of decent size. Compared to the current commercialized alternatives for ocular blood flow monitoring (e.g. laser speckle flowgraphy and Doppler ultrasound), LDH definitely holds a strong hand. Secondly, considering the additional information power Doppler choroidal images have to offer compared to ICG-A and OCT, LDH could also find a use for choroidal vasculature imaging. For both of these applications, LDH seems full of promise for further clinical research because of the new insights it can provides to understand the role of blood flow in the pathophysiology of diseases affecting the eye.

The addition of a reference beam to perform laser Doppler measurements, which in turns allows to use higher frame rates, is the key factor in performing high quality LDH measurements. The full access to the Doppler spectrum allows to isolate the lowly shifted photon (due to global movement) from the highly shifted photon. Both the measurement of the retinal blood flow waveform and the mapping of the choroidal vasculature are made using the highly Doppler shifted part of light.

Overall, the most important limitations of the instrument include the use of a fast camera and the lack of quantitative flow measurements in physical units. The fast camera provides cumbersome stack of images that requires a significant computational power to be processed rapidly, and does not provide real-time visualization of the blood flow as desired by medical doctors. However in can be reasonably expected that in a relatively near future there will be commercialized streaming cameras with a throughput sufficient to perform LDH measurements in real-time. The absence of flow measurements in real physical units is a second clear limitation of the instrument, as it would be useful that LDH provides measurements that allow intra and inter-individual comparison in order to proceed to clinical trials. Using the raw power Doppler without any calibration may prove insufficient to compare measurements from one person to another because some variable parameters such as the pupil size probably have an impact on the power Doppler value. However theoretically, it should be possible to derive flow and velocity measurements in absolute units after a calibration of the instrument. Finally, there is reasonable hope that we can identify relevant biomarkers based on the waveform variations such as the resistivity or pulsatility index.

## 6.2 Perspectives

### Pathological cases

The end goal for LDH is to be introduced into a clinical setting to image patients with pathologies where blood flow plays a central role. The instrument was set inside the Quinze-Vingts hospital in Paris at the beginning of my thesis to that very end, but unfortunately to this date no experiments has been made on diseases eyes for lack of safety authorizations. However the authorization has finally come in July 2019, and we are now allowed to image the large cohorts of people with various diseases constituted by the hospital. The exploration will be made in conjunction with other imaging devices (OCT, adaptive optics imaging, etc) and in collaboration with medical doctors from the hospital. Considering the limitations of the instruments under its current version such as the high sensibility to fixational eye problems (especially micro-saccades), some patients would be better subject for the instruments than other. Patients with fixation problems (for example because of a damaged central vision) would not be ideal subjects.

### Towards quantitative and reproducible measurements

As mentioned above, a necessary step for our instrument would be to study if the power Doppler and mean frequency shift metrics that were used during my thesis have the potential to be quantitative, and reproducible. A first step would be to derive the real physical units of volume and velocity behind the power Doppler and mean frequency shift based on the theory developed for laser Doppler flowmetry. Then the reproducibility of the measurements need to be studied: how the pupil size, eye orientation, iris pigmentation, corneal and lens opacity etc influence the power Doppler values needs to be known. An examination protocol based on these criteria to ensure maximum reproducibility of the measurements should be established. Right now, intra and inter-individual reproducibility has not been explored.

### Physiological tests

In Chapter 5 we saw that it seemed possible to measure simultaneously the retinal and choroidal blood flow in favorable areas where both types of vessels are visible. However the influence of multiple scattering in the RPE needs to be better understood. One way to verify that the retinal and choroidal blood flow measurements realized with LDH truthfully reflect retinal and choroidal variations would be to monitor the values upon physiological stimulations. For example, we would expect only the retinal vasculature to be capable of autoregulation of the blood flow. Thus, for example in cases of hypoxia/hyperoxia, a decrease/increase in blood flow should be observed in the retina but the choroidal blood flow would be left intact, as has been found by other means of measuring blood flow in these two vasculatures [101, 102].

### Ocular pulsations

In Chapter 3, we saw that because LDH measures the complex light field, it is able to detect the asymmetry of the Fourier spectrum, and thus the algebraic Doppler frequency shift, which yields the direction of the velocity. This feature could be used to measure the ocular pulsations. The theory behind this phenomena is that as the choroid is filled with blood during systole, its volume increases and it pushes the retina forward, leading to an increase in intra-ocular pressure, and mechanical oscillations of the retina up to the 7th Fourier harmonic of the heartbeat frequency [103, 104]. Monitoring these oscillations seems doable with LDH, which would have the advantage to make measurements with a very good temporal resolution. These measurements would be made simultaneously to the

regular LDH measurement of blood flow. Considering the expected velocity of the retinal displacement, the very low frequency range should be used to reveal these oscillations. However, in the attempts I have made during my thesis, I was not able to reveal these oscillations because of two limitations: (i) unfortunately fixational eye movements also strongly contribute to the Doppler broadening at these frequencies, and (ii) the total duration of the measurements with the fast camera is limited to a few seconds. Longer acquisition time (with another camera or using the camera burst mode), with improved signal processing to isolate the expected signal may work to reveal ocular pulsations with LDH.

### **3D modeling of the choroidal circulation**

To the best of my knowledge, LDH is the first ophthalmic instrument able to perform non an arteriovenous differentiation in the choroid. One of the limitations of the instrument is that it does not have strong axial sectioning abilities. OCT, on the contrary has excellent sectioning abilities and is able to image most vessels of the choroid because of the shadowing artifacts. So coupling the OCT volumetric information of the choroidal vasculature with the arteriovenous identification capability of LDH could help create a 3D model of flow circulation the choroid.

### **Iris blood flow**

The iris vasculature is supplied by the two long posterior ciliary arteries and drained by the vortex veins; it plays a role in supplying the cornea and muscles to contract or dilate the pupil. It is another optically accessible tissue where blood flow can be measured, which remains an interesting tissue although it has been less studied than the retinal or choroidal vasculatures. At some point in my thesis we have considered imaging the iris with LDH. Several difficulties require a little bit of work around to be overcome. First it would require adapting the optical conjugation. Secondly, the iris pigmentation contains melanin which diffuses light, which complicates imaging. Then the presence of the eye pupil at the center of the iris, with a size that varies from subject to subject. This is especially problematic because if a parallel illumination scheme is used, the light is focused on the retina which drastically limits the beam power due to safety limitations. I did not take the time to work on this but LDH seems like a good candidate for this task because of its ability to select strongly Doppler shifted light that allows it to work with multiply scattered light.

### **Retinal pulse wave velocity**

The propagation of blood flow in arteries is made at the speed of the pulse pressure wave. The pulse wave propagation velocity depends on the properties of the vasculature (mainly arterial stiffness). With Doppler ultrasound, the propagation of the pulse wave can be inferred from measurements at two remote locations. However the biomechanical properties of arteries are not the same in large arteries of the body and in the relatively smaller retinal arteries. Thus measuring the retinal pulse wave velocity in order to obtain information about stiffness of retinal arteries would be interesting. So far only one group seems to have obtained reliable measurements of the retinal pulse wave velocity with results consistent with measurements in other parts of the body [105] (although these results are controversial), but with a method that seems complicated to use in a clinical setting. The propagation speed in young and healthy subjects is expected to be around 5-7 m/s in the aorta, and around 1 m/s in the retina. Thus with a field of view of about 4x4 mm, a vessel in the diagonal would 5 mm long, and a temporal resolution of 2 ms to observe the propagation of the flow wave between two points located exactly opposite on the diagonal. This is very close the temporal resolution limit of LDH to make clear measurements. Increasing the field of view imaged on the retina, and developing an efficient method to

filter the signal and measure the phase delay between two signals may be enough to make the PWV measurements.

### **Modification of the instrument**

To face the current limitation of the instrument and improve the results, several changes may be considered. First, the quality of choroidal images would probably benefit from working with a wavelength further in the near-infrared spectrum. As the RPE and photoreceptor layers become optically more transparent with a greater wavelength, we would expect to have sharper images of the choroid, and maybe reveal smaller choroidal structures. However the camera sensitivity also comes into consideration, as it decreases with greater wavelength. A wavelength of 850 nm would be an interesting tradeoff between these two specifications.

Secondly, another optical configuration could be considered in order to increase the field of view. In the present configuration, the pupil size limits the extent of the retinal field of view and the pupil is visible on LDH images for eyes with not fully dilated pupil. Instead of focusing the laser beam in the front focal plane of the eye, it would be possible to focus light closer to the cornea so that the pupil cannot obstruct the illuminating laser beam. Volk lens are especially designed for the purpose of focusing light on the cornea. However the current eye ISO safety standard strictly limits the illumination on the cornea to 20 mW/cm<sup>2</sup> in group 1 for any wavelength between 770 and 1400nm. So it would be necessary to work with a wavelength lower than 770 nm if we were to focus the laser beam on the cornea. Otherwise the laser beam could be focused slightly before or after the cornea so that the energy would be more spread on the corneal surface, but it would require a precise positioning of the patient's head in front of the device to make sure the distance cornea - focusing spot is respected.

Other variations of the instrument include the possibility to insert a swept-source laser diode where there is now a single-frequency laser diode and make full-field SS-OCT in the same configuration in order to combine both OCT and LDH information over the same field of view at a small cost.

Finally, the choroidal images provided by LDH are very promising but the process to make a 5 × 5 montage is at present quite long. It would be possible to take advantage of the fact that to image the choroidal vasculature, the high temporal resolution is not needed, only the fast sampling rate (in the 10-100 kHz range). An instrument based on line-field LDH might be able to make images over a large field of view over longer time period (a few seconds to capture the whole field of view), and benefit from the flexibility offered by line-field instruments, while using a cheaper sensor array adapted to the line-field scheme.

### **Comparison with laser speckle contrast imaging**

Laser Doppler and laser speckle contrast are two different ways of studying the same phenomena, i.e. analyzing intensity fluctuations of coherent light to produce a blood flow contrast. In laser speckle, the contrast is calculated as the local standard deviation of intensity fluctuations normalized by the mean intensity over a few pixel wide window (spatially, temporally, or spatio-temporally). In laser Doppler, the intensity fluctuations are analyzed with a Fourier approach which gives more latitude to isolate a specific contribution by filtering certain frequency ranges, which is done in laser speckle contrast imaging by acquiring images with different exposure times. A holographic version of laser speckle contrast analysis could be implemented on our setup: Instead of having the light from the retina self-interfere and form speckle on the camera, it could be interfering with a reference beam. This approach may prove useful for the slow camera that performs narrowband laser Doppler measurements (sampling frequency only allows to capture a small portion of the Doppler spectrum). Indeed with this camera, the sampling rate is not fast enough

to follow the speckle fluctuations, so a speckle contrast method would seem more suitable because it relies on the exposure time being longer than the speckle decorrelation time. It would be possible to use the slightly modify the current instrument in order to make the test by simply conjugating the retinal and camera planes. This way, the speckled image of the retina would form on the sensor and we would be in the right condition to make laser speckle contrast measurements. Then it would be possible to simply make the speckle contrast images with and without the holographic reference beam in order to determine if it brings an additional sensitivity. It would be interesting to study for example if having access to the phase of the wave field in a holographic version of laser speckle contrast imaging would be useful or if the speckle intensity fluctuations already contain all the useful information to make blood flow measurements.

### **Use the computational possibilities offered by holography**

Finally, an interesting research axis would be to try to take advantage of the possibilities offered by digital holography. The complex light field can be reconstructed in any plane between the camera sensor and the sensor, and then it can be modified, partially reconstructed, or used in conjunction with strong image processing tools to increase the signal to noise ratio.

Several groups have shown in the last few years that it was possible to compensate for the eye aberration in holographic setup, either iteratively by maximization for a metric accounting for the image quality [94, 95], or by evaluation the wavefront error by a sub-aperture correlation scheme [106, 107]. As these techniques are also able to compensate in case of anisoplanatism, they would probably be able to correct for the slight distortion and out-of-focusing occurring in the corner of LDH images. These problems might be introduced by aberrations in the optical system or because of the retinal curvature, but it should be possible to correct them all the same.

A second use of the computational possibilities of digital holography demonstrated in the last few years is to select the light according to the wavevector direction. In the computed k-space it is possible to isolate different backscattering directions, which is especially useful for Doppler measurements. This has been used to measure the expansion of a biological tissue under photocoagulation with a high temporal resolution and 3-D resolution [108], and then in vivo for flow measurements in retinal vessel in a very similar configuration [109]. It has also been used to in another form of laser Doppler holography in a dual-beam transmission microscopy setup to reconstruct full 3-D images of zebrafish from single holograms [110, 111]. More sophisticated ways of using the Doppler effect measured with our instrument could be developed borrowing from these applications.

Finally, one of the particularities of our instrument is to have no axial sectioning capabilities, and a large depth of field. We rely on this large depth of field to image both the retina and choroid at the same time. However as we saw in section 4.4, this depth of field is sometimes not enough, and will especially not be enough for subject with an unusually thick choroid (up to 600-700  $\mu\text{m}$ ). Because the depth of field decreases with the square of the numerical aperture, this would become even more problematic in the future if the numerical aperture of the system was to increase when changing the instrument configuration. However this problem has been encountered elsewhere in digital holography, and solutions have been developed. In holography, the complex light field is recorded on a 2-D sensor and the field retrieval is done by retro-propagation in a series of planes adjacent to the object to obtain a 3-D image of the object. Extended depth of focus allows to fuse the information from the multiple reconstruction planes in order to obtain a single 2-D image that is more resolved (less out-of-focus features). Applying this concept to our data would help improve visibility of choroidal features when the focus is made on retinal vessels, or vice versa.

### 6.3 Supplementary materials

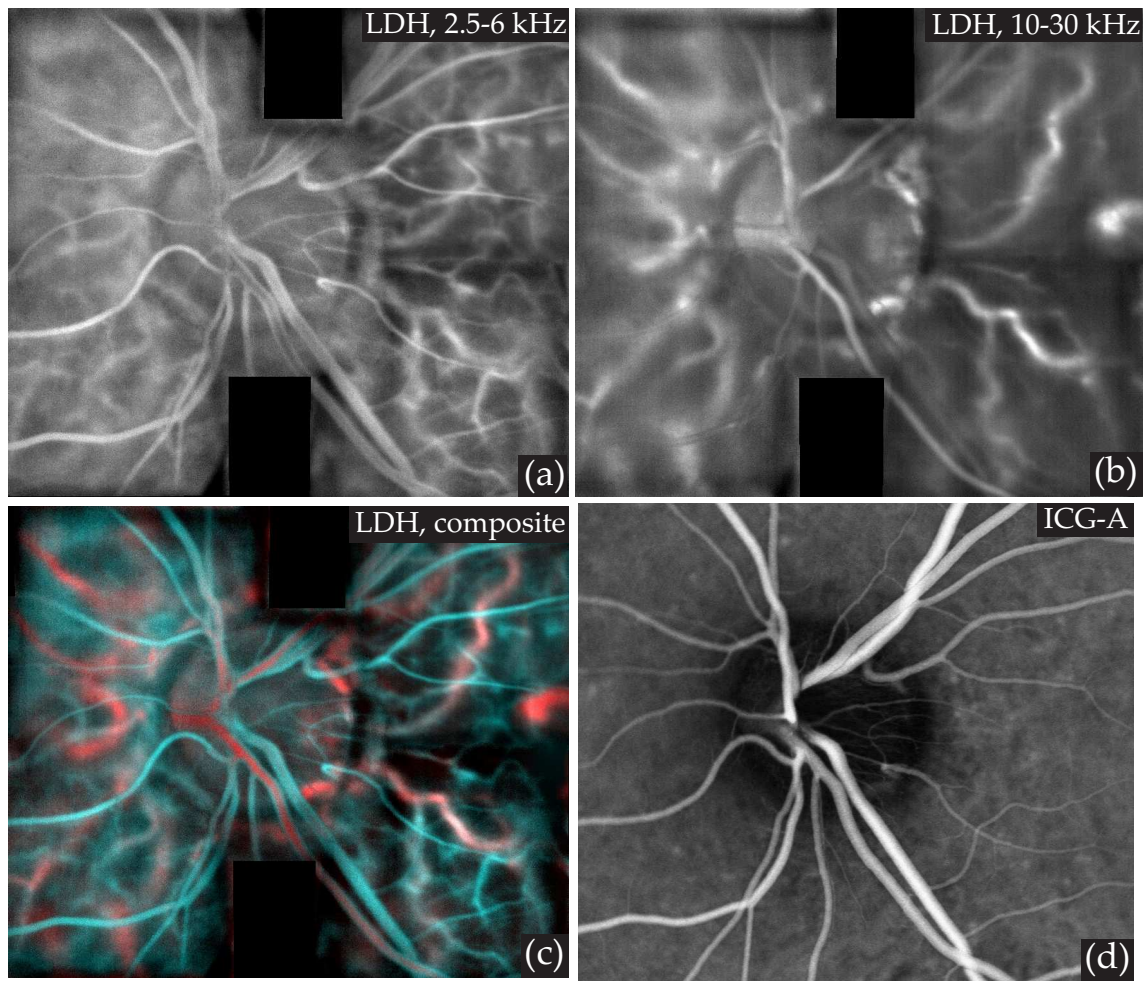


Figure 6.1: LDH montage of holograms recorded using a longer focal length for the lens in front of the eye in an attempt to improve lateral resolution. (a) and (b): low and high frequency power Doppler montages. (c): LDH color composite montage. (d): ICG-A, late phase.

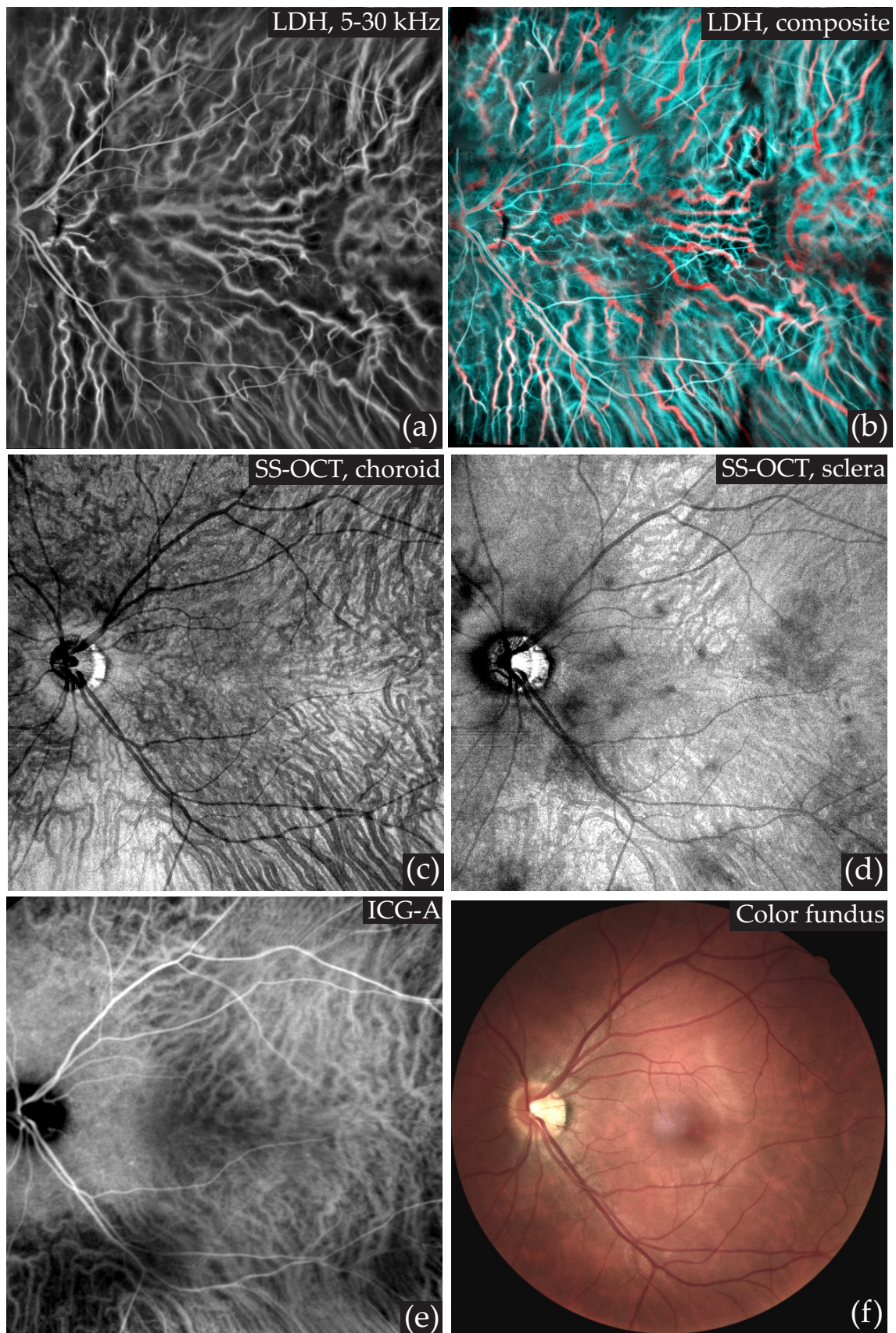


Figure 6.2: Multimodal imaging in an OS eye. (a) and (b): LDH power Doppler (5-30 kHz) and composite color image (2.5-6 kHz in cyan and 10-30 kHz in red). (c) and (d): SS-OCT (Plex Elite 9000 - Zeiss) of the choroid and sclera, respectively. (e): ICG-A, late phase. (f): Color fundus.

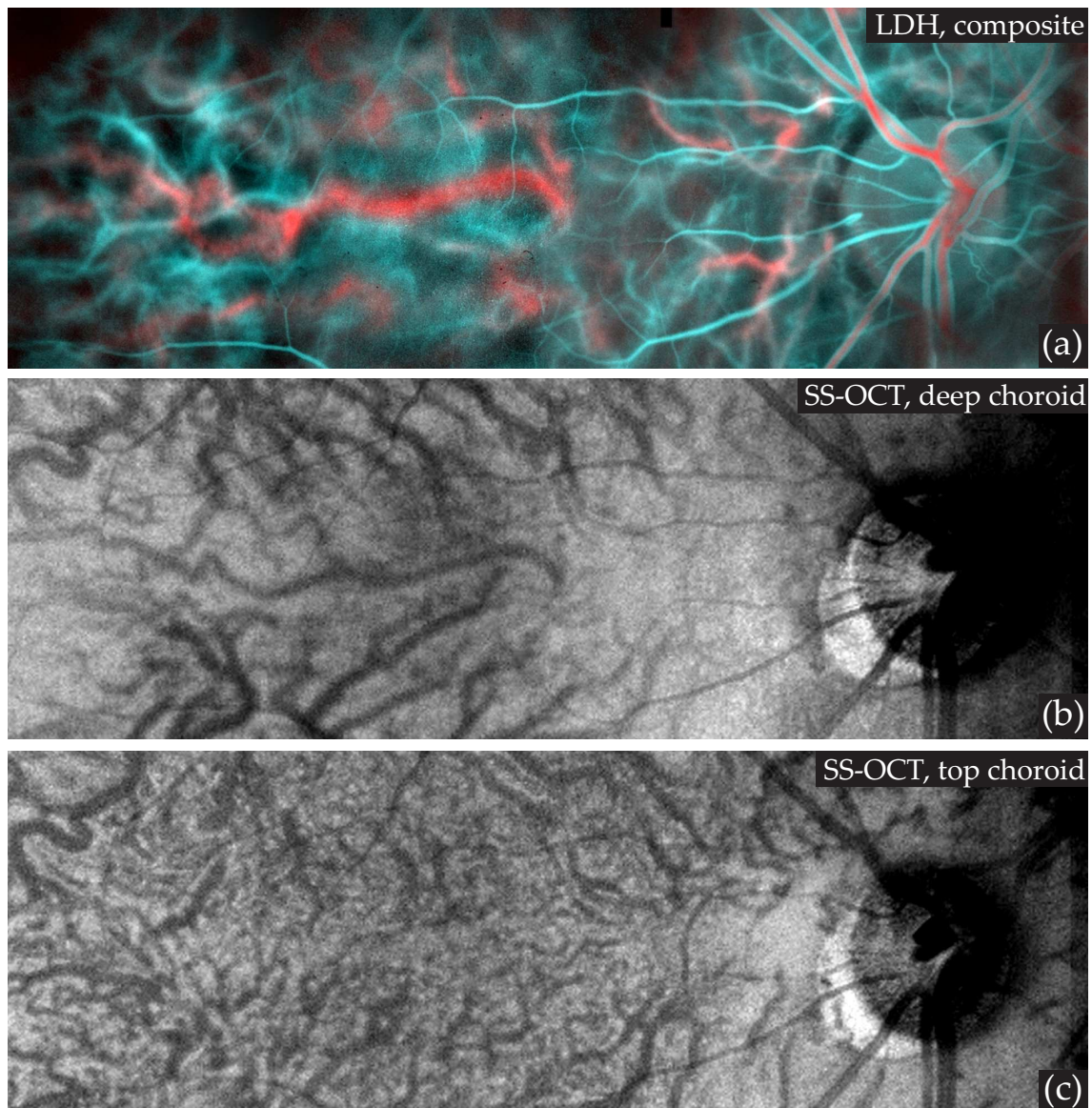


Figure 6.3: Multimodal imaging in another subject eye. (a) LDH: composite color image. (b) and (c): SS-OCT (Plex Elite 9000 - Zeiss) of the deep and superficial choroid, respectively.

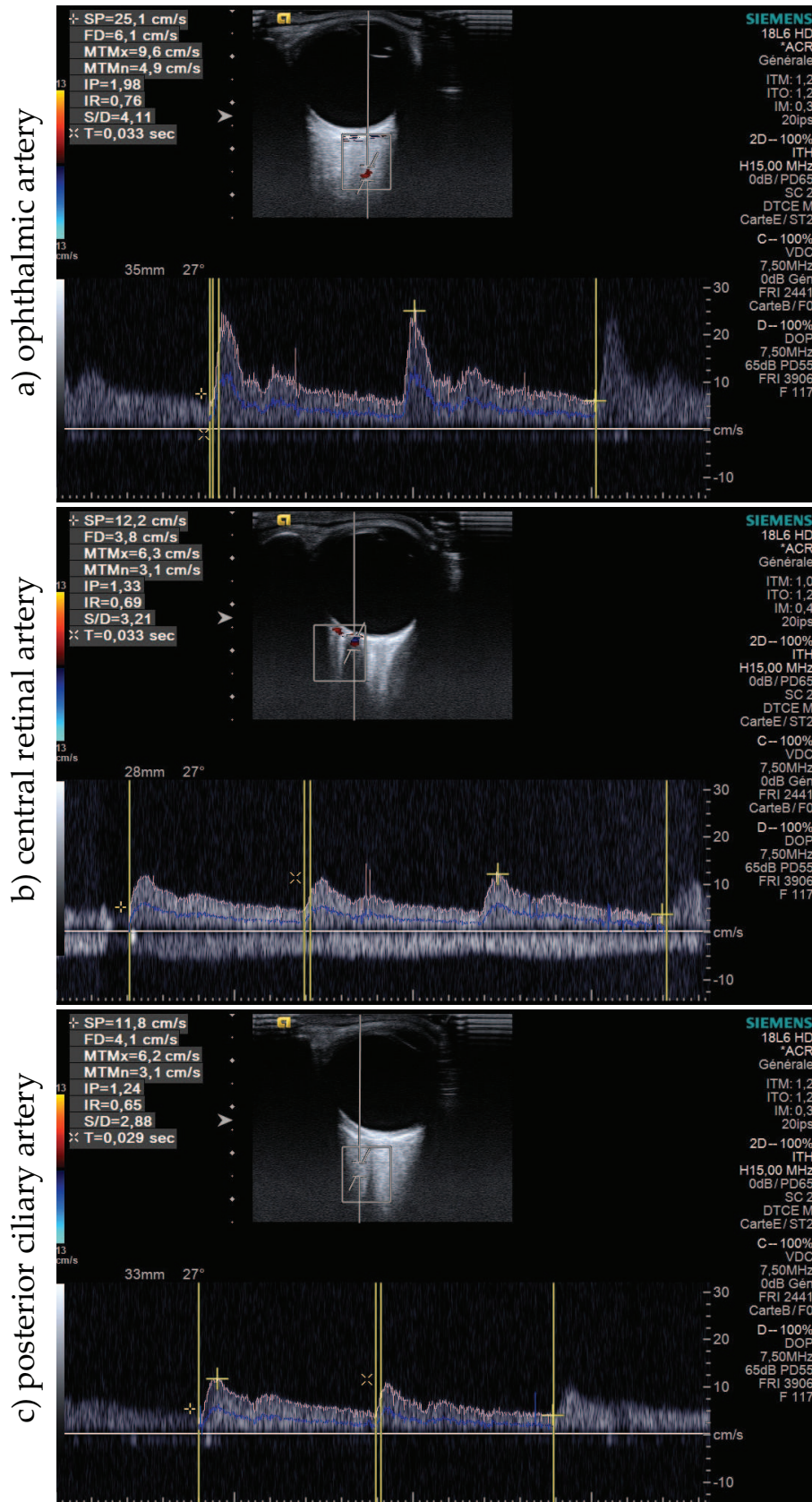


Figure 6.4: Blood flow measured with Doppler ultrasound: (a) Ophthalmic artery. (b) Central retinal artery. (c) Posterior ciliary artery. The instrument provides measurements in physical units.

## 6.4 Scientific contribution

### Publications

L. Puyo, J.-P. Huignard, and M. Atlan. Off-axis digital holography with multiplexed volume Bragg gratings. *Applied optics*, 57(12):3281–3287, 2018.

L. Puyo, M. Paques, M. Fink, J.-A. Sahel, and M. Atlan. In vivo laser Doppler holography of the human retina. *Biomedical Optics Express*, 9(9):4113–4129, 2018.

L. Puyo, M. Paques, M. Fink, J.-A. Sahel, and M. Atlan. Choroidal vasculature imaging with laser Doppler holography. *Biomedical Optics Express*, 10(2):995–1012, Feb 2019.

L. Puyo, M. Paques, M. Fink, J.-A. Sahel, and M. Atlan. Waveform analysis of human retinal and choroidal blood flow with laser Doppler holography. *Biomedical Optics Express*, 10(10):4942–4963, Oct 2019.

### Presentations

L. Puyo, M. Paques, M. Fink, J.-A. Sahel, and M. Atlan. Laser Doppler holography reveals retinal blood flow in humans. *Journal of Vision: Fall Vision Meeting*, 17(15):30–30, 2017. Washington DC.

L. Puyo, M. Fink, M. Paques, and M. Atlan. Laser doppler perfusion imaging of human retina using digital holography (conference presentation). In *Ophthalmic Technologies XXVIII*, volume 10474, page 1047405. International Society for Optics and Photonics, 2018. San Francisco.

L. Puyo, M. Paques, M. Fink, J.-A. Sahel, and M. Atlan. Retinal blood flow imaging by narrowband and wideband digital holography. *ARVO Imaging in the Eye*. Honolulu.

L. Puyo, M. Paques, M. Fink, J. A. Sahel, and M. Atlan. Holographic laser Doppler retinal imaging. *Investigative Ophthalmology & Visual Science: ARVO*, 59(9):5861–5861, 2018. Honolulu.

L. Puyo, M. Paques, M. Fink, J.-A. Sahel, and M. Atlan. Non-invasive and high temporal resolution choroidal and retinal blood flow imaging using laser doppler holography (conference presentation). In *Ophthalmic Technologies XXIX*, volume 10858, page 1085811. International Society for Optics and Photonics, 2019. San Francisco.

L. Puyo, M. Paques, M. Fink, J.-A. Sahel, and M. Atlan. Waveform analysis and vessel type identification in the retina with laser Doppler holography. *ARVO Imaging in the Eye*. Vancouver.

L. Puyo, M. Paques, M. Fink, J.-A. Sahel, and M. Atlan. Laser Doppler holography to analyze the flow in the deep choroidal vasculature. *ARVO*. Vancouver.

L. Puyo, M. Paques, M. Fink, J.-A. Sahel, and M. Atlan. Ultrafast digital holography for in vivo retinal blood flow imaging and assessment of flow resistance. *OSA Digital Holography and 3-D Imaging*. Bordeaux.

L. Puyo, M. Paques, M. Fink, J. A. Sahel, and M. Atlan. Analysis of retinal and choroidal images measured by laser Doppler holography. *SPIE Optical Metrology*. Munich.

L. Puyo, M. Paques, M. Fink, J. A. Sahel, and M. Atlan. Non-invasive imaging of the choroidal vasculature with laser Doppler holography. *European Conferences on Biomedical Optics*. Munich.

L. Puyo, M. Paques, M. Fink, J. A. Sahel, and M. Atlan. Imaging and analyzing choroidal blood flow non-invasively with laser Doppler holography. *Euretina*. Paris.

# Chapter 7

## Résumé en français

### 7.1 Introduction

La circulation oculaire revêt un intérêt majeur pour mieux comprendre les pathologies vasculaires de la rétine comme la rétinopathie diabétique, le glaucome et les occlusions veineuses. Pour améliorer la compréhension de la pathogénèse de ces maladies, les dépister plus précocement, et une mieux évaluer l'efficacité des traitements administrés, la mesure du débit sanguin oculaire est fondamentale. Une meilleure gestion de ces maladies est d'autant plus critique que leur prévalence est croissante du fait du vieillissement de la population. Le fond de l'œil est également un objet d'intérêt pour étudier de manière pratique la vascularisation chez l'homme, et les dérèglements provoqués à l'échelle microvasculaire par des maladies cardiovasculaires. L'hypertension artérielle, par les interactions remarquées mais encore non comprises qu'elle entretient avec les pathologies vasculaires de la rétine est la cible de beaucoup d'interrogations. Enfin, la rétine est également le seul tissu cérébral accessible aux instruments optiques de manière non-invasive. Des études récentes ont montré que le développement de la maladie d'Alzheimer est vraisemblablement provoqué par un affaiblissement du flux sanguin cérébral. La vascularisation rétinienne reflète dans une certaine mesure la vascularisation cérébrale et pourrait donc être riche d'enseignement pour l'étude de la maladie d'Alzheimer.

Jusqu'à présent, aucun instrument développé pour étudier le flux sanguin oculaire n'a pu répondre pleinement aux attentes des cliniciens. Pour être tout-à-fait pertinente, l'angiographie du fond de l'œil doit relever de nombreux défis techniques. En premier lieu, l'instrument idéal doit fournir un contraste quantitatif de flux sanguin, i.e. l'intensité de l'image doit être liée au débit local de sang dans les vaisseaux (principalement des globules rouges). Ces mesures doivent être faites avec une résolution temporelle de l'ordre de la milliseconde pour observer les variations cardiaques du flux sanguin, et ne pas être affecté par un flou de bougé due aux mouvements naturels et incontrôlables de l'œil. Enfin, il est souvent très utile de disposer d'informations 2D, autrement dit d'images, afin de comparer facilement la perfusion de vaisseaux voisins. Les premiers instruments optiques d'imagerie du flux sanguin oculaire reposaient sur des techniques invasives qui ont fait leurs preuves depuis les années 1970. L'injection d'un agent de contraste fluorescent comme le vert d'indocyanine ou la fluorescéine dans le système vasculaire permet de révéler les vaisseaux sanguins très efficacement comme illustré en Fig. 7.2(a). Ces instruments ont permis d'étudier approximativement les ralentissements circulatoires, les fuites, ou encore les néovascularisations très fréquentes dans les pathologies vasculaires de la rétine. Ces méthodes pèchent cependant par leur côté invasif et leur trop faible résolution temporelle. Plus important encore, le contraste des images reflète seulement la présence de l'agent de contraste fluorescent et n'est donc qu'indirectement lié au débit sanguin local : les mesures ne sont absolument pas quantitatives.

Les dernières décennies ont vu l'émergence de plusieurs méthodes d'angiographie non-

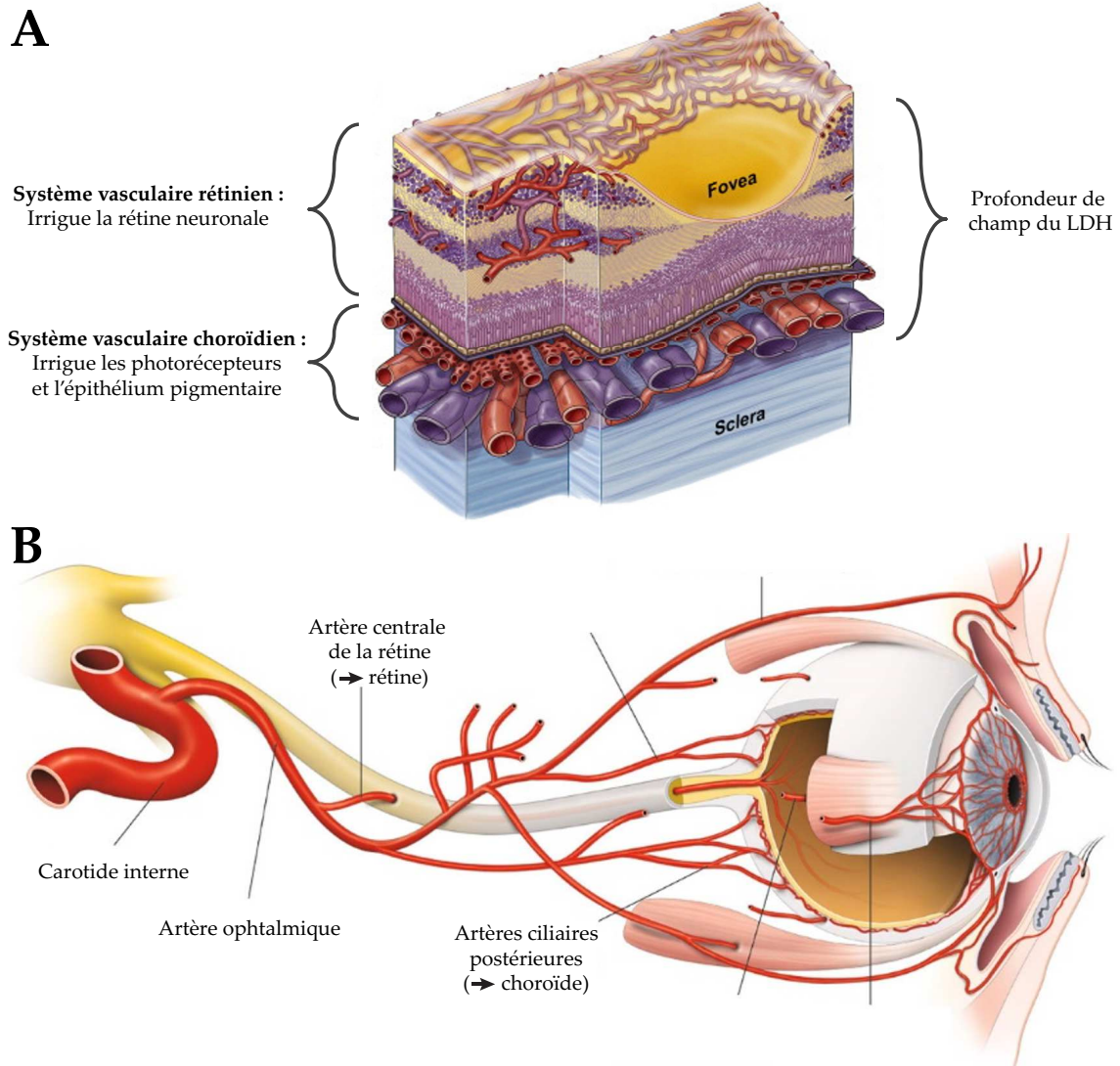


Figure 7.1: Schéma de la vascularisation du fond de l'œil. (A) La carotide interne donne naissance à l'artère ophtalmique qui elle-même irrigue à la fois l'artère centrale de la rétine et les artères ciliaires postérieures. L'artère centrale de la rétine pénètre dans l'œil par le nerf optique et perfuse le système vasculaire rétinien. La circulation choroïdienne est quant à elle alimentée par les artères ciliaires postérieures. (B) Vue en coupe du fond d'œil : les couches rétinienne et choroïdienne sont séparées au niveau du complexe choriocapillaire - épithélium pigmentaire. La vascularisation rétinienne perfuse la rétine neuronale tandis que la choroïde alimente les photorécepteurs et l'épithélium pigmentaire. La profondeur de champ du LDH permet d'imager simultanément ces deux réseaux vasculaires.

invasives. La plupart des instruments non invasifs utilisés pour la mesure du flux sanguin oculaire reposent sur l'analyse du contraste de speckle ou d'effet Doppler. Ces deux approches utilisent les fluctuations d'intensité de la lumière cohérente provoquées par les objets en mouvement pour mesurer le flux sanguin [112]. Les globules rouges, parce qu'ils se déplacent à grande vitesse relativement au reste de la rétine, deviennent eux-mêmes une source de contraste. Trois méthodes de mesure de flux sanguin oculaires se dégagent de l'ensemble des techniques existantes parce qu'elles ont abouti à la commercialisation d'instruments : la tomographie par cohérence optique angiographique ("OCT-angiographie"), la flowgraphie laser speckle, et la débitmétrie laser Doppler.

Depuis la première démonstration en laboratoire en 1991 [51], la tomographie par cohérence optique (OCT) a connu un développement spectaculaire en ophtalmologie car

elle offre la possibilité d'imager la rétine en coupe, et donc de surveiller efficacement les décollements de la rétine. L'OCT-angiographie est un développement plus récent basé sur l'analyse des fluctuations d'intensité du signal d'OCT pour former des images de flux sanguin, cf Fig. 7.2(b). Pour ce faire, la variance locale du signal de speckle est calculée à partir de quelques mesures répétées [113]. L'OCT-A permet ainsi de réaliser des cartes en 3D du système vasculaire rétinien, suffisamment précises pour imager les capillaires. Cette technique a été largement utilisée pour étudier la relation entre les pathologies oculaires et l'anatomie vasculaire rétinienne et choroïdienne [114, 52]. Cependant, les critères morphologiques qui peuvent être étudiés en OCT-A comme la densité de capillaire, l'étendue de la zone avasculaire centrale ne donnent pas d'information sur la qualité de la perfusion sanguine. L'OCT-A ne fournit pas d'informations quantitatives sur le débit sanguin des vaisseaux car la morphologie d'un réseau vasculaire n'est pas toujours liée à sa perfusion. Par exemple l'épaisseur de la choroïde est très variable chez le sujet sain et ne reflète pas le débit sanguin qui s'écoule dans les vaisseaux choroïdiens. Une seconde limitation de l'OCT-A est que la résolution temporelle requise pour observer les variations de flux au cours du cycle cardiaque est hors de portée des instruments d'OCT-A car ils leur faut environ une seconde pour réaliser une seule mesure angiographique.

La flowgraphie laser speckle (LSFG) est une autre technique d'angiographie basée sur la mesure des fluctuations d'intensité de la figure de speckle [61]. Des images en-face de la rétine sont formées sur le capteur d'une caméra et plusieurs images successives sont combinées pour générer un contraste de flux sanguin, comme montrée en Fig. 7.2(c). A la différence de l'OCT-A, le LSFG est uniquement 2D, dans une configuration dite plein champ. Ceci permet au LSFG d'avoir une résolution temporelle suffisante (quelques dizaines de millisecondes) pour observer les changements de flux sanguin au cours du cycle cardiaque. La principale limitation du LSFG est que les mesures sont réalisées dans un système d'unités arbitraires qui ne varie pas linéairement avec le débit. En effet la plage de linéarité de la mesure est déterminée par le temps d'exposition des images qui correspond à un certain temps de décorrélation du speckle. Les mesures de cet instrument sont donc faiblement quantitatives.

Enfin, la débitmétrie laser Doppler (laser Doppler flowmetry, LDF en anglais) permet de mesurer le flux sanguin avec une très bonne résolution temporelle (de l'ordre de la milliseconde) et dans un système d'unités arbitraire dont la quantitativité est satisfaisante [72]. Le principe du débitmètre laser Doppler est de mesurer l'élargissement Doppler de la lumière cohérente induit par le déplacement des globules rouges dans les vaisseaux sanguins. Le décalage de fréquence est mesuré au moyen d'interférences entre la lumière décalée en fréquence par l'effet Doppler (diffusée par des globules rouges) et la lumière non décalée en fréquence (diffusé par des particules statiques). L'inconvénient de cette méthode est que le flux n'est mesuré qu'en un seul point : pour réaliser une image il faut utiliser un système à balayage et mesurer le signal Doppler successivement point par point. Cependant cela prend trop de temps de constituer une image entière, et il n'est plus possible d'échantillonner les variations de flux sanguin liés aux cycles cardiaques [79]

La méthode sur laquelle j'ai travaillé pendant ma thèse est appelé holographie laser Doppler (LDH). Cette technique est conceptuellement proche de la débitmétrie laser Doppler par la manière dont elle forme un contraste angiographique. Le principe du LDH est de faire interférer la lumière rétrodiffusée par l'œil avec un faisceau de référence sur le capteur d'une caméra. On peut donc comprendre le LDH comme une version interférométrique et plein champ du LDF. Dans le LDH, le champ optique servant de lumière non décalée en fréquence est le faisceau de référence, ce qui permet d'introduire un gain de cohérence qui rend la mesure plus sensible. Ceci permet d'augmenter autant que nécessaire la puissance du champ de référence illuminant une caméra ultrarapide, afin de saturer à loisir l'image enregistrée. Avec le LDH il devient possible de travailler avec un temps d'exposition très faible en configuration plein champ, et donc de mesurer l'élargissement Doppler de l'ordre de quelques dizaines de kHz avec la fréquence d'échantillonnage qui

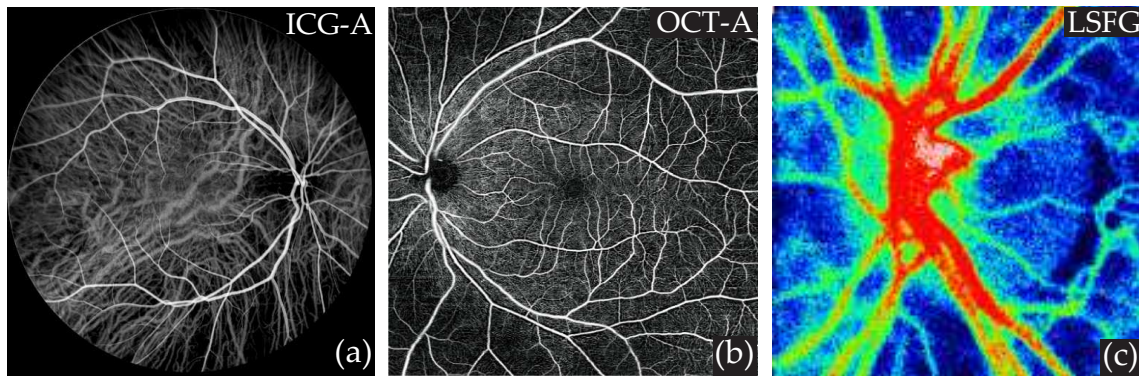


Figure 7.2: Imagerie de la vascularisation du fond de l'oeil avec les instruments commerciaux de l'état de l'art. (a) L'angiographie au vert d'indocyanine (ICG-A) est une méthode invasive permettant de révéler la rétine et la choroïde. (b) L'angiographie par tomographie en cohérence optique (OCT-A) est une méthode très récente qui permet de révéler les vaisseaux rétiniens de manière non-invasive. (c) La flowgraphie par contraste de speckle (LSFG) permet de mesurer les variations de flux sanguin au cours du cycle cardiaque. Dans l'ensemble les mesures de ces instruments laissent à désirer en matière de quantitativité et en résolution temporelle.

convient. Le contraste angiographique est tiré de l'élargissement Doppler de la lumière rétrodiffusée par la rétine par une analyse de Fourier. Les images de flux sanguins dites "power Doppler" sont calculées à partir de l'intégration de la densité spectrale de puissance. Les modifications du flux sanguin au cours des cycles cardiaques peuvent être révélées par une analyse à transformée de Fourier à temps court. Le LDH avait été précédemment utilisé pour imager le flux sanguin dans l'oeil du rongeur [11], nous présentons ici les premières mesures de flux sanguin par LDH dans l'oeil humain. Ce résumé est organisé de la façon suivante : la méthode est présentée dans la première partie, puis les deux parties suivantes traitent des résultats obtenus dans la rétine et dans la choroïde.

## 7.2 L'holographie laser Doppler

### 7.2.1 Mesures laser Doppler

Les techniques de laser Doppler visent à mesurer la vitesse d'un objet à partir des décalages de fréquence optique induits par effet Doppler sur un faisceau laser qu'il rétrodiffuse. Dans le cas de diffusion simple de la lumière par une particule en mouvement, le décalage de fréquence Doppler est proportionnel à la vitesse de la particule, à sa direction et aux directions des vecteurs d'ondes impliqués :

$$\omega_D = (\mathbf{k}_s - \mathbf{k}_i) \cdot \mathbf{v} \quad (7.1)$$

où  $\mathbf{k}_i$  est le vecteur d'onde incident,  $\mathbf{k}_s$  le vecteur d'onde diffusée et  $\mathbf{v}$  le vecteur de vitesse instantanée du diffuseur. La fréquence optique de la lumière diffusée est modifiée d'une quantité appelée décalage Doppler. Ces décalages de fréquence individuels ont un effet statistique lorsque l'on considère le spectre du faisceau laser entier diffusé par l'ensemble des diffuseurs constituant l'objet. Lorsque l'objet sondé par le faisceau laser est un tissu biologique, la lumière est diffusée par un large ensemble de particules ayant une grande distribution de vitesse. L'effet induit sur la densité spectrale de puissance de la lumière diffusée est qualifié d'élargissement Doppler.

On considère que dans la rétine la plupart des diffuseurs sont relativement statiques, à l'exception des cellules dans les vaisseaux sanguins comme les globules rouges qui se déplacent rapidement (jusqu'à quelques dizaines de mm/s) et peuvent induire de grands

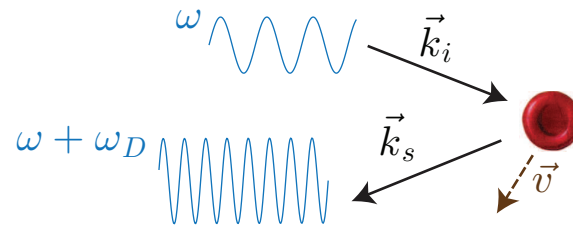


Figure 7.3: Décalage de fréquence Doppler d'un faisceau optique lors de la diffusion par une particule en mouvement : le décalage de fréquence est proportionnel à la vitesse du diffuseur et au produit scalaire entre le vecteur vitesse et la différence des vecteurs d'ondes impliqués.

décalages de fréquence Doppler (jusqu'à quelques dizaines de kHz). Le flux sanguin est donc le principal responsable de l'élargissement Doppler à haute fréquence. Toutefois, la lumière diffusée par les globules rouges est également diffusée avant ou après par des diffuseurs statiques [77]. Cette situation de diffusion multiple implique un certain degré de randomisation des vecteurs d'onde incidents et diffusés, de sorte que l'information qu'elle contient sur la direction du flux sanguin est perdue. En d'autres termes, les mesures de flux sanguin calculées à partir de l'élargissement Doppler sont relativement indépendantes de l'angle entre un vaisseau sanguin et l'axe optique.

Lorsque l'on fait interférer un faisceau de référence (non décalé en fréquence) avec la lumière rétrodiffusée par l'œil, le spectre de battement des fluctuations d'intensité correspond au spectre d'élargissement Doppler. Une analyse de Fourier des fluctuations d'intensité permet de mesurer ce spectre Doppler, et à partir de là le flux sanguin de la zone sondée par le faisceau laser. On considère généralement que le décalage en fréquence moyen correspond à la vitesse moyenne des diffuseurs, et que l'intégrale du spectre au-dessus d'une certaine fréquence donne le nombre de diffuseurs se déplaçant au-delà de la vitesse équivalente, ce qui correspond au volume de sang dans la zone sondée.

### 7.2.2 Présentation de l'instrument

Le dispositif optique du LDH est illustré en Fig. 7.4 ; c'est un interféromètre optique fibré de type Mach-Zehnder. La source de lumière est une diode laser monofréquence à fibre optique monomode à 45 mW (Newport SWL-7513-H-P) à longueur d'onde  $\lambda = 785$  nm. La rétine est éclairée avec une exposition constante de 1,5 mW sur une zone circulaire de quelques mm de diamètre. Le faisceau laser est focalisé dans le plan focal avant de l'œil de sorte que la lumière est collimatée à l'intérieur de l'œil et illumine la rétine sur une zone étendue. Ce niveau d'irradiation est conforme aux niveaux d'exposition de la norme internationale pour les instruments ophtalmiques ISO 15004-2:2007. Les expériences ont reçu l'autorisation d'un comité de protection des personnes ainsi que de l'ANSM (étude IMA-MODE).

Un cube séparateur de faisceaux polarisé (PBS) est utilisé dans le bras de l'objet pour éclairer l'œil et recueillir la lumière rétrodiffusée par la rétine. Le PBS sépare les polarisations linéaires : il réfléchit entièrement le faisceau lumineux d'illumination et seule la composante à polarisation transverse de la lumière rétrodiffusée par la rétine est transmise vers les voies d'imagerie. Ce montage permet de filtrer la réflexion spéculaire sur la cornée parce qu'elle conserve la polarisation initiale, tout en laissant passer la moitié de la lumière diffusée dans la rétine qui est dépolarisée à cause de la diffusion multiple et de la biréfringence des tissus intermédiaires. Le faisceau de référence  $E_{LO}$  est collimaté et considéré comme monochromatique et stable, sa polarisation est ajustée avec une plaque demi-onde et un polariseur pour optimiser les interférences. Les ondes objet et référence sont combinées à l'aide d'un cube séparateur de faisceau non polarisant et elles interfèrent

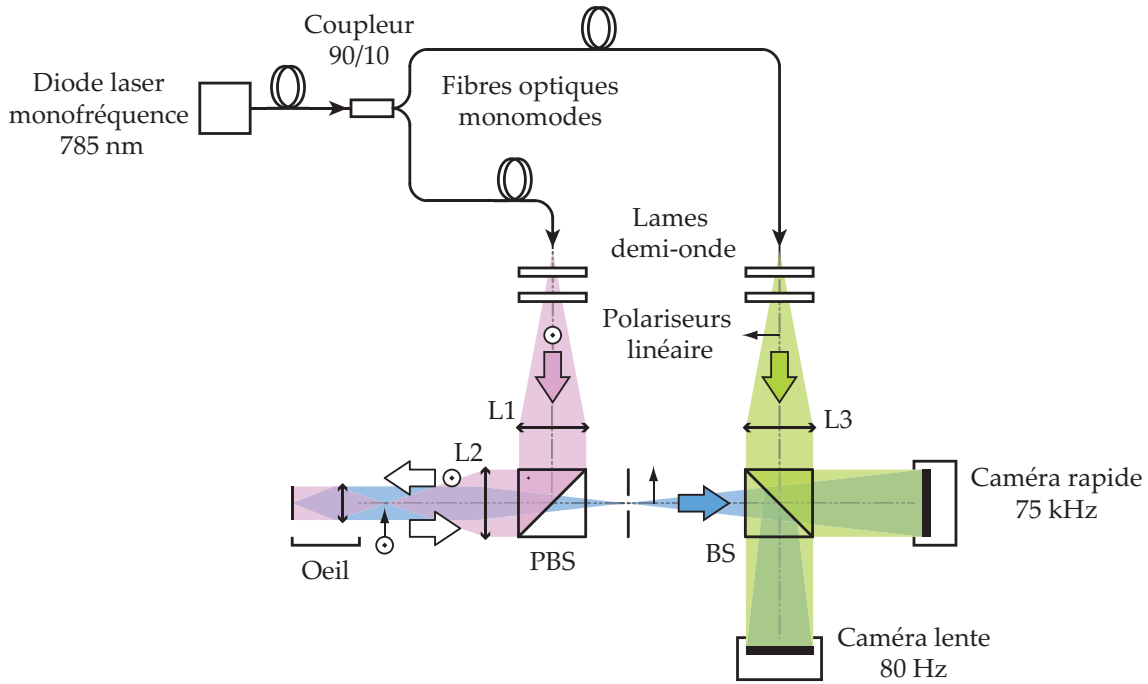


Figure 7.4: Schéma optique du LDH. L1, L2 et L3 sont des lentilles convergentes. BS : Cube séparateur. PBS : Cube séparateur de polarisations. La source de lumière est une diode laser mono-fréquence (SWL-7513-H-P, Newport) fibrée à un coupleur. La sortie 90% du coupleur est utilisée par le bras de l'objet pour illuminer l'œil. La lumière rétrodiffusée par la rétine est élargie par effet Doppler ; elle interfère avec le faisceau de référence sur deux voies d'imagerie. Une caméra lente (80 Hz) est utilisée pour la visualisation de l'expérience en temps réel, et une caméra ultra-rapide (75 kHz) est utilisée pour enregistrer des données traitées en temps différé.

sur les capteurs des deux caméras.

Ces deux caméras sont utilisées pour réaliser des mesures holographiques. La même figure d'interférence est enregistrée simultanément sur leurs deux capteurs : une caméra CMOS lente (Ximea - xiQ, cadence 80 Hz,  $2048 \times 2048$  pixels, encodée sur 8 bit, taille des pixels  $5.5 \mu\text{m}$ ) pour contrôler en temps réel l'expérience, et une caméra CMOS ultra-rapide (Ametek - Phantom V2511, cadence jusqu'à 75 kHz en format  $512 \times 512$ , efficacité quantique 40%, profondeur des pixels 12 bits, taille des pixels  $28 \mu\text{m}$ ) dont les données sont traitées en temps différé. Ces caméras lente et ultrarapide réalisent des mesures respectivement à bande étroite et à bande large. La caméra ultrarapide fournit des mesures de flux sanguin de meilleure qualité mais les images sont enregistrées sur sa mémoire embarquée, il faut donc plusieurs minutes pour transférer l'enregistrement sur l'ordinateur (de taille typique de 132 go). La caméra lente permet de contrôler en temps réel l'expérience avec une mesure de plus faible qualité. Avec l'approche à large bande, la fréquence de la caméra Nyquist permet d'échantillonner sans aliasing l'ensemble du spectre Doppler, alors qu'avec l'approche à bande étroite, seule une petite partie du spectre Doppler est utilisée efficacement. La partie qui suit détaille l'approche suivie pour traiter les images de la caméra rapide.

### 7.2.3 Traitement des images

L'interferogramme formé sur la caméra est décrit par l'équation  $I = |E_{LO} + E|^2$ , où  $E$  est le champ optique élargi par effet Doppler, et  $E_{LO}$  le champ optique de référence. La fréquence du laser est  $3.8 \times 10^{14}$  Hz, les décalages de fréquence Doppler pour les tissus biologiques sont donc extrêmement faibles devant la fréquence optique du laser. Cependant, dans les

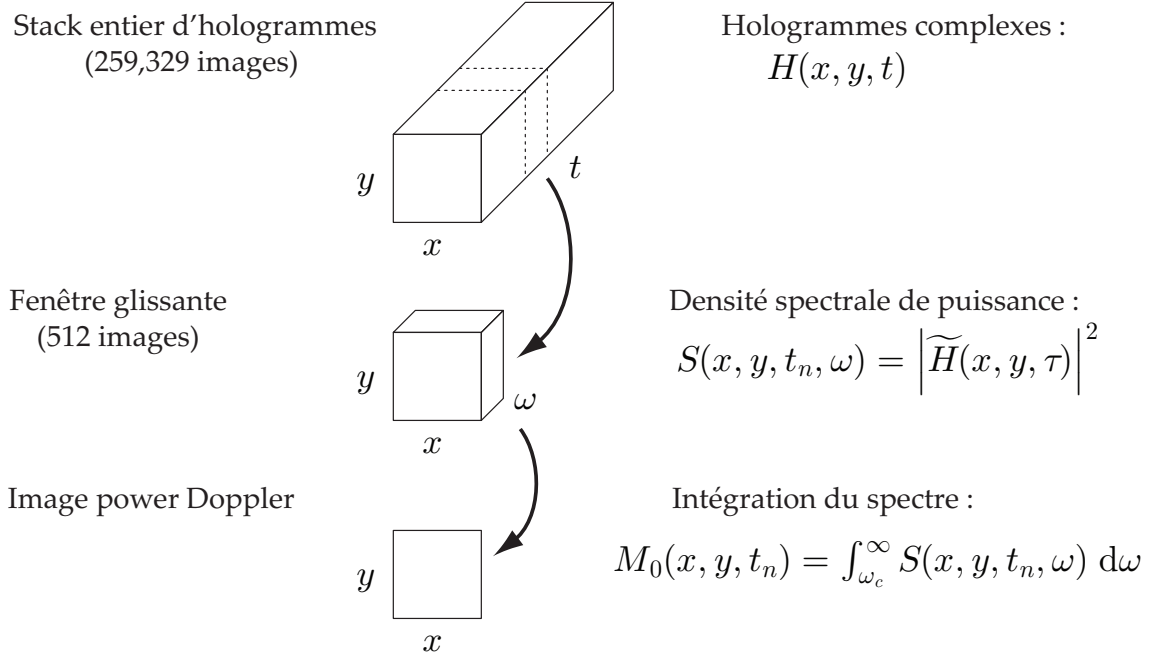


Figure 7.5: Analyse par transformée de Fourier à temps court. Une fenêtre glissante d'hologrammes est déplacée le long de la pile complète d'hologrammes reconstruits ; pour chaque fenêtre, la densité spectrale de puissance Doppler (DPSD) est calculée à partir de l'amplitude carré de la transformée de Fourier suivant l'Eq. (7.3). Une image unique dont le contraste révèle les flux sanguin est obtenue en intégrant les hautes fréquences de la DPSD suivant l'Eq. (7.4). L'image obtenue  $M_0$  est appelée image power Doppler. Des exemples d'images power Doppler pour différentes tailles de fenêtre glissante sont présentées en Fig. 7.6.

termes croisés d'interférence, la fréquence du champ optique s'annule et il ne reste que la fréquence de battement induit par l'effet Doppler. Pour les vaisseaux rétiens, la largeur typique du spectre d'élargissement Doppler peut monter jusqu'à quelques dizaines de kHz. La fréquence d'acquisition de la caméra rapide (jusqu'à 75 kHz) est donc suffisamment grande pour échantillonner les fluctuations d'intensité du spectre Doppler sans qu'il n'y ait d'aliasing. Le traitement des données consiste à mesurer les fluctuations locales des hologrammes pour retrouver un contraste de flux sanguin.

Les deux caméras réalisent des mesures holographiques. La caméra lente donne une estimation de la qualité de la reconstruction holographique qui est également valable pour la caméra rapide ; en outre, elle est capable de produire un contraste lié au flux sanguin qui permet de visualiser la zone rétinienne en cours d'imagerie pendant l'acquisition, ce qui n'est pas possible avec la caméra rapide. Le rendu holographique en temps réel se fait avec notre logiciel (Holovibes, développé par Michael Atlan) qui effectue de lourds calculs sur carte graphique. La caméra rapide est utilisée pour les mesures à large bande de l'élargissement Doppler. Les interférogrammes sont enregistrés sur le capteur à  $512 \times 512$  pixel avec une fréquence d'acquisition de  $f_s = 75$  kHz. Les interférogrammes de cette caméra sont enregistrés sur sa mémoire embarquée et ne sont donc pas accessible en temps réel ; ils sont traités en temps différé avec Matlab. Ce traitement débute avec le calcul de propagation numérique des hologrammes à valeurs complexes  $H(x, y)$ , effectué par propagation du spectre angulaire des interférogrammes enregistrés  $I(x, y)$  qui convient aux reconstructions en champ proche [83] :

$$H(x, y, z) \approx \iint \hat{I}(k_x, k_y) \exp(ik_z z) \exp(ik_x x + ik_y y) dk_x dk_y \quad (7.2)$$

où  $\hat{I}(k_x, k_y)$  est la transformée de Fourier spatiale de l'interférogramme  $I(x, y)$ . L'axe optique est suivant  $z$ , et  $k_x$ ,  $k_y$  et  $k_z = \sqrt{k^2 - k_x^2 - k_y^2}$  sont les projections des vecteurs d'onde le long des directions  $x$ ,  $y$  et  $z$  respectivement. Ensuite, une analyse par transformée de Fourier à temps court (STFT) est utilisée pour mesurer les changements de spectre Doppler au cours du temps, et donc révéler les variations dynamiques de flux sanguin. Les variations au cours du temps de la densité spectrale de puissance Doppler (DPSD) sont résolues par une fenêtre glissante constituée de  $j_{\text{win}}$  hologrammes consécutifs  $H$  dont le principe est illustré dans la Fig. 7.5. Pour chaque fenêtre, une seule image avec un contraste de flux sanguin est formée à partir de la DPSD. Tout d'abord, une transformée de Fourier rapide est effectuée le long de la dimension temporelle de la fenêtre, puis la densité spectrale de puissance est estimée à partir de l'amplitude au carré de la transformée de Fourier :

$$S(x, y, t_n, \omega) = \left| \int_{t_n}^{t_n + \sigma_{\text{win}}} H(x, y, \tau) \exp(-i\omega\tau) d\tau \right|^2 \quad (7.3)$$

À partir de cette densité spectrale de puissance, il est possible de calculer la puissance du spectre  $M_0$  ainsi que sa fréquence moyenne  $f_{\text{mean}}$  :

$$M_0(x, y, t_n) = \int S(x, y, t_n, \omega) d\omega \quad (7.4)$$

$$f_{\text{mean}}(x, y, t_n) = \frac{\int S(x, y, t_n, \omega) \omega d\omega}{\int S(x, y, t_n, \omega) d\omega} \quad (7.5)$$

L'intégrale du spectre, ou moment d'ordre zéro, permet d'obtenir ce qui est appelé ici une image power Doppler  $M_0$ . L'aire sous la courbe de la DPSD représente le nombre de photons ayant été décalés en fréquence au-dessus d'un certain seuil, et donc le nombre diffuseurs se déplaçant à une vitesse supérieure au seuil de fréquence. Les images  $M_0$  représentent donc la quantité de globules rouges en mouvement, c'est-à-dire le volume sanguin. Le décalage en fréquence moyen  $f_{\text{mean}}$  est quant à lui censé refléter la vitesse moyenne de la zone échantillonnée. La bande de fréquence sur laquelle est mené le calcul de  $M_0$  et  $f_{\text{mean}}$  résulte d'un compromis entre la qualité du signal et la sensibilité aux petits flux. En effet les basses fréquences contiennent à la fois le signal Doppler due aux mouvements globaux de l'œil, et celui des faibles vitesses, donc des faibles flux. En pratique, la limite basse d'intégration du spectre est généralement choisie entre 2 et 10 kHz.

Une fois l'image  $M_0$  ou  $f_{\text{mean}}$  calculée, la fenêtre glissante est déplacée le long de la dimension temporelle de la pile d'hologrammes. De cette façon, une séquence d'images power Doppler est constituée et permet de mesurer le débit sanguin à chaque instant du cycle cardiaque. Les variations de débit sanguin au sein d'une fenêtre ne peuvent pas être distinguées, la résolution temporelle de l'instrument est donc déterminée par la taille de la fenêtre utilisée. Pour une fréquence d'échantillonnage  $f_S$ , la durée de la fenêtre et donc la résolution temporelle est  $\sigma_{\text{win}} = \frac{j_{\text{win}}}{f_S}$ .

En conclusion, l'œil est illuminé avec une diode laser monofréquence. Le déplacement des globules rouges dans les vaisseaux provoque un élargissement Doppler du faisceau rétrodiffusé. On mesure cet élargissement par interférence avec un faisceau de référence pour retrouver des informations sur le flux sanguin. Le traitement du signal repose sur une analyse de Fourier à fenêtre glissante.

### 7.3 Premiers résultats dans la rétine *in vivo*

Nous présentons dans cette section des images obtenues en imageant des rétines humaines *in vivo* dans le cadre de l'étude IMA-MODE. Des images power Doppler  $M_0$  issues d'une mesure à  $f_S = 60$  kHz sont présentées dans la Fig. 7.6. Des tailles  $j_{\text{win}}$  de fenêtre d'analyse

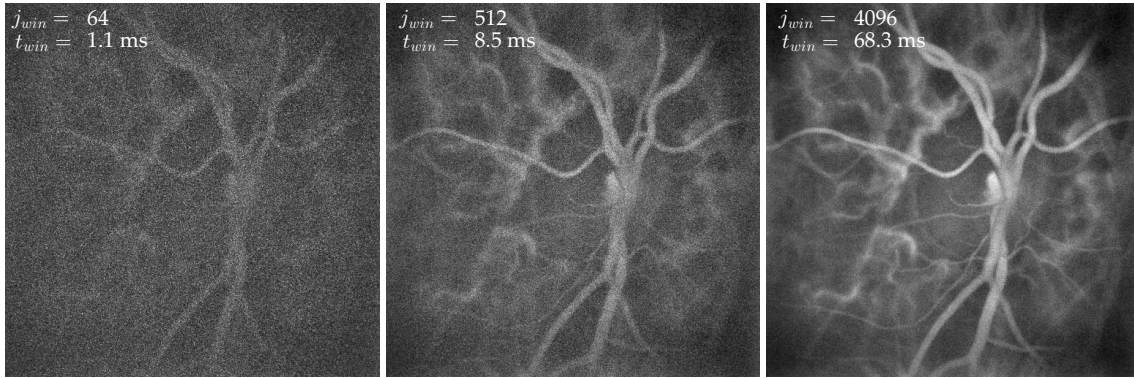


Figure 7.6: Exemples d'images power Doppler  $M_0$  calculées avec des tailles de fenêtre à temps court  $j_{win} = 64, 512$  et  $4096$  hologrammes (i.e.  $\sigma_{win} = 1.1$  ms,  $8.5$  ms et  $68.3$  ms). Ces images révèlent les structures vasculaires de la rétine de manière non-invasive sur un champ d'environ  $4 \times 4$  mm. Une fenêtre plus longue améliore le rapport signal sur bruit mais diminue la résolution temporelle de la mesure.

de 64, 512 et 4096 hologrammes ont été utilisé, ce qui équivaut à des résolution temporelles de  $\sigma_{win} = 1.1$  ms,  $8.5$  ms et  $68.3$  ms. Ces images révèlent les structures vasculaires de la rétine de manière non-invasive. En effet, l'élargissement Doppler est plus grand dans les zones plus vascularisées grâce à l'important débit d'écoulement (globules rouges se déplaçant à grande vitesse). Comme on intègre la DPSD filtrée passe-haut, les vaisseaux sanguins sont les structures les plus brillante des images  $M_0$  car ce sont les zones où le spectre Doppler est le plus large.

La largeur choisie pour la fenêtre à temps court  $\sigma_{win}$  résulte d'un compromis entre la résolution temporelle et le rapport signal sur bruit. Une fenêtre plus longue améliore considérablement le rapport signal sur bruit mais diminue la résolution temporelle de la mesure. L'intégration du signal sur une période de temps plus longue améliore le SNR car moyenner la mesure sur plus de points en temps permet de réduire le bruit de la mesure spectrale. Cependant ceci n'est valable qu'à condition que l'amplitude des déplacements latéraux reste limitée à moins que quelques pixels, sinon il peut y avoir un flou de bougé dommageable à l'image. Ainsi, pour des fenêtres excessivement longues, les mouvements involontaires des yeux limitent l'amélioration du rapport signal-bruit. Par ailleurs, il n'est pas possible de séparer deux événements se produisant au cours d'une même fenêtre : la durée de la fenêtre glissante  $\sigma_{win}$  définit la résolution temporelle de l'instrument.

Dans la Fig. 7.7, on s'intéresse à mieux comprendre les exigences en termes de fréquence d'acquisition pour réaliser des mesures laser Doppler holographique à large bande. Pour ce faire, la même zone d'une rétine humaine est mesurée avec différentes fréquences d'acquisitions et sur plusieurs bandes spectrales. Quatre mesures centrées sur la tête du nerf optique ont été effectuées à des fréquences d'échantillonnage de 10, 20, 39 et 75 kHz avec la caméra Phantom V2511. Pour chaque mesure, le temps d'exposition de la caméra a été réglé au maximum (soit respectivement 100, 50, 25,6, 13,3  $\mu$ s). La rétine a été éclairée avec la même exposition pour toutes les acquisitions, seule la puissance du bras de référence a été ajustée en utilisant des densités neutres afin d'ajuster la saturation des pixels. Pour chaque mesure, les images power Doppler ont été calculées sur des bandes de fréquences accessibles parmi 1-3, 3-5, 5-10, 10-19.5 et 19.5-37.5 kHz. Cela permet d'étudier l'effet de la bande de fréquence de calcul de  $M_0$  et de la fréquence d'échantillonnage  $f_s$  sur les mesures power Doppler.

L'analyse par STFT est effectuée avec des tailles de fenêtres glissantes de  $j_{win} = 128, 256, 512, 1024$  hologrammes pour les acquisitions à  $f_s = 10, 20, 39,$  et  $75$  kHz. Ainsi, les résolutions temporelles des analyses STFT sont approximativement les mêmes pour toutes les acquisitions ( $\sigma_{win} \approx 13$  ms). Pour chaque mesure, le signal power Doppler  $M_0$

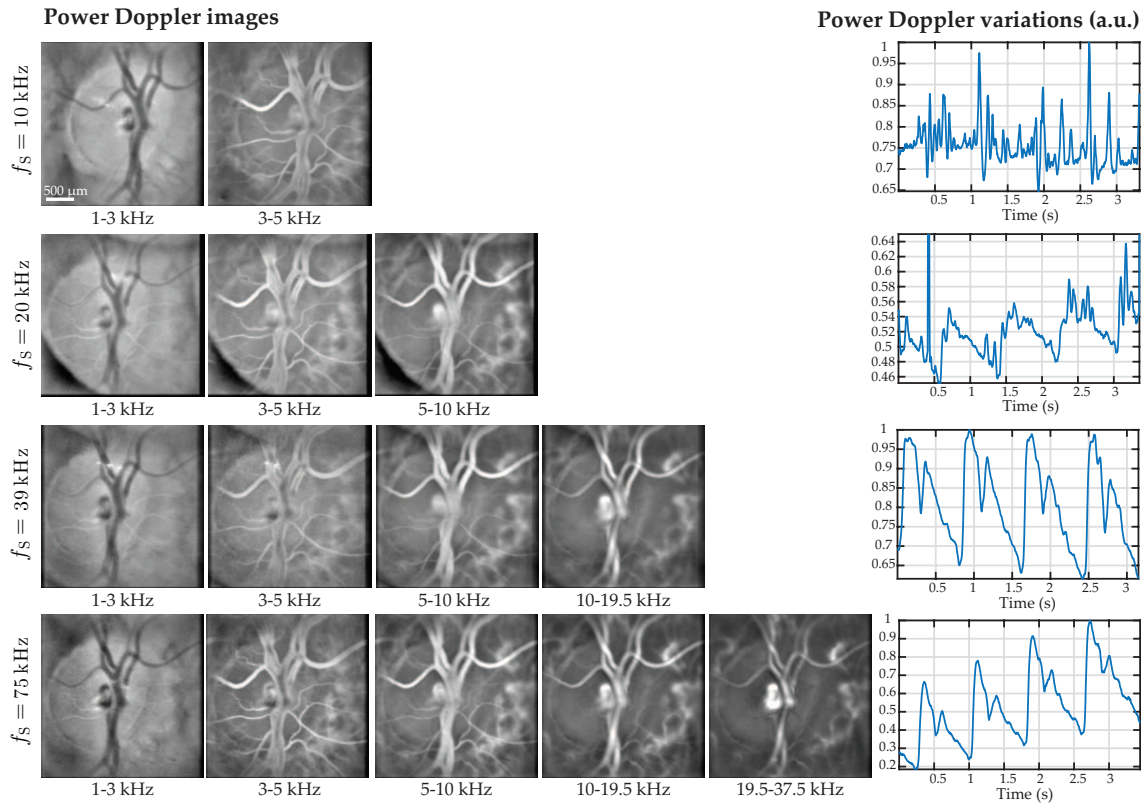


Figure 7.7: Etude sur l'effet de la fréquence d'acquisition et de la bande spectrale de calcul de  $M_0$ . La même zone d'une rétine humaine est mesurée avec une fréquence d'acquisition de 10, 20, 39 et 75 kHz. Pour les fréquences les plus basses, l'onde de pouls n'est pas mesurable car le signal dynamique est dominé par le bruit. De plus les images montrent que le contraste au cœur de vaisseau est sombre à cause du sous-échantillonnage de l'élargissement Doppler. A contrario à très haute fréquence, le signal cardiaque est bien mesuré car le spectre est convenablement échantillonné tout en étant séparé des contributions parasites.

a été mesuré dans une même région d'intérêt centré sur l'artère centrale de la rétine. Le signal dynamique est calculé en utilisant les bandes de fréquences les plus élevées possibles selon la fréquence d'échantillonnage :  $[f_1, f_2] = 3-5$  kHz, 5-10 kHz, 10-19.5 et 19.5-37.5 kHz, pour  $f_s = 10, 20, 39$  et 75kHz respectivement. Les images power Doppler à basse fréquence montrent un signal plus faible dans la lumière du vaisseau car l'élargissement Doppler y est sous-échantillonné. Le signal dynamique mesuré avec la bande de fréquence la plus basse 3-5 kHz ne permet pas d'observer les variations lié au cycle cardiaque car le signal est dominé par le bruit. Cependant, pour la bande de fréquences supérieure (5-10 kHz), la courbe typique de l'onde de pouls artérielle est reconnaissable. Lorsqu'un battement cardiaque se produit, l'augmentation de la vitesse des globules rouges dans les vaisseaux provoque momentanément un élargissement spectral Doppler plus important qui est révélé par l'analyse par STFT. Une dernière observation est que pour les deux bandes de fréquences les plus élevées, la différence est moindre. En y regardant de plus près, il est cependant possible de voir qu'un sous-échantillonnage se produit brièvement au moment du pic systolique.

La conclusion de la Fig. 7.7 est donc qu'il nous faut mesurer l'élargissement spectral Doppler jusqu'à des fréquences d'échantillonnage de l'ordre de 75 kHz. Pour une fréquence d'échantillonnage trop faible, la partie de la DPSD correspondant au flux sanguin pulsatile est sous-échantillonnée, aliasée et mélangée à des fréquences basses de plus grande amplitude et n'est pas récupérable. Le signal de power Doppler est alors incomplet et les

mesures ne sont pas correctement représentatives du flux sanguin.

### 7.3.1 Mesures de flux dans les artères et veines de la rétine

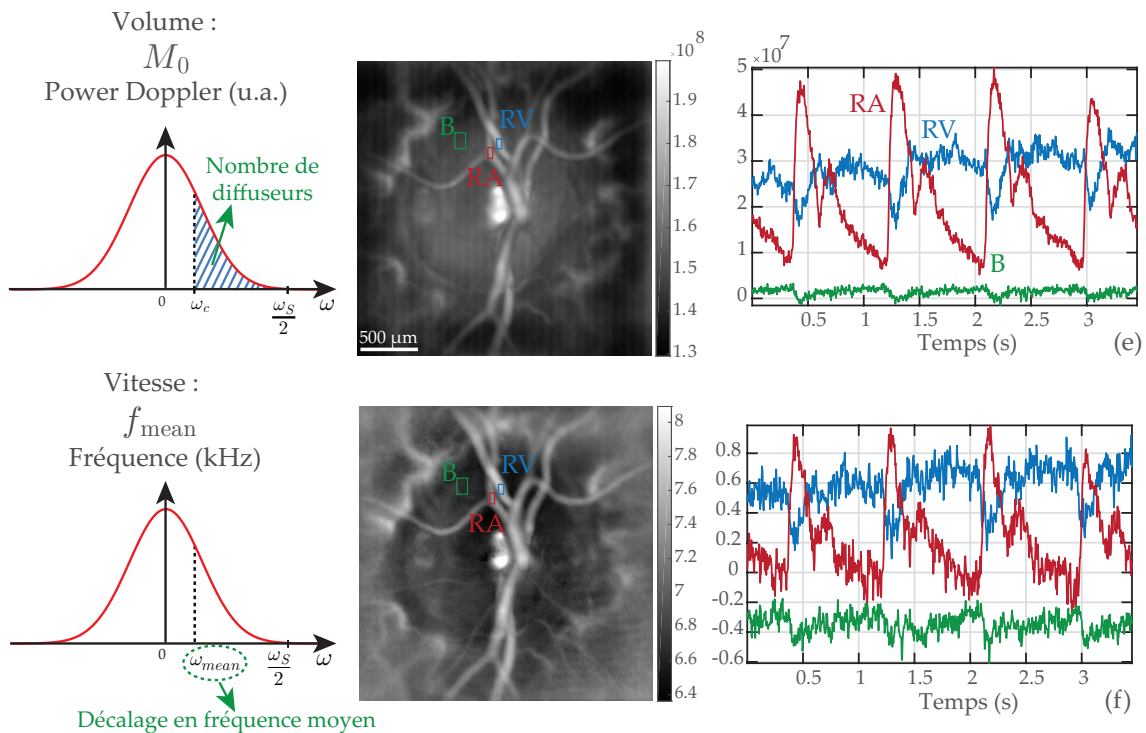


Figure 7.8: Power Doppler  $M_0$  et décalage en fréquence moyen  $f_{mean}$  sont calculés à partir de la même mesure. Le power Doppler représente le volume sanguin alors que le décalage en fréquence mesure la vitesse locale moyenne. Les traces temporelles sont mesurées dans une artère (rouge) et une veine (bleu) de la rétine, et dans une zone dépourvue de vaisseaux visibles (vert). L'onde de pouls est nettement visible dans l'artère mais pas dans la veine.

Comme nous venons de le voir, la résolution temporelle de l'instrument est suffisamment bonne pour observer les variations pulsatiles de flux sanguin qui se produisent au cours du cycle cardiaque. Nous explorons ici les mesures qu'il est possible de réaliser dans les artères et veines de la rétine. Dans la Fig. 7.8, on mesure les variations pulsatiles dans une artère (rouge), une veine (bleu) et une zone dépourvue de larges vaisseaux (vert). La moyenne spatiale de power Doppler  $M_0$  de décalage en fréquence moyen  $f_{mean}$  est calculée dans ces trois régions d'intérêt.

Une première observation est qu'à première vue, power Doppler et décalage en fréquence moyen semblent donner sensiblement les mêmes résultats sur les images et sur les traces temporelles. Le power Doppler est moins bruité, c'est pourquoi on le préférera au décalage en fréquence moyen dans la suite de ce résumé.

Pendant la systole (où la tension artérielle est maximale à la suite de la contraction des muscles cardiaques) et la diastole (détente des muscles cardiaques et tension artérielle minimale), on observe des variations de flux sanguin dans les vaisseaux. Cependant ces variations ne sont pas les mêmes dans les artères et dans les veines. Dans l'artère on observe l'onde de pouls, et dans la veine un signal de forme cycloïdale. Le flux sanguin est plus fort dans l'artère que dans la veine pendant la systole, et à l'inverse plus faible pendant la diastole. L'amplitude de variation du signal dans l'artère est donc plus grande que dans la veine. Cette observation est en accord avec ce que l'on attend d'un point de vue physiologique, car l'ondée systolique de flux sanguin est amortie par la barrière des

capillaires. Le LDH est donc capable de mesurer avec une haute résolution temporelle et quantitativement, bien que seulement dans un système d'unités arbitraires, les variations de flux sanguin. Cependant mesurer la forme des variations de flux peut déjà apporter des nouveaux renseignements sur le système vasculaire, car la forme de l'onde de pouls est déterminée par les caractéristiques physiologiques du corps.

### 7.3.2 Différenciation artério-veineuse

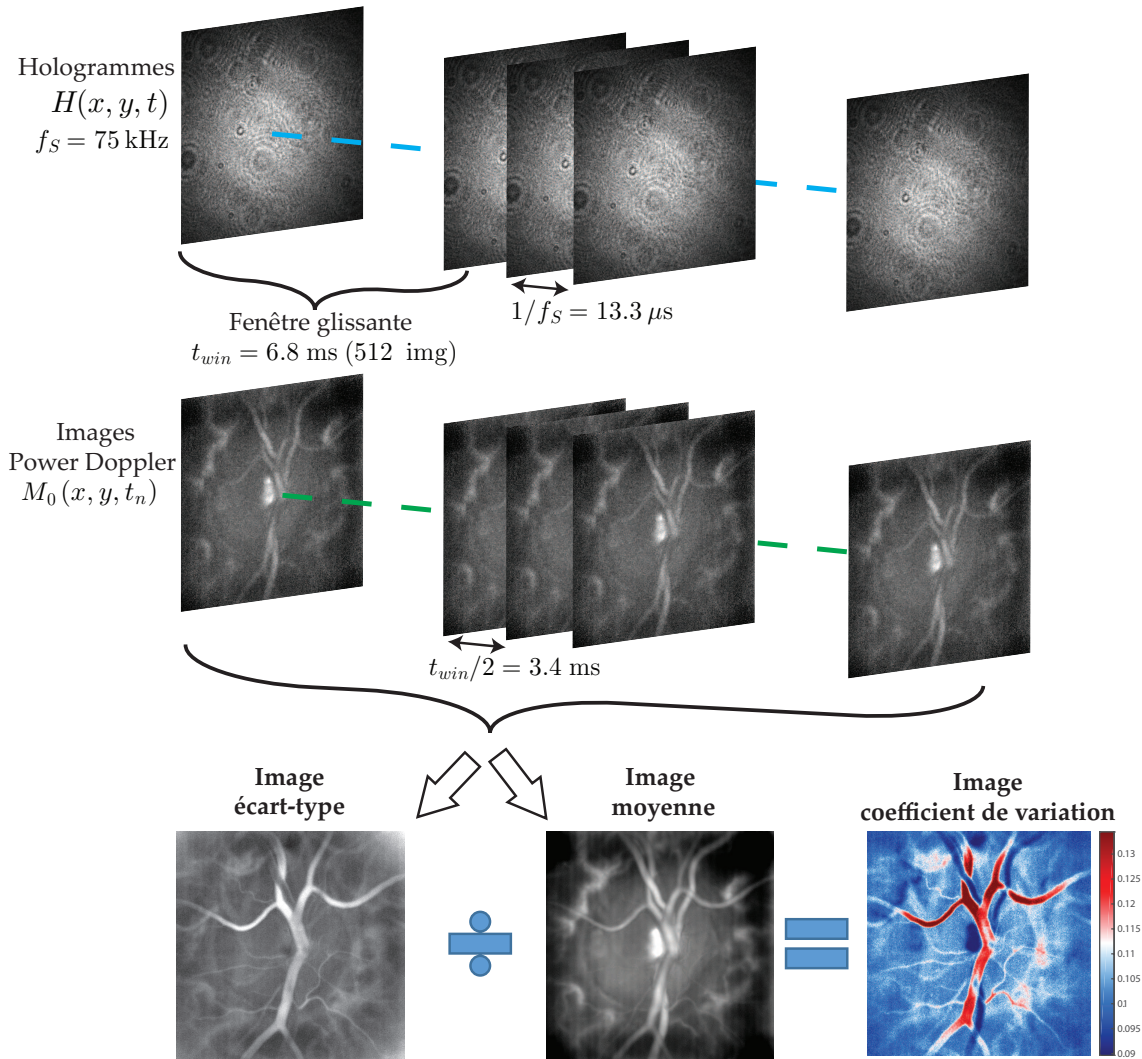


Figure 7.9: Résumé du traitement d'images. A partir de la pile initiale d'hologrammes, l'analyse par STFT fournit un film d'images power Doppler qui révèlent les variations de flux sanguin au cours du temps. On calcule les images écart-type et moyenne de ce film, et on calcule leur ratio ce qui permet d'obtenir une image du coefficient de variation local. Cette image différencie efficacement les artères et les veines de la rétine car les variations systolodiastoliques de flux sanguin sont plus grandes dans les artères.

Il est possible d'utiliser le fait que les variations de flux sanguin sont plus grandes dans les artères que dans les veines pour les différencier automatiquement. Le traitement d'images pour arriver à ce résultat est présenté dans la Fig. 7.9. La pile initiale d'hologrammes est analysée par STFT et on génère un film d'images power Doppler qui révèlent les variations de flux sanguin dans la rétine au cours du temps. A partir de ce film, on calcule deux images : l'image écart-type et l'image moyenne. Le rapport de ces deux images nous donne une image du coefficient de variation, calculé en chaque pixel suivant

la dimension temporelle. Cette image permet de différencier efficacement les artères et les veines de la rétine car la moyenne du flux est la même dans les artères et veines, mais les variations sont plus fortes dans les artères que dans les veines. En conséquence, le coefficient de variation est plus élevé dans les artères que dans les veines. Avec le gradient de couleur choisie pour représenter cette image, les artères ressortent en rouge et les veines en bleu.

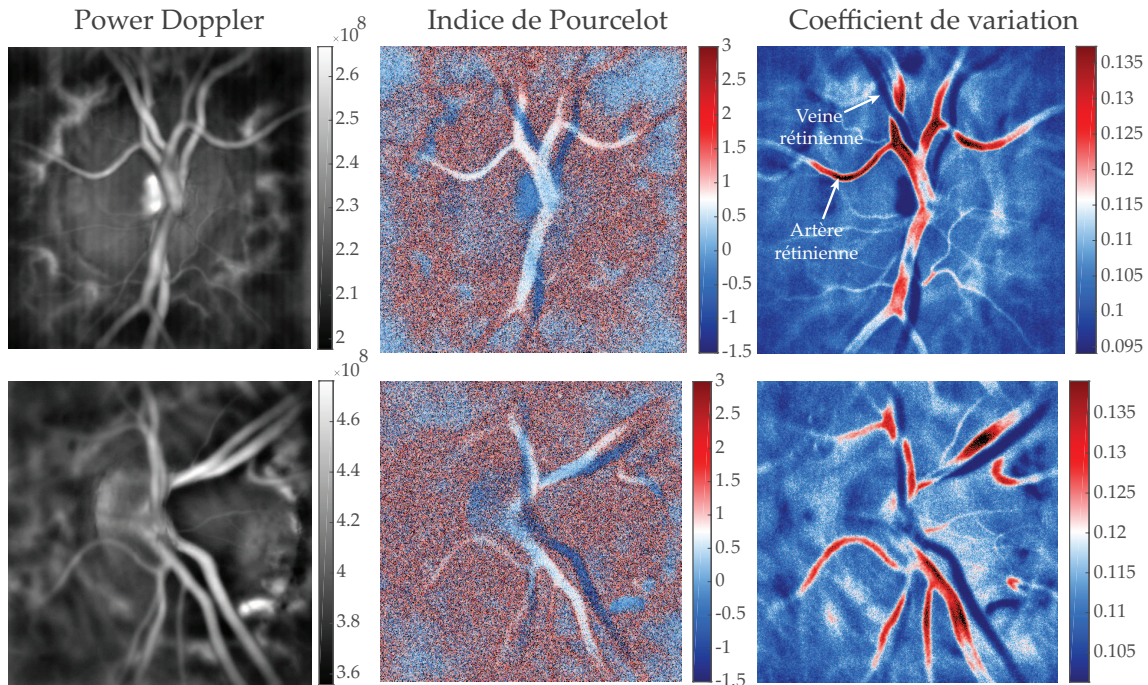


Figure 7.10: Flux sanguin moyen et variations cardiaques. Sur les images power Doppler moyennées sur un cycle cardiaque, les artères et les veines ne peuvent être pas distinguées car le volume transporté pendant un cycle cardiaque est le même. Cependant, sur les images où l'on calcule l'indice de Pourcelot ou bien le coefficient de variation, les artères et les veines sont différenciées car le flux sanguin varie de manière différente dans les artères et les veines. Ces cartes permettent de caractériser de manière quantitative les variations de flux.

Dans la Fig. 7.10, on analyse le flux sanguin moyen et ses variations au cours du cycle cardiaque. Sur les images power Doppler moyennées sur un cycle cardiaque, les artères et les veines ne peuvent être distinguées car le volume total transporté pendant un cycle cardiaque est le même dans les deux types de vaisseaux. Cependant, sur les images où l'on calcule l'indice de Pourcelot ou bien le coefficient de variation, les artères et les veines sont différenciées car le flux sanguin varie de manière différente dans les artères et les veines. Ces cartes permettent de caractériser de manière quantitative les variations de flux qui se produisent au cours du cycle cardiaque.

## 7.4 Application à l'imagerie de la choroïde

La choroïde est un tissu hautement vascularisé qui pourvoit aux besoins des photorécepteurs et de l'épithélium pigmentaire rétinien. L'implication de la choroïde dans les maladies de la rétine suscite un intérêt croissant. Cependant, l'étude de l'anatomie de la choroïde et de la circulation des flux sanguins choroïdiens reste difficile car il n'existe pas d'instrument capable de l'imager de manière satisfaisante. En effet les photorécepteurs et cellules épithéliales forment une barrière optique difficilement franchissable pour les instruments conventionnels. Nous montrons ici que le LDH peut imager les vaisseaux

choroïdiens avec une résolution spatiale comparable à celle de l'ICG-A ou de l'OCT. A l'inverse de ces deux méthodes, le LDH image la choroïde avec un contraste fonctionnel en flux sanguin, ce qui lui permet de différencier les artères et veines choroïdiennes.

#### 7.4.1 Le LDH révèle non-invasivement la choroïde

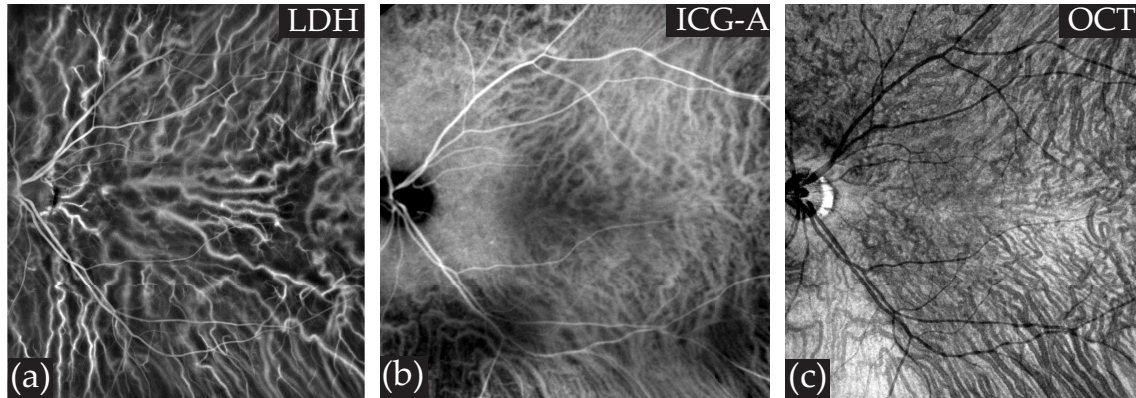


Figure 7.11: Imagerie multimodale de la choroïde. (a) Le LDH est capable de révéler de manière non-invasive les vaisseaux choroïdiens avec un contraste de flux sanguin (montage de 5x5 images). (b) L'ICG-A est une méthode invasive qui permet de révéler correctement les veines de la choroïde, mais pas les artères. Le contraste de l'image est lié à la présence du colorant. (c) L'OCT en-face permet de révéler les vaisseaux de la choroïde mais comme pour l'ICG, le contraste n'est pas fonctionnel.

On compare dans la Fig. 7.11 les images de la choroïde que l'on peut obtenir avec notre instrument et avec les instruments commerciaux qui font référence pour l'imagerie de la choroïde. Les images en Fig. 7.11(a), (b) et (c) montrent respectivement la choroïde d'un même œil imagé par LDH, ICG-A (Spectralis, Heidelberg), et OCT en-face (Plex Elite 9000, Zeiss). Il est très intéressant de remarquer que chacune de ces images révèle la choroïde, mais que ce ne sont pourtant pas exactement les mêmes vaisseaux qui sont révélés avec chacun des instruments.

Pour mieux interpréter ces images, il faut garder en tête la manière dont elles sont formées. En ICG-A, les structures vascularisées sont révélées grâce à la présence du colorant. Cet agent de contraste circule d'abord dans le réseau artériel, puis dans la choriocapillaire, avant de s'attarder longuement dans le système veineux. L'ICG-A ne peut donc révéler que très fugacement le réseau artériel de la choroïde, mais est assez efficace pour révéler le réseau veineux. L'OCT permet également de faire des images de la choroïde grâce au phénomène de diffusion vers l'avant de la lumière par les globules rouges. Les vaisseaux choroïdiens apparaissent alors avec un contraste sombre sur les images d'OCT en-face. Cependant ce contraste n'est pas lié au débit sanguin, les images d'OCT permettent de visualiser le réseau vasculaire choroïdien mais sont finalement de peu d'intérêt pour les cliniciens car elles ne permettent pas d'obtenir plus d'informations sur la circulation du flux sanguin.

Enfin, le LDH est sensible à l'élargissement Doppler et aux fortes vitesses, et nous avons pu comprendre grâce à ces premières images de la choroïde avec un contraste quantitatif de flux qu'il y a de fortes différences entre flux veineux et flux artériels. L'asymétrie unique du réseau vasculaire choroïdien fait que le sang circule beaucoup plus vite dans les artères que dans les veines : le LDH révèle donc mieux les artères que les veines de la choroïde.

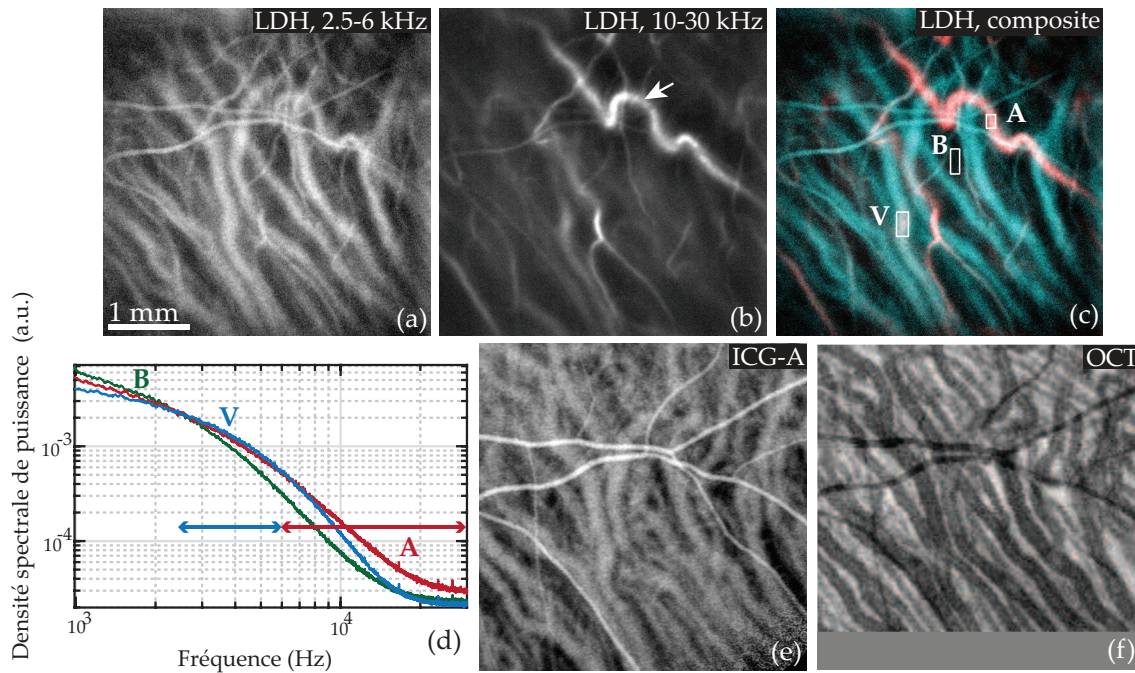


Figure 7.12: Analyse hyperspectrale en LDH et comparaison avec autres modalités d'imageries. (a) et (b) : Images power Doppler basses (2.5-6 kHz) et hautes (10-30 kHz) fréquences. (c) Image composite couleur obtenue par combinaison des deux images précédentes. (d) Mesure du spectre Doppler dans 3 régions d'intérêts (A, V, B), les veines se dégagent à basse fréquence alors que les artères ressortent à haute fréquence. (e) et (f) : images d'ICG-A et d'OCT de la même région, aucune différenciation des vaisseaux n'est possible, les artères de la choroïde ne sont pas ou peu visibles.

#### 7.4.2 Différenciation artério-veineuse par analyse des débits

Dans la Fig. 7.12, on mène une analyse hyperspectrale du signal Doppler afin de mieux comprendre quelles sont les structures que l'on observe en LDH, en ICG-A et en OCT. La même zone est imagée avec ces trois modalités, mais cette fois on analyse différemment le signal laser Doppler. Au lieu de constituer une seule image power Doppler pour toutes les fréquences Doppler en intégrant la DPSD de 2 à 30 kHz (cf. Eq. 7.4), on constitue deux images en utilisant deux bandes de fréquence, basse et haute. Ces deux images révèlent les faibles flux sanguins (basses fréquences) et les forts flux sanguins (hautes fréquences). On peut voir en Fig. 7.12(a) et (b) que ce sont pas les mêmes vaisseaux sanguins qui apparaissent à basse et à haute fréquence. Cette différence est très flagrante lorsque l'on combine en une seule image composite ces deux images basse/haute fréquence en utilisant les couleurs cyan/rouge en Fig. 7.12(c). La comparaison avec l'ICG-A et l'OCT est frappante car ces deux modalités d'imageries ne révèlent pas ou peu les artères de la choroïde.

En somme, nous montrons ici qu'une analyse de Fourier du spectre Doppler permet de différencier les vaisseaux choroïdiens en fonction de leur flux sanguin. Cette analyse conduit à une différenciation artério-veineuse qui n'a pas d'équivalent dans les autres modalités d'imagerie de la choroïde.

On cherche ici à investiguer comment la profondeur des artères dans le réseau choroïdien (i.e. positionnement en superficie ou au fond de la choroïde) affecte leur visibilité avec le LDH. En effet la choroïde est un tissu à 3D où les vaisseaux sont complètement emmêlés. Dans la Fig. 7.13(a), (b) et (c), on montre la même zone imagée par LDH, ICG-A, et OCT en-face. On montre dans la Fig. 7.13(d) le long d'une artère plusieurs coupes (aux endroits indiqués par les flèches) avec un instrument d'OCT commercial, et

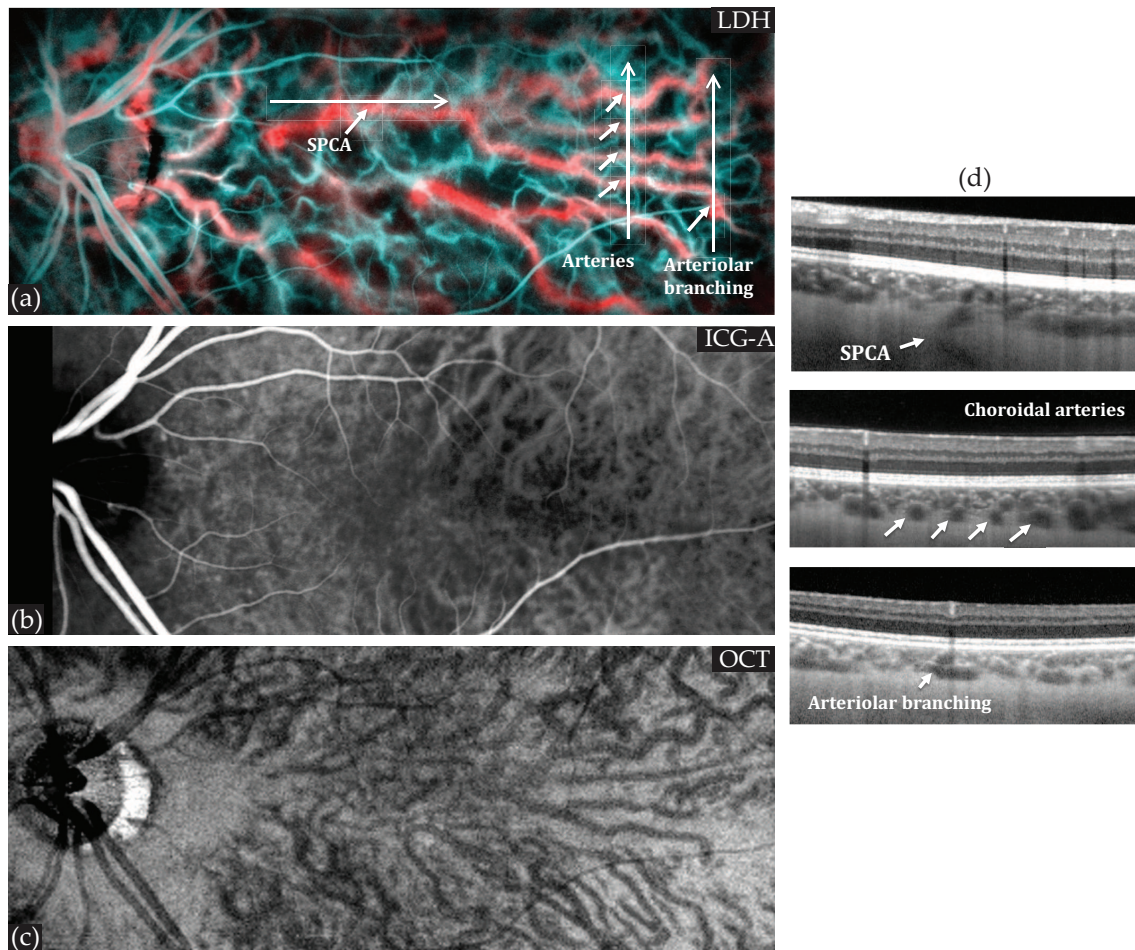


Figure 7.13: Analyse des images de LDH en combinaison avec l'OCT. (a) Image composite de LDH avec les basses/hautes fréquences en cyan/rouge : les artères et artérioles de la choroïde sont visibles. (b) et (c): ICG-A et OCT en face de la même région, les vaisseaux de type artériel y sont peu ou pas visibles. (d) Vue en coupe par OCT dans les zones indiqués en (a) montrant que l'on peut observer en LDH les artères depuis les artères ciliaires postérieures de la sclère jusqu'aux branchements pré-capillaires. Malgré leur position au fond de la choroïde, les artères choroïdiennes sont très bien observées avec le LDH.

on peut retrouver les mêmes vaisseaux et ainsi situer en profondeur les vaisseaux révélés par le LDH.

On peut voir que malgré leur position au fond de la choroïde, les artères choroïdiennes peuvent être très bien révélées avec le LDH. Il est même possible de suivre une artère choroïdienne de la SPCA sclérale jusqu'au moment où elle se ramifie en artérioles. Les images en face d'ICG-A et d'OCT montrent que ces structures vasculaires de la choroïde ne peuvent pas ou à peine être révélées par les autres modalités d'imagerie. Le LDH est donc capable d'imager cette partie de l'anatomie avec un contraste tout-à-fait inédit. Cependant le LDH fournit des images 2D, et il est très intéressant de combiner les informations de flux du LDH et de profondeur en OCT pour avoir une encore meilleure compréhension de l'anatomie choroïdienne.

La Fig. 7.14 illustre l'utilité du contraste composite basse/haute fréquence apporté par le LDH par rapport à l'ICG-A et à l'OCT sur un champ étendu. L'image en Fig. 7.14(a) a été générée en suivant le processus décrit précédemment, basses/hautes fréquences en cyan/rouge. Encore une fois, les images en Fig. 7.14(b) et (c) ont été obtenues avec les instruments commerciaux qui font référence pour l'imagerie de la choroïde. On peut

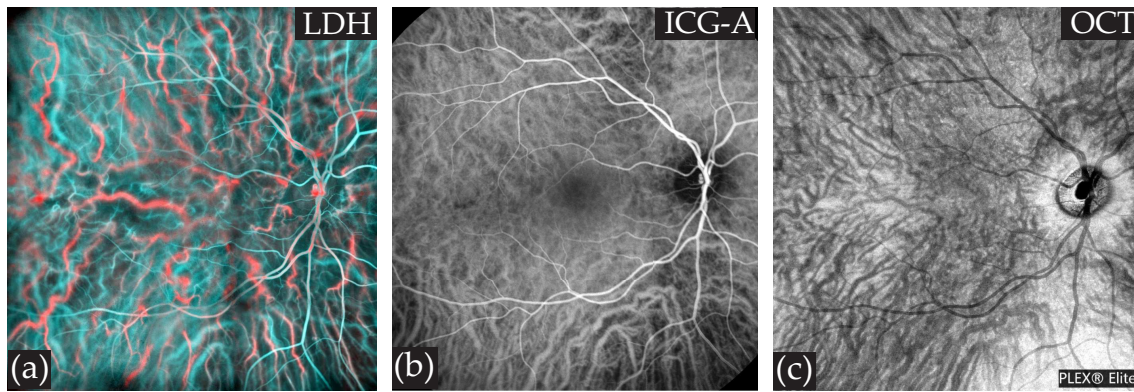


Figure 7.14: Imagerie multimodale de la choroïde. (a) L'image composite du LDH permet de révéler à la fois les artères et les veines de la choroïde et de les identifier (montage de 5x5 images). (b) L'ICG-A ne révèle efficacement que les veines de la choroïde. (c) L'OCT permet de révéler indifféremment les deux types de vaisseaux mais ne permet pas de les identifier.

retrouver certains vaisseaux en communs sur les trois images. Le contraste fonctionnel du LDH permet de mieux interpréter comment le flux sanguin circule à l'intérieur des vaisseaux choroïdiens.

#### 7.4.3 Différenciation artério-veineuse rétinienne et choroïdienne

Dans la Fig. 7.15, nous démontrons la capacité du LDH à effectuer une différenciation artério-veineuse dans la rétine et la choroïde en utilisant une méthode adaptée pour chaque réseau vasculaire. Dans la Fig. 7.15, on montre d'abord une image grand champ en SLO, où deux sous-régions sont encadrées et imagées par ICG-A et OCT. Ces images ne permettent pas de discrimination artério-veineuse, ni dans la rétine ni dans la choroïde. On montre dans la partie inférieure de la Fig. les images de ces mêmes régions que l'on fait en LDH. Comme nous l'avons montré précédemment, avec les images du coefficient de variation local, les artères de la rétine ressortent en rouge vif et les veines en bleu profond. De la même manière, les images composites basses/hautes fréquences permettent de différencier les artères et veines de la choroïde : les artères choroïdiennes se distinguent clairement en rouge car elles transportent un flux plus important, tandis que les veines choroïdiennes peuvent être vues en cyan.

Le LDH est capable d'effectuer une différenciation artério-veineuse de tous les vaisseaux du pôle postérieur de l'œil car il effectue des mesures quantitatives du flux sanguin. Pour le système vasculaire rétinien, la discrimination se fait sur la base de l'hémodynamique respective des artères et des veines en utilisant des cartes du coefficient de variation. Dans la choroïde, la ségrégation artério-veineuse repose sur la capacité d'analyser le flux dans les vaisseaux choroïdiens : le flux dans les artères est plus fort que dans les veines. L'ICG-A et l'OCT, comme ils n'ont pas de contraste quantitatif, ne sont pas en mesure d'apporter une information aussi riche sur le flux sanguin.

## 7.5 Conclusion et perspectives

En conclusion, les travaux menés dans le cadre de cette thèse démontrent un fort potentiel clinique en ophtalmologie pour le LDH en raison de la richesse des informations qu'il fournit. Dans la première partie de ce résumé, nous avons décrit le fonctionnement de l'instrument. L'œil est illuminé avec une diode laser monofréquence et le flux de globules rouges dans les vaisseaux provoque un élargissement Doppler du faisceau rétrodiffusé. On mesure cet élargissement par interférence avec un faisceau de référence pour retrouver

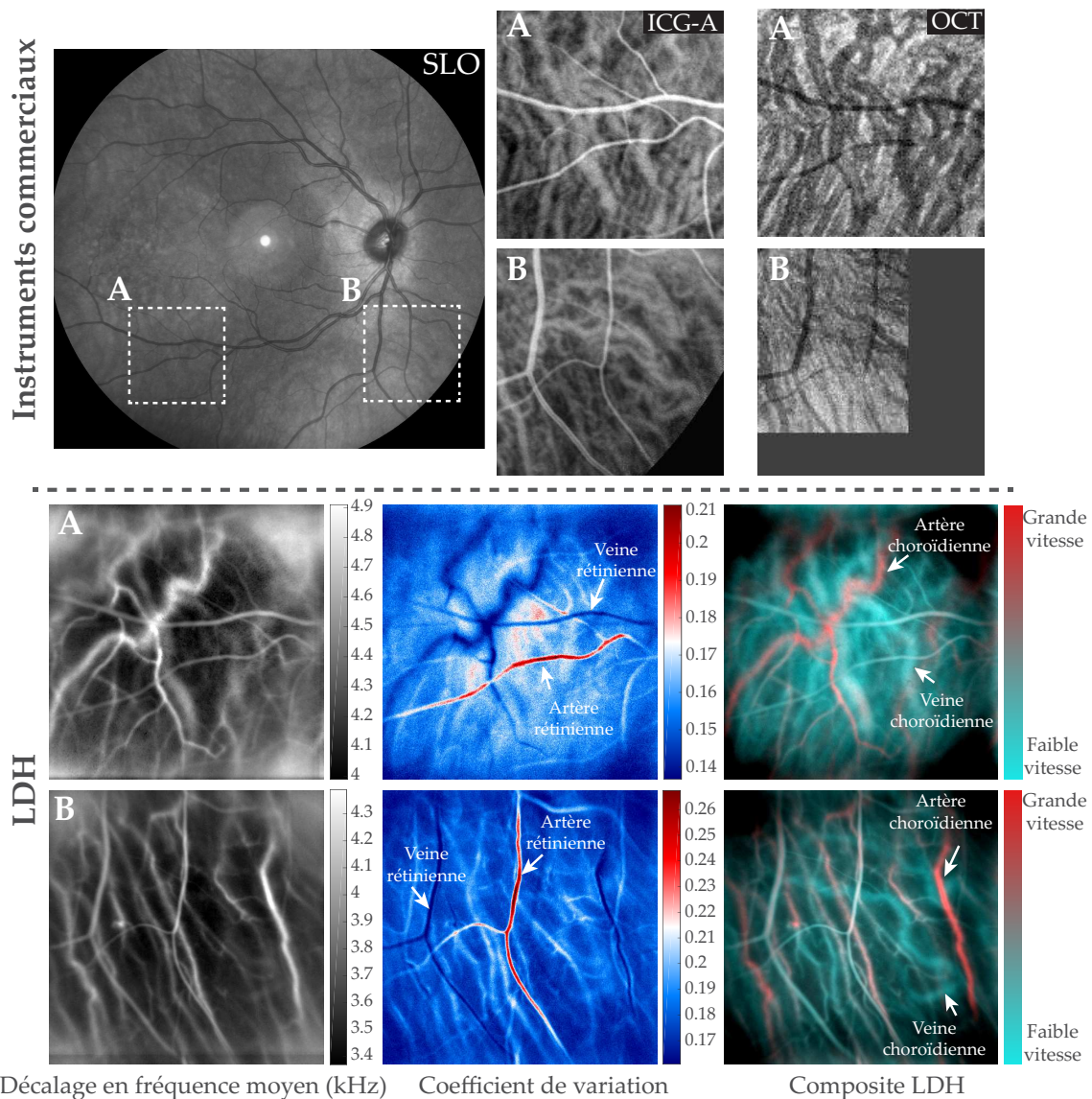


Figure 7.15: Imagerie de deux zones A et B par instruments commerciaux et par LDH : le SLO, l'ICG-A et l'OCT ne permettent pas de différencier les vaisseaux veineux/artériels de la rétine et de la choroïde. Le LDH permet quant à lui de révéler différemment les vaisseaux artériels et veineux à la fois de la rétine et choroïde en mesurant les variations temporelles de flux sanguin (rétine) ou en utilisant une analyse en fréquence Doppler (choroïde). Le contraste fonctionnel dont dispose le LDH est donc très utile pour étudier la vascularisation du fond de l'oeil.

des informations sur le flux sanguin. Le traitement du signal repose sur une analyse de Fourier à fenêtre glissante. Les images de flux sanguin sont calculées à partir de l'énergie du spectre filtré passe-haut. L'ajout d'un faisceau de référence pour effectuer des mesures Doppler laser est le facteur clé pour effectuer des mesures LDH de haute qualité grâce au gain de cohérence qu'il introduit. L'accès complet au spectre Doppler permet de séparer la lumière faiblement décalée (i.e. mouvements globaux) de la lumière fortement décalée (i.e. flux sanguin) et ainsi de réaliser de mesure de haute qualité.

A la vue de ces travaux, au moins deux importantes applications se distinguent pour l'instrument en ophtalmologie. Premièrement, nous avons démontré sa capacité à effectuer des mesures du débit sanguin rétinien avec une très bonne combinaison de résolution spatiale/temporelle/débit sur un champ de vue étendu. Grâce à ces mesures, nous avons pu trouver des comportements d'écoulement dynamiques distincts dans les artères et les

veines rétiniennes mais visiblement interreliés. Il a également été démontré que le LDH permet de réaliser une cartographie complète de l'indice de résistivité locale qui offre la possibilité d'identifier sans ambiguïté les artères et veines rétiniennes en fonction de leurs variations systolodiastoliques propres. Comparativement aux instruments commercialisés pour la mesure du débit sanguin oculaire, le LDH a certainement une carte à jouer grâce à sa résolution temporelle inégalée et sa capacité à réaliser des mesures quantitatives.

Deuxièmement, compte tenu de la richesse des images de la choroïde obtenues par le LDH comparativement à l'ICG-A et l'OCT, le LDH pourrait également améliorer notre compréhension de l'anatomie et de la circulation du flux sanguin dans ce réseau vasculaire encore mal connu. Nous avons montré que le LDH peut révéler de manière non-invasive le réseau vasculaire choroïdien, et particulièrement le réseau artériel en raison du plus grand débit sanguin dans les artères. Il a aussi été montré que le LDH permet de distinguer les artères et les veines du pôle postérieur de l'œil grâce à une analyse spectrale de l'élargissement Doppler. Combinée aux informations volumétriques apportées par l'OCT, le LDH offre la possibilité d'obtenir des informations essentielles sur la physiologie de la choroïde de manière non invasive. Le LDH pourrait donc considérablement aider à mieux comprendre l'implication de la choroïde dans certaines maladies de la rétine, comme la chorioretinopathie séreuse centrale.

Ces travaux de thèse démontrent donc que le LDH semble être prometteur pour l'étude des pathologies vasculaires affectant l'œil. Le LDH pourrait en particulier être utile pour une meilleure compréhension de l'étiologie des affections de la rétine, éventuellement leur dépistage plus précoce, et enfin pour un meilleur suivi des traitements administrés en s'assurant que l'œil est correctement perfusé.



# Bibliography

- [1] Carl Sagan. *Pale blue dot: A vision of the human future in space*. Random House Digital, Inc., 1997.
- [2] Irvin Rock and Jack Victor. Vision and touch: An experimentally created conflict between the two senses. *Science*, 143(3606):594–596, 1964.
- [3] Claire Nollett, Barbara Ryan, Nathan Bray, Catey Bunce, Robin Casten, Rhianon Tudor Edwards, David Gillespie, Daniel J Smith, Miles Stanford, and Tom H Margrain. Depressive symptoms in people with vision impairment: a cross-sectional study to identify who is most at risk. *BMJ open*, 9(1):e026163, 2019.
- [4] Matthew A Windsor, Sissi JJ Sun, Kevin D Frick, Eric A Swanson, Philip J Rosenfeld, and David Huang. Estimating public and patient savings from basic research, a study of optical coherence tomography in managing antiangiogenic therapy. *American journal of ophthalmology*, 185:115–122, 2018.
- [5] Costantino Iadecola. Neurovascular regulation in the normal brain and in alzheimer’s disease. *Nat Rev Neurosci*, 5(5):347–360, May 2004.
- [6] Gilbert T Feke, Bradley T Hyman, Robert A Stern, and Louis R Pasquale. Retinal blood flow in mild cognitive impairment and alzheimer’s disease. *Alzheimer’s & Dementia: Diagnosis, Assessment & Disease Monitoring*, 1(2):144–151, 2015.
- [7] Jean C Cruz Hernández, Oliver Bracko, Calvin J Kersbergen, Victorine Muse, Mohammad Haft-Javaherian, Maxime Berg, Laibaik Park, Lindsay K Vinarcsik, Iryna Ivasyk, Daniel A Rivera, et al. Neutrophil adhesion in brain capillaries reduces cortical blood flow and impairs memory function in alzheimer’s disease mouse models. *Nature neuroscience*, 22(3):413, 2019.
- [8] M. Simonutti, M. Paques, J. A. Sahel, M. Gross, B. Samson, C. Magnain, and M. Atlan. Holographic laser doppler ophthalmoscopy. *Opt. Lett.*, 35(12):1941–1943, 2010.
- [9] Caroline Magnain, Amandine Castel, Tanguy Boucneau, Manuel Simonutti, Isabelle Ferezou, Armelle Rancillac, Tania Vitalis, José-Alain Sahel, Michel Paques, and Michael Atlan. Holographic laser doppler imaging of microvascular blood flow. *JOSA A*, 31(12):2723–2735, 2014.
- [10] B. Samson and M. Atlan. Short-time fourier transform laser doppler holography. *Journal of the European Optical Society - Rapid publications*, 8(0), 2013.
- [11] Mathilde Pellizzari, Manuel Simonutti, Julie Degardin, J-A Sahel, Mathias Fink, Michel Paques, and Michael Atlan. High speed optical holography of retinal blood flow. *Optics Letters*, 41(15):3503–3506, 2016.
- [12] Choroidal Vascular Network. Developmental anatomy of the retinal and choroidal vasculature. *The Retina and Its Disorders*, 179, 2011.

- [13] JP Campbell, M Zhang, TS Hwang, ST Bailey, DJ Wilson, Y Jia, and D Huang. Detailed vascular anatomy of the human retina by projection-resolved optical coherence tomography angiography. *Scientific reports*, 7:42201, 2017.
- [14] Mircea Mujat, Yang Lu, Gopi Maguluri, Youbo Zhao, Nicusor Iftimia, and R Daniel Ferguson. Visualizing the vasculature of the entire human eye posterior hemisphere without a contrast agent. *Biomedical Optics Express*, 10(1):167–180, 2019.
- [15] Sohan Singh Hayreh. Posterior ciliary artery circulation in health and disease the weisenfeld lecture. *Investigative Ophthalmology & Visual Science*, 45(3):749–757, 2004.
- [16] Albert Alm and Anders Bill. Ocular and optic nerve blood flow at normal and increased intraocular pressures in monkeys (*macaca irus*): a study with radioactively labelled microspheres including flow determinations in brain and some other tissues. *Experimental Eye Research*, 15(1):15–29, 1973.
- [17] Albert Alm and Anders Bill. The oxygen supply to the retina, ii. effects of high intraocular pressure and of increased arterial carbon dioxide tension on uveal and retinal blood flow in cats: A study with radioactively labelled microspheres including flow determinations in brain and some other tissues. *Acta physiologica Scandinavica*, 84(3):306–319, 1972.
- [18] Leonard M Parver. Temperature modulating action of choroidal blood flow. *Eye*, 5(2):181, 1991.
- [19] Leonard M Parver, Charles Auker, and David O Carpenter. Choroidal blood flow as a heat dissipating mechanism in the macula. *American journal of ophthalmology*, 89(5):641–646, 1980.
- [20] A Bill, G Sperber, and K Ujiie. Physiology of the choroidal vascular bed. *International ophthalmology*, 6(2):101–107, 1983.
- [21] Michel E Safar. Arterial stiffness as a risk factor for clinical hypertension. *Nature Reviews Cardiology*, 15(2):97, 2018.
- [22] Michel E Safar and Patrick Lacolley. Disturbance of macro-and microcirculation: relations with pulse pressure and cardiac organ damage. *American Journal of Physiology-Heart and Circulatory Physiology*, 293(1):H1–H7, 2007.
- [23] L Pourcelot. Diagnostic ultrasound for cerebral vascular diseases. *Present and future of diagnostic ultrasound*, pages 141–147, 1976.
- [24] Susana Martinez-Conde, Stephen L Macknik, Xoana G Troncoso, and Thomas A Dyar. Microsaccades counteract visual fading during fixation. *Neuron*, 49(2):297–305, 2006.
- [25] Susana Martinez-Conde, Stephen L Macknik, and David H Hubel. The role of fixational eye movements in visual perception. *Nature reviews neuroscience*, 5(3):229, 2004.
- [26] Susana Martinez-Conde. Fixational eye movements in normal and pathological vision. *Progress in brain research*, 154:151–176, 2006.
- [27] Douglas R Anderson. What happens to the optic disc and retina in glaucoma? *Ophthalmology*, 90(7):766–770, 1983.
- [28] Harry A Quigley. Neuronal death in glaucoma. *Progress in retinal and eye research*, 18(1):39–57, 1999.

- [29] William H. Morgan, Martin L. Hazelton, and Dao-Yi Yu. Retinal venous pulsation: Expanding our understanding and use of this enigmatic phenomenon. *Progress In Retinal And Eye Research*, 55:82–107, 2016.
- [30] Josef Flammer, Mona Pache, and Thérèse Resink. Vasospasm, its role in the pathogenesis of diseases with particular reference to the eye. *Progress in retinal and eye research*, 20(3):319–349, 2001.
- [31] Ali S Hafez, Regina Bizzarro, Denise Descovich, and Mark R Lesk. Correlation between finger blood flow and changes in optic nerve head blood flow following therapeutic intraocular pressure reduction. *Journal of glaucoma*, 14(6):448–454, 2005.
- [32] Yukihiro Shiga, Hiroshi Kunikata, Naoko Aizawa, Naoki Kiyota, Yukiko Maiya, Yu Yokoyama, Kazuko Omodaka, Hidetoshi Takahashi, Tomoki Yasui, Keiichi Kato, et al. Optic nerve head blood flow, as measured by laser speckle flowgraphy, is significantly reduced in preperimetric glaucoma. *Current Eye Research*, 41(11):1447–1453, 2016.
- [33] Anna Sophie Mursch-Edlmayr, Nikolaus Luft, Dominika Podkowinski, Michael Ring, Leopold Schmetterer, and Matthias Bolz. Laser speckle flowgraphy derived characteristics of optic nerve head perfusion in normal tension glaucoma and healthy individuals: a pilot study. *Scientific Reports*, 8(1):5343, 2018.
- [34] Lloyd Paul Aiello, Robert L Avery, Paul G Arrigg, Bruce A Keyt, Henry D Jampel, Sabera T Shah, Louis R Pasquale, Hagen Thieme, Mami A Iwamoto, John E Park, et al. Vascular endothelial growth factor in ocular fluid of patients with diabetic retinopathy and other retinal disorders. *New England Journal of Medicine*, 331(22):1480–1487, 1994.
- [35] Tim M Curtis and Tom A Gardiner. Ocular blood flow in diabetes: Contribution to the microvascular lesions of diabetic retinopathy. In *Ocular Blood Flow*, pages 365–387. Springer, 2012.
- [36] Vinod Patel, Salwan Rassam, Richard Newsom, Jutta Wiek, and Eva Kohner. Retinal blood flow in diabetic retinopathy. *Bmj*, 305(6855):678–683, 1992.
- [37] Thomas A Ciulla, Alon Harris, Paul Latkany, Heidi C Piper, Oliver Arend, Hana Garzozzi, and Bruce Martin. Ocular perfusion abnormalities in diabetes. *Acta Ophthalmologica Scandinavica*, 80(5):468–477, 2002.
- [38] Allen C Clermont and Sven-Erik Bursell. Retinal blood flow in diabetes. *Microcirculation*, 14(1):49–61, 2007.
- [39] Constantin J Pournaras, Efstratios Mendrinou, and Jean-Antoine C Pournaras. Age-related macular degeneration: Hemodynamic changes. In *Ocular Blood Flow*, pages 389–409. Springer, 2012.
- [40] Juan E Grunwald, Seenu M Hariprasad, and Joan DuPont. Effect of aging on foveolar choroidal circulation. *Archives of Ophthalmology*, 116(2):150–154, 1998.
- [41] Juan E Grunwald, Seenu M Hariprasad, Joan DuPont, Maureen G Maguire, Stuart L Fine, Alexander J Brucker, Albert M Maguire, and Allen C Ho. Foveolar choroidal blood flow in age-related macular degeneration. *Investigative ophthalmology & visual science*, 39(2):385–390, 1998.

- [42] Ephraim Friedman, Sara Krupsky, Anne Marie Lane, Setsuko S Oak, Eric S Friedman, Kathleen Egan, and Evangelos S Gragoudas. Ocular blood flow velocity in age-related macular degeneration. *Ophthalmology*, 102(4):640–646, 1995.
- [43] Peter Gæde, Pernille Vedel, Nicolai Larsen, Gunnar VH Jensen, Hans-Henrik Parving, and Oluf Pedersen. Multifactorial intervention and cardiovascular disease in patients with type 2 diabetes. *New England Journal of Medicine*, 348(5):383–393, 2003.
- [44] Toco YP Chui, Dean A VanNasdale, and Stephen A Burns. The use of forward scatter to improve retinal vascular imaging with an adaptive optics scanning laser ophthalmoscope. *Biomedical optics express*, 3(10):2537–2549, 2012.
- [45] R. D. Ferguson, D. X. Hammer, A. E. Elsner, R. H. Webb, S. A. Burns, and J. J. Weiter. Wide-field retinal hemodynamic imaging with the tracking scanning laser ophthalmoscope. *Optics Express*, 12:5198–+, August 2004.
- [46] Zhangyi Zhong, Benno L Petrig, Xiaofeng Qi, and Stephen A Burns. In vivo measurement of erythrocyte velocity and retinal blood flow using adaptive optics scanning laser ophthalmoscopy. *Optics express*, 16(17):12746–12756, 2008.
- [47] Boyu Gu, Xiaolin Wang, Michael D Twa, Johnny Tam, Christopher A Girkin, and Yuhua Zhang. Non-invasive in vivo characterization of erythrocyte motion in human retinal capillaries using high-speed adaptive optics near-confocal imaging. *Biomedical Optics Express*, 9(8):3653–3677, 2018.
- [48] Andreas Wartak, Florian Beer, Sylvia Desissaire, Bernhard Baumann, Michael Pircher, and Christoph K Hitzenberger. Investigating spontaneous retinal venous pulsation using doppler optical coherence tomography. *Scientific Reports*, 9(1):4237, 2019.
- [49] Gang Sun, Xiaoyan Liu, Ling Gao, Pu Zhang, Siyuan Wang, and Yandan Zhou. Automatic measurement of global retinal circulation in fluorescein angiography. *Journal of biomedical optics*, 23(6):065006, 2018.
- [50] Justin V Migacz, Iwona Gorczynska, Mehdi Azimipour, Ravi Jonnal, Robert J Zawadzki, and John S Werner. Megahertz-rate optical coherence tomography angiography improves the contrast of the choriocapillaris and choroid in human retinal imaging. *Biomedical Optics Express*, 10(1):50–65, 2019.
- [51] David Huang, Eric A Swanson, Charles P Lin, Joel S Schuman, William G Stinson, Warren Chang, Michael R Hee, Thomas Flotte, Kenton Gregory, Carmen A Puliafito, et al. Optical coherence tomography. *science*, 254(5035):1178–1181, 1991.
- [52] Sarah Mrejen and Richard F Spaide. Optical coherence tomography: imaging of the choroid and beyond. *Survey of Ophthalmology*, 58(5):387–429, 2013.
- [53] WooJhon Choi, Kathrin J Mohler, Benjamin Potsaid, Chen D Lu, Jonathan J Liu, Vijaysekhar Jayaraman, Alex E Cable, Jay S Duker, Robert Huber, and James G Fujimoto. Choriocapillaris and choroidal microvasculature imaging with ultrahigh speed oct angiography. *PloS one*, 8(12):e81499, 2013.
- [54] Kanheng Zhou, Shaozhen Song, Qinqin Zhang, Zhongdi Chu, Zhihong Huang, and Ruikang K Wang. Visualizing choriocapillaris using swept-source optical coherence tomography angiography with various probe beam sizes. *Biomedical Optics Express*, 10(6):2847–2860, 2019.

- [55] A. F. Fercher and J. D. Briers. Flow visualisation by means of single-exposure speckle photography. *Opt. Commun.*, 37:326–330, 1981.
- [56] AF Fercher, M Peukert, and E Roth. Visualization and measurement of retinal blood flow by means of laser speckle photography. *Optical Engineering*, 25(6):256731, 1986.
- [57] J. D. Briers and Sian Webster. Laser speckle contrast analysis (lasca): a non-scanning, full-field technique for monitoring capillary blood flow. *Journal of Biomedical Optics*, 1(2):174–179, 1996.
- [58] Lisa M. Richards, S. M. Shams Kazmi, Janel L. Davis, Katherine E. Olin, and Andrew K. Dunn. Low-cost laser speckle contrast imaging of blood flow using a webcam. *Biomed. Opt. Express*, 4(10):2269–2283, Oct 2013.
- [59] Ashwin B Parthasarathy, Erica L Weber, Lisa M Richards, Douglas J Fox, and Andrew K Dunn. Laser speckle contrast imaging of cerebral blood flow in humans during neurosurgery: a pilot clinical study. *Journal of biomedical optics*, 15(6):066030–066030, 2010.
- [60] SM Shams Kazmi, Lisa M Richards, Christian J Schrandt, Mitchell A Davis, and Andrew K Dunn. Expanding applications, accuracy, and interpretation of laser speckle contrast imaging of cerebral blood flow. *Journal of Cerebral Blood Flow & Metabolism*, 2015.
- [61] Tetsuya Sugiyama, Makoto Araie, Charles E Riva, Leopold Schmetterer, and Selim Orgul. Use of laser speckle flowgraphy in ocular blood flow research. *Acta Ophthalmologica*, 88(7):723–729, 2010.
- [62] Klemens Fondi, Ahmed M. Bata, Nikolaus Luft, Katarzyna J. Witkowska, René M. Werkmeister, Doreen Schmidl, Matthias Bolz, Leopold Schmetterer, and Gerhard Garhöfer. Evaluation of flicker induced hyperemia in the retina and optic nerve head measured by laser speckle flowgraphy. *PLoS One*, 13(11):e0207525, 2018.
- [63] Nikolaus Luft, Piotr A. Wozniak, Gerold C. Aschinger, Klemens Fondi, Ahmed M. Bata, René M. Werkmeister, Doreen Schmidl, Katarzyna J. Witkowska, Matthias Bolz, Gerhard Garhöfer, et al. Ocular blood flow measurements in healthy white subjects using laser speckle flowgraphy. *PLoS One*, 11(12):e0168190, 2016.
- [64] Satoru Tsuda, Hiroshi Kunikata, Masahiko Shimura, Naoko Aizawa, Kazuko Omodaka, Yukihiro Shiga, Masayuki Yasuda, Yu Yokoyama, and Toru Nakazawa. Pulse-waveform analysis of normal population using laser speckle flowgraphy. *Current Eye Research*, 39(12):1207–1215, 2014.
- [65] Yukihiro Shiga, Kazuko Omodaka, Hiroshi Kunikata, Morin Ryu, Yu Yokoyama, Satoru Tsuda, Toshifumi Asano, Shigeto Maekawa, Kazuichi Maruyama, and Toru Nakazawa. Waveform analysis of ocular blood flow and the early detection of normal tension glaucoma. *Investigative ophthalmology & visual science*, 54(12):7699–7706, 2013.
- [66] Takeshi Iwase, Kentaro Yamamoto, Eimei Ra, Kenta Murotani, Shigeyuki Matsui, and Hiroko Terasaki. Diurnal variations in blood flow at optic nerve head and choroid in healthy eyes: diurnal variations in blood flow. *Medicine*, 94(6), 2015.
- [67] David Briers, Donald D Duncan, Evan R Hirst, Sean J Kirkpatrick, Marcus Larsson, Wiendelt Steenbergen, Tomas Stromberg, and Oliver B Thompson. Laser speckle contrast imaging: theoretical and practical limitations. *Journal of biomedical optics*, 18(6):066018, 2013.

- [68] François Tranquart, Olivier Bergès, Patricia Koskas, Sophie Arsene, Christian Rossazza, Pierre-Jean Pisella, and Léandre Pourcelot. Color doppler imaging of orbital vessels: personal experience and literature review. *Journal of Clinical Ultrasound*, 31(5):258–273, 2003.
- [69] Leopold Schmetterer and Jeffrey Kiel. *Ocular blood flow*. Springer Science & Business Media, 2012.
- [70] Ingeborg Stalmans, Evelien Vandewalle, Douglas R Anderson, Vital P Costa, Ronald EP Frenkel, Gerhard Garhofer, Juan Grunwald, Konstantin Gugleta, Alon Harris, Christopher Hudson, et al. Use of colour doppler imaging in ocular blood flow research. *Acta ophthalmologica*, 89(8):e609–e630, 2011.
- [71] Raksha Urs, Jeffrey A Ketterling, CH Alfred, Harriet O Lloyd, Billy YS Yiu, and Ronald H Silverman. Ultrasound imaging and measurement of choroidal blood flow. *Translational vision science & technology*, 7(5):5–5, 2018.
- [72] CE Riva, S Harino, BL Petrig, and RD Shonat. Laser doppler flowmetry in the optic nerve. *Experimental eye research*, 55(3):499–506, 1992.
- [73] CE Riva, SD Cranstoun, JE Grunwald, and BL Petrig. Choroidal blood flow in the foveal region of the human ocular fundus. *Invest. Ophthalmol. Vis. Sci.*, 35(13):4273–4281, 1994.
- [74] Martial Henri Geiser, Ulrich Diermann, and Charles E Riva. Compact laser doppler choroidal flowmeter. *Journal of Biomedical optics*, 4(4):459–465, 1999.
- [75] Charles E Riva, Martial Geiser, and Benno L Petrig. Ocular blood flow assessment using continuous laser doppler flowmetry. *Acta ophthalmologica*, 88(6):622–629, 2009.
- [76] Charles E Riva, Martial Geiser, and Benno L Petrig. Ocular blood flow assessment using continuous laser doppler flowmetry. *Acta Ophthalmologica*, 88(6):622–629, 2010.
- [77] R. Bonner and R. Nossal. Model for laser doppler measurements of blood flow in tissue. *Applied Optics*, 20:2097–2107, 1981.
- [78] Robert F Bonner and Ralph Nossal. Principles of laser-doppler flowmetry. In *Laser-Doppler blood flowmetry*, pages 17–45. Springer, 1990.
- [79] G Michelson, B Schmauss, MJ Langhans, J Harazny, and MJ Groh. Principle, validity, and reliability of scanning laser doppler flowmetry. *J. Glaucoma.*, 5(2):99–105, 1996.
- [80] Georg Michelson, Jargen Welzenbach, Istvan Pal, and Joana Harazny. Functional imaging of the retinal microvasculature by scanning laser doppler flowmetry. *International Ophthalmology*, 23(4):327–335, July 2001.
- [81] DM Squirrell, A Watts, D Evans, C Mody, and JF Talbot. A prospective evaluation of the heidelberg retina flowmeter in diagnosing ischaemia following branch retinal vein occlusion: a masked, controlled comparison with fluorescein angiography. *Eye*, 15(3):261, 2001.
- [82] Vincent Bacot, Matthieu Labousse, Antonin Eddi, Mathias Fink, and Emmanuel Fort. Time reversal and holography with spacetime transformations. *Nature Physics*, 12(10):972, 2016.

- [83] Joseph W Goodman. *Introduction to Fourier optics*. Roberts and Company Publishers, 2005.
- [84] U. Schnars and W. P. O. Juptner. Digital recording and numerical reconstruction of holograms. *Meas. Sci. Technol.*, 13:R85–R101, 2002.
- [85] Thomas Kreis. *Handbook of holographic interferometry*. 2005.
- [86] Charles E Riva. Laser doppler techniques for ocular blood velocity and flow. In *Ocular Blood Flow*, pages 123–146. Springer, 2012.
- [87] <http://holovibes.com>.
- [88] L Puyo, I Ferezou, A Rancillac, M Simonutti, M Paques, J-A Sahel, M Fink, and Michael Atlan. Pulsatile microvascular blood flow imaging by short-time fourier transform analysis of ultrafast laser holographic interferometry. In *Biomedical Engineering International Conference (BMEiCON), 2015 8th*, pages 1–5. IEEE, 2015.
- [89] Mathieu Leclercq and Pascal Picart. Digital fresnel holography beyond the shannon limits. *Opt. Express*, 20(16):18303–18312, Jul 2012.
- [90] E. Cuche, P. Marquet, and C. Depeursinge. Simultaneous amplitude-contrast and quantitative phase-contrast microscopy by numerical reconstruction of fresnel off-axis holograms. *Applied Optics*, 38:6994, 1999.
- [91] Etienne Cuche, Pierre Marquet, and Christian Depeursinge. Spatial filtering for zero-order and twin-image elimination in digital off-axis holography. *Applied Optics*, 39(23):4070, 2000.
- [92] A.E. Siegman. The antenna properties of optical heterodyne receivers. *Applied Optics*, 5(10):1588, 1966.
- [93] Vincent J Corcoran. Directional characteristics in optical heterodyne detection processes. *Journal of Applied Physics*, 36(6):1819–1825, 1965.
- [94] Dierck Hillmann, Hendrik Spahr, Carola Hain, Helge Sudkamp, Gesa Franke, Clara Pfäffle, Christian Winter, and Gereon Hüttmann. Aberration-free volumetric high-speed imaging of in vivo retina. *Scientific reports*, 6:35209, 2016.
- [95] Helge Sudkamp, Dierck Hillmann, Peter Koch, Malte vom Endt, Hendrik Spahr, Michael Münst, Clara Pfäffle, Reginald Birngruber, and Gereon Hüttmann. Simple approach for aberration-corrected oct imaging of the human retina. *Optics letters*, 43(17):4224–4227, 2018.
- [96] Laurin Ginner, Tilman Schmoll, Abhishek Kumar, Matthias Salas, Nastassia Pricoupenko, Lara M. Wurster, and Rainer A. Leitgeb. Holographic line field en-face oct with digital adaptive optics in the retina in vivo. *Biomed. Opt. Express*, 9(2):472–485, Feb 2018.
- [97] Peng Xiao, Viacheslav Mazlin, Kate Grieve, José-Alain Sahel, Mathias Fink, and A Claude Boccara. In vivo high-resolution human retinal imaging with wavefront-correctionless full-field oct. *Optica*, 5(4):409–412, 2018.
- [98] Robert W Knighton and Xiang-Run Huang. Linear birefringence of the central human cornea. *Investigative ophthalmology & visual science*, 43(1):82–86, 2002.
- [99] Kristina Irsch, Boris Gramatikov, Yi-Kai Wu, and David Guyton. Modeling and minimizing interference from corneal birefringence in retinal birefringence scanning for foveal fixation detection. *Biomedical optics express*, 2(7):1955–1968, 2011.

- [100] Hani N Sabbah and Paul D Stein. Valve origin of the aortic incisura. *American Journal of Cardiology*, 41(1):32–38, 1978.
- [101] Joanna Kur, Eric A Newman, and Tailoi Chan-Ling. Cellular and physiological mechanisms underlying blood flow regulation in the retina and choroid in health and disease. *Progress in retinal and eye research*, 31(5):377–406, 2012.
- [102] Constantin J Pournaras, Elisabeth Rungger-Brändle, Charles E Riva, Sveinn H Hardarson, and Einar Stefansson. Regulation of retinal blood flow in health and disease. *Progress in retinal and eye research*, 27(3):284–330, 2008.
- [103] K Singh, C Dion, S Costantino, M Wajszilber, MR Lesk, and T Ozaki. Development of a novel instrument to measure the pulsatile movement of ocular tissues. *Experimental eye research*, 91(1):63–68, 2010.
- [104] Kanwarpal Singh, Carolyne Dion, Marcelo Wajszilber, Tsuneyuki Ozaki, Mark R Lesk, and Santiago Costantino. Measurement of ocular fundus pulsation in healthy subjects using a novel fourier-domain optical coherence tomography. *Investigative ophthalmology & visual science*, 52(12):8927–8932, 2011.
- [105] Hendrik Spahr, Dierck Hillmann, Carola Hain, Clara Pfäffle, Helge Sudkamp, Gesa Franke, and Gereon Hüttmann. Imaging pulse wave propagation in human retinal vessels using full-field swept-source optical coherence tomography. *Optics letters*, 40(20):4771–4774, 2015.
- [106] Abhishek Kumar, Wolfgang Drexler, and Rainer A Leitgeb. Subaperture correlation based digital adaptive optics for full field optical coherence tomography. *Optics express*, 21(9):10850–10866, 2013.
- [107] Laurin Ginner, Abhishek Kumar, Daniel Fechtig, Lara M Wurster, Matthias Salas, Michael Pircher, and Rainer A Leitgeb. Noniterative digital aberration correction for cellular resolution retinal optical coherence tomography in vivo. *Optica*, 4(8):924–931, 2017.
- [108] Hendrik Spahr, Clara Pfäffle, Peter Koch, Helge Sudkamp, Gereon Hüttmann, and Dierck Hillmann. Interferometric detection of 3d motion using computational sub-apertures in optical coherence tomography. *Optics express*, 26(15):18803–18816, 2018.
- [109] Laurin Ginner, Andreas Wartak, Matthias Salas, Marco Augustin, Michael Niederleithner, Lara M Wurster, and Rainer A Leitgeb. Synthetic subaperture-based angle-independent doppler flow measurements using single-beam line field optical coherence tomography in vivo. *Optics letters*, 44(4):967–970, 2019.
- [110] Dario Donnarumma, Alexey Brodoline, Daniel Alexandre, and Michel Gross. 4d holographic microscopy of zebrafish larvae microcirculation. *Optics Express*, 24(23):26887–26900, 2016.
- [111] Alexey Brodoline, Nitin Rawat, Daniel Alexandre, Nicolas Cubedo, and Michel Gross. 4d compressive sensing holographic microscopy imaging of small moving objects. *Optics Letters*, 44(11):2827–2830, 2019.
- [112] J. A. Briers and S. Webster. Quasi real-time digital version of single-exposure speckle photography for full-field monitoring of velocity or flow fields. *Optics Comm.*, 116:36–42, 1995.

- [113] Ruikang K Wang, Lin An, Peter Francis, and David J Wilson. Depth-resolved imaging of capillary networks in retina and choroid using ultrahigh sensitive optical microangiography. *Optics letters*, 35(9):1467–1469, 2010.
- [114] Amir H Kashani, Chieh-Li Chen, Jin K Gahm, Fang Zheng, Grace M Richter, Philip J Rosenfeld, Yonggang Shi, and Ruikang K Wang. Optical coherence tomography angiography: A comprehensive review of current methods and clinical applications. *Progress in Retinal and Eye Research*, 2017.





## RÉSUMÉ

---

Cette thèse porte sur l'introduction de l'holographie laser doppler (LDH) au domaine de l'ophtalmologie afin d'imager le flux sanguin dans le pôle postérieur de l'œil. Les anomalies de perfusion jouent un rôle central dans le développement des pathologies oculaires, ce qui nécessite le développement d'instruments appropriés pour mieux le comprendre. Le LDH avait déjà démontré sa capacité à effectuer une imagerie non invasive et quantitative du flux sanguin, mais uniquement chez les rongeurs. Dans cette thèse, il est montré qu'avec une caméra rapide et une analyse à transformée de Fourier à temps court sur l'élargissement Doppler, le LDH peut imager les changements de flux sanguin dans la rétine humaine au cours du cycle cardiaque avec une résolution de quelques millisecondes. Le LDH permet de mesurer les variations systolodiastoliques propres aux artères et veines rétinienne et peut être utilisée pour cartographier en plein champ l'indice de résistivité local permettant l'identification sans ambiguïté des artères et des veines de la rétine. Le LDH peut également être utilisé pour révéler la choroïde avec une qualité de contraste similaire à celle d'instruments de pointe basés sur l'angiographie au vert d'indocyanine et la tomographie par cohérence optique, mais contrairement à ces méthodes, le LDH fournit en outre un contraste quantitatif du flux sanguin. Cette capacité a été utilisée pour mettre en évidence de grandes différences de débit sanguin entre les artères et les veines choroïdiennes, une caractéristique qui peut être exploitée pour effectuer une autre différenciation artérioveineuse adaptée aux vaisseaux choroïdiens. Les décalages de fréquence Doppler plus élevés de la lumière diffusée dans les artères choroïdiennes permettent au LDH d'être particulièrement efficace pour les révéler, dans certains cas dès leur formation au niveau des artères ciliaires postérieures jusqu'aux ramifications artériolaires. Globalement, la résolution temporelle incomparable avec laquelle le LDH est capable de mesurer le flux sanguin et les nouveaux contrastes avec lequel il permet d'imager la choroïde en font un instrument prometteur pour la suite des applications cliniques.

## MOTS CLÉS

---

Holographie, Ophtalmologie, Laser Doppler, Rétine, Choroïde, Imagerie.

## ABSTRACT

---

This PhD thesis aimed at introducing laser Doppler holography (LDH) into the field of ophthalmology in order to image blood flow in the eye posterior pole. Perfusion abnormalities play a central role in the development of ocular pathologies, which calls for the development of suitable instruments to elucidate it. LDH had previously demonstrated its ability to perform non-invasive and quantitative blood flow imaging with a high temporal resolution, but only in rodents. In this thesis, it is demonstrated that with a fast camera and a short-time Fourier transform analysis of the Doppler broadening, LDH can image blood flow changes in the human retina during cardiac cycles with a resolution of a few milliseconds. LDH is able to measure distinct systolodiastolic variations in retinal arteries and veins, and can be used for a full field mapping of the local resistivity index that allows unambiguous identification of retinal arteries and veins. LDH can also be used to reveal the choroid with a contrast quality similar to that of state of art instruments based on indocyanin-green angiography and optical coherence tomography, but unlike these methods LDH additionally provides a quantitative blood flow contrast. This ability was used to bring to light large differences of blood flow between choroidal arteries and veins, which is a feature that can be exploited to perform another arteriovenous differentiation appropriate for choroidal vessels. The higher Doppler frequency shifts of light scattered in choroidal arteries allows LDH to be especially efficient to reveal them, in some cases from their formation at short posterior ciliary arteries all the way to the arterioles branching. Overall, the unmatched temporal resolution with which LDH is able to measure blood flow and the new insight it provides into the choroid are especially full of promise for further clinical applications.

## KEYWORDS

---

Holography, Ophthalmology, Laser Doppler, Retina, Choroid, Imaging.